Heteropolyacids and its modified version for the transformation of renewable feedstock's to value-added products

by

Mulik Nagesh Laxman
10CC19J26003

A thesis submitted to the
Academy of Scientific & Innovative Research
for the award of the degree of
DOCTOR OF PHILOSOPHY
in
SCIENCE

Under the supervision of
Dr. Vijay V. Bokade

CSIR National Chemical Laboratory, Pune

Academy of Scientific and Innovative Research
AcSIR Headquarters, CSIR-HRDC campus
Sector 19, Kamla Nehru Nagar,
Ghaziabad, U.P. – 201 002, India

Oct 2023

CERTIFICATE

This is to certify that the work incorporated in this Ph.D. thesis entitled, "*Heteropolyacids and its modified version for the transformation of renewable feedstock's to value-added products*", submitted by *Mulik Nagesh Laxman* to the Academy of Scientific and Innovative Research (AcSIR) in fulfillment of the requirements for the award of the Degree of *Doctor of Philosophy in Science*, embodies original research work carried-out by the student. We, further certify that this work has not been submitted to any other University or Institution in part or full for the award of any degree or diploma. Research material(s) obtained from other source(s) and used in this research work has/have been duly acknowledged in the thesis. Image(s), illustration(s), figure(s), table(s) etc., used in the thesis from other source(s), have also been duly cited and acknowledged.

(Signature of Student)
Name: Mulik Nagesh Laxman
Date: 11/09/2023

(Signature of Supervisor)
Name: Dr. V. V. Bokade
Date 11/09/2023

STATEMENTS OF ACADEMIC INTEGRITY

I Mulik Nagesh Laxman, a Ph.D. student of the Academy of Scientific and Innovative Research (AcSIR) with Registration No. 10CC19J26003 hereby undertake that, the thesis entitled "*Heteropolyacids and its modified version for the transformation of renewable feedstock's to value-added products*" has been prepared by me and that the document reports original work carried out by me and is free of any plagiarism in compliance with the UGC Regulations on *"Promotion of Academic Integrity and Prevention of Plagiarism in Higher Educational Institutions (2018)"* and the CSIR Guidelines for "*Ethics in Research and in Governance (2020)".*

SIGNATURE OF THE STUDENT

Date: 11/09/2023
Place: Pune

It is hereby certified that the work done by the student, under my supervision, is plagiarism-free in accordance with the UGC Regulations on *"Promotion of Academic Integrity and Prevention of Plagiarism in Higher Educational Institutions (2018)"* and the CSIR Guidelines for "*Ethics in Research and in Governance (2020)".*

SIGNATURE OF THE SUPERVISOR

Name : Dr. V. V. Bokade
Date : 11/09/2023
Place : Pune

Acknowledgment

The work presented in this dissertation becomes a reality with the kind support and help of many individuals. I want to acknowledge all my teachers, family members, friends, and well-wishers who always motivated me to complete this long journey confidently. I would like to extend my sincere thanks to all of them. First of all, it is a great pleasure to acknowledge my deepest thanks and gratitude to my research guide, Dr. Vijay Bokade, for his constant inspiration, motivation, guidance, and constructive criticism which helped me a lot to focus and implement my views in a proper perspective.

My sincere thanks to the former and present Head, of the Catalysis and Inorganic Chemistry Division Dr. D. Srinivas, Dr. C. S. Gopinath, and Dr. S. B. Umbarkar for allowing me to utilize the divisional facility. Former and present Director of CSIR-NCL for providing infrastructure to carry out the research work and AcSIR is acknowledged for the registration for Ph.D.

I take this opportunity to offer my sincere thanks to my DAC members, Dr. S. B. Mhaske, Dr. V. H. Rane, and Dr. S. B. Umbarkar for their constant evaluation, suggestions, and advice during my Ph.D. work.

I am also profoundly indebted to Dr. Ashish Orpe, Dr. Prashant Niphadkar, and Mr. Harishchandra Jagtap for their valuable help and support. I would like to thank the technical staff of NCL from whom I always get help in analysis Mr. Gholap sir. Mr. Deo sir, Dr. Gaydhankar, Mr. R. Jha sir.

I am also grateful to all my lab-mates Venkatesh, Pranjali, Shrinidhi, Aadesh, Amit, Dr. Nandan, Swapnil, Jidnyasa, Aboli, Anshita, Ankita, Simmy for their worthy support and *cooperation in completing my work. I am also grateful to my friends Dr. Dhananjay Doke, Ravindra, Tushar, Ankit, Meera mam, Seema, Shubham, Gorakh, Dr. Sagar, Dr. Anthony, who helped me in various aspects during my tenure at NCL.*

Words are not enough to express my love and gratitude to my family members. It gives me great pleasure to thank my parents, my sisters, and my brother for always providing unconditional support and helping me over the years. Finally, I would like to thank my beloved wife Supriya for her tremendous patience, unfailing support, and encouragement throughout my pursuits. A special thanks to my cute little daughter Sharanya who has directly and indirectly inspired and energized me daily for work.

……… Nagesh L. Mulik

CONTENT

List of Abbreviations i

List of Symbols and Units ii

List of Schemes iii

List of Figures iii

List of Tables vi

Chapter 1

Introduction

1.1 Biomass is a potential source of fuel and chemicals 2

1.1.1 Classification of biomass 3

1.1.2 Composition and structure of lignocellulosic components 4

1.1.2.1 Composition of lignocellulosic biomass 4

1.1.2.2 Structure of cellulose 4

1.1.2.3 Structure of Hemicellulose 5

1.1.2.4 Structure of lignin components 5

1.2 Conversion processes of lignocellulosic biomass to value-added products 6

1.3 Value-added chemicals from carbohydrate biomass 8

1.3.1 Alkyl levulinate as a platform chemical 12

1.3.2 Furfuryl ether as a platform chemical 13

1.4 Heteropoly acids for biomass valorization 13

1.5 Scope and Objective of the Thesis 16

1.5.1 Scope of the Thesis 16

1.5.2 The objectives of the thesis 17

1.6 References 17

Chapter 2

Glucose Conversion to Ethyl Levulinate Over Zr-exchanged HPW catalyst and Sn-betas as a co-catalyst

2.1 Introduction 25

2.2 Experimental 27

2.2.1 Materials 27
2.2.2 Catalyst preparation 27
2.2.2.1 Synthesis of Zr Exchanged HPW 27
2.2.2.2 Synthesis of Lewis acid co-catalysts 28
2.2.2.2.1 Synthesis of Sn-beta 28
2.2.2.2.2 Synthesis of SnO_2 28
2.2.2.2.3 Synthesis of TiO_2 29
2.2.3 Characterization of the catalysts 29
2.2.4 Reaction procedure 30
2.3 Results and Discussion 31
2.3.1 Catalysts characterization 31
2.3.1.1 X-ray diffraction 31
2.3.1.2 FT-IR 32
2.3.1.3 N_2 physisorption 33
2.3.1.4 NH_3-TPD 33
2.3.1.5 Pyridine FTIR 34
2.4 Catalytic activity 37
2.4.1 Effect of Process Variables on EL synthesis from Glucose 39
2.4.1.1 The effect of glucose concentrations 41
2.4.1.2 The influence of reaction temperature 43
2.4.1.3 Effect of the Catalyst Loading 44
2.5 Comparison of the present catalytic system with the literature 45
2.6 Conclusions 45
2.7 References 46

Chapter 3

Furfuryl alcohol conversion to Ethyl furfuryl ether over Recyclable Cs exchanged HPW catalyst

3.1 Introduction 50
3.2 Experimental 51
3.2.1 Materials and methods 51

3.2.2 Catalyst synthesis 52
3.2.2.1 Cs exchanged HPW 52
3.2.2.2 Ce Exchanged HPW ($H_1Ce_2PW_{12}O_{40}$) 52
3.2.2.3 Mg Exchanged HPW ($H_1Mg_2PW_{12}O_{40}$) 52
3.2.3 Characterization of the catalysts 53
3.2.4 Reaction procedure and analysis 54
3.3 Results and discussion 55
3.3.1 Catalysts characterization 56
3.3.1.1 X-Ray diffraction 56
3.3.1.2 N_2-Physisorption 57
3.3.1.3 X-ray photoelectron spectroscopy 58
3.3.1.4 NH_3-TPD 60
3.3.1.5 Pyridine-FTIR 61
3.3.2 Etherification of Furfuryl Alcohol with Ethanol to Ethyl Furfuryl Ether 62
3.3.3 Catalyst Screening 64
3.3.4 Influence of Cs insertion in $H_3PW_{12}O_{40}$ on the acidity and catalytic activity 65
3.3.5 Effect of molar ratio 67
3.3.6 Effect of Temperature 69
3.3.7 Effect of catalyst loading 70
3.3.8 Effect of reaction time 71
3.3.9 Catalyst regeneration 72
3.4 Comparison of the present catalytic system with the literature 74
3.5 Conclusions 75
3.6 References 76

Chapter 4

Alcoholysis of Furfuryl alcohol and Furfuryl aldehyde over UiO-66-NH_2-HPW catalyst

4.1 Introduction 79
4.2 Experimental 81
4.2.1 Materials and methods 81

4.2.2 Catalyst synthesis 81
4.2.2.1 Synthesis of UiO66-NH_2 MOF 81
4.2.2.2 Immobilization of HPW on UiO-66-NH_2 81
4.2.3 Catalyst characterization 82
4.2.4 Reaction procedure and analysis 83
4.3 Results and Discussion 84
4.3.1 Catalysts characterization 84
4.3.1.1 X-Ray diffraction 84
4.3.1.2 SEM, TEM, and elemental mapping 85
4.3.1.3 ATR-FTIR 87
4.3.1.4 X-ray photoelectron spectroscopy 88
4.3.1.5 N_2-Physisorption 91
4.3.1.6 NH_3-TPD 93
4.3.2 Catalyst screening 94
4.3.3 Optimization of reaction parameters 95
4.3.3.1 Effect of catalyst amount 95
4.3.3.2 Effect of Temperature 96
4.3.3.3 Effect of reaction time 97
4.3.3.4 Effect of type of alcohol 98
4.3.3.5 Catalysts reusability 100
4.3.4 Catalytic conversion of FFR 103
4.4 Comparison of the present catalytic system with the literature 104
4.5 Conclusions 106
4.6 References 106

Chapter 5

Summary and Conclusion

Summary and Conclusion 109
Thesis abstract 115
List of papers and patents 116

Published papers

List of abbreviations

AL	**Alkyl Levulinate**
ATIR-FTIR	**Attenuated Total Reflection-Fourier Transformed Infrared**
BL	**Butyl Levulinate**
BET	**Brunauer–Emmett–Teller**
EFE	**Ethyl furfuryl ether**
EDAX	**Energy Dispersive X-ray Spectroscopy**
EL	**Ethyl Levulinate**
ELA	**Ethyl lactate**
EMF	**Ethoxy methyl furfural**
FID	**Flame Ionization Detector**
FTIR	**Fourier Transformed Infrared**
FE	**Furfuryl ether**
FAlc	**Furfuryl alcohol**
FFR	**Furfural**
GC	**Gas Chromatography**
GCMS	**Gas Chromatography-Mass Spectroscopy**
HPLC	**High-Performance Liquid Chromatography**
HPAs	**Heteropolyacids**
HPW	**Tungstophosphoric acid**
HRTEM	**High Resolution Transmission Electron Microscopy**
IPA	**Isopropanol**
MFE	**Methyl furfuryl ether**
MOF	**Metal-Organic frameworks**
SEM	**Scanning Electron Microscopy**
TEM	**Transmission Electron Microscopy**
TPD	**Temperature-programmed Desorption**
TPA	**Tungstophosphoric acid**

TCD	**Thermal conductivity detector**
XRD	**X-ray diffraction**
XPS	**X-ray Photoelectron Spectroscopy**

List of Symbols & Units

a.u.	Arbitrary Unit
°C	Celsius (unit of measurement for temperature)
cm^{-1}	Wavenumber
h	Hour (s)
Mol	Mole (s)
nm	Nanometer
%	Percentage
α	Alpha
θ	Theta
mmol	millimole
μmol	micromole
kV	Kilovolt
min	minutes
eV	electronvolts
β	beta

List of Schemes and Figures

List of Schemes

Scheme 2.1.	**Direct conversion of Glucose to EL**	**37**
Scheme 3.1	**Etherification of furfuryl alcohol to ethyl furfuryl ether**	**63**
Scheme 4.1	**Schematic illustration of post-synthetic formulation of UiO-66-NH_2-HPW from UiO-66-NH_2**	**91**
Scheme 4.2	**Catalytic conversion of FALc to FE and AL**	**94**
Scheme 4.3	**Scheme 4.3 Catalytic conversion of FFR to FALc, FE, AL**	**103**

List of Figures

Figure 1.1	**Biomass sources**	**2**
Figure 1.2	**Classification of biomass**	**3**
Figure 1.3	**Structure of cellulose**	**4**
Figure 1.4	**Structure of Hemicellulose**	**5**
Figure 1.5	**Structure of lignin components**	**6**
Figure 1.6	**Biomass conversion methods**	**7**
Figure 1.7	**Route to obtain Glucose and Furfuryl alcohol**	**9**
Figure1.8	**Transformation of sugars into useful chemicals**	**11**
Figure 1.9	**Organic transformation of Alkyl levulinates**	**13**
Figure 1.10	**Keggin structure of HPA**	**14**
Figure 1.11	**Some unique properties of Heteropolyacids**	**11**

Figure 2.1	XRD profiles of Bronsted acids (a) $H_3PW_{12}O_{40}$, $H_2Zr_1PW_{12}O_{40}$, $H_2Zr_1PW_{12}O_{40}$, and ZrO_2 and Lewis acids (b) TiO_2, SnO_2 and Sn-β	31
Figure 2.2	FT-IR spectra of $H_3PW_{12}O_{40}$, $H_2Zr_1PW_{12}O_{40}$, and $H_2Zr_1PW_{12}O_{40}$	32
Figure 2.3	NH_3-TPD profiles of $H_3PW_{12}O_{40}$, $H_2Zr_1PW_{12}O_{40}$, and $H_2Zr_1PW_{12}O_{40}$	34
Figure 2.4	Py-FTIR spectra of HPW, $H_2Zr_1PW_{12}O_{40}$, and $H_2Zr_1PW_{12}O_{40}$ and Sn-beta	35
Figure 2.5	Py-FTIR spectra of individual Sn-beta and Physical combinations of #$H_1Zr_2PW_{12}O_{40}$ + Sn-beta and *$H_2Zr_1PW_{12}O_{40}$ + Sn-beta	36
Figure 2.6	Mechanism of Alkyl levulinate and Alkyl lactate formation from glucose	41
Figure 2.7	Effect of glucose concentration.	42
Figure 2.8	Effect of temperature	43
Figure 2.9	Effect of catalyst loading.	44
Figure 3.1	Powder XRD of (a) $H_3PW_{12}O_{40}$ and $Cs_xH_{3-x}PW_{12}O_{40}$ samples and (b) $H_1Mg_2PW_{12}O_{40}$, and $H_1Ce_2PW_{12}O_{40}$	56
Figure 3.2	XP spectra of $H_3PW_{12}O_{40}$ and $Cs_xH_{3-x}PW_{12}O_{40}$ samples as a function of Cs content (a) W4f XP spectra of $H_3PW_{12}O_{40}$ and $Cs_xH_{3-x}PW_{12}O_{40}$ samples (b) O 1s XP spectra of $H_3PW_{12}O_{40}$ and $Cs_xH_{3-x}PW_{12}O_{40}$ samples (c) Cs $3d_{5/2}$ XP spectra of $Cs_xH_{3-x}PW_{12}O_{40}$ sample	59
Figure 3.3	NH_3 Temperature Programmed Desorption profiles	60
Figure 3.4	Pyridine IR spectra of $H_3PW_{12}O_{40}$ and $Cs_xH_{3-x}PW_{12}O_{40}$ samples	62
Figure 3.5	Catalyst screening as a function of total acidity	64
Figure 3.6	Effect of Cs insertion on the acidity and catalytic activity	67
Figure 3.7	Effect of the molar ratio of FAlc to ethanol	68
Figure 3.8	Effect of Temperature	69

Figure 3.9	**Effect of catalyst loading concerning to FAlc**	**70**
Figure 3.10	**Effect of reaction time**	**72**
Figure 3.11	**Catalyst Reusability**	**73**
Figure 3.12	**Powder XRD of fresh, spent, and regenerated $H_1Cs_2PW_{12}O_{40}$ samples**	**74**
Figure 4.1	**Powder XRD of parent UiO-66-NH_2 and UiO-66-NH_2-HPW**	**84**
Figure 4.2	**SEM image of (A) UiO-66-NH_2 and (B) UiO-66-NH_2-HPW**	**85**
Figure 4.3	**HR-TEM image of (A) UiO-66-NH_2 and (B) UiO-66-NH_2-HPW**	**85**
Figure 4.4	**STEM image and Elemental mapping of UiO-66-NH_2-HPW**	**86**
Figure 4.5	**STEM image and Elemental mapping of UiO-66-NH_2**	**86**
Figure 4.6	**ATR-FTIR of parent UiO-66-NH_2 and UiO-66-NH_2-HPW**	**87**
Figure 4.7	**(A) XPS survey scan of UiO-66-NH_2 and UiO-66-NH_2-HPW, and high-resolution XPS data of UiO-66-NH_2 and UiO-66-NH_2-HPW (B) N 1, (C) O 1s, (D) Zr 3d, (E) C 1s**	**89**
Figure 4.8	**High-resolution XPS data of W 4f and P 2p scan of UiO-66-NH_2-HPW**	**89**
Figure 4.9	**Nitrogen adsorption-desorption isotherms of UiO-66-NH_2 and UiO-66-NH_2-HPW**	**92**
Figure 4.10	**Temperature-programmed Ammonia desorption of UiO-66-NH_2 and UiO-66-NH_2-HPW**	**93**
Figure 4.11	**Effect of UiO-66-NH_2-HPW amount**	**95**
Figure 4.12	**Effect of Temperature on the catalytic activity of UiO-66-NH_2-HPW**	**96**
Figure 4.13	**Effect of Time on the catalytic activity of UiO-66-NH_2-HPW**	**98**

Figure 4.14 Effect of type of alcohol type on etherification and alcoholysis of FALc over UiO-66-NH_2-HPW 99

Figure 4.16 Catalyst recycling for FALc conversion over UiO-66-NH_2-HPW in Ethanol 100

Figure 4.17 Powder XRD of Fresh and used catalyst (UiO-66-NH_2-HPW) with an image of fresh and used catalyst in the inset 101

Figure 4.18 ATR-FTIR of Fresh and used catalyst (UiO-66-NH2-HPW) 102

Figure 4.19 Catalytic hydrogenation of FFR over UiO-66-NH_2-HPW in the presence of different alcohols as a solvent and hydrogen donor 103

List of tables

Table 1.1 List of biomass-derived platform chemicals 8

Table 2.1 Physicochemical characteristics of the catalyst 33

Table 2.2 Catalyst screening for glucose to EL conversion 37

Table 2.3 Effect of the Catalyst Composition 39

Tablev2.4 Comparison of the present catalytic system with the literature 45

Table 3.1 Surface properties of $H_3PW_{12}O_{40}$ and $Cs_xH_{3-x}PW_{12}O_{40}$ samples 58

Table 3.2 Investigation of Acidic Properties by NH_3 temperature programmed desorption and B/L ratio (Pyridine-FTIR) of $H_3PW_{12}O_{40}$, and $Cs_xH_{3-x}PW_{12}O_{40}$ samples. 61

Table 3.3 Comparison of the present catalytic system with the literature 74

Table 4.1 SEM-EDAX analysis of the chemical composition of UiO-66-NH_2 and UiO-66-NH_2-HPW 90

Table 4.2 Surface properties and Ammonia TPD acidity of UiO-66-NH_2 and UiO-66-NH_2-HPW 91

Table 4.3 **Activity comparison of parent and modified Catalyst** **94**

Table 4.4 **Comparison of the present catalytic system with the literature** **105**

Chapter-1

Introduction

1.1. Biomass is a potential source of fuel and chemicals

Renewable energy sources are becoming more crucial as a result of the exponential rise in the consumption of fossil fuels. Since biomass has so many uses in the fields of bioenergy, biofuel, biomaterials, and other fields, it was found to be the key to this passage [1,2]. "Biomass" is a general term that refers to any renewable organic material that is obtained from plants or animals, and it includes residues and waste from crop production, wood, animals, and aquatic plants, as well as municipal and other waste as depicted in Figure 1.1. Furthermore, plants absorb atmospheric CO2 for photosynthesis, a process that converts CO2 and water into carbohydrates and oxygen in the presence of sunlight. Plants produce the vast majority of biomass, and their growth has no effect on the amount of carbon dioxide in the atmosphere; in fact, it can reduce it.

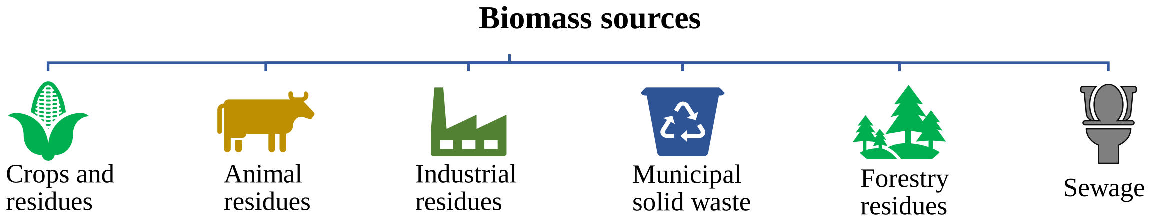

Figure 1.1. Biomass sources

The availability of biomass varies widely across different areas and nations, depending on factors such as temperature, land use, agricultural methods, and natural resources. India is a diverse country with a wide range of climatic conditions, topographies, and agricultural systems, all of which influence biomass resource availability. A recent study covered by the Government of India's Ministry of New and Renewable Energy revealed that the country now has access to 750 million metric tons of biomass each year [3]. The study showed estimated spare biomass availability at about 230 million metric tons per annum of agricultural residues. As a result, biomass is abundant and inexpensive, and these features make biomass a sustainable source for future chemical and energy demands [4–8]. The economy shifted from nonrenewable to renewable sources due to diminishing resources, political concerns, and the negative environmental effects of CO2 emissions from the consumption of fossil fuel feedstocks, such as global warming and pollution [9–12]. Moreover, lignocellulosic biomass is the most prominent natural and renewable resource in modern industrial society compared to fossil feedstocks [13]. It is an economical, easily available alternative, however, besides the huge potential of biomass, unfortunately currently much of the lignocellulosic biomass is used to burn for energy generation [14]. As a result, researchers have concentrated on the utilization of diverse byproducts obtained from lignocellulosic biomass for the utilization to synthesize fuels and chemicals.

1.1.1. Classification of biomass

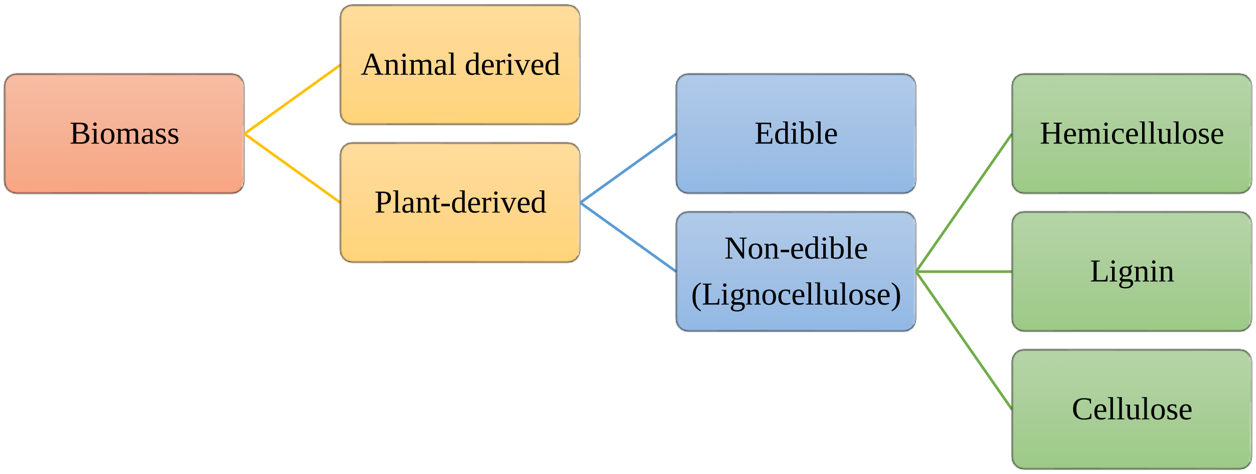

Figure 1.2. Classification of biomass

Biomass is classified into two types based on its origin: animal-derived and plant-derived. Animal manure and other items derived from it comprise animal biomass. Plant byproducts and products are classified as plant-derived biomass, which is further categorized as edible and non-edible biomass. The basic components of lignocellulosic biomass, often known as non-edible plant-derived biomass, are cellulose, hemicellulose, and lignin. These components are held together by various covalent and noncovalent interactions [15]. According to the information stipulated biomass can be categorized as shown in Figure 1.2.

1.1.2. Composition and structure of lignocellulosic components

1.1.2.1. Composition of lignocellulosic biomass

The basic constituents of lignocellulosic biomass are carbon (47-53%), hydrogen (5.9-6.1%), and oxygen (40-45%), with minor amounts of sulfur, nitrogen, and different minerals such as sodium, potassium, iron, magnesium, and manganese. Biomass feedstocks have a higher oxygen concentration than fossil feedstocks. The key components of lignocellulosic biomass are 35–50% cellulose, 20–35 hemicellulose, and 20–35% lignin. The remaining material consists of minerals, wax, ash, protein, lipids, and oils [4,15,16].

1.1.2.2.Structure of cellulose

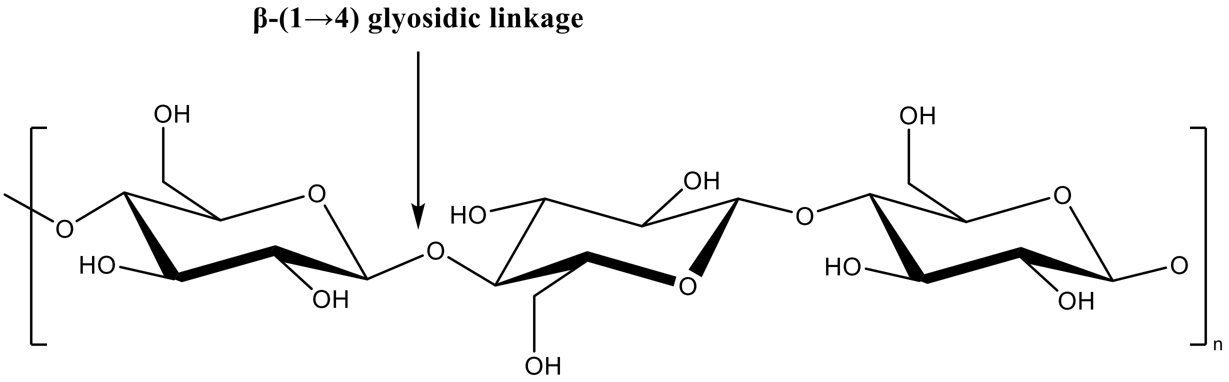

Figure 1.3: Structure of cellulose

The bulk of polysaccharides comprises cellulose, which accounts for around half of all lignocellulosic biomass. The homopolysaccharide cellulose is constituted of linearly arranged D-glucose units that are linked together by β-(1→4) glycosidic linkages (Figure 1.3) [17]. The hydrogen bonds that exist between and within cellulose molecules cause them to crystallize. Because of strong β-(1→4) glycosidic bonding, cellulose cannot be digested directly by any vertebrate, including humans, while some symbiotic bacteria present in the digestive tracts of herbivorous mammals create the enzyme that breaks down cellulose. Although it is not edible to humans, cellulose is employed in a variety of everyday activities, including the creation of paper and, clothes.

1.1.2.3. Structure of Hemicellulose

Hemicelluloses, the polysaccharide produced by the plants, account for around 30% of lignocellulosic biomass. In contrast to cellulose, hemicellulose is the hetero- or homo-polysaccharide consisting of numerous C5 and C6 sugars, and its composition is relay on the plant 15,18. Based on their composition, hemicelluloses can be categorized as glucomannan, Xylan, arabinan, arabinogalactan, and so on18. Typically, hardwood hemicellulose contains xylan, whereas softwood hemicellulose is composed of glucomannan 18. Other monosaccharides, such as arabinose and glucuronic acid, can be found in trace levels in xylan-containing materials such as beech wood, oat flour, and cereal wood. Only pure xylan produced by sea algae contains a homopolymer of xylose.

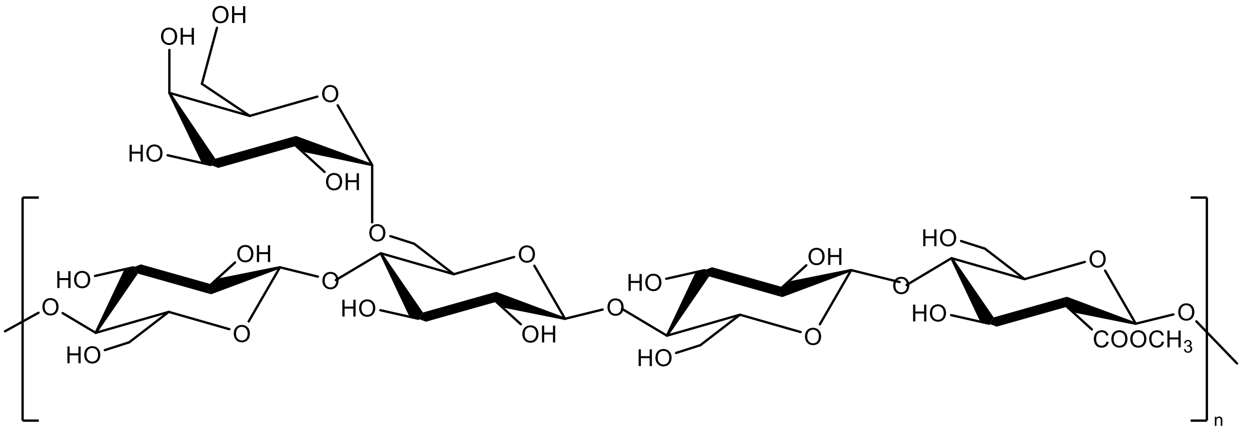

Figure 1.4: Structure of Hemicellulose

1.1.2.4.Structure of lignin components

Lignin is a complex, branching polymer of aromatic chemicals that reports 15-30% of lignocellulosic biomass 4,16,19. This complex, branching polymer of the lignin contains some common budling blocks such as Coniferyl alcohol, Sinapyl alcohol, and Coumaryl alcohol 19; and their structures are shown in Figure 1.5. The specific structure of lignin is debatable and it is affected by a variety of conditions, including plant type, environment, and age. According to studies, the separation process can cause structural alteration and has a major impact on the structure and functional groups present in lignin. Different species, and even different parts of the same plant, may have different amounts and compositions of lignin. Hardwoods are reported to have the second-highest levels of lignin, whereas grasses have the lowest 15.

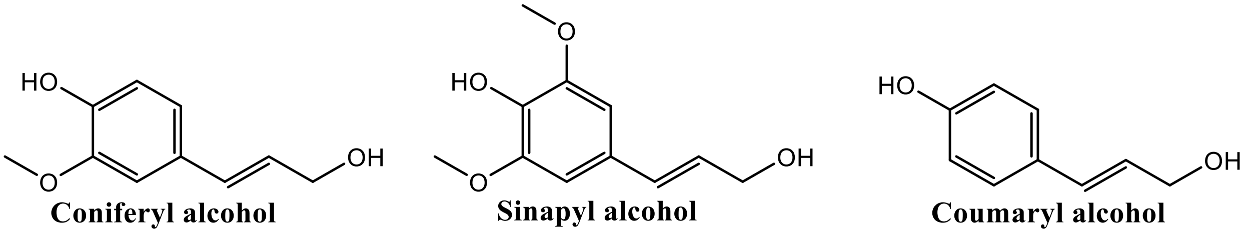

Figure 1.5. Structure of lignin components

1.2. Conversion processes of lignocellulosic biomass to value-added products

Before getting into the specifics of chemicals obtained from lignocellulosic biomass utilizing various conversion strategies, we must first comprehend these processes. After the pretreatment process, biomass can be converted into a variety of products 20. The pretreatment of lignocellulosic materials aims to eliminate the cellulose-covering lignin and hemicellulose, decrease crystallinity, increase porosity, enhance the formation of sugar units through hydrolysis, and stop biomass degradation in inhibitory byproducts for subsequent conversion processes 19–21. The following are examples of common biomass energy conversion process categories: The next paragraphs provide an overview of the conversion processes depicted in Figure 1.6.

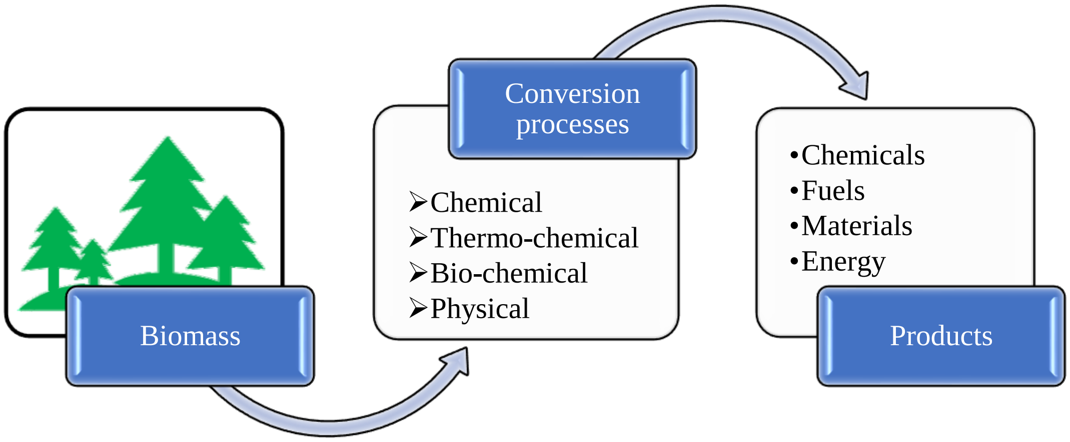

Figure 1.6 Biomass conversion methods

Chemical processes: These techniques comprise the chemical conversion of biomass or derived feedstock into different types of products. It has been extensively researched how lignocelluloses, can be transformed into other molecules with added value. Although starch, an edible feedstock, can be used in biorefineries, the conversion of lignocellulosic biomass, which is inedible to humans, is the only issue covered in this article. A homogeneous catalyst, such as mineral acid (HCl, H_2SO_4)[22–24] and some solid acids such as metal oxides, sulfonated carbon amberlyst, and zeolites, Heteropoly acids[25–32] are used to convert lignocellulosic biomass into sugars, furans, sugar acids, sugar alcohols, and so on.

Thermo-chemical processes: These are the processes that transform biomass into chemical compounds that can be utilized to generate energy more quickly, although they do not directly generate energy. These compounds have a higher energy density and more controlled burning properties than untreated biomass. For instance, the calorific value of wood is about 3000 kcal/kg, and the calorific value of bio-oil, which is made by pyrolyzing biomass, is about 10,000 kcal/kg. Pyrolysis oil, often referred to as bio-oil, is created by heating biomass for a bit of time at 350–500 °C in an oxygen-free environment. Char and tar are seen to build beside the oil. Biomass can be gasified at high temperatures (700–900°C) with a controlled oxygen supply to create syngas. This procedure results in some charcoal and producing gas from the partially burned biomass. Incomplete combustion produces CO_2 and H_2O which are further reduced to make CO and H_2. The gaseous result of gasification contains around 20% H_2, 20% CO, 3% CH_4, and 10% CO_2 (the remaining nitrogen)[4,5,15].

Biochemical processes: Microbes are used in these processes to convert biomass into different products. One of the earliest known biochemical processes is the anaerobic fermentation of biomass such as animal manure and crop waste to produce methane-rich biogas. Under anaerobic conditions, a methanogenic bacterial culture transforms biomass into biogas with a methane level of roughly 55%. There are numerous reports in the literature of enzymatic hydrolysis of polysaccharides such as cellulose and hemicellulose to produce monomer sugars, as well as sugar fermentation to produce ethanol[15,33,34].

Physical process: High-quality vegetable or seed oils can be extracted from biomass in a straightforward manner [35]. For instance, it is accepted as a suitable feedstock for the synthesis of biodiesel using vegetable oil from plants like Jatropha curcas and soapnut (Sapindus mukorossi). The plant's gathered oils can be transformed into fuel (biodiesel) by a base-catalyzed transesterification reaction. Also found in plants are materials like rubber, adhesives, and derived colors.

1.3. Value-added chemicals from carbohydrate biomass

Table 1.1 List of biomass-derived platform chemicals

Carbon species	Important chemical platforms
C2	Ethanol, Ethylene, Acetic acid, oxalic acid, glycolic acid
C3	Glycerol, Acetone, Propanediol, Lactic acid, acrylic acid
C4	1,2,4-butane triol, 1-butanol, 1,3-butane diol, Formic acid, Succinic acid, malic acid, Aspartic acid
C5	Xylose Arabinose, Furfural, Levulinic acid, glutamic acid
C6	5-HMF, Lysine, Sucrose, Sorbitol, Adipic acid, Citric acid

The compounds derived from petrochemical resources that can be used as platform chemicals consist of propylene, 1,3, -butadiene, alkanes like ethane and butane, and aromatics such as benzene, xylene, and toluene, [29,36]. Currently, a similar method is employed to generate platform molecules from lignin and carbohydrates [37]. These substances, which are listed in Table 1.1, have been identified by researchers as having the potential to be used as building blocks. Those building blocks can be derived from primary biomass products such as cellulose, starch, hemicellulose, lignin, proteins, and oils [36,38]. Using carbohydrates as reactants, several of those on the list can be produced. Liquid-phase approaches are preferred for biomass processing due to their high functionality, reactivity, and low volatility. Biotechnological/chemical approaches can generally be used to produce a range of essential fuels and important chemical intermediates from carbohydrates [39–41]. The top 12 important value-added chemicals derived from biomass selected by the US DOE can be converted into alcohols, furans, and acids [42,43].

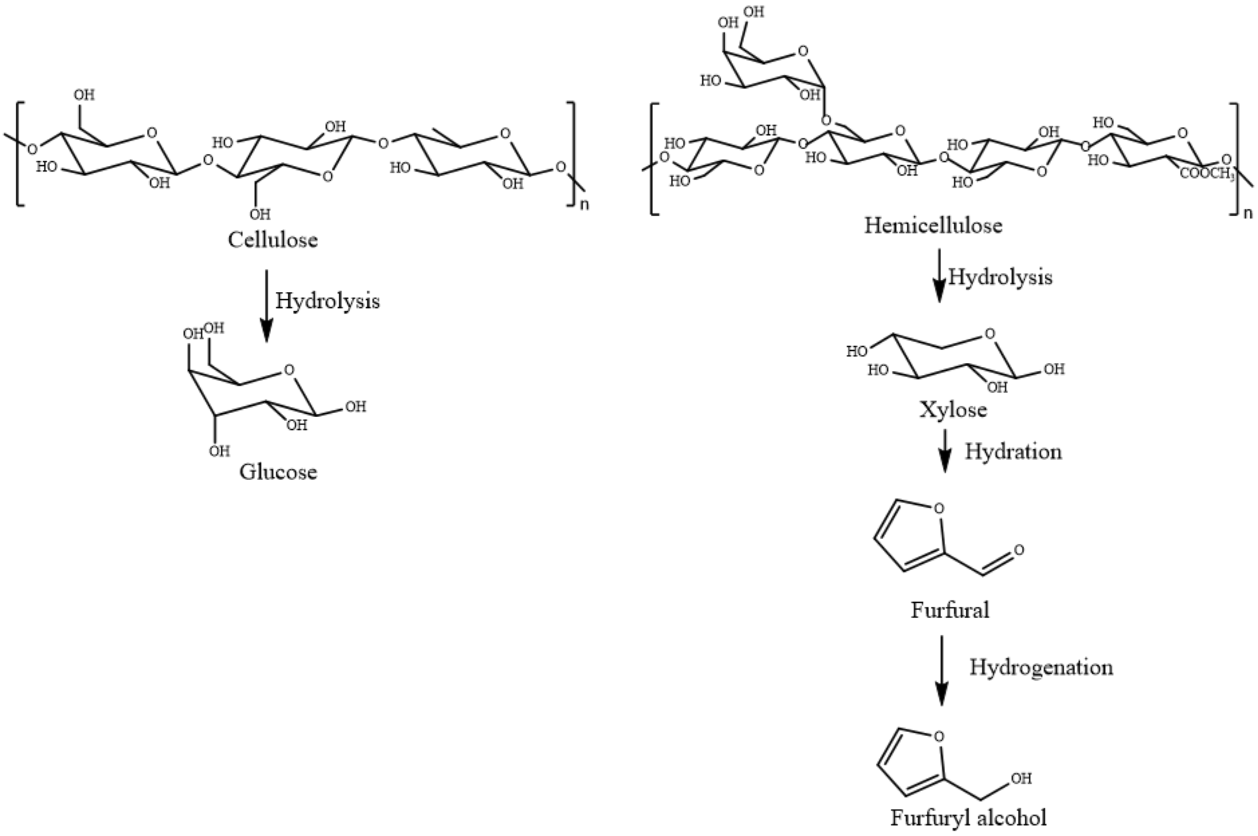

Figure 1.7 Route to obtain Glucose and Furfuryl alcohol

The effective conversion of these biomass-derived components into useful chemicals serves as a model for biomass utilization strategies. The carbohydrates of cellulose and hemicellulose components in lignocellulose can be depolymerized into monosaccharide sugars (such as glucose, fructose, and xylose) and some soluble intermediates via enzymatic or acidic hydrolysis (as shown in Figure 1.7) [44–49]. Using enzymes (amylases) or acids, sugar cane or sugar beets can be hydrolyzed to produce glucose on an industrial scale from starch-rich crops like corn, wheat, or potatoes [45,46]. The market value of glucose can vary depending on factors such as production costs, demand, and regional differences. In 2021, the price of glucose typically ranged from around $0.35 to $0.60 per pound (lb) or $770 to $1,320 per metric ton. According to a precedence, research report the glucose market size was exhibited at USD 47.88 billion in 2022 and was expected to grow in 2023 [50]. Glucose is used in various industries, including food and beverage, pharmaceuticals, and industrial applications. It's used as a sweetener, a source of energy in medical formulations, and as a raw material in chemical processes.

Similarly, furfuryl alcohol is produced industrially by dehydrating pentoses (such as xylose) found in these materials using acid catalysts to form furfural, which is subsequently hydrogenated to furfuryl alcohol (as shown in Figure 1.7) [51–53]. The price of furfuryl alcohol can also fluctuate based on supply, demand, and production factors. In 2021, its price was approximately $1,200 to $1,600 per metric ton [54,55]. Furfuryl alcohol is primarily used in the production and manufacture of various chemicals, including pharmaceuticals and agricultural chemicals.

Lignocellulose chemical transformation undergoes a variety of processes such as dehydration, hydrolysis, isomerization, aldol condensation, hydrogenation, oxidation, and reforming to produce compounds with important applications [56]. Figure 1.8 shows the chemical transformation of sugars to render an array of useful chemicals.

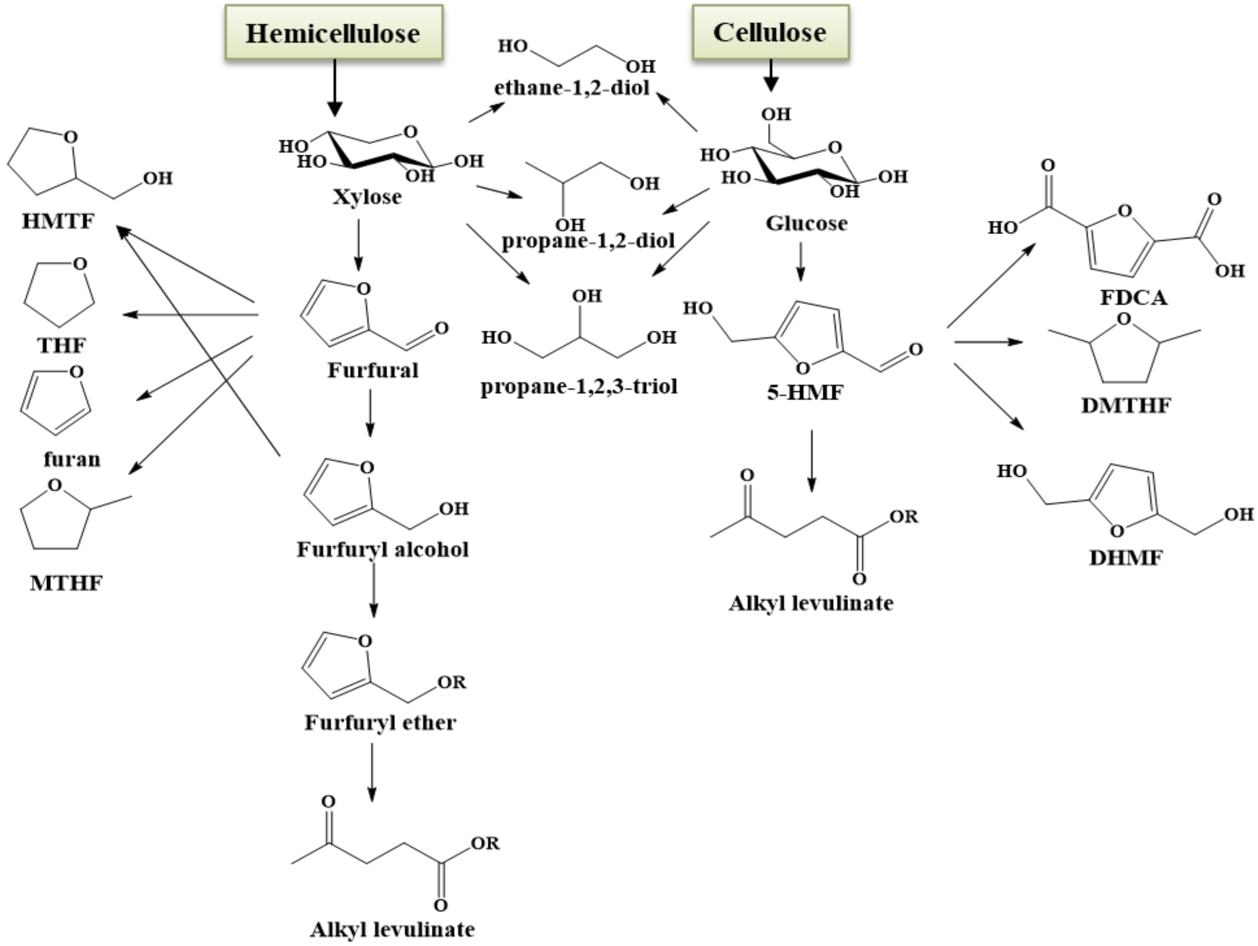

Figure1.8. Transformation of sugars into useful chemicals

Catalytic biomass conversion to platform compounds, which can be used directly as precursors in the manufacture of more valuable chemicals, is one approach for biomass valorization. Among biomass-derived compounds, glucose, furfural, and furfuryl alcohol are seen to be highly promising compounds because they provide a renewable route for turning biomass into benign products. Both alkyl levulinate (AL) and furfuryl ether (FE) are part of the broader bio-based chemicals sector, which has been experiencing growth due to increased interest in sustainable and environmentally friendly alternatives to petrochemicals. Recently, alkyl levulinates and furan derivatives have drawn more attention because of their potential use as biofuel bio-additives, and feedstocks for pharmaceuticals, to derive plastics, and uses in fragrance industries [57–62]. The ultimate objective of this thesis is to provide knowledge regarding the use of modified heteropolyacids as solid acid catalysts in the conversion of glucose and furfuryl alcohol into biofuels and additives (AL and FE). Hence various aspects of these important chemical feedstocks derived from lignocellulose are discussed below in more detail.

1.3.1. Alkyl levulinate a platform chemical

The term "platform chemical" refers to a compound that can undergo various chemical transformations to produce a variety of useful products. Due to their distinctive physicochemical characteristics and reactivities, ALs are one of the lignocellulosic-based compounds that have drawn a lot of interest. These compounds are essential for manufacturing pharmaceuticals, insecticides, perfumes, and functional materials [42,57,63]. ALs are a class of adaptable and promising chemicals with a broad variety of possible industrial uses[60]. AL is recognized as an important platform chemical for conversion into various interesting derivatives [64], as presented in Figure 1.9. Levulinic esters have different physicochemical features that can be customized to chemical and process industry applications where they are used like solvents and additives, fragrance agents, flavorings, and so on. [60,65] Levulinic acid esters have a large potential as gasoline additives due to their identical characteristics to those of fatty acid methyl esters, as well as their low toxicity, stability, and high lubricity [66]. Levulinate esters, such as butyl levulinate (BL) and, ethyl levulinate (EL) have been tested successfully as oxygenates, improving the lubricity, freezing point, conductivity, and combustion emission of the gasoline [30,67]. In 2021, the global market for levulinic acid and its derivatives was valued at $ 26.35 million, and it is expected to rise by $61.04 million. Similarly, the global market for ethyl levulinate was worth $ 14.3 billion in 2020, and it is expected to rise substantially in the following years due to new uses and production methods [68,69].

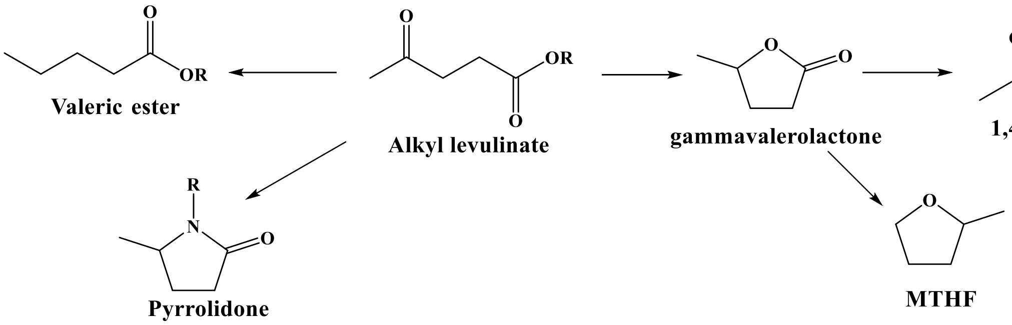

Figure 1.9 Organic transformation of Alkyl levulinates

1.3.2. Furfuryl ether as a platform chemical

Furanics are heterocyclic compounds derived from hexose and pentose sugars that have. These oxygen-containing compounds have been employed as octane and cetane number enhancers in gasoline and diesel. [58,70,71]. The commonly used oxygenate furanic compound fuels can be synthesized from hexose or pentose sugars through catalytic transformation. One such furanic that is increasingly becoming important is furfuryl ethers. It has been reported that furfuryl ether (FE) possesses a high-octane number [70,71]. For instance, the octane number and cetane number of ethyl furfuryl ether (EFE) were reported to be 89 and 18.4 respectively [71]. Furfuryl ethers such as EFE and Methyl Furfuryl ether (MFE) are also used as important flavor compounds [72].

Due to the highly reactive nature of the reaction (reactant and products), the role of acidity must be taken into consideration as it might alter the reaction pathway and generate undesirable adverse reactions [73–75]. In the current research, AL and FE synthesis was performed with the acidity of heterogenized hetero-poly acids being fine-tuned, to explore its effect and provide insights into the appropriate acidity for such complex reactions.

1.4. Heteropoly acids for biomass valorization

The development of environmentally friendly procedures and the complexity of the carbohydrate feedstock both provide significant difficulties for the design of biomass conversion catalysts. In many cases, a solid acid catalyst is preferable to a liquid acid catalyst for reducing waste formation and facilitating simple catalytic separation. HCl and H_2SO_4 are examples of homogeneous Brønsted acids, while zeolites, metal oxides, and metal phosphides are examples of solid Brønsted acids.) [29,62,76,77] can be used. Furthermore, heteropolyacids (HPAs) work particularly well in hydration/dehydration reactions due to their variable redox and tunable acidic properties. Due to their distinctive structures and remarkable physicochemical characteristics, such as strong Brønsted acidity, high solubility, high proton mobility, and, rapid multi-electron transfer HPAs are the best catalyst options [78–80]. HPA catalysts have Lewis-acid metals, acidic protons, and different (one or two) types of acidic sites, either kind of acidic site can operate as an active site in acid catalysis[81].

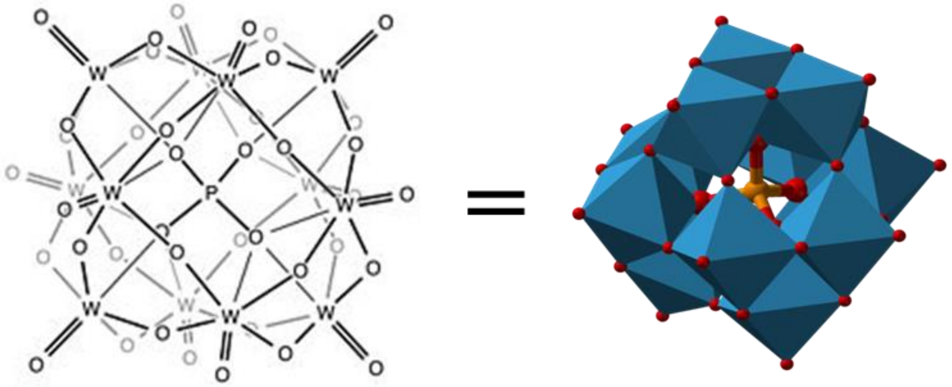

Figure 1.10 Keggin structure of HPA

HPAs can be distinguished from solid acids due to their high solubility in both water and organic solvents. Three-dimensional (polyoxometalate) acidic protonated clusters of early transition metal joined by oxygen atoms. POMs are known as hetero-poly anions when there are two distinct metals present. Oxoanions of the central heteroatom X (P^{5+}, Si^{4+}, and so on) are surrounded by oxyanions of the addenda atom M (W^{6+}, Mo^{6+}, and so on) [82]. The Keggin structure (as shown in Figure 1.10), which is made up of POMs of the type $XM_{12}O_{40}$n, is the most recognized and stable POM structure. The fundamental structure of HPAs (Figure 1.10) depicts 12 corner- and edge-linked octahedral MO_6n units surrounding the central tetrahedral XO_4n unit. The secondary structure is made up of the water of crystallization, which surrounds the anion in addition, and the tertiary structure is made up of the constructed solid particles [83].

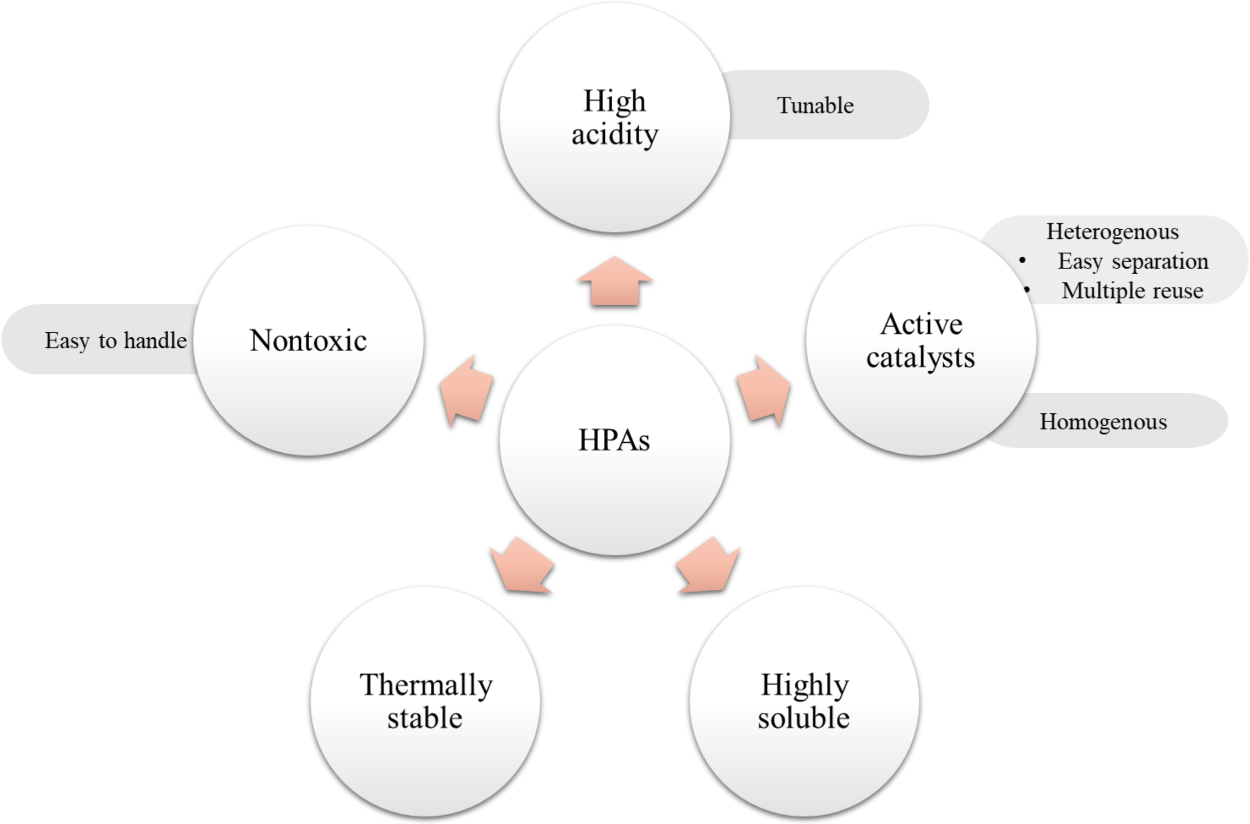

Figure 1.11 Some unique properties of Heteropolyacids

As shown in Figure 1.11, HPA catalysts have some unique properties such as high acidity; comparable to or even stronger than traditional mineral acids like sulfuric acid [80], and tunability; the acidity of HPAs can be tailored to the optimal level for specific biomass conversion reactions enhancing catalytic efficiency and selectivity[84]. High water tolerance, high thermal stability, compatible with a wide range of renewable feedstocks. In many circumstances, HPAs allow biomass conversion processes to take place under moderate conditions (lower temperatures and pressures) than other catalysts necessitate. This contributes to the preservation of the desired product's integrity. As a result, their use as catalysts for biomass transformation is appropriate. HPAs are frequently utilized in research and industry, particularly the commercially accessible ones such as $H_3PW_{12}O_{40}$ (HPW), $H_3PMo_{12}O_{40}$ (HPMo), $H_4SiW_{12}O_{40}$ (HSiW), and $H_4SiMo_{12}O_{40}$ (HSiMo).

While heteropolyacids offer numerous advantages for biomass transformation, it's important to note that the choice of catalyst depends on the specific reaction and feedstock under consideration. Researchers continue to explore and develop catalysts that best suit the requirements of different biomass conversion processes. In gas-solid, liquid-solid, and heterogeneous catalysis, heteropoly compounds are frequently used because of their acidity, oxidizing power, and ability to maintain the molecular character of the heteropolyanion in the solid state. The HPA, $H_3PW_{12}O_{40}$ is the one that is regularly used among all of the HPAs. It is unsuitable for the selective synthesis of particular biomass derivatives and requires balanced Lewis and Brønsted acid sites [81,85–87]. Pure HPAs have a tiny surface area and are about 10 nm in size. It is critical to be able to recycle HPA catalysts enough to sustainably valorize biomass and construct industrial-scale processes. To address this shortcoming, increase the hydrophobicity of HPAs, and construct a heterogeneous catalysis system, we used two different strategies in this work to convert commercially available HPW into a heterogeneous catalyst: metal exchange (Zr, Cs,) and immobilization using a metal-organic framework (UiO66-NH2) as a support.

1.5. Scope and Objective of the Thesis:

1.5.1. Scope of the Thesis:

The following are some issues with the previously known procedures for producing alkyl levulinates and furfuryl ethers from glucose and furans:

- ➢ Use of homogenous acid catalyst: difficult recovery and corrosiveness of catalyst
- ➢ Use of costly Ionic liquids: high cost and needs a multistep process for separation and purification

➢ Use of traditional zeolites and acid-functionalized clays: low catalytic activity and deactivates due to pore blockage by humin's formation and leaching of active sites

➢ Low yield and selectivity for Al and FE production from sugars and furans

➢ Catalyst recyclability and regeneration

To solve the aforementioned obstacles, an efficient, green, one-pot process for converting lignocellulosic-based sugar and furanics to Al and FE must be developed. Another significant difficulty is the stability and reuse of catalysts. Catalysts with high recyclability and exploitability across a wide range of reaction conditions should be developed for the conversion of a variety of substrates (glucose, furfuryl aldehyde, and furfuryl alcohol).

1.5.2. The objectives of the thesis:

Considering the challenges indicated earlier, our main goal of the thesis is to use relatively cheaper, highly acidic Heteropoly acids as a heterogeneous (recoverable and recyclable) catalyst. It is well known that heteropolyacid is hydrothermally stable but very soluble in a polar solution, and the conversion of lignocellulosic biomass and associated sugars and chemicals to ethers and esters occurs in polar solvents. So our key objectives are as follows:

➢ Modification heteropoly acid: to generate heterogeneity and to alter physicochemical properties

➢ Use of modified heteropoly acid as a recoverable/reusable catalyst for valorization lignocellulosic feedstock/derived Sugars and furanic to FE and AL.

1.6. References

1 R. Reshmy, E. Philip, A. Madhavan, R. Sirohi, A. Pugazhendhi, P. Binod, M. Kumar Awasthi, N. Vivek, V. Kumar and R. Sindhu, *Bioresour Technol*, 2022, **344**, 126241.

2 N. Adlakha, R. Bhatnagar and S. S. Yazdani, *Biomass for Bioenergy and Biomaterials*, , DOI:10.1201/9781003158486/BIOMASS-BIOENERGY-BIOMATERIALS-RAKESH-BHATNAGAR-NIDHI-ADLAKHA-SYED-SHAMS-YAZDANI.

3 *Ministry of New and Renewable Energy, Government of India*.

4 W.-J. Liu and H.-Q. Yu, *ACS Environ. Au.*, 2021, **2**, 98–144.

5 N. L. Panwar, R. Kothari and V. V. Tyagi, *Renewable and Sustainable Energy Reviews*, 2012, **16**, 1801–1816.

6 A. I. Osman, N. Mehta, A. M. Elgarahy, A. Al-Hinai, A. H. Al-Muhtaseb and D. W. Rooney, *Environmental Chemistry Letters 2021 19:6*, 2021, **19**, 4075–4118.

7 H. M. Zabed, S. Akter, J. Yun, G. Zhang, F. N. Awad, X. Qi and J. N. Sahu, *Renewable and Sustainable Energy Reviews*, 2019, **105**, 105–128.

8 M. Casau, M. F. Dias, J. C. O. Matias and L. J. R. Nunes, *Resources 2022, Vol. 11, Page 35*, 2022, **11**, 35.

9 J. P. Lange, *Biofuels, Bioproducts and Biorefining*, 2007, **1**, 39–48.

10 J. P. Amigues, A. A. Le Kama and M. Moreaux, *J Econ Dyn Control*, 2015, **55**, 89–112.

11 A. Greiner, L. Gruene and W. Semmler, *Environ Dev Econ*, 2014, **19**, 417–439.

12 M. Usman, D. Balsalobre-Lorente, A. Jahanger and P. Ahmad, *Renew Energy*, 2022, **183**, 90–102.

13 M. Mujtaba, L. Fraceto, M. Fazeli, S. Mukherjee, S. M. Savassa, G. Araujo de Medeiros, A. do Espírito Santo Pereira, S. D. Mancini, J. Lipponen and F. Vilaplana, *J Clean Prod*, 2023, 136815.

14 S. Bhuvaneshwari, H. Hettiarachchi and J. N. Meegoda, *International Journal of Environmental Research and Public Health 2019, Vol. 16, Page 832*, 2019, **16**, 832.

15 A. Tursi, *Biofuel Research Journal*, 2019, **6**, 962–979.

16 A. Tursi and F. Olivito, *Advances in Bioenergy and Microfluidic Applications*, 2021, 3–39.

17 D. Klemm, B. Heublein, H.-P. Fink, A. Bohn, D. Klemm and H.-P. Fink, *Angew. Chem. Int. Ed*, 2005, **44**, 22.

18 J. Rao, Z. Lv, G. Chen and F. Peng, *Prog Polym Sci*, 2023, 140.

19 A. Lorenci Woiciechowski, C. J. Dalmas Neto, L. Porto de Souza Vandenberghe, D. P. de Carvalho Neto, A. C. Novak Sydney, L. A. J. Letti, S. G. Karp, L. A. Zevallos Torres and C. R. Soccol, *Bioresour Technol*, 2020, **304**, 122848.

20 V. B. Agbor, N. Cicek, R. Sparling, A. Berlin and D. B. Levin, *Biotechnol Adv*, 2011, **29**, 675–685.

21 M. Shahabazuddin, B. K. Banuvalli, N. Mulik, A. Pande, V. Bokade and S. N. Mudliar, *Biomass Convers Biorefin*, , DOI:10.1007/s13399-021-01565-z.

22 T. Zhao, Y. Zhang, G. Zhao, X. Chen, L. Han and W. Xiao, *Fuel Processing Technology*, 2018, **180**, 14–22.

23 T. Runge and C. Zhang, *Ind Eng Chem Res*, 2012, **51**, 3265–3270.

24 M. Signoretto, S. Taghavi, E. Ghedini and F. Menegazzo, *Molecules*, 2019, 24.

25 S. Saravanamurugan and A. Riisager, *ChemCatChem*, 2013, **5**, 1754–1757.

26 H. Li, Z. Fang, J. Luo and S. Yang, *Appl Catal B*, 2017, **200**, 182–191.

27 S. Zhou, X. Yang, Y. Zhang, L. Jiang, L. Zhou, T. Lu and Y. Su, *Cellulose*, 2019, **26**, 9135–9147.

28 S. Zhao, G. Xu, J. Chang, C. Chang, J. Bai, S. Fang and Z. Liu, *Bioresources*, 2015, **10**, 2223–2234.

29 K. I. Shimizu and A. Satsuma, *Energy Environ Sci*, 2011, 4, 3140–3153.

30 K. Alamgir Ahmad, M. Haider Siddiqui, K. K. Pant, K. D. P. Nigam, N. P. Shetti, T. M. Aminabhavi and E. Ahmad, *Chemical Engineering Journal*, 2022, **447**, 137550.

31 J. Nelson Appaturi, J. Andas, Y. K. Ma, B. Lee Phoon, S. Muazu Batagarawa, F. Khoerunnisa, M. Hazwan Hussin and E. P. Ng, *Fuel*, 2022, **323**, 124362.

32 M. A. Hanif, S. Nisar and U. Rashid, *Catal Rev Sci Eng*, 2017, **59**, 165–188.

33 R. C. Saxena, D. K. Adhikari and H. B. Goyal, *Renewable and Sustainable Energy Reviews*, 2009, **13**, 167–178.

34 J. R. Rostrup-Nielsen, *Science (1979)*, 2005, 308, 1421–1422.

35 R. Abdulla, E. S. Chan and P. Ravindra, *Crit Rev Biotechnol*, 2011, **31**, 53–64.

36 B. Nikolau, M. A. Perera, L. Brachova and B. Shanks, *The Plant Journal*, 2008, **54**, 536–545.

37 F. Cherubini, *Energy Convers Manag*, 2010, **51**, 1412–1421.

38 T. Werpy and G. Petersen, *Us Nrel*, 2004, Medium: ED; Size: 76 pp. pages.

39 Y. Gu, Y. Jiang, H. Wu, X. Liu, Z. Li, J. Li, H. Xiao, Z. Shen, H. Dong, Y. Yang, Y. Li, W. Jiang and S. Yang, *Biotechnol J*, 2011, **6**, 1348–1357.

40 Y.-N. Zheng, L.-Z. Li, M. Xian, Y.-J. Ma, J.-M. Yang, X. Xu and D.-Z. He, *J Ind Microbiol Biotechnol*, 2009, **36**, 1127–1138.

41 B. G. Harvey and H. A. Meylemans, *Journal of Chemical Technology & Biotechnology*, 2011, **86**, 2–9.

42 J. J. Bozell and G. R. Petersen, *Green Chemistry*, 2010, **12**, 525–728.

43 B. Kamm, *Angewandte Chemie International Edition*, 2007, **46**, 5056–5058.

44 J. Chapman, A. E. Ismail and C. Z. Dinu, *Catalysts 2018, Vol. 8, Page 238*, 2018, **8**, 238.

45 J. Wang, J. Xi and Y. Wang, *Green Chemistry*, 2015, **17**, 737–751.

46 M. J. E. C. Van Der Maarel, B. Van Der Veen, J. C. M. Uitdehaag, H. Leemhuis and L. Dijkhuizen, *J Biotechnol*, 2002, **94**, 137–155.

47 P. E. V. Paul, V. Sangeetha and R. G. Deepika, *Recent Developments in Applied Microbiology and Biochemistry*, 2019, 107–125.

48 K. Yan, G. Wu, T. Lafleur and C. Jarvis, *Renewable and Sustainable Energy Reviews*, 2014, **38**, 663–676.

49 G. G. Millán and H. Sixta, *Catalysts 2020, Vol. 10, Page 1101*, 2020, **10**, 1101.

50 Glucose Market Significantly Expanded and Will Hit Revenue USD 75.62 BN by 2032, https://www.precedenceresearch.com/press-release/glucose-market, (accessed 24 August 2023).

51 Furfuryl alcohol | Industrial processing | Silvateam, https://www.silvateam.com/en/products-and-services/industrial-processing/furfuryl-alcohol.html, (accessed 30 August 2023).

52 Furfuryl Alcohol - IFC, https://www.furan.com/products/furfuryl-alcohol/, (accessed 30 August 2023).

53 P. Bajpai, *Biorefinery in the Pulp and Paper Industry*, 2013, 65–98.

54 Furfuryl Alcohol Market Size & Share Report, 2021-2028, https://www.grandviewresearch.com/industry-analysis/furfuryl-alcohol-market, (accessed 2 September 2023).

55 Furfuryl Alcohol Market Size, Share, Growth Analysis, By Application, End-User - Industry Forecast 2023-2030, https://www.skyquestt.com/report/furfuryl-alcohol-market, (accessed 2 September 2023).

56 A. Corma Canos, S. Iborra and A. Velty, *Chem Rev*, 2007, **107**, 2411–2502.

57 J. Felipe Leal Silva, R. Grekin, A. Pinto Mariano and R. aciel Filho, , DOI:10.1002/ente.201700594.

58 M. J. Climent, A. Corma and S. Iborra, *Green Chemistry*, 2014, **16**, 516–547.

59 Q. Cao, W. Zhang, S. Luo, R. Guo and D. Xu, *Energy and Fuels*, 2021, **35**, 12725–12733.

60 A. Démolis, N. Essayem and F. Rataboul, *ACS Sustain Chem Eng*, 2014, **2**, 1338–1352.

61 D. R. Cha, T. E. Davies, S. H. Taylor and A. E. Graham, *ACS Sustainable Chem. Eng.*, 2018, 4996–5002.

62 F. Zaccheria, N. Scotti, N. Ravasio and D. E. E. Dbe, *catalysts*, , DOI:10.3390/catal9020172.

63 X. Liu, W. Yang, Q. Zhang, C. Li and H. Wu, *Front Chem*, 2020, **8**, 794.

64 L. Yan, Q. Yao and Y. Fu, *Green Chemistry*, 2017, **19**, 5527–5547.

65 R. Marcel, T. Durillon, L. Djakovitch, F. Fache and F. Rataboul, *ChemistrySelect*, 2019, **4**, 3329–3333.

66 G. Shrivastav, T. S. Khan, M. Agarwal and M. A. Haider, *ACS Sustain Chem Eng*, 2017, **5**, 7118–7127.

67 E. Christensen, A. Williams, S. Paul, S. Burton and R. L. McCormick, *Energy & Fuels*, 2011, **25**, 5422–5428.

68 *Ethyl Levulinate Market Size, Share, Price, Outlook 2023-2028*, .

69 *Ethyl Levulinate Market Size | Industry Report, 2022*, .

70 R. J. Haan and J.-P. Lange, .

71 F. B. Ahmad, M. A. Kalam, Z. Zhang and H. H. Masjuki, *Energy Conversion and Management: X*, , DOI:10.1016/j.ecmx.2022.100222.

72 B. Vanderhaegen, H. Neven, L. Daenen, K. J. Verstrepen, H. Verachtert and G. Derdelinckx, *J Agric Food Chem*, 2004, **52**, 1661–1668.

73 J. M. Pin, N. Guigo, A. Mija, L. Vincent, N. Sbirrazzuoli, J. C. van der Waal and E. de Jong, *ACS Sustain Chem Eng*, 2014, **2**, 2182–2190.

74 X. Gao, L. Peng, H. Li and K. Chen, *Bioresources*, 2015, **10**, 6548–6564.

75 S. J. Dee and A. T. Bell, *ChemSusChem*, 2011, **4**, 1166–1173.

76 J. N. Appaturi and J. Andas, *Advanced Catalysis for Drop-in Chemicals*, 2022, 291–311.

77 J. Dai, L. Peng and H. Li, *Catal Commun*, 2018, **103**, 116–119.

78 C. Travers, N. Essayem, M. Delage and S. Quelen, *Catal Today*, 2001, **65**, 355–361.

79 I. V. Kozhevnikov and K. I. Matveev, *Appl Catal*, 1983, **5**, 135–150.

80 M. N. Timofeeva, *Appl Catal A Gen*, 2003, **256**, 19–35.

81 M. Tao, L. Xue, Z. Sun, S. Wang, X. Wang and J. Shi, *Sci Rep*, , DOI:10.1038/srep13764.

82 U. B. Mioc and Z. P. Nedić, in *Encyclopedia of Membranes*, eds. E. Drioli and L. Giorno, Springer Berlin Heidelberg, Berlin, Heidelberg, 2015, pp. 1–3.

83 K. Narasimharao, D. R. Brown, A. F. Lee, A. D. Newman, P. F. Siril, S. J. Tavener and K. Wilson, *J Catal*, 2007, **248**, 226–234.

84 Z. Sun, X. Duan, P. Gnanasekarc, N. Yan and J. Shi, , DOI:10.1007/s13399-020-00802-1/Published.

85 C. Megías-Sayago, S. Navarro-Jaén, F. Drault and S. Ivanova, *Catalysts 2021, Vol. 11, Page 1395*, 2021, **11**, 1395.

86 N. S. M. Azlan, C. L. Yap, S. Gan and M. B. A. Rahman, *Ind Crops Prod*, 2022, **181**, 114778.

87 S. Dutta, *RSC Adv*, 2012, **2**, 12575–12593.

Chapter-2

Glucose Conversion to Ethyl Levulinate Over Zr-exchanged HPW catalyst and Sn-betas as a co-catalyst

2.1 Introduction

As natural energy resources (fossil fuels) are depleting, the use of renewable feedstocks is emerging as a new sustainable alternative. Based on its wide availability, agricultural biomass may be the best option among the other potential options. Direct biomass or carbohydrates derived from biomass can be catalyzed into specialty and fine chemicals and fuel additives. Alkyl levulinates (AL) have specific physicochemical properties that can be tailored to various chemicals and process industry applications such as crude oil additives, solvents, flavorings, fragrance agents, and so on. [1,2] Because of their similar qualities to fatty acid methyl esters, as well as their low toxicity, high stability, and lubricity, AL have a significant potential as gasoline additives [3]. They are regarded as promising from the perspective of sustainability since they originate from "renewable feedstock" and have a positive impact on the ideas of "less hazardous chemical syntheses," "safer solvents and auxiliaries," and "inherently safer chemistry for accident avoidance." Levulinate esters, such as ethyl levulinate (EL) and butyl levulinate (BL), have been investigated as oxygenate additives, boosting the conductivity, lubricity, and freezing point of fuels, and lowering combustion emissions [1,3–6]. Amongst these esters, Ethyl Levulinate (EL) is the most preferable ester over methyl and butyl, due to its higher mixing properties with biodiesel [4,6,7]. The application of these biofuel additives will enhance the consumption of biodiesel in the automotive sector of the world.

EL can be synthesized by esterification of Levulinic acid (LA) and it is also reported that Furfuryl alcohol from xylose can also be converted into EL using acid catalysts[8–11]. The direct conversion of Glucose to AL will be more cost-effective, and the creation of a highly effective catalytic system for the one-pot transformation of sugars into AL will be beneficial. Because glucose is less expensive and more abundant, the direct catalytic translation of glucose to EL is an appealing choice in terms of academic and industrial relevance [12].

EL synthesis from carbohydrates such as glucose was studied over various catalysts such as HCL, H_3PO_4, H_2SO_4, H_2SO_4-Al (OTf)$_3$, SO_4^{2-}- ZrO_2, SO_4^{2-}- ZrO_2/SBA-15, Amberlyst-35 and H-USY (zeolite) [13–18]. Among homogenous catalysts, H_2SO_4-Al(OTf)$_3$ having both Brønsted and Lewis acidity showed 64.9% EL at 180 °C in 3 h [18] and heterogeneous catalysts such as HUSY showed maximum yield EL (41%) EL at 160°C in 20 h.[13] According to the literature, a catalyst with only Lewis or Brønsted acidity is not suitable for converting glucose to EL because Brønsted acidity is required for the subsequent reactions of hydration and dehydration of fructose to EL, whereas Lewis acidity is primarily required for isomerizing glucose to fructose. As a result, a catalyst with the proper balance of Brønsted and Lewis acidity is more beneficial than a catalyst with exclusively acidic sites. Jiang et al. reported a mixed catalytic system comprised of Lewis (Sn-Beta) and Brønsted (SO_4^{2-}/ZrO_2) acidic catalysts for the synthesis of methyl levulinate (ML) [17].

HPAs are a fascinating family of well-defined strong solid Brønsted acids with outstanding catalytic activity in a wide range of acid-catalyzed processes [19–25]. However, HPAs are not much explored for the transformation of cellulose, glucose, and fructose to fine and specialty chemicals and fuel additives because of their solubility in polar mediums like water and alcohol. To overcome this drawback of HPAs, in our previous work [26], HPA tungstophosphoric acid ($H_3PW_{12}O_{40}$) was modified by exchanging proton with zirconia (Zr) and was used as a heterogenized catalyst in a polar medium, so that it can be used in carbohydrate chemistry effectively where hydration, dehydration, and rehydration reactions are prominent. The catalytic applicability of Zr-modified HPW for the one-step conversion of glucose to EL is described in this chapter. The direct one-step conversion of glucose to EL using a synergetic physical mixture of $H_2Zr_1PW_{12}O_{40}$ + Sn-Beta with Brønsted and Lewis acidity is examined to maximize EL production and convert wider glucose concentrations under milder working conditions.

2.2 Experimental

2.2.1 Materials

Zirconium nitrate and Keggin-type tungstophosphoric acid (AR) were purchased from Thomas Baker, Mumbai (India), tetraethyl ammonium hydroxide (TEAOH, aq. 40% solution, V.P. Chemicals), tetraethyl orthosilicate (TEOS, 98%, Silbond), Tin (IV) chloride ($SnCl_4.5H_2O$, 98%, Loba Chem), hydrofluoric acid (HF, 48 wt %, Thomas Baker), sodium aluminate (43.8% Al_2O_3, 39.0% Na_2O, Loba Chem), perchloric acid ($HClO_4$, 70%, Merck), sodium hydroxide (NaOH, 98 % AR Loba Chem), Tin (IV) chloride ($SnCl_4.5H_2O$, 98%, Loba Chem), silica sol (40% SiO_2, Loba Chem), CTAB, NH_4OH, TBOT, and IPA.

Chemicals and analytical standards Glucose from Loba Chem, EFE, EL, and FAlc were procured from Sigma Aldrich and Ethanol from Changshu Hongsheng Fine Chemical China

2.2.2 *Catalyst Preparation*

2.2.2.1 *Synthesis of Zr Exchanged HPW*

We synthesized Zr exchanged HPW samples by adding 0.25 and 0.5 mmol aqueous solution of $ZrO(NO_3)_2.xH_2O$ dropwise to a 1 mmol aqueous solution of $H_3[PW_{12}O_{40}].nH_2O$ (tungstophosphoric acid/HPW) vigorously combined. The resulting milky suspension was allowed to rest for 12 hours at room temperature. At a temperature of 100℃, water slowly evaporated in an oil bath to produce the white powder. The samples were then calcined for 3 hours at 350 °C after being dried for 12 hours in a 120 °C oven. The catalysts were labeled $H_2Zr_1PW_{12}O_{40}$ and $H_1Zr_2PW_{12}O_{40}$ for ease of use.

2.2.2.2 *Synthesis of Lewis acid co-catalysts*

2.2.2.2.1 *Synthesis of Sn-beta*

According to a prior report, [27] Sn-beta was synthesized. To make Sn-beta, 42.4 g of TEOS and 39.69 g of TEAOH were combined while being vigorously stirred. At a temperature of 30 °C, the stirring was continued. We observed the weight loss (about 17%) brought on by the release of ethanol. With continual stirring, 0.58 g of $SnCl_4.5H_2O$ in 10 ml water and 4.5 g of HF were added to this mixture. The aforesaid mixture was then vigorously stirred while 2.84 g of 70% aqueous perchloric acid, employed as a promoter, was added. This process was repeated until a homogenous gel was formed. This gel's estimated molar composition was SiO2: 0.0083 SnO2: 0.54 TEAOH: 0.54 HF: 0.1 HClO4: 7.5 H_2O. After that, a 30-day hydrothermal treatment at 140 °C was performed on the obtained gel in an autoclave. Vacuum filtration was used to separate the solid after crystallization, and it was then dried at 120°C for four hours. After that, the dry product was air-calcined at 550°C for 12 hours.

2.2.2.2.2 *Synthesis of SnO_2*

The surfactant-based based approach is used to produce SnO_2 powder. In a typical synthesis, three grams of CTAB were combined with 25 ml of water, and the resulting mixture was stirred until it became homogenous. The CTAB solution was then mixed with 2 ml of NH_4OH (25-weight percent solution) solution that had been diluted with 8 ml of distilled water. The above-mentioned ammonical CTAB solution was then gently added while being constantly stirred, 2.5 g $SnCl_45H_2O$ dissolved in 25 ml pure deionized water. The resultant slurry was aged at room temperature for 48 hours after being continuously stirred for 3 hours. The aged slurry was further filtered, the wet cake was washed with distilled water, dried at ambient temperature, and then subjected to a 5-hour calcination process at 500 °C.

2.2.2.2.3 *Synthesis of TiO_2*

TiO_2 was synthesized using the sol-gel method. A typical synthesis consisted of the addition of 4.23 g of TBOT with constant stirring, in an (42 g) IPA. The mixture was agitated after the addition was finished for a further six hours, and then it was dried at 80 °C. The dry powder was then heated to 550 °C in the air for 9 hours at a heating rate of 1 °C/mi.

2.2.3 *Characterization of the catalysts*

Catalyst powder X-ray diffraction (XRD) patterns were acquired using a PANalytical system (model Xpert-PRO-1712) and monochromated Cu K radiation (=0.154) in the 5o to 90^o range.

To assess the textural qualities of materials, a typical nitrogen adsorption equipment (Micromeritics ASAP 2010 system) was employed. The Brunauer-Emmett-Teller (BET) method was used to analyze the sample's specific surface area.

Using a MicromeriticsAutoChem (2910, USA) with a thermal conductivity detector, the total acidity and acid strength related to each site were determined. The material was dehydrated for 1 hour at 300 °C in He (30 cm3 min1) before the measurements. After that, the temperature was lowered to 100 °C, and the sample was exposed for an hour to a gas stream composed of 10% NH_3 and He. He was then used to flush it for an additional hour. By increasing the temperature to 800 °C, the NH_3 desorption was performed in He flows (30 cm3 min1) at a rate of 10 °C min1. A TCD was used to calculate the amount of desorbed ammonia.

On a Thermo-Nicolet 670 spectrometer, an FTIR spectrum between 400 and 4000 cm-1 was acquired. A JASCO J810 spectrometer with a peltier water circulation thermostated six locations automatic cell changer and a variable slit system was utilized to capture the spectra.

Another application of IR spectroscopy is to find out the type of active sites on the catalyst surface (mainly acidic and basic sites) by using various probe molecules. Pyridine is one of the most often utilized probes because it can provide information on both the Lewis and Brønsted acid sites simultaneously. The IR bands from pyridine coordinated to Lewis acid sites appear at 1450 and 1620 cm^{-1}, while the typical bands of pyridine hydrogen bound at a Brønsted acid site appear in the areas of 1400-1477 cm^{-1}, 1485-1490 cm^{-1}, and 1580-1600 cm^{-1} [28–30].

Ex-situ pyridine-FTIR was used to determine the type of acid sites (Brønsted and/or Lewis) present in the catalyst. Using a high vacuum, a catalyst powder sample was cooled to ambient temperature after being activated at 200°C for two hours. Then, it was subjected to pyridine vapors for two hours. By activating at 100°C for two hours while under a high vacuum, the physisorbed pyridine was driven off. The Fourier Transform Infrared Spectroscopy (FTIR) of the IR spectra was carried out using a Bruker Alpha-P ATR FTIR spectrometer, and the B/L ratio was computed using the published method [28].

2.2.4 *Reaction procedure*

A 30 ml capacity SS316 stainless steel reactor with a pressure gauge was used for all reactions. In a typical reaction, 0.37 g of glucose, 50 weight percent catalyst for the glucose weight, and 12 mL of ethanol were introduced to the reactor. The reactor was then heated to a temperature between 140 and 200°C with constant stirring at 800 rpm for 3 hours. The reactor then cooled to room temperature in a cold-water bath at the end of the reaction to quench the reaction. The catalyst was then separated by centrifugation, and the centrifuged sample was diluted in ethanol before being analyzed using gas chromatography and HPLC. The following equations were used to compute glucose conversion and yield of EMF, EL, and ELA.

.

$$\%\ Conversion = \left(\frac{Initial\ moles\ of\ glucose - Final\ moles\ of\ glucose}{Initial\ moles\ of\ glucose}\right) * 100$$

$$\%\,Yield = \left(\frac{moles\ of\ product\ Formed}{Initial\ glucose\ moles}\right) * 100$$

2.3 Results and Discussion

2.3.1 Catalysts characterization

2.3.1.1 X-ray diffraction

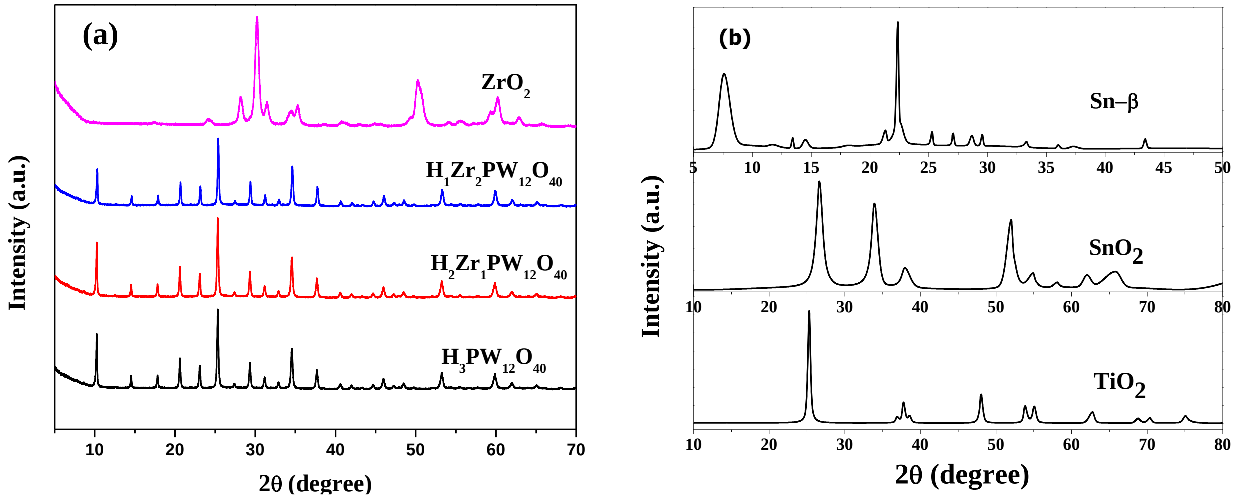

Figure 2.1 XRD profiles of Bronsted acids (a) $H_3PW_{12}O_{40}$, $H_2Zr_1PW_{12}O_{40}$, $H_2Zr_1PW_{12}O_{40}$, and ZrO_2 and Lewis acids (b) TiO_2, SnO_2 and Sn-β

The powder X-ray diffraction pattern of $H_3PW_{12}O_{40}$, $H_2Zr_1PW_{12}O_{40}$, $H_2Zr_1PW_{12}O_{40}$, and ZrO_2 are presented in Figure 2.1 (a). The XRD pattern of $H_3PW_{12}O_{40}$ and $H_xZr_{3-x}PW_{12}O_{40}$ exhibits diffraction peaks of Keggin structure at 2 θ = 10.5°, 18.3°, 23.7°, 26.1°, 30.2°, 35.6°and 38.8°, which are also assigned to a body-centered cubic structure [26]. However, there is no extra peak corresponding to ZrO_2 or peak due to a change in the Keggin structure. This indicates that Zr may have been incorporated into the Keggin structure.

The XRD diffraction pattern for the Sn-beta sample was comparable with the structure of standard zeolite beta, with no impurity phases detected, as shown in Figure 2.1. (b) [27,31] and XRD diffraction patterns of SnO_2 and TiO_2 also showed pure crystalline phase[32,33].

2.3.1.2 *FT-IR*

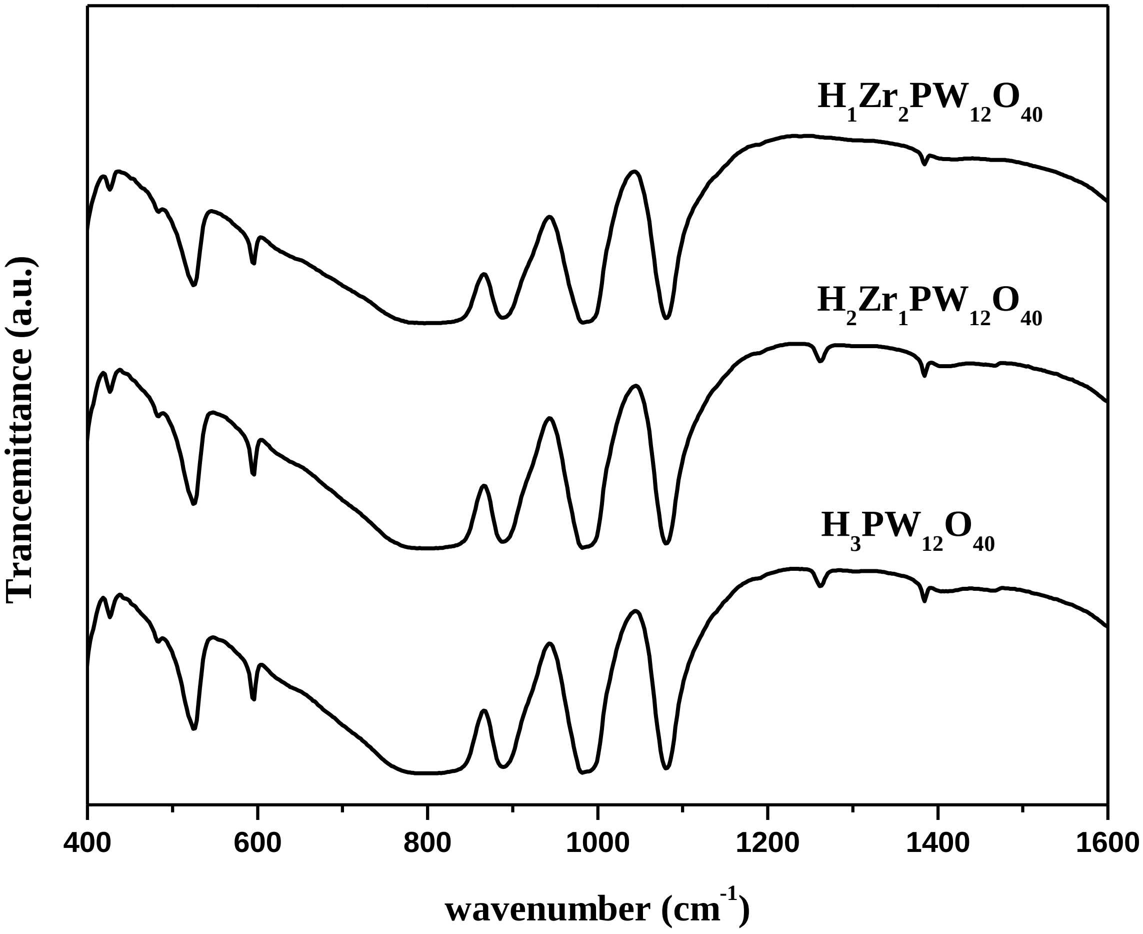

Figure 2.2 FT-IR spectra of $H_3PW_{12}O_{40}$, $H_2Zr_1PW_{12}O_{40}$, and $H_2Zr_1PW_{12}O_{40}$

The FT-IR spectra revealed bands at 1080, 983, 890, and 820 cm^{-1}, which are ascribed to the asymmetric vibrations of P-O (oxygen atoms bound to three W atoms and one P), W-O (terminal oxygen atom), W-O-W (corner sharing bridging oxygen atom), and W-O-W (edge sharing bridging oxygen atom) respectively[34]. These bands are the typical characteristic bands of the Keggin structure [34,35]. The FTIR data show that a Keggin structure was maintained during the proton exchange of zirconium with $H_3PW_{12}O_{40}$.

2.3.1.3 *N_2 physisorption*

The BET surface area and crystallite size of $H_3PW_{12}O_{40}$, $H_2Zr_1PW_{12}O_{40}$, and $H_1Zr_2PW_{12}O_{40}$ have been tabulated in Table 2.1. No noticeable influence of Zr on BET surface area was observed, the BET surface area of all samples remained in the range of 4–6 m^2/g.

2.3.1.4 *NH_3-TPD*

Table 2.1 Physicochemical characteristics of the catalyst

Sample	Total Acidity µmol/g	BET surface area m^2/g	Crystallite Size (nm)
$H_3PW_{12}O_{40}$	1241	4	42.52
$H_2Zr_1PW_{12}O_{40}$	1511	3	42.50
$H_1Zr_2PW_{12}O_{40}$	1310	6	44.68

The acidity of the Zr exchanged samples was calculated by using NH_3-TPD analysis and data is given in Table 2.1. The parent sample that is HPW has shown total acidty1241 µmol/g while Zr exchanged samples show a slight increase in total acidity, $H_2Zr_1PW_{12}O_{40}$ was found to be increased to 1511 µmol/g, and the sample with more Zr that is $H_1Zr_2PW_{12}O_{40}$ have shown total acidity of 1310 µmol/g. However, a reduction in acidity (1310 µmol/g) of $H_1Zr_2PW_{12}O_{40}$ has been observed compared to $H_2Zr_1PW_{12}O_{40}$. This decline in total acidity with the increase in Zr may be ascribed to the amorphous part of Keggin which reduces the accessibility of acidic active sites of Keggin unit [26]. While TPD profiles are shown in Figure 2.3 have not shown many more changes.

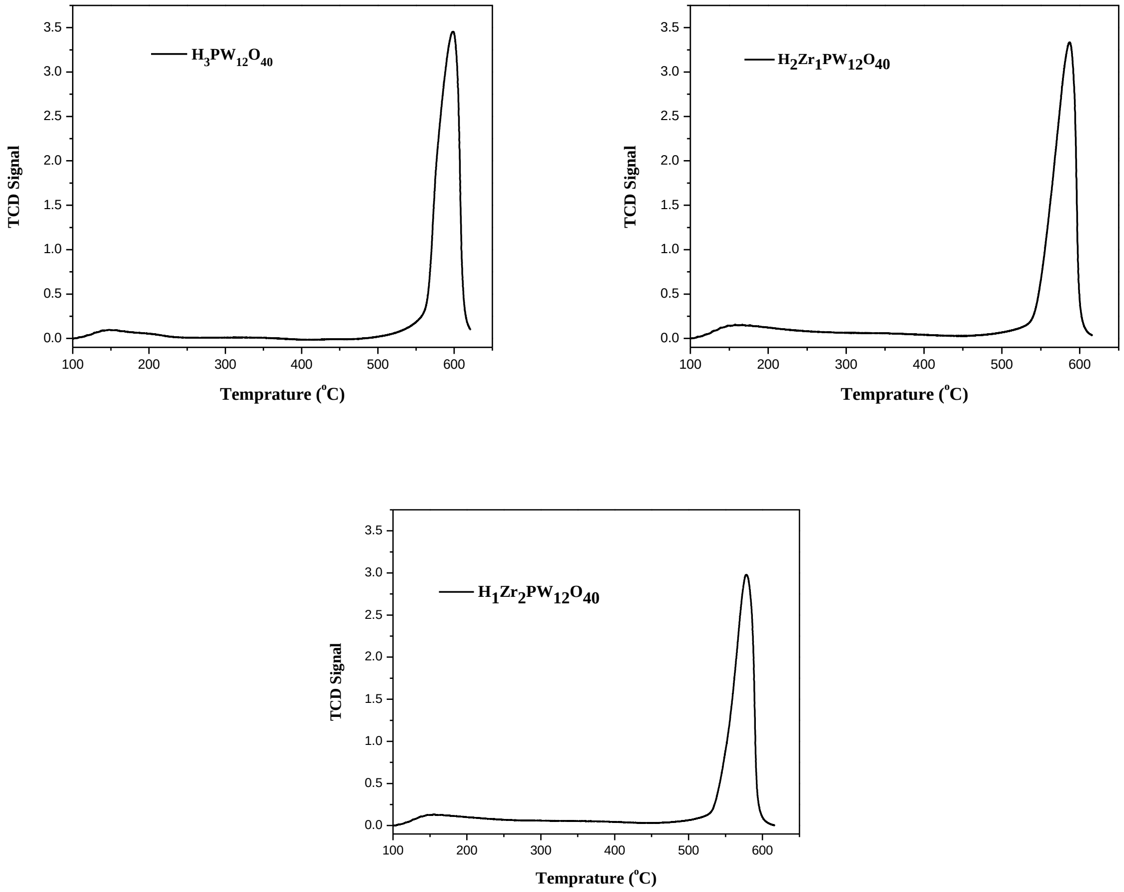

Figure 2.3 NH_3-TPD profiles of $H_3PW_{12}O_{40}$, $H_2Zr_1PW_{12}O_{40}$, and $H_2Zr_1PW_{12}O_{40}$

2.3.1.5 Pyridine FTIR

Pyridine vibrations adsorbed on Lewis acid sites are normally represented by the bands at 1450 cm-1 and 1610 cm-1, whereas those of pyridine adsorbed on Brønsted acid sites are typically represented by the bands at 1489 cm-1 and 1635 cm-1. The combination of pyridine absorption on Brønsted and Lewis acid sites results in the band at 1540 cm-1 [28–30].

Figure 2.4. shows individual Py-FTIR spectra of Sn-beta, $H_3PW_{12}O_{40}$, $H_2Zr_1PW_{12}O_{40}$, and $H_1Zr_2PW_{12}O_{40}$. The Py-FTIR of Sn-beta majorly shows intense bands of Lewis acid sites at 1450 cm^{-1} and 1610 cm^{-1}, while the phosphotungstic acid and Zr exchanged phosphotungstic acid have

shown an intense band for Brønsted acid sites at 1489 cm^{-1}, and there is the small band at 1450 cm^{-1} started appearing for the sample with higher Zr exchange/ content ($H_1Zr_2PW_{12}O_{40}$).

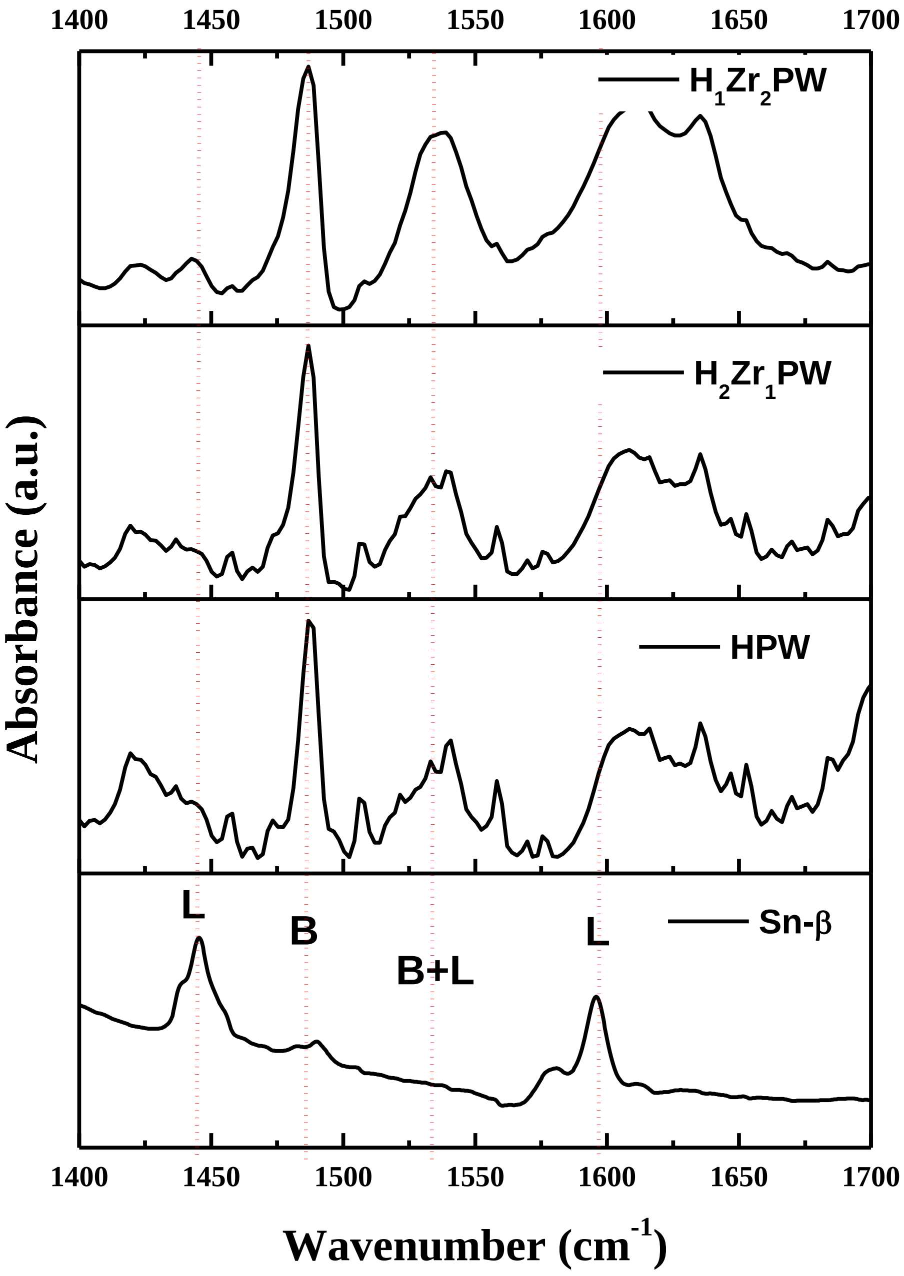

Figure 2.4 Py-FTIR spectra of HPW, $H_2Zr_1PW_{12}O_{40}$, and $H_2Zr_1PW_{12}O_{40}$ and Sn-beta

To obtain the proper Lewis and Brønsted acid sites desirable for the selective alcoholysis of glucose to AL, we used a mixture of Sn-beta as a Lewis acid component and Brønsted acidic Zr exchanged HPW samples.

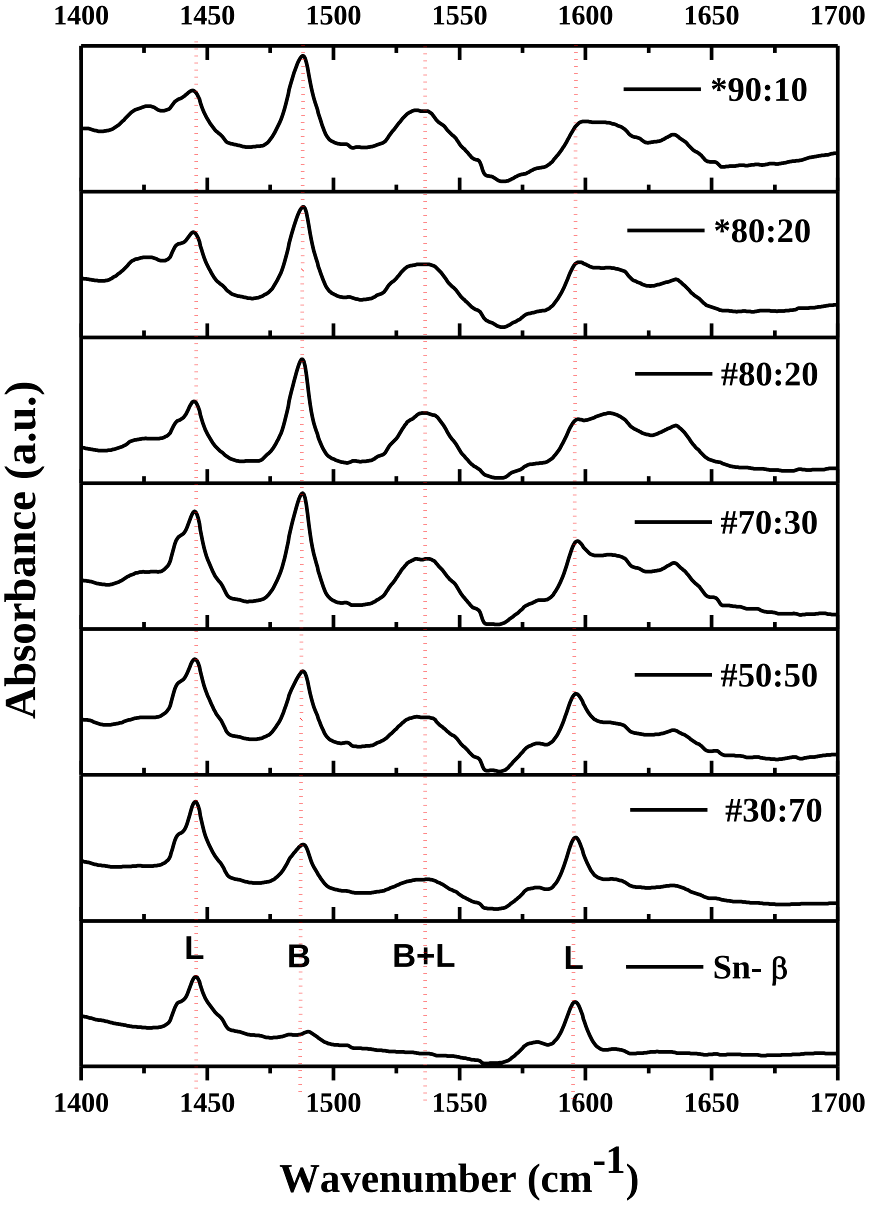

Figure 2.5 Py-FTIR spectra of individual Sn-beta and Physical combinations of #$H_1Zr_2PW_{12}O_{40}$ + Sn-beta and *$H_2Zr_1PW_{12}O_{40}$ + Sn-beta

To identify the relative Lewis and Brønsted sites, we performed an ex-situ Pyridine IR study of various ranges of the physical mixture, and the Spectra are displayed in Figure 2.5. From Figure 2.5 it can be confirmed that with an increase in Zr exchanged HPW in the physical mixture of Sn-beta and Zr-HPW samples the band at 1489 cm^{-1} corresponding to Brønsted acid sites started appearing and the peak goes on increasing with higher content of Brønsted acid component that is Zr-HPW. So, we have calculated the relative B/L ratio of each sample using a Brønsted acid peak at 1489 cm^{-1} and a Lewis acid peak at 1450 $cm^{-1,}$ and data are given in Table 2.3.

2.4 Catalytic activity

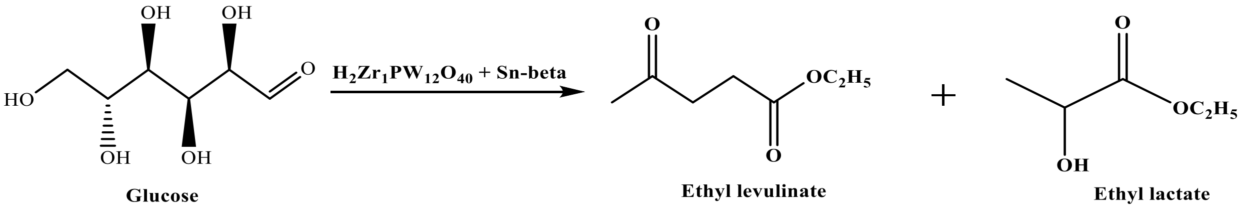

Scheme 2.1. Direct conversion of Glucose to EL

Table 2.2. Catalyst screening for glucose to EL conversion

Entry	Name of catalyst	% Conversion	% EMF yield	% EL yield	% ELA yield
1	$H_1Zr_2PW_{12}O_{40}$	98	0.0	14.0	0.0
2	$H_2Zr_1PW_{12}O_{40}$	99	0.0	26	0.0
3	Sn-Beta	95	10	0.0	18
4	$H_2Zr_1PW_{12}O_{40}$ + TiO_2 (80:20)	96	0.0	14.5	0.0
5	$H_2Zr_1PW_{12}O_{40}$ + SnO_2 (80:20)	97	0.0	26	0.0
6	$H_1Zr_2PW_{12}O_{40}$ + Sn-Beta (80:20)	99	1.4	34.7	33
7	$H_2Zr_1PW_{12}O_{40}$ + Sn-Beta (80:20)	99	3.2	48	16.4

8	$H_1Zr_2PW_{12}O_{40}$ + Sn-Beta (50:50)	97	1.5	34	53

Reaction conditions; 160°C, catalyst loading: 50% w.r.t. glucose, Glucose concentration: 50g/lit, 3hrs, 600rpm

Conventionally, EL can be synthesized by esterification of LA and it is also reported that Furfuryl alcohol from xylose can be converted into EL using acid catalysts. However, LA and Furfuryl alcohol can be synthesized from carbohydrates but they need to be purified for further conversion to EL. However, there is another route in which carbohydrates or carbohydrate-derived sugars can be directly converted to EL in the ethanolic medium by acid catalysis (scheme 2.1.)

The catalytic conversion of Glucose to EL was carried out by using different Lewis and Brønsted + Lewis catalysts (Table 2.2). Entry 1 and 2 of Table 2.2 presented the product distribution on partly substituted H+ proton of HPA with Zr making the catalyst partly insoluble (50%) in the polar medium like ethanol. In all the cases, glucose conversion is in the range of 95-100%. Apart from EL, another product formation was 5- Ethoxymethyl furfural (EMF); Ethyl lactate (ELA); and a minor contribution of humins and other polymeric compounds. Entry 1 and 2, formed EL 14 and 26% yield respectively. The activity has increased with the presence of more H+ ions in the catalyst. This catalyst has shown activity due to the presence of Brønsted acidity. In the presence of only Lewis acidic catalyst viz; Sn-beta, as per reaction mechanism (Figure 2.6) it is expected that Lewis acidic catalyst will favor ELA (18%) formation than EL (0%). The reaction is stuck up to 5-EMF (10%) Entry 4 to 8 of Table 2.2.; reveal the results with a physical mixture of Lewis + Brønsted acidic catalyst. It was found that the existence of highly Lewis acid catalyst viz; Sn-beta and its percentage in whole catalyst loading, leads to more formation of ELA than EL. Whereas, less Lewis acidic catalyst like TiO_2 and SnO_2 (entries 4 and 5) shows less ELA formation due to a reduction in the rate of Lewis acidic reaction like isomerization and retro-aldol condensation. Entries 6 and 8; gave the same EL (34%) despite having variation in the percentage of Sn-beta, whereas ELA formation has increased in case of a 50:50 ratio of $H_1Zr_2PW_{12}O_{40}$ +Sn-Beta as compared to 80:20, as more Lewis acid sites due to increasing in Sn-beta contribution increases Lewis acidic reaction which leads to the formation of ELA. Amongst all studied catalysts physical mixture of $H_2Zr_1PW_{12}O_{40}$ + Sn-Beta (80:20) combination gave maximum formation of EL (47.6%). This confirmed that proper combination with B+L and B/L >2.5 ratio is vital for the conversion of glucose to EL in one step.

2.4.1 *Effect of Process Variables on EL synthesis from Glucose*

It is generally known that the synthesis of EL necessitates Brønsted as well as Lewis acidity [17]. The current study established Brønsted and Lewis acidity in the catalyst by combining Zr-HPA (Brønsted acid) and Sn-beta (Lewis acid). Different combinations of Brønsted and Lewis acids, B/L ratio from 0.68 to 3.9 were prepared (Table 2.3.) by changing the weight ratio of Zr-HPA and Sn-beta from 30:70 to 90:10. Table 2.3. represents the catalytic performance in comparison with the B/L ratio.

Table 2.3. Effect of the Catalyst Composition

Entry	**Catalysts**	**Weight ratios**	**% Conv.**	**% EMF yield**	**% EL yield**	**% ELA yield**	**B/L ratio**
1	$H_1Zr_2PW_{12}O_{40}$ + Sn-Beta	30:70	95	2.4	36.0	50	0.68
2	$H_1Zr_2PW_{12}O_{40}$ + Sn-Beta	50:50	96	1.5	34	52	1.2
3	$H_1Zr_2PW_{12}O_{40}$ + Sn-Beta	70:30	97	1.2	32	40	1.9
4	$H_1Zr_2PW_{12}O_{40}$ + Sn-Beta	80:20	96	1.4	35	34	2.6
5	$H_2Zr_1PW_{12}O_{40}$ + Sn-Beta	80:20	97	3.2	48	16	3.7

6	$H_2Zr_1PW_{12}O_{40}$ + Sn-Beta	90:10	98	1.1	35	9	3.9

Reaction conditions: 160°C, catalyst loading: 50% w.r.t. glucose, glucose concentration: 50g/lit, 3hrs, 600 rpm.

It is clear from the catalytic performance study, that the combination of Brønsted acidic (Zr-HPA) and Lewis acidic (Sn-Beta) is crucial for EL yield. Nevertheless, the composition of Zr-HPA and Sn-Beta governs the actual B/L ratio which is an important parameter to get the maximum yield of EL. Table 2.3, presented the product distribution of $H_1Zr_2PW_{12}O_{40}$ and $H_2Zr_1PW_{12}O_{40}$ in combination with Sn-beta at different weight ratios. In the case of the 30:70 synergetic catalyst combinations of $H_1Zr_2PW_{12}O_{40}$ and Sn-beta with a B/L ratio of 0.68, entry 1 in Table 2.2 has shown EMF, EL, and ELA yield of 2.4%, 36%, and 50% respectively. The remarkably higher by-product yield (ELA) is probably due to the lower B/L ratio (0.68) which gives higher Lewis acidity and follows retro aldol condition over dehydration. In the case of 50:50 & and 70:30 weight ratio (entries No 2 & 3) the B/L ratio increased by 1.2 & and 1.9 respectively, the identical activity as a catalyst with a 30:70 ratio was observed. Above B/L ratio 1.9 ELA formation has decreased. In combination with H_1Zr_2TPA and Sn-beta in the ratio of 80:20 (entry no. 4) having a B/L ratio of 2.6 decreases the ELA formation from 50 to 34 at an identical EL yield of 35. In the case of $H_2Zr_1PW_{12}O_{40}$ and Sn-beta (80:20) having a B/L ratio of 3.7 increases the EL formation from 35 to 48 % at lower ELA formation of 16%, formation of EMF (1.1 to 1.4%) is same in all the cases. Further increase in $H_2Zr_1PW_{12}O_{40}$ contribution from 80% to 90% reduces the EL formation by 13% and ELA formation by 7%, this reduction in EL and ELA is mainly due to humins formation. Thus, the optimum combination of $H_2Zr_1PW_{12}O_{40}$ and Sn-beta (80:20) having a B/L ratio of 3.7 is crucial for the maximum formation of EL with the lower contribution of ELA and humins.

From the above study, it is speculated that the said reaction followed three steps namely isomerization, dehydration, and retro-aldol condensation. The catalyst $H_2Zr_1PW_{12}O_{40}$ in combination with Sn-Beta gives Brønsted and Lewis acidity so the present study confirms that when the contribution of $H_2Zr_1PW_{12}O_{40}$ is more means a higher B/L ratio leads to an increase in EL formation. Whereas, when the $H_2Zr_1PW_{12}O_{40}$ contribution is lower and more Sn-beta means the B/L ratio is low and it follows retro-aldol condensation steps leading to the formation of ELA. The optimum contribution of $H_2Zr_1PW_{12}O_{40}$ and Sn-beta 80:20 having a B/L ratio of 3.7 is crucial to maximize the yield of EL and suppress the ELA formation. In addition to this, the generation of EMF was also detected. Thus, the present experimental results validate the proposed mechanism (shown in Figure 2.6).

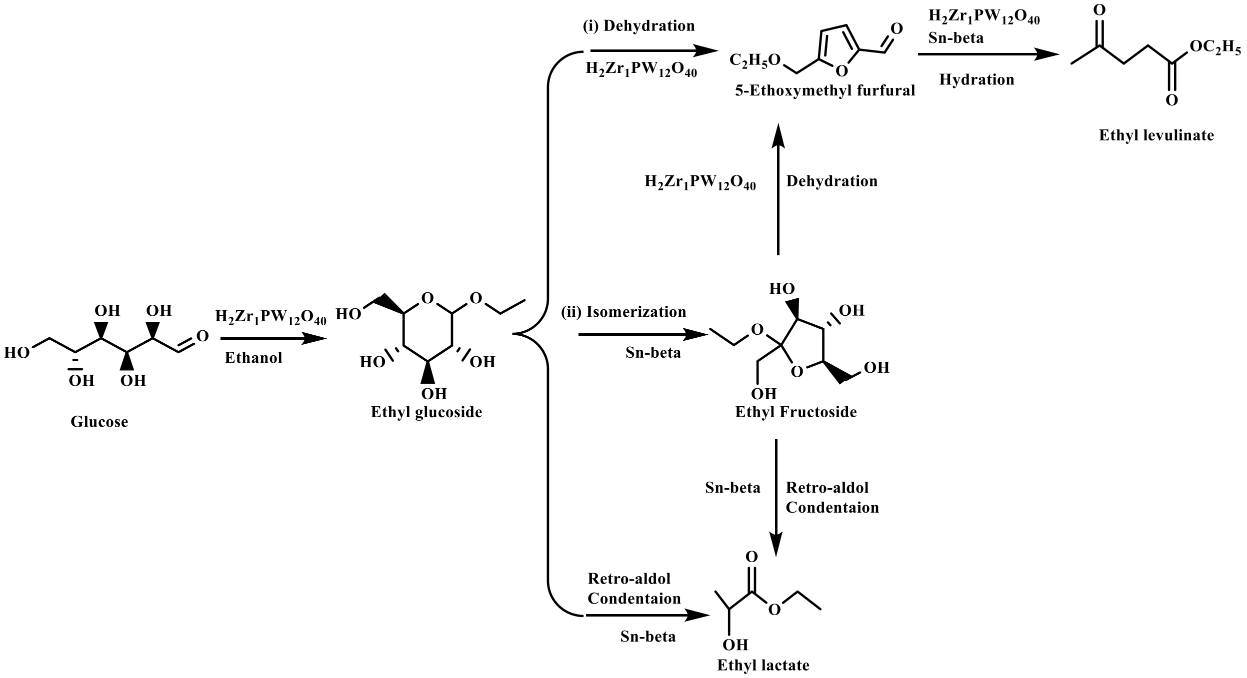

Figure 2.6 Mechanism of Alkyl levulinate and Alkyl lactate formation from glucose

2.4.1.1 *The effect of glucose concentrations*

The effect of glucose concentrations (25–50 g/L) which is an important parameter to study, was explored on an 80:20 physical mixture of $H_2Zr_1PW_{12}O_{40}$ + Sn-Beta (80:20) at 160◦C for 3 hours. As illustrated in Figure 2.7, as glucose concentration increased from 25 to 50 g/L, keeping ethanol concentration the same, EL yield and ELA yield were found to decrease from 47% to 39% and from 38 to 26%, respectively. This drop-in activity with a surge in glucose concentration is due to the slighter solubility of glucose in ethanol, as the glucose concentration rises. This lower glucose solubility reduces the rate of substrate mass transfer without chemical reaction, which affects catalyst activity. Thus, 30 g/L initial glucose concentration was used for further experiments.

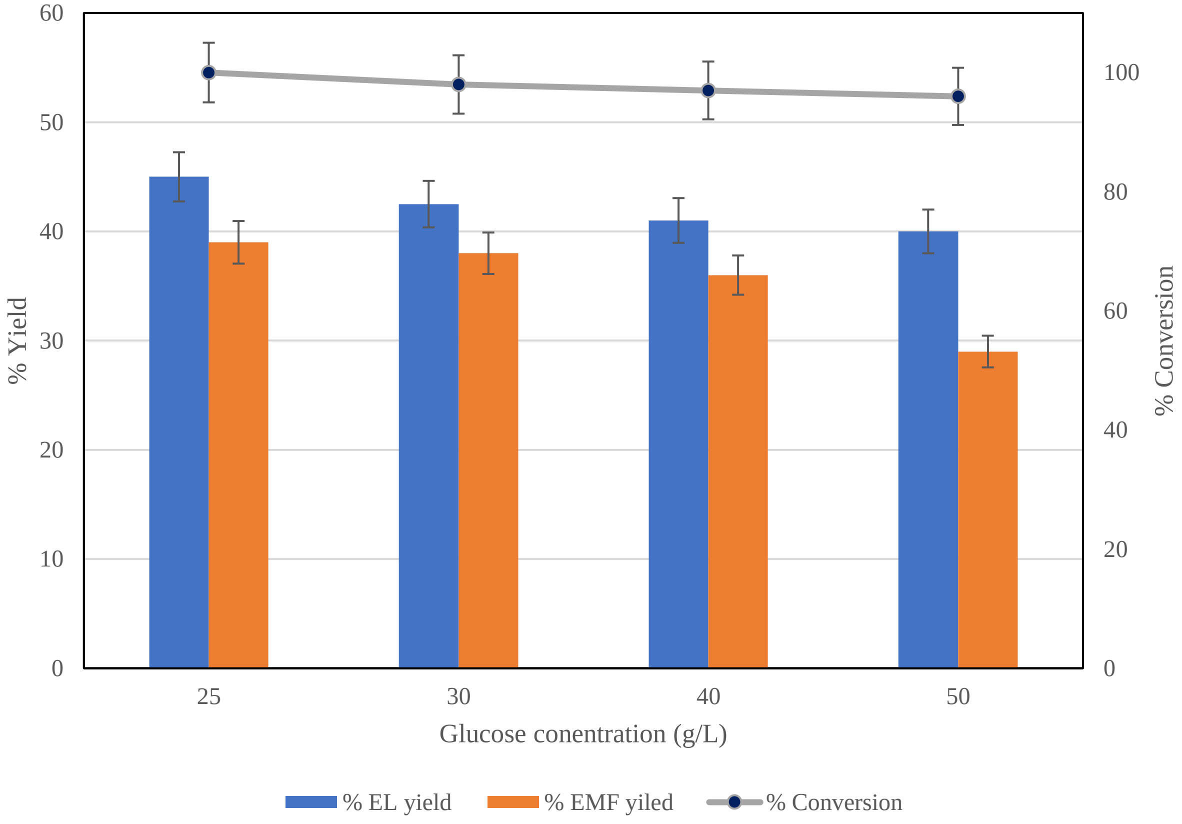

Figure 2.7 Effect of glucose concentration.

Reaction conditions: - 50% catalyst w.r.t. glucose, 160°C, 3hrs, stirring 800rpm.

2.4.1.2 *The influence of reaction temperature*

The effect of reaction temperature on the conversion of glucose to EL is a critical parameter to investigate. The results of the physical mixture of $H_2Zr_1PW_{12}O_{40}$+ Sn-beta (80:20) as a function of reaction temperature are plotted in Figure 2.8 It was noted that, as the reaction temperature raised from 140°C to 180°C, the EL was found to be improved from 45 to 54%, with the identical formation of ELA (30%). Above 180°C, the EL and ELA decreased substantially. This is mostly owing to the formation of additional humins at 200°C, which deposit on the active sites of the catalyst, reducing activity due to deactivation. After the reaction catalyst turned deep brown from white at 200°C.

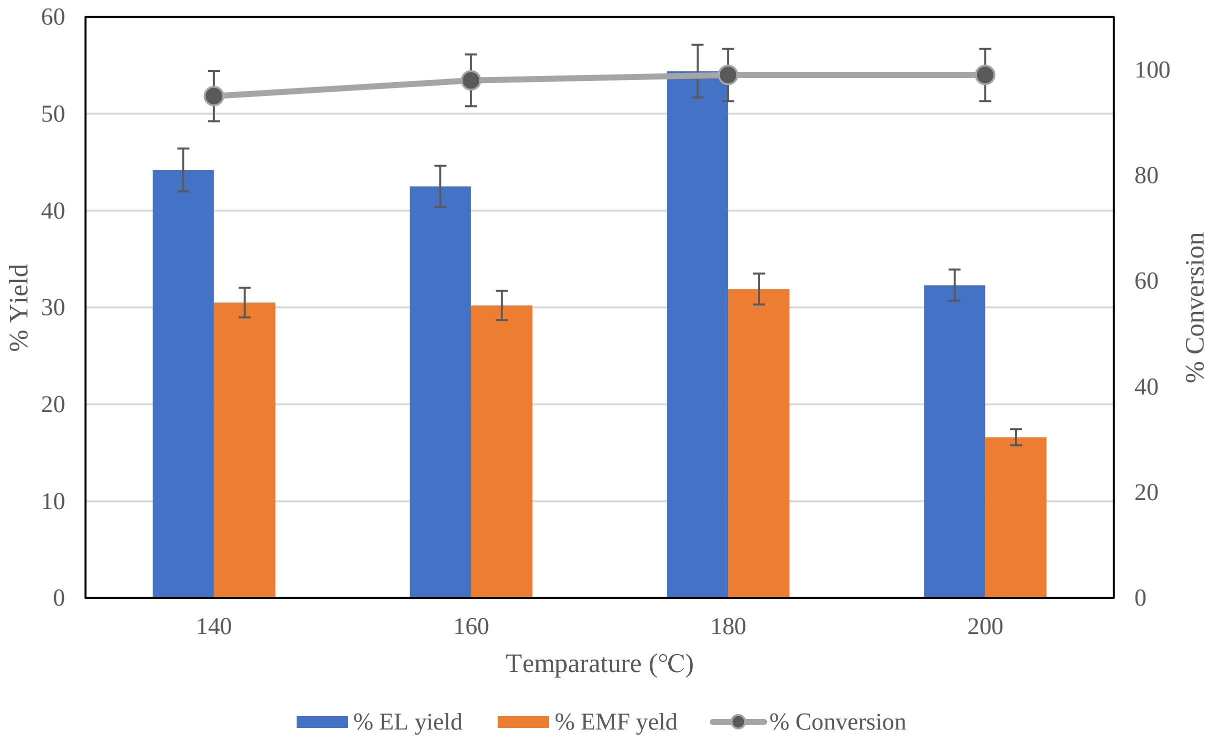

Figure 2.8 Effect of temperature

Reaction conditions: - (80:20 $H_2Zr_1PW_{12}O_{40}$ + Sn-Beta) 50% catalyst w.r.t. glucose, 30g/L glucose concentration, 3hr, 800rpm

2.4.1.3 *Effect of the Catalyst Loading*

Figure 2.9 confirmed that as the catalyst loading increases from 25% to 50%, the EL and ELA formation increases from 29% to 54% and 18% to 32%, respectively. This increase in activity is mainly due to a rise in active catalyst sites, which upsurge the reaction rates and activity. Above 50% catalyst loading (this is high enough for most of the reaction); more catalyst concentration will hinder the mass transfer of substrates and their interaction with each other at the catalyst surface and inside the catalyst pores, reducing catalyst activity.

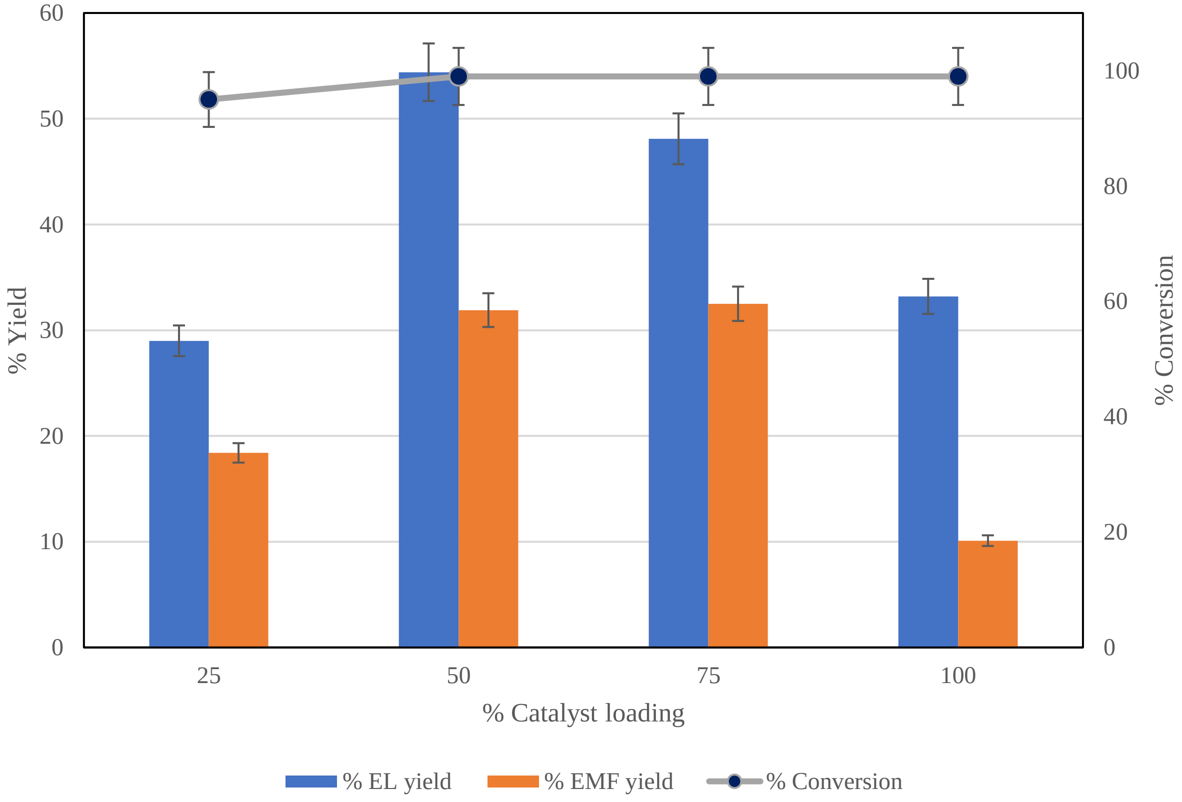

Figure 2.9 Effect of catalyst loading.

Reaction conditions: - (80:20 $H_2Zr_1PW_{12}O_{40}$ *+ Sn-Beta) 50% cat w.r.t. glucose, 30g/L glucose conc., 180°C Temp., 3hr, 800rpm*

2.5 Comparison of the present catalytic system with the literature

Table 2.4 Comparison of the present catalytic system with the literature

Sr. No.	Catalyst	Reaction Parameters				% Conversion	% EL Yield	% EMF Yield	Ref. No.
		Catalyst Loading (wt. %)	Glucose concentration (g/L)	Temp. (°C)	Time h				
1	K-HPW-1	75	20	150	2	99.2	14.5	1.5	[16]
2	$Ti_{0.75}TPA$	2.5	4.51	120	6	100	21	-	[36]
3	20% HPW/H-ZSM-5	150	20	160	2	-	19.1	-	[37]
4	Amberlyst-15	20	12	180	2	94.3	39.2	15	[38]
5	5KCC-1/Al–SO_3H	50	24.2	200	6	-	42.3	-	[39]
6	80:20 $H_2Zr_1PW_{12}O_{40}$ + Sn-Beta	50	30	180	3	99	54	31	This work

In Table 2.4, our investigation was compared with recent and outstanding research for the conversion of glucose to EL. It can be observed that the EL yields of 14.5%–54% were achieved by various heterogeneous catalysts under different reaction conditions. Under the catalysis of 5KCC-1/Al–SO_3H, a high EL yield of 42.3% could be obtained at a high temperature of 200 °C [39]. While conventional high acidic resin Aberlyst-15 showed a remarkably 39.2 % EL yield[38] and HPA-based catalysts such as K-HPW-1, $Ti_{0.75}TPA$, and 20% HPW/H-ZSM-5 reported relatively low EL yield[16,36,37]. Surprisingly, the EL yield (54%) obtained by 80:20 $H_2Zr_1PW_{12}O_{40}$ + Sn-Beta catalyst surpassed those obtained by the published catalysts. Moreover, the DPW-CeSiM catalysis was conducted at relatively mild reaction conditions (180 °C and 3 h).

2.6 Conclusions

The present study investigated the right combination of Brønsted and Lewis acidic catalyst and its percentage for the maximization of direct glucose transformation to EL in one step. $H_2Zr_1PW_{12}O_{40}$ + Sn-beta with an 80:20 weight ratio was found to be an ideal blend for the maximum EL yield (54%). Another advantage of the study is to use of HPA-based material for polar-solvent-based reactions. In this case, $H_2Zr_1PW_{12}O_{40}$ is an HPA having Brønsted as well as Lewis acidity by exchanging the H+ proton with Zr. This combination also improves the heterogeneity of the HPA-based sample in the polar medium by 50%. The current study also discovered that this combined physical mixture of $H_2Zr_1PW_{12}O_{40}$ + Sn-beta can bear glucose concentrations up to 30g/L. Therefore, it can be concluded that the correct ratio of B and L catalysts is essential for the one-step direct conversion of glucose to EL.

2.7 References

1 A. Démolis, N. Essayem and F. Rataboul, *ACS Sustain Chem Eng*, 2014, **2**, 1338–1352.

2 R. Marcel, T. Durillon, L. Djakovitch, F. Fache and F. Rataboul, *ChemistrySelect*, 2019, **4**, 3329–3333.

3 G. Shrivastav, T. S. Khan, M. Agarwal and M. A. Haider, , DOI:10.1021/acssuschemeng.7b01316.

4 E. Christensen, A. Williams, S. Paul, S. Burton and R. L. Mccormick, , DOI:10.1021/ef201229j.

5 K. Alamgir Ahmad, M. Haider Siddiqui, K. K. Pant, K. D. P. Nigam, N. P. Shetti, T. M. Aminabhavi and E. Ahmad, *Chemical Engineering Journal*, 2022, **447**, 137550.

6 K. C. Badgujar, V. C. Badgujar and B. M. Bhanage, *Catal Today*, 2023, **408**, 9–21.

7 J. Felipe Leal Silva, R. Grekin, A. Pinto Mariano and R. aciel Filho, , DOI:10.1002/ente.201700594.

8 A. F. Peixoto, R. Ramos, M. M. Moreira, O. S. G. P. Soares, L. S. Ribeiro, M. F. R. Pereira, C. Delerue-Matos and C. Freire, *Fuel*, 2021, **303**, 121227.

9 X. Kong, Y. Zhu, Z. Fang, J. A. Kozinski, I. S. Butler, L. Xu, H. Song and X. Wei, *Green Chemistry*, 2018, **20**, 3657–3682.

10 K. Y. Nandiwale and V. v. Bokade, *Environ Prog Sustain Energy*, 2015, **34**, 795–801.

11 K. Y. Nandiwale, S. K. Sonar, P. S. Niphadkar, P. N. Joshi, S. S. Deshpande, V. S. Patil and V. v. Bokade, *Appl Catal A Gen*, 2013, **460–461**, 90–98.

12 C. Antonetti, D. Licursi and A. M. R. Galletti, *Catalysts 2020, Vol. 10, Page 961*, 2020, **10**, 961.

13 S. Saravanamurugan and A. Riisager, *ChemCatChem*, 2013, **5**, 1754–1757.

14 L. Peng, L. Lin, J. Zhang, J. Shi and S. Liu, *Appl Catal A Gen*, 2011, **397**, 259–265.

15 G. Morales, A. Osatiashtiani, B. Hernández, J. Iglesias, J. A. Melero, M. Paniagua, D. Robert Brown, M. Granollers, A. F. Lee and K. Wilson, *Chemical Communications*, 2014, **50**, 11742–11745.

16 S. Zhao, G. Xu, C. Chang, S. Fang, Z. Liu and F. Du, *Catalysts*, 2015, **5**, 1897–1910.

17 L. Jiang, L. Zhou, J. Chao, H. Zhao, T. Lu, Y. Su, X. Yang and J. Xu, *Appl Catal B*, 2018, **220**, 589–596.

18 J. Dai, L. Peng and H. Li, *Catal Commun*, 2018, **103**, 116–119.

19 C. Travers, N. Essayem, M. Delage and S. Quelen, *Catal Today*, 2001, **65**, 355–361.

20 T. Okuhara and T. Nakato, *Catalysis Surveys from Japan*, 1998, **2**, 31–44.

21 M. A. Hanif, S. Nisar and U. Rashid, *Catal Rev Sci Eng*, 2017, **59**, 165–188.

22 Y. Zhou, G. Chen, Z. Long and J. Wang, *RSC Adv*, 2014, 4, 42092–42113.

23 M. Samaniyan, M. Mirzaei, R. Khajavian, H. Eshtiagh-Hosseini and C. Streb, *ACS Catal*, 2019, 9, 10174–10191.

24 L. Leclercq, A. Mouret, A. Proust, V. Schmitt, P. Bauduin, J.-M. Aubry and V. Nardello-Rataj, *Chem. Eur. J.*, 2012, **18**, 14352–14358.

25 K. Inumaru, T. Ishihara, Y. Kamiya, T. Okuhara and S. Yamanaka, *Angew. Chem. Int. Ed.*, 2007, **46**, 7625–7628.

26 N. L. Mulik, P. S. Niphadkar, K. v Pandhare and V. v Bokade, *ChemistrySelect*, 2018, **3**, 832–836.

27 P. S. Niphadkar and P. N. Joshi, *Advanced Porous Materials*, 2015, **2**, 204–211.

28 A. E. R. S. Khder, H. M. A. Hassan and M. S. El-Shall, *Appl Catal A Gen*, 2012, **411–412**, 77–86.

29 M. Tao, L. Xue, Z. Sun, S. Wang, X. Wang and J. Shi, *Sci Rep*, , DOI:10.1038/srep13764.

30 X. Yang, Y. Liu, X. Li, J. Ren, L. Zhou, T. Lu and Y. Su, , DOI:10.1021/acssuschemeng.8b00177.

31 G. Xiong, H. Yang, L. Liu and J. Liu, , DOI:10.1039/d2ra06366b.

32 M. Aziz, S. S. Abbas, W. R. W. Baharom and W. Z. W. Mahmud, *Mater Lett*, 2012, **74**, 62–64.

33 P. M. Kibasomba, S. Dhlamini, M. Maaza, C. P. Liu, M. M. Rashad, D. A. Rayan and B. W. Mwakikunga, *Results Phys*, 2018, **9**, 628–635.

34 J. A. Dias, E. Caliman and S. C. L. Dias, *Microporous and Mesoporous Materials*, 2004, **76**, 221–232.

35 K. Srilatha, R. Sree, B. L. A. P. Devi, P. S. S. Prasad, R. B. N. Prasad and N. Lingaiah, *Bioresour Technol*, 2012, **116**, 53–57.

36 S. R. B., K. K. P., D. L. D. and N. Lingaiah, *Catal Today*, 2018, **309**, 269–275.

37 S. Zhao, G. Xu, J. Chang, C. Chang, J. Bai, S. Fang and Z. Liu, *Bioresources*, 2015, **10**, 2223–2234.

38 J. Feng, T. Fan, C. Ma, Y. Xu, J. Jiang and H. Pan, *J Agric Food Chem*, 2020, **68**, 13760–13769.

39 Z. Zhang, Z. Huang and H. Yuan, *New Journal of Chemistry*, 2021, **45**, 5526–5539.

Chapter 3

Furfuryl alcohol conversion to Ethyl furfuryl ether over Recyclable Cs exchanged HPW catalyst

3.1 Introduction

As crude oil supplies decline and global demand for fossil fuels rises, alternative renewable sources such as biomass, solar, and water splitting must be considered. Because of its great sustainability, biomass may be the most chosen option among these. Biomass is a readily available, renewable carbon-based source for value-added chemicals and biofuels, notably agricultural waste. In India, the availability of biomass based on agricultural waste, such as rice husk, wheat straw, rice straw, and sugarcane bagasse, accounts for over 75% of the total. A vital first step towards improving the environment and a sustainable economy is to use renewable biomass[1]. The Biofuels Directive of the European Union (EU) Commission emphasizes a 20% biofuel blend. Therefore, in the current and future state of the planet, research on bio-based technologies, particularly furan catalytic converting technologies, is essential. One of the most noteworthy furan derivatives, furfuryl alcohol (FAlc), was produced industrially by hydrogenating furfural, which has the potential to serve as a platform chemical for the production of more useful compounds [2–5]. Due to their useful fuel qualities, Furanic ethers are an important class of chemicals that can be employed as gasoline additives or in diesel blends [6–8]. According to the analytical analysis by Lange et al. al., among the investigated products from Furan upgrading, ethyl furfural ether (EFE) demonstrates a very low carbon footprint with a high octane number (ON 110). [9] Furfuryl ether can also be used to make ethyl levulinate (EL) and other fuel molecules like alkyl tetrahydrofuryl ether. Furanic ethers are an appealing class of potential biofuel to consider because of their wide range of applications [10–13]. Furanic ethers are an appealing class of potential biofuel to consider because of their wide range of applications

Due to the ability of these compounds for self-polymerization to humins, [14] furanics (Furfural, FAlc, and HMF) have poor acid stability and pose substantial limitations when used in harsh conditions. As a result, there has been little research on the catalytic etherification of furfuryl alcohol. Catalysts such as ZSM-5, Zr-SBA-15, and Amberlyst-15 have been documented in a few reports [9,15,16]. It appears that the acid catalyst, particularly the Lewis and Brønsted acid catalyst blend, may be operative for this reaction.

The heteropolyacids (HPAs) are a special type of strong solid Brønsted acid that exhibits exceptional catalytic activity in a wide range of acid-catalyzed activities, including the manufacture of biofuel [16–22]. Due to the high instability of furanic compounds, HPA, as it is, has a strong Brønsted acidity, which may promote the creation of additional humins. Additionally, HPAs are soluble in polar media like alcohol or water. By replacing the H^+ proton of HPAs with other monovalent ions such as NH_4^+, Cs^+, K^+, Rb^+, etc., it is possible to decrease Brønsted acidity and render HPA insoluble in the polar medium [23–27]. In comparison to other monovalent ions, Cs^+ appears to be more favored since its mirror replacement with H^+ reduces the Brønsted acid site, promotes the creation of new Lewis acid sites, increases surface area, creates mesoporosity, and also aids in the total insolubility of HPA in a polar solution [23–27].

This chapter therefore concentrated on the synthesis of a Cs-modified HPA catalyst and its characterization using various methods, including X-ray photoelectron spectroscopy (XPS), X-ray diffraction (XRD), ammonia-temperature programmed desorption (TPD), nitrogen adsorption, and FTIR (Fourier transform infrared spectroscopy). The etherification of furfural alcohol to ethyl furfuryl ether was one of the furanic reactions for which the catalyst had been evaluated.

3.2 Experimental

3.2.1 Materials and Methods

Cesium nitrate (LR), and Keggin-type 12-tungstophosphoric acid (AR) were purchased from Thomas Baker, Mumbai (India) and analytical standard's EFE, EL, and FAlc were purchased from Sigma Aldrich, Ethanol from Changshu Hongsheng Fine chemical China.

3.2.2 Catalyst synthesis

3.2.2.1 Cs exchanged HPW

The procedure for the synthesis of $Cs_xH_{3-x}PW_{12}O_{40}$ (x = 0.5,1,2,2.5) is similar to be reported [24]. We have prepared Cs exchanged HPW samples as $H_{2.5}Cs_{0.5}PW_{12}O_{40}$, $H_2Cs_1PW_{12}O_{40}$, $H_1Cs_2PW_{12}O_{40}$, and $H_{0.5}Cs_{2.5}PW_{12}O_{40}$, for this we added 0.5 mmol, 1 mmol, 2 mmol and 2.5 mmol aqueous solution of $CsNO_3$ to the aqueous 1 mmol solution of $H_3[PW_{12}O_{40}].nH_2O$ under constant stirring for 30 min at room temperature. The resulting milky suspension was allowed to age at room temperature for 12 hours. Water was slowly evaporated at 100 °C in an oil bath to get the white powder. The samples were then dried in an oven at 120 °C for 12 hours and calcined at 350 °C for 3 hours.

3.2.2.2 *Ce Exchanged HPW ($H_1Ce_2PW_{12}O_{40}$)*

Ce Exchanged HPW was made by dropwise adding 0.5 mmol of an aqueous solution of $Ce(NO_3)3.6H_2O$ to a 1 mmol aqueous solution of $H_3[PW_{12}O_{40}].nH_2O$ (tungstophosphoric acid/HPW) under vigorous stirring. The resulting milky suspension was left at room temperature for 12 hours. The white powder was obtained by slowly evaporating water in an oil bath at 100 °C. The samples were then dried in an oven at 120 °C for 12 hours before being calcined at 350 °C for 3 hours. For convenience, we designated the catalysts as $H_1Ce_2PW_{12}O_{40}$.

3.2.2.3 Mg Exchanged HPW ($H_1Mg_2PW_{12}O_{40}$)

Mg Exchanged HPW sample was prepared using the aforesaid procedure; for this, a 1 mmol solution of $Mg(NO_3)2.6H_2O$ aqueous solution was added dropwise to a 1 mmol solution of $H_3[PW_{12}O_{40}]. nH_2O$ under vigorous stirring. The resulting milky suspension was left to age at room temperature for 12 hours. Slow evaporation of water in an oil bath at 100 °C was used to generate the white powder. The samples were then dried in an oven at 120 °C for 12 hours before being calcined at 350 °C for 3 hours. For convenience, we have named the catalysts $H_1Mg_2PW_{12}O_{40}$.

3.2.3 Characterization of the catalysts

Using a PANalytical system (model Xpert-PRO-1712) and monochromated Cu K radiation (=0.154) in the 5o to 90o range, X-ray diffraction (XRD) patterns of catalyst powder were obtained.

To assess the textural qualities of materials, a typical volumetric nitrogen adsorption equipment (Micromeritics ASAP 2010 system) was employed. The Brunauer-Emmett-Teller (BET) method was used to calculate the sample's specific surface area.

Using a MicromeriticsAutoChem (2910, USA) fitted with a thermal conductivity detector, the total acidity and acid strength related to each site were determined. The material was dehydrated for 1 hour at 300 °C in He (30 cm3 min1) before the measurements. The temperature was then lowered to 100 °C, and the sample was exposed to a gas stream that included 10% NH_3 in He to allow NH_3 to adsorb for an hour. He was then used to flush it for an additional hour. By increasing the temperature to 800 °C, the NH_3 desorption was performed in He flows (30 cm3 min1) at a rate of 10 °C min1. A thermal conductivity detector (TCD) was used to calculate the amount of desorbed ammonia.

On a Thermo-Nicolet 670 spectrometer, an FTIR spectrum between 400 and 4000 cm-1 was acquired. A JASCO J810 spectrometer with a peltier water circulation thermostated six locations automatic cell changer and a variable slit system was utilized to capture the spectra.

Another application of IR spectroscopy is to find out the type of active sites on the catalyst surface (mainly acidic and basic sites) by using various probe molecules. One of the often-used probes is pyridine since it can offer data on both the Lewis and Brønsted acid sites at the same time. The IR bands from pyridine coordinated to Lewis acid sites appear at 1450 and 1620 cm^{-1}, while the typical bands of pyridine hydrogen bound at a Brønsted acid site appear in the areas of 1400-1477 cm^{-1}, 1485-1490 cm^{-1}, and 1580-1600 cm^{-1} [28–30].

Ex-situ pyridine-FTIR was used to determine the type of acid sites (Brønsted and/or Lewis) present in the catalyst. Using a high vacuum, a catalyst powder sample was cooled to ambient temperature after being activated at 200°C for two hours. Then, it was subjected to pyridine vapors for two hours. By activating at 100°C for two hours while under a high vacuum, the physisorbed pyridine was driven off. The Fourier Transform Infrared Spectroscopy (FTIR) of the IR spectra was carried out using a Bruker Alpha-P ATR FTIR spectrometer, and the B/L ratio was computed using the published method [28].

The Perkin-Elmer Optima 3000DV inductive coupled plasma-optical emission spectroscopy (ICP-OES) was used to check the heterogeneity of the catalyst using the reaction mixture after the reaction.

3.2.4 Reaction procedure and analysis

Reactions were carried out in a high-pressure Parr reactor (4871 series controller) with a volume of 100 mL and external temperature and stirring controllers. Based on the FALc concentration, 7.2 mmol of FAlc, 360 mmol of alcohol, and 20% catalyst were loaded in a typical reaction. The reactor was then sealed and placed in a heating unit with stirring at 300 rpm. After the reaction was completed, the reactor was cooled to room temperature in a cooling water bath and the reaction mixture centrifuged to isolate the used catalyst. The used catalyst was washed and dried before being utilized in the next run to test its reusability.

The quality of the liquid products was determined using gas chromatography-mass spectrometry (GC-MS-QP2020 NX, Shimadzu) using a TR-5 MS column (30 m 250 m 0.25 m). The quantitative analysis of liquid products was performed using a Varian CP-3800 series with an RTX-5 capillary column (60 m 320 m 0.25 m) fitted with a flame ionization detector (FID). For both GCMS and GC analyses, the following temperature program was used: the initial temperature was 50 °C, followed by heating at a rate of 20 °C/min to 220 °C. The quantities of product samples were quantified using external standard curves with commercial samples. Product yields were calculated as the ratio of moles of the product obtained to moles of the substrate in the feed. The EFE yield was determined using FALc calibration data that is not widely available and was validated by GCMS. The following equations were used to calculate product yield and conversion:

$$\%\,Conversion = \frac{FALc\ initial\ moles - FALc\ final\ moles}{FALc\ initial\ moles} * 100$$

$$\%\,Yield = \frac{moles\ of\ product}{FALc\ initial\ moles} * 100$$

$$Weight\ of\ humin = Residue\ collected(dried) - Weight\ of\ Catalyst$$

$$\%\,Humin = \frac{Weight\ of\ humin}{Initial\ weight\ of\ FALc} * 100$$

3.3 Results and Discussion

3.3.1 Catalysts characterization

All catalysts produced were characterized using various techniques such as Nitrogen adsorption, XRD, XPS, and TPD, and the results are reported in Tables 3.1 and 3.2.

3.3.1.1 X-Ray diffraction

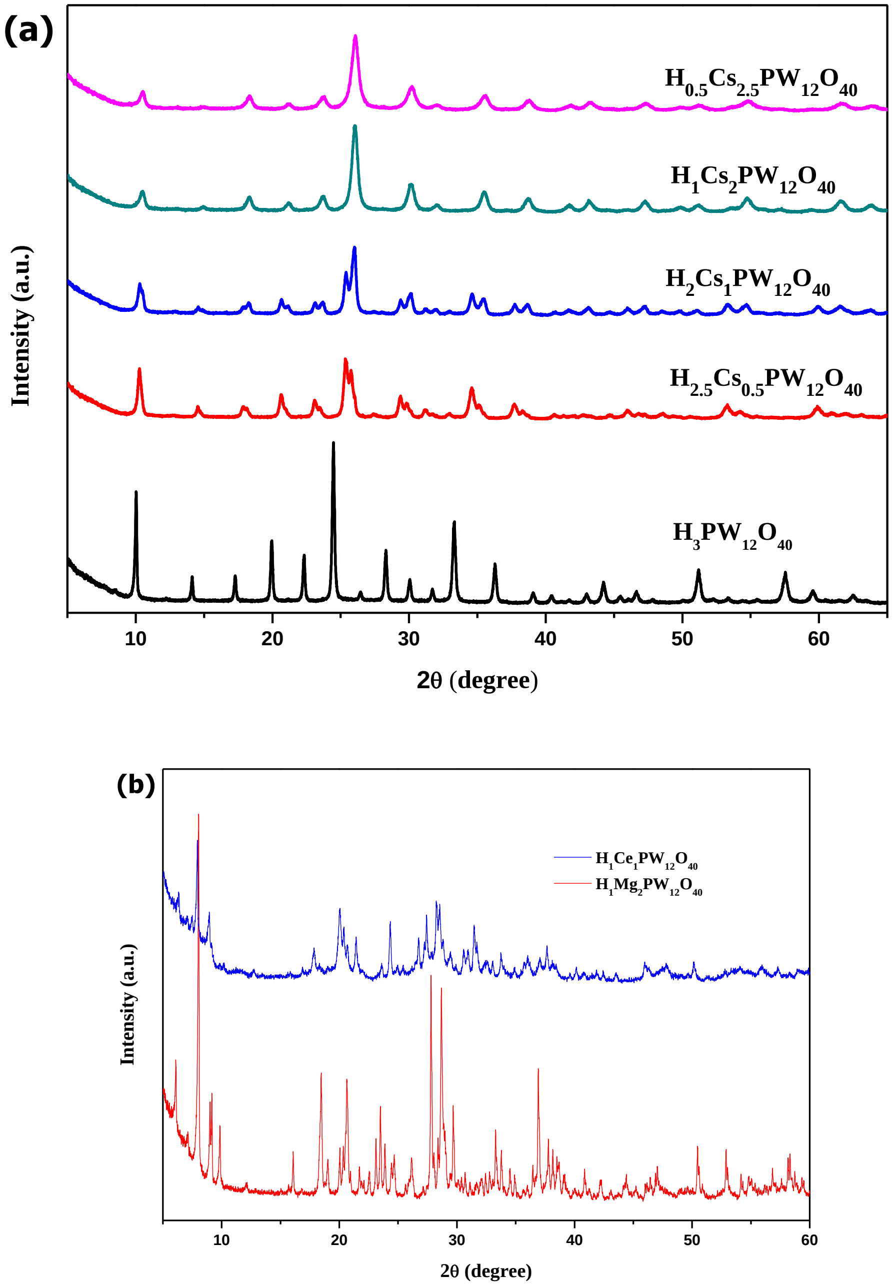

Figure 3.1. *Powder XRD of (a) $H_3PW_{12}O_{40}$ and $Cs_xH_{3-x}PW_{12}O_{40}$ samples and (b) $H_1Mg_2PW_{12}O_{40}$, and $H_1Ce_2PW_{12}O_{40}$*

The structural changes as a function of Cs, Ce, and Mg exchange with H^+ in $H_3PW_{12}O_{40}$ were carried out by XRD (Figure 3.1. a and b). All Cs exchanged samples have shown a typical cubic crystalline XRD pattern of Keggin units. After initial Cs doping in $H_{2.5}Cs_{0.5}PW_{12}O_{40}$, a new set of peaks at 2 thetas of 25.6° evolve as shoulders on the main 25° of $H_3PW_{12}O_{40}$ reflections. Diffraction peaks related to free acid vanish as the Cs level exceeds x = 2. The shift in $H_3PW_{12}O_{40}$ peaks toward higher angles (shift by 1.4°) in the $Cs_xH_{3-x}PW_{12}O_{40}$ samples is consistent with the body-centered cubic structure of $Cs_3PW_{12}O_{40}$ salts [23]. The effect of Cs exchange was studied by calculating its crystallite size (D nm) with Scherrer's equations (Table 3.1). The crystallinity was observed to be decreased from 100% (plane HPA) to 66% due to the insertion of Cs+ up to 2.5 in the HPA Keggin framework. The corresponding crystallite size was also found to drop down to 14nm from 40nm. This is likely because of bond stretching due to the insertion of Cs in the Keggin framework, which weakens the structure and so, the crystallinity and crystallite size. In the case of Magnesium ($H_1Mg_2PW_{12}O_{40}$) insertion in $H_3PW_{12}O_{40}$ leads to a partial loss of keggin structure along with the formation of WO species, its reflections can be seen in XRD (Figure 3.1. b) whereas cerium ($H_1Ce_2PW_{12}O_{40}$) insertion in $H_3PW_{12}O_{40}$ leads to complete collapsed of Keggin structure.

3.3.1.2 N_2-Physisorption

The BET surface area (Table 3.1.) pointed out that as Cs insertion in $H_3PW_{12}O_{40}$ increases from 0 to 2.5 the corresponding surface area was found to be improved from $4m^2/g$ to $43.2m^2/g$ and mesopore surface area has elevated to $16m^2/g$. According to the literature Cs insertion in HPA generates micro-crystallites which lead to void formation [25,26]. As the insertion of Cs increases the void formation and bond stretching increase which creates more surface area and mesoporosity.

Table 3.1. Surface properties of $H_3PW_{12}O_{40}$ and $Cs_xH_{3-x}PW_{12}O_{40}$ samples

Entry	Catalyst name	% Crystallinity (relative)	The crystallite size (nm)	BET Surface area m^2/g	Mesopore surface area (m^2/g)
1	$H_3PW_{12}O_{40}$	100	40	4	-
2	$H_{2.5}Cs_{0.5}PW_{12}O_{40}$	93	13	4.2	0.06
3	$H_2Cs_1PW_{12}O_{40}$	83	21	9.1	3.1
4	$H_1Cs_2PW_{12}O_{40}$	69	17	36.4	10
5	$H_{0.5}Cs_{2.5}PW_{12}O_{40}$	66	14	43.2	16

3.3.1.3 X-ray photoelectron spectroscopy

The high-resolution XP spectra of W 4f and O 1s (Figure 3.2) tell the W and O environments are disturbed on Cs exchange. Figure 3.2 a shows XP spectra of W4f7/2 of $H_3PW_{12}O_{40}$ occur at 35.7 eV with a peak width of 2.8eV, after Cs exchange (0.5 to 2.5) this peak shifted to lower binding energy from 35.7 to 35.6 eV confirmed that new binding of W is generated with the insertion of Cs. This shift is more at Cs2.5 than at Cs0.5, confirming the stretching of W bonding. A similar trend was also observed for O1s (Figure 3.2 b) with the binding energy of the O 1s reducing from 530.8 to 530.5 eV with increasing Cs exchange from 0 to 2.5 in $H_3PW_{12}O_{40}$. It is speculated that Cesium's more electropositive nature enhanced the electron density of both O and W by reducing their binding energies. Figure 3.2 c. depicts the XP spectra of Cs 3d5/2 before Cs exchange, which causes an increase in intensity as well as an expansion in the area under the peak. The first binding energy peak at 724.1eV with a peak width of 1.18 eV and the second binding energy peak at 738.1eV with a peak width of 1.16 eV was found to be elevated with an increase in Cs doping: 1.26 (Cs1), 1.28 (Cs2), 1.29 eV (Cs2.5) for first binding energy and 1.18 (Cs1), 1.41 (Cs2), 1.42 eV (Cs2.5). It indicates that an increase in Cs doping leads to saturation of Cs on the surface.

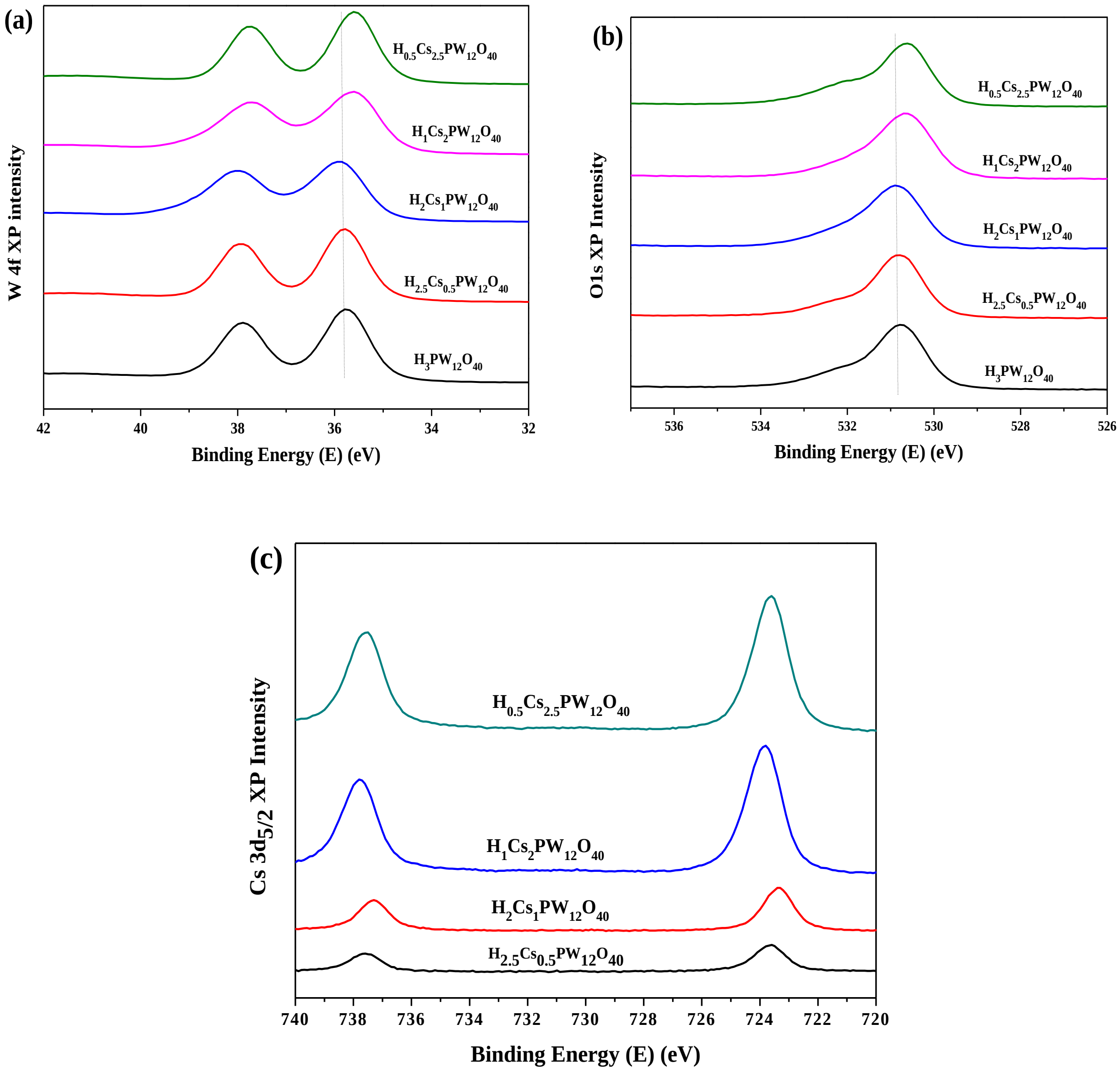

Figure 3.2. *XP spectra of $H_3PW_{12}O_{40}$ and $Cs_xH_{3-x}PW_{12}O_{40}$ samples as a function of Cs content (a) W4f XP spectra of $H_3PW_{12}O_{40}$ and $Cs_xH_{3-x}PW_{12}O_{40}$ samples (b) O 1s XP spectra of $H_3PW_{12}O_{40}$ and $Cs_xH_{3-x}PW_{12}O_{40}$ samples (c) Cs $3d_{5/2}$ XP spectra of $Cs_xH_{3-x}PW_{12}O_{40}$ sample*

3.3.1.4 NH_3-TPD

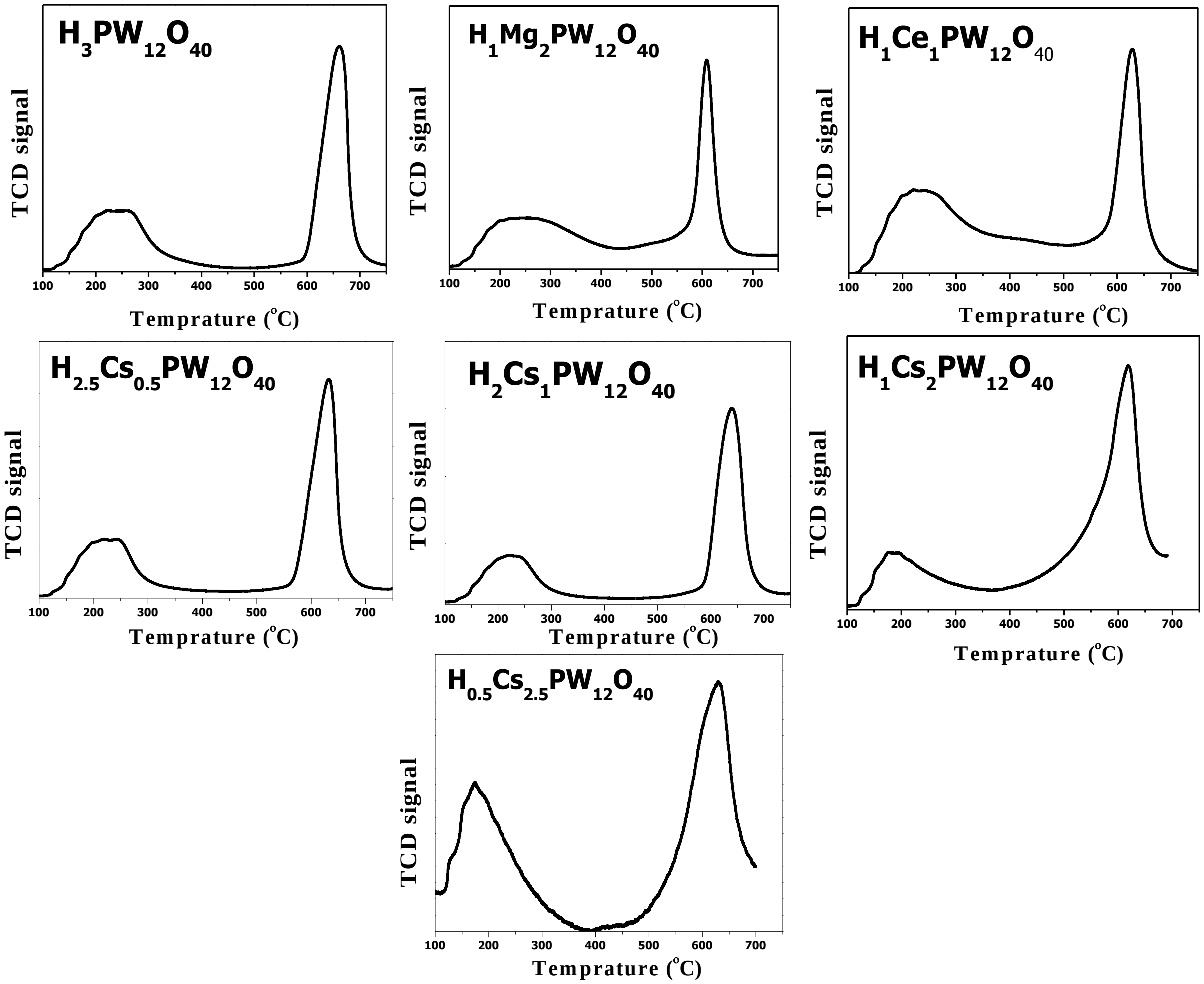

Figure 3.3. NH_3 Temperature Programmed Desorption profiles

Table 3.2. represents the acidic properties of all studied catalysts investigated by NH_3-TPD and Pyridine-FTIR. TPD profiles of Mg, Ce, and Cs-exchanged tungstophosphoric acid catalysts are provided in Figure 3.3. All samples showed distinctive desorption in two temperature ranges: 150°C to 250°C and 600°C to 700°C. The intensity of the high-temperature desorption peak was decreased as the Cesium content increased. The high-temperature desorption peak's strength reduced as the cesium content increased. In the case of Cs insertion of 0.5, 1, 2, and 2.5 moles in exchange with H^+ proton, the strong acidity was observed to be reduced to 12, 42, 62 and 82 %,

respectively whereas weak acidity was decreased by 40, 51, 72 and 84%, respectively. These results are obvious, due to less availability of H^+ protons for acidity.

Table 3.2. Investigation of Acidic Properties by NH_3 temperature programmed desorption and B/L ratio (Pyridine-FTIR) of $H_3PW_{12}O_{40}$, and $Cs_xH_{3-x}PW_{12}O_{40}$ samples.

Entry	**Catalyst name**	**weak acidity (µmol/g)**	**strong acidity (µmol/g)**	**S/W ratio**	**Total acidity (µmol/g)**	**B/L ratio**
1	$H_3PW_{12}O_{40}$	994.1	1541.8	1.5	2536	na
2	$H_{2.5}Cs_{0.5}PW_{12}O_{40}$	595.3	1356.6	2.2	1952	5.8
3	$H_2Cs_1PW_{12}O_{40}$	478.7	881.2	1.8	1360	4.3
4	$H_1Cs_2 PW_{12}O_{40}$	277.4	585	2.1	786	3.6
5	$H_{0.5}Cs_{2.5}PW_{12}O_{40}$	152.5	211.4	1.3	364	1.7

3.3.1.5 Pyridine-FTIR

The type of acidity is also an important factor to consider for any organic transformation, many intermediate steps are dependent on both the acid sites (Brønsted along Lewis acid sites). Figure 3.4 represents the PY-IR spectra of the $H_3PW_{12}O_{40}$ and $Cs_xH_{3-x}PW_{12}O_{40}$ samples taken after ex-situ Pyridine adsorption. The bands at 1450 cm^{-1} and 1610 cm^{-1} are typically attributed to pyridine vibrations adsorbed on Lewis acid sites, whereas the bands at 1489 cm-1 and 1635 cm^{-1} are attributed to pyridine vibrations adsorbed on Brønsted acid sites, and the band at 1540 cm^{-1} is caused to the combined effect of pyridine absorption on Brønsted and Lewis acid sites [28–30]. From Figure 3.4 the parent $H_3PW_{12}O_{40}$ has shown a band at ~ 1489 cm^{-1} while the Cs exchanged samples contain Brønsted acidity (band at ~ 1489 cm^{-1}) with an increase in Cs continents started to develop lewis acid sites which are assigned at ~ 1450 cm^{-1} and intensity of this characteristic band is also increased with increase in Cs content and from relative intensities of Peaks for Lewis (~ 1450 cm^{-1}) and Brønsted acid sites (~ 1489 cm^{-1}) calculated the B/L acid ratio given in Table 3.2.

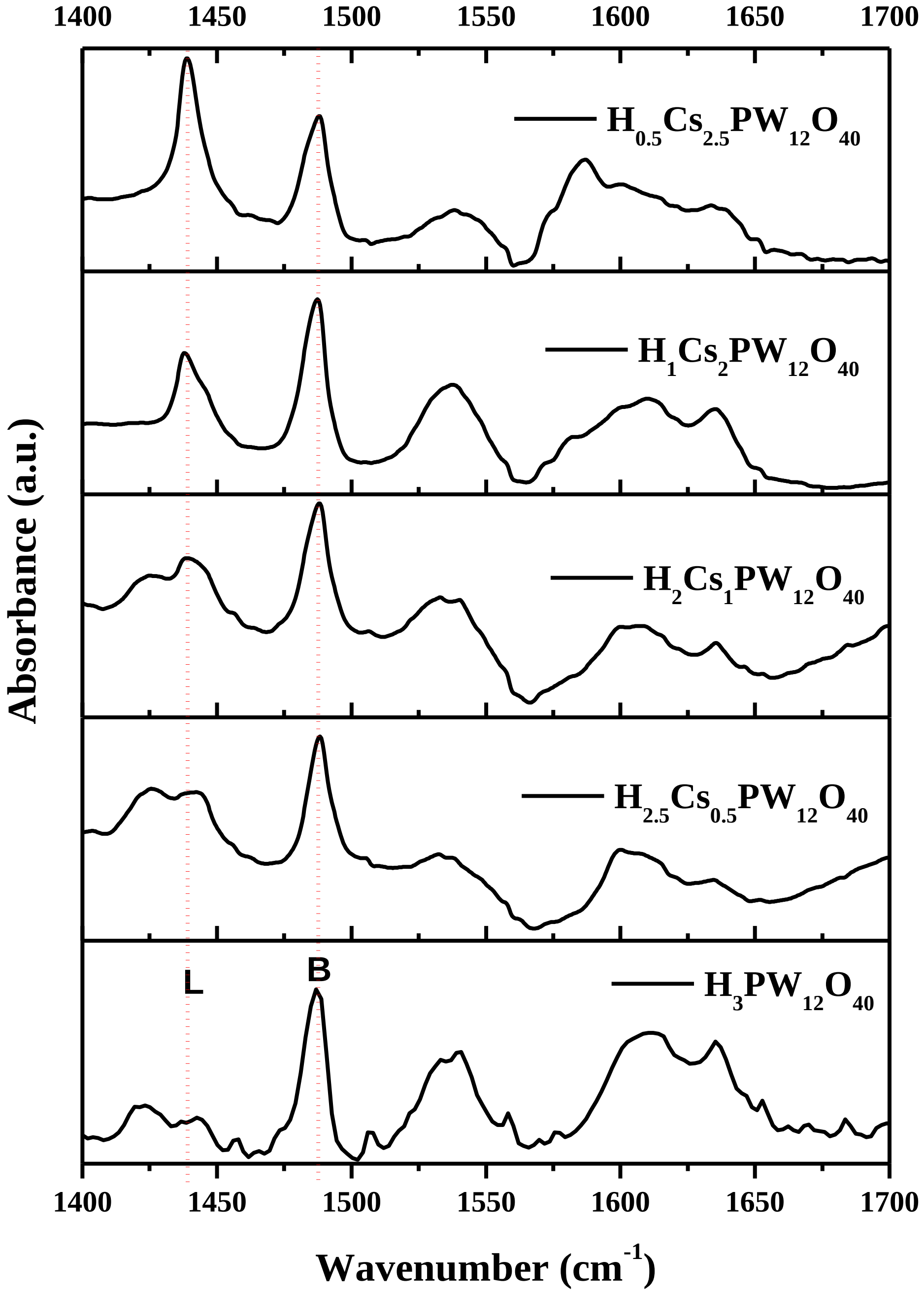

Figure 3.4 Pyridine IR spectra of $H_3PW_{12}O_{40}$ and $Cs_xH_{3-x}PW_{12}O_{40}$ samples

3.3.2 Etherification of Furfuryl Alcohol with Ethanol to Ethyl Furfuryl Ether

Catalytic transformation of furanic compounds to value-added products is an important reaction to investigate aiming for a new potential catalyst with an improved yield of the desired product. In this work, the prepared and well-characterized Cs inserted $Cs_xH_{3-x}PW_{12}O_{40}$ catalyst having Brønsted and Lewis acidity was evaluated for etherification of furfuryl alcohol to ethyl furfuryl ether a biofuel additive (Scheme 3.1).

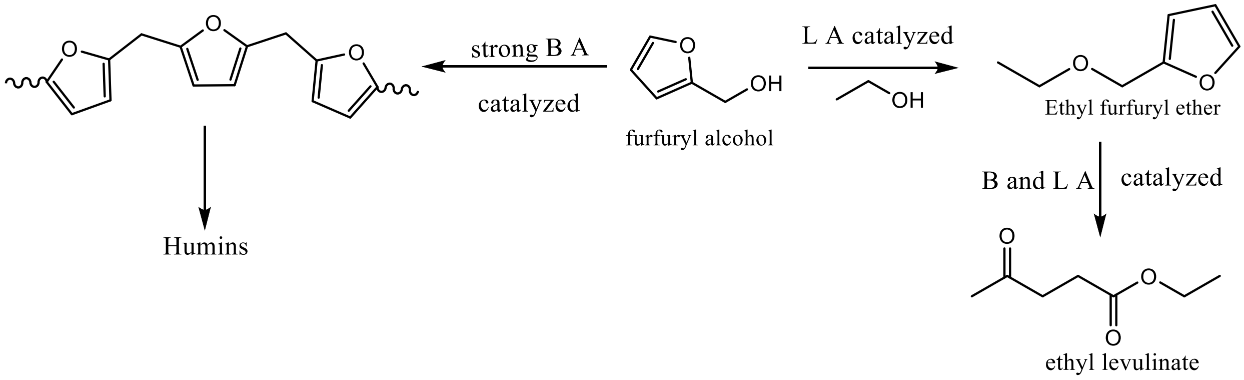

Scheme 3.1 Etherification of furfuryl alcohol to ethyl furfuryl ether

Ethyl furfuryl ether (EFE) and ethyl levulinate (EL) are the two primary biofuel products that are produced when furfuryl alcohol is etherified on a Lewis or Lewis + Brønsted acidic catalyst [16, 17]. Amongst the two, ethyl furfuryl ether is more advantageous in terms of its utilization as a blend in petroleum diesel or 100% replacement. If higher Brønsted acidity is present in the catalyst then there is a chance of polymerization of furfuryl alcohol and then to humin’s. Thus, the proper combination of Lewis and Brønsted properties is required to have the desired biofuel products. The present study is an attempt to selectively synthesize ethyl furfuryl ether than ethyl levulinate. Thus, this study was mainly focused on the formation of EFE as the main product over Lewis + Brønsted acidic properties of the $Cs_xH_{3-x}PW_{12}O_{40}$ catalyst.

3.3.3 Catalyst Screening

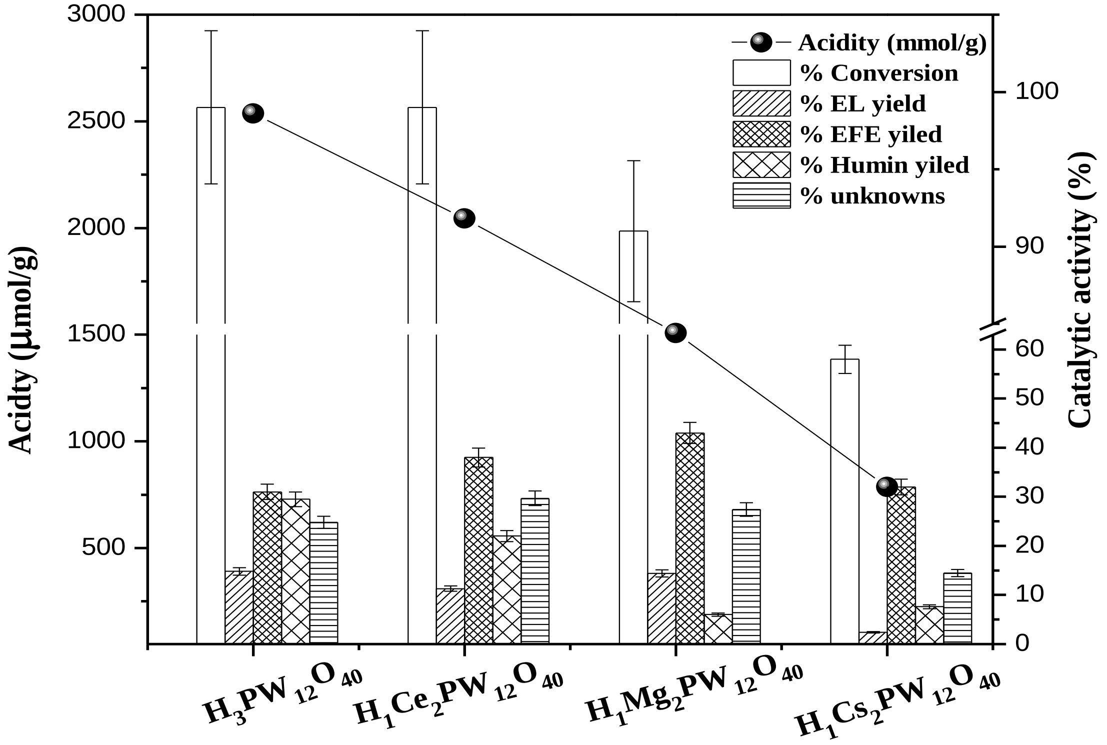

Figure 3.5 Catalyst screening as a function of total acidity

Reaction conditions: - 1:10 FAlc/Ethanol mol. Ratio, 110 ℃ Temp, 2.5h Time, 5 wt. % w.r.t. FAlc Catalyst

Being highly Brønsted acidity of $H_3PW_{12}O_{40}$ tends to have almost 98% conversion of FAlc. The activity trends follow $H_3PW_{12}O_{40}$ = $H_1Ce_2PW_{12}O_{40}$>$H_1Mg_2PW_{12}O_{40}$ (90%) >$H_1Cs_2PW_{12}O_{40}$ (58%) which is in the replica of acidity values (Figure 3.5). EFE formation was observed to be maximum (43%) with $H_1Mg_2PW_{12}O_{40}$ as compared to $H_1Ce_2PW_{12}O_{40}$ (35%); $H_1Cs_2PW_{12}O_{40}$ (32%) and $H_3PW_{12}O_{40}$ (28%). EL formation is in the range of 10-15% which is forming at the expense of EFE consumption. The lowest formation of EL (3%) is recorded for $H_1Cs_2PW_{12}O_{40}$. The humins formation of 25-30% was found with highly acidic catalysts viz; $H_3PW_{12}O_{40}$ and

$H_1Ce_2PW_{12}O_{40}$, whereas in the case of $H_1Mg_2PW_{12}O_{40}$ and $H_1Cs_2PW_{12}O_{40}$, it is <10%. The unknown product due to side reactions of furfuryl alcohol was found to be a maximum of 25-30% with the catalysts having considerably high B and L acidity, whereas in the case of $H_1Cs_2PW_{12}O_{40}$ which is less acidic than other studies showed the unknown formation of 15%. Even though $H_3PW_{12}O_{40}$; $H_1Ce_2PW_{12}O_{40}$ and $H_1Mg_2PW_{12}O_{40}$ are highly active catalysts for this reaction these catalysts are almost completely soluble in ethanol (polar medium) whereas $H_1Cs_2PW_{12}O_{40}$ is completely insoluble. According to the report, the introduction of Cs in HPA knocks out $H_5O_2^+$ moiety and strongly interacts with W=O and W-O-W by bridging terminal attachment leading to the widening of structure, and the sample becomes insoluble in the polar medium [31].

Because the catalyst should be more reusable; the process should have a clean and green approach $H_1Cs_2PW_{12}O_{40}$ is the best option to go ahead and optimize the process parameters to improve the activity and EEF yield. Thus; the optimization of process parameters was done on the $H_1Cs_2PW_{12}O_{40}$ catalyst.

3.3.4 *Influence of Cs insertion in $H_3PW_{12}O_{40}$ on the acidity and catalytic activity*

From the above discussion, it can be concluded that the Cs-exchanged sample ($H_1Cs_2PW_{12}O_{40}$) was found to be more useful for this type of reaction. So, the various amounts of Cs inserted samples (from 0.5 to 2.5 moles) in HPW were prepared meticulously and screened under the identical reaction conditions, ICP-OES of the reaction mixture after the reaction was done to check the heterogeneity of the catalyst, and all Cs exchanged samples has shown no sign of W from HPA unit and no sign identical leaching in the reaction mixture. The graphical data of all the Cs-exchanged samples under an identical set of reaction conditions are given in Figure 3.6 After 0.5 moles Cs exchange designated as $H_{2.5}Cs_{0.5}PW_{12}O_{40}$, there is a 24% loss in total acidity (1952µmol/g) along with the generation of Lewis acid sites Figure 3.4 with a 5.8 B/L ratio, showed

35% EFE, 14.4% EL yield 26% humin's, and 24% unknowns at the complete conversion of FAlc. In the case of $H_2Cs1PW_{12}O_{40,}$ there is a 47% loss in total acidity than the parent, and the generation of more Lewis acids with a 4.3 B/L ratio showed 39% EFE, 13.4% EL, 19.9% humins, and 25% unknowns with complete conversion of FAlc. Yet there is a 24 % and 47 % drop in total acidity of $H_{2.5}Cs_{0.5}PW_{12}O_{40}$ and $H_2Cs1PW_{12}O_{40}$ sample has high B/L ratio (5.8 and 4.3 respectively) indicating the number of Brønsted acid sites till present there and responsible for complete conversion of FAlc as like parent ($H_3PW_{12}O_{40}$). Further increase in Cs exchange from 1 to 2 moles leads to a 69% drop in total acidity, especially in Brønsted acidity leading to a B/L ratio of 3.6, showed 58% FAlc conversion 32% EFE, 2.4% EL, 14.5% unknowns and 7.6% humin's. The high drop in humins generation, EL formation, and high EFE selectivity is due to the low Brønsted acidity (3.6 B/L) with low total acidity (786µmol/g) which might be slowing down the poly-condensation among FAlc and ethanolysis of formed EFE. According to Figure 3.6 and Table 3.2, increasing the Cs exchange from 0.5 to 2 results in a continuous decline in overall acidity and the formation of additional Lewis acid sites. This allows less EL and humins as well as unknown compound formation without compromising EFE yield. Above Cs insertion of 2, i.e., $H_{0.5}Cs_{2.5}PW_{12}O_{40}$ there is a drastic drop in total acidity ~ 85% (364µmol/g) than the parent with the formation of more Lewis acid sites, which leads to only 5% FAlc conversion and 2% EFE, 0.9% EL, 1.5% humins and 1.8% unknowns' formations. Among Cs inserted samples, $H_1Cs_2PW_{12}O_{40}$ with a 3.6 B/L ratio showed a high selectivity of 55% with 30% EFE yield and 60% FAlc conversion. It may be due to the cumulative effect of moderate acidity, B/L ratio, and high surface area ($43m^2/g$). Thus, further optimization of parameters was done using the $H_1Cs_2PW_{12}O_{40}$ catalyst.

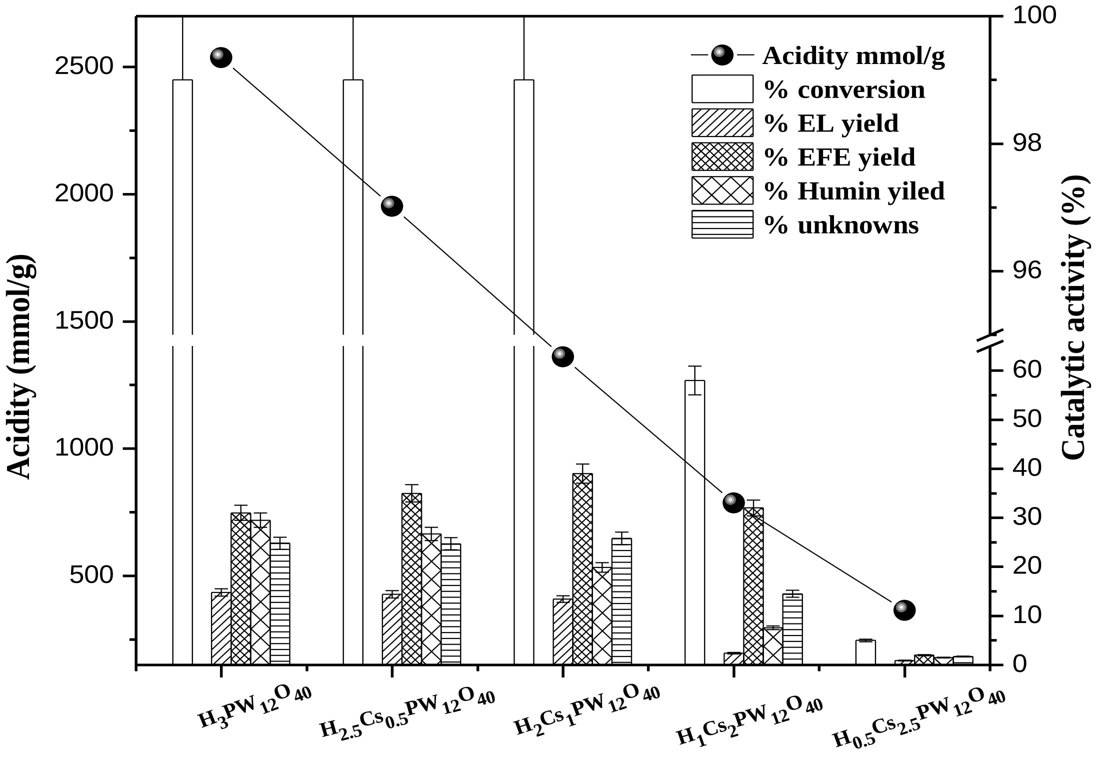

Figure 3.6 Effect of Cs insertion on the acidity and catalytic activity

Reaction conditions: - 1:10 FAlc/Ethanol mol. Ratio, 110 ℃ Temp, 2.5h Time, 5 wt. % w.r.t. FAlc Catalyst

3.3.5 Effect of molar ratio

The substrate concentration is a critical process parameter that influences the utilization efficiency of FAlc and the final product concentrations. Experiments were carried out with ethanol concentrations ranging from 1:2.5 to 1:20 FAlc to Ethanol mole ratio, and the results are shown in Figure 3.7. As can be seen from Figure 6 there is the impact of ethanol concentration on conversion, with an increase in ethanol concentration there is a drop in FAlc conversion and maximum conversion was observed at 1: 2.5 which is 61%. The formation of EFE is marginally reduced from 34% (1:2.5) to 33% (1:5) and was identical up to 1:15. Above, the 1:15 ratio, the

EFE yield has decreased to 25% (1:20). EL formation has shown an unstable range of <5%, whereas the humins contribution was 12% (1:2.5) to 6% (1:20). Higher formation of humins at 1:2.5 may be due to the more concentration of FAlc. The unknown formations were in the range of 15-17%. Thus, the 1:10 (FAlc: ethanol) molar ratio looks to be optimum for this reaction to get optimum FAlc conversion and EFE yield with the lower formation of humins

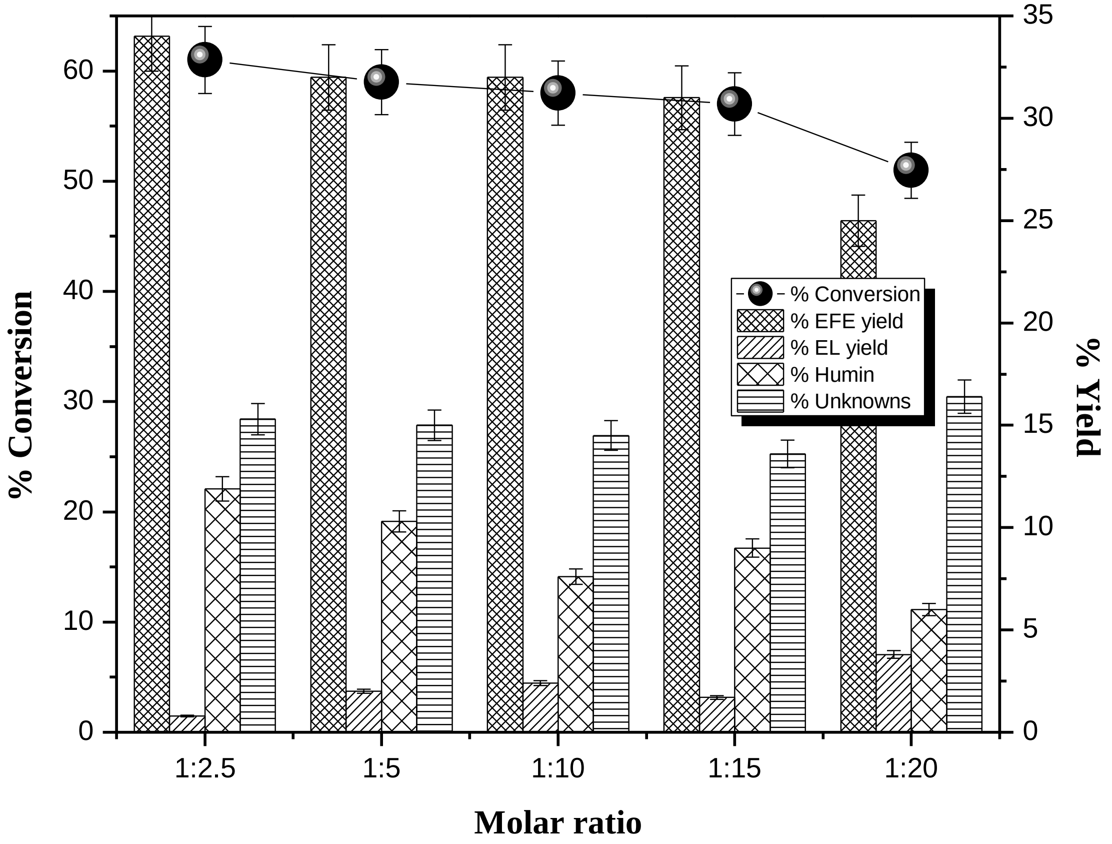

Figure 3.7 Effect of the molar ratio of FAlc to ethanol

Reaction conditions: - 110°C Temp, 2.5h Time, 5 wt. % catalyst loading w. r.t. FAlc.

3.3.6 Effect of Temperature

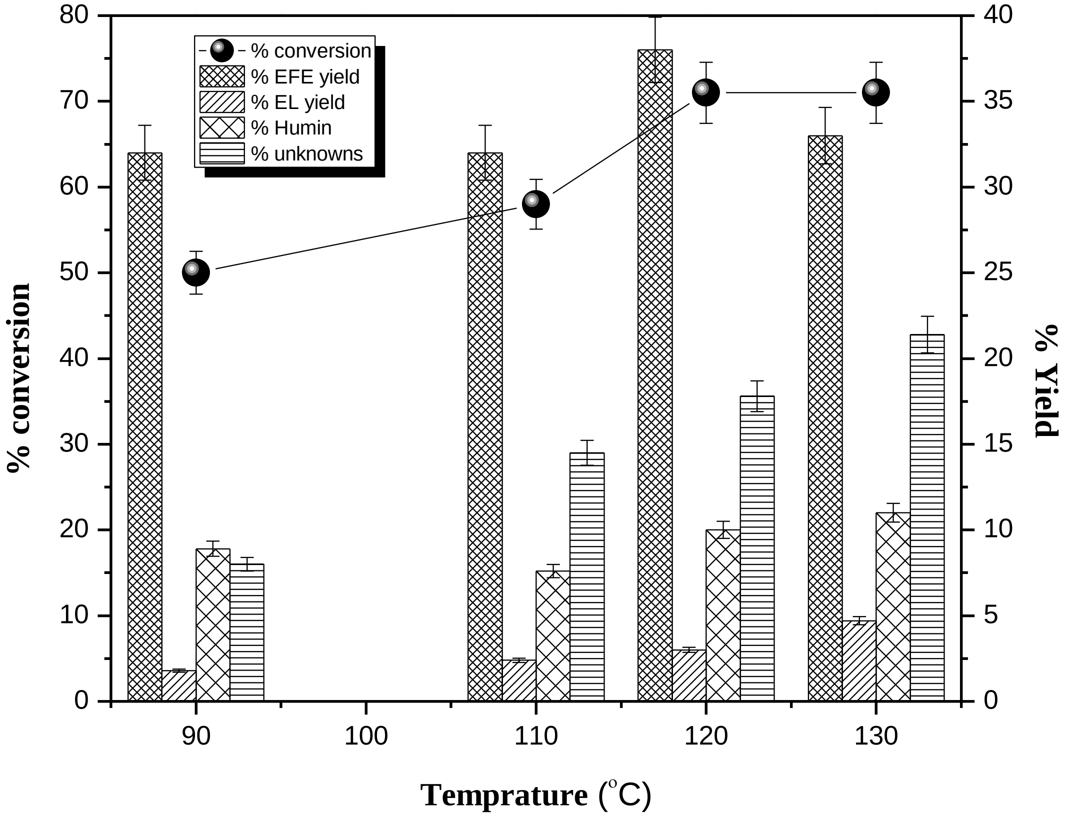

Figure 3.8 Effect of Temperature

Reaction conditions: - 1:10 FAlc/Ethanol mol. Ratio, 2.5h Time, 5 wt. % catalyst loading w.r.t. FAlc.

Temperature affects the etherification and esterification processes. Temperature effects on FAlc conversion and product yield were investigated, and the experiments were carried out at temperatures ranging from 90 °C to 130 °C. The FAlc conversion increased from 50% to 72% as the temperature rose from 90°C to 120°C. After that, the FAlc conversion was identical. As the temperature rises, the rate of reaction increases, boosting the etherification reaction of FAlc to

EFE. The further ethanolysis of EFE to EL and condensation to humins is almost the same at 3% and 7%, respectively. The unknown products were increased from 8 % to 15%, this is obvious at the higher temperature. Above 110 °C, at 120 °C maximum, an EFE yield of 37% was observed. Above 120 °C, other reactions rate is higher over the etherification rate which leads to an increase in EL; humins, and unknown formation at the cost of EFE. Thus, 120 °C was found to be the identical temperature for the maximum formation of EFE.

3.3.7 Effect of Catalyst Loading

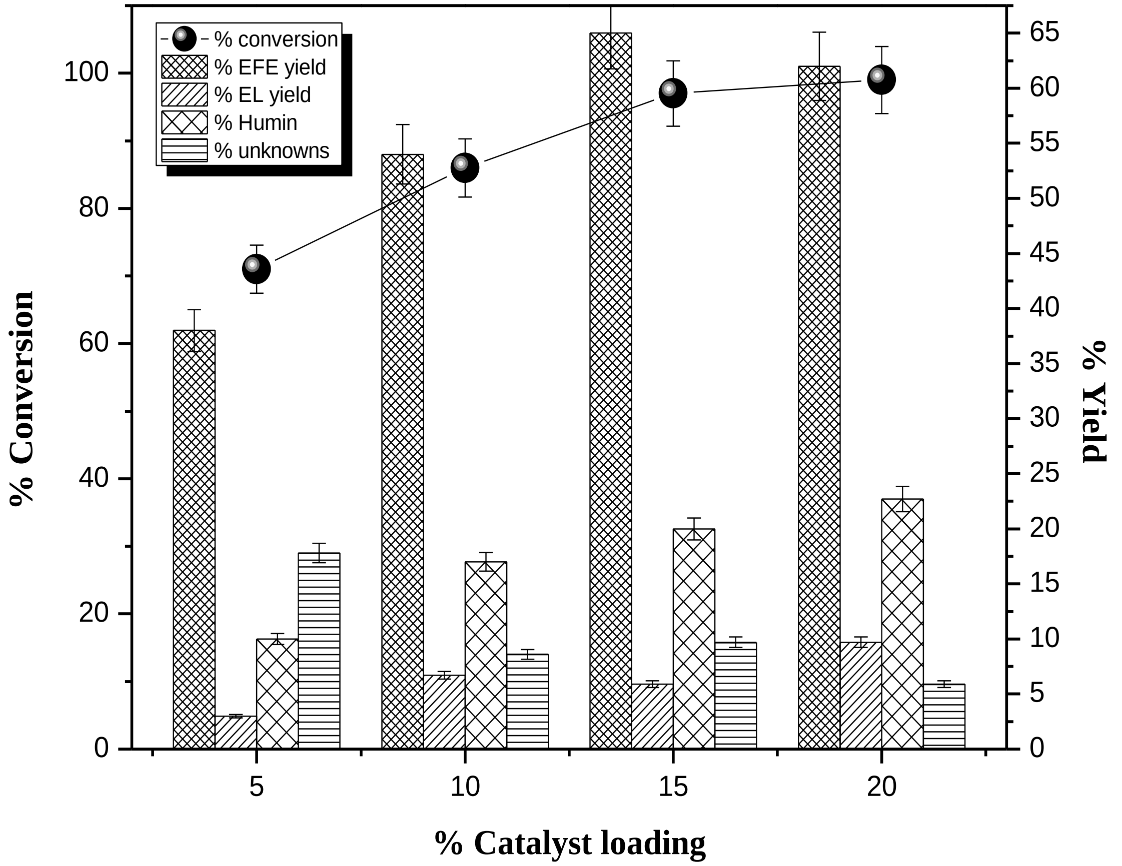

Figure 3.9 Effect of catalyst loading concerning to FAlc

Reaction conditions: 1:10 FAlc to Ethanol mol ratio, 2.5 h Time, 120 °C Temp.

Enhancement in the active site by increasing catalyst loading is also one of the important parameters to consider for process optimization. Higher availability of active sites improves overall activity or conversion. The FAlc conversion was increased from 70% to 95% by increasing catalyst loading from 5% to 15%. This increase in active sites also changes the overall product distribution due to favoring one reaction over others. In the present study, etherification of FAlc to EFE was favored in a major way with an increment in EFE formation up to 65% (15 wt. % catalyst loading) from 38% (5 wt. % catalyst loading). A similar increasing trend of 10% was also observed for humins generation with a rise in catalyst loading to 15%, whereas, unknown product formation was reduced up to 10% with EL formation of 5%. Above, 15% catalyst loading almost identical FAlc conversion was found with a marginal decrease in EFE yield by 2%.

3.3.8 Effect of reaction time

Time is another key component to consider when studying catalytic activity. To determine the shortest time required to complete FAlc conversion, the other optimal parameters were used 15% catalyst loading, a 1:10 molar ratio of FAlc to Ethanol, and a reaction temperature of 120°C. After 0.5, 1.5, and 2.5 hours of rigorous analysis, the reaction was stopped and quenched. Initially at 0.5hr, conversion of FAlc and yield of EFE is 88% and 58% respectively which is increased up to 93% and 61% within 1.5hrs, Further reaction was carried out up to 2.5hrs and got almost complete conversion (97%) yielding 65% EFE along with 6% EL, 20% humins and remaining are unknowns. Within 0.5h there is a 60% EFE yield and there is only 7% EL formation along with 20% humins due to the fastest etherification and Polycondensation, however further ethanolysis of EFE to EL becomes much slower and complex and require more time to produce[14].

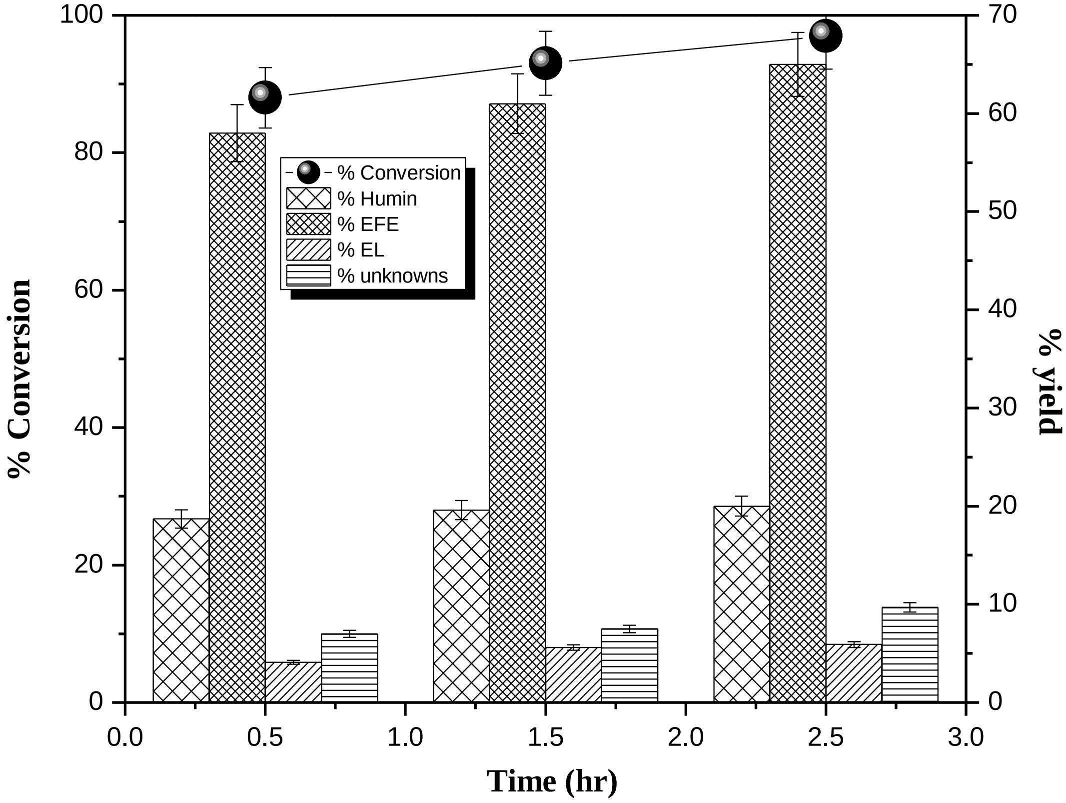

Figure 3.10 Effect of reaction time

Reaction conditions: - 1:10 FAlc to Ethanol mol. ratio, 15 wt. % Catalyst loading w.r.t. FAlc, 120 °C Temp

3.3.9 Catalyst regeneration

In FAlc conversion catalyst regeneration and its reusability is an important issue because of the formation of insoluble humins which block the active sites. It is quite difficult to dissolve the humins,[32,33] by taking consideration of the standard analytical protocol developed for the dissolution of humins type poly-condensed compound in wood and pulp approved by the standard analytical Technical Association of the Pulp and Paper Industry (TAPPI) “T204 cm 97”. Using said protocol used catalyst having humins was washed with a solvent mixture of THF + Acetone

(50:50 ratio) for 1h to regenerate the catalyst. After washing and drying at 120 °C for 4 h catalyst has shown only 20% FAlc conversion and 12% EFE. In another case, the used catalyst having humins was washed with THF + Acetone (50:50 ratio) for 1h and then was calcined at 350 °C for 5h which has shown a regain in catalyst activity as that of fresh (Figure 3.11) and was maintained for next two cycles. Figure 3.12 depicts XRD plots for fresh; spent, and treated (washing + calcination) catalysts It confirmed that after washing with a mixture of THF and Acetone and calcination at 350 °C for 5h catalyst regained its crystallinity as compared to the spent catalyst.

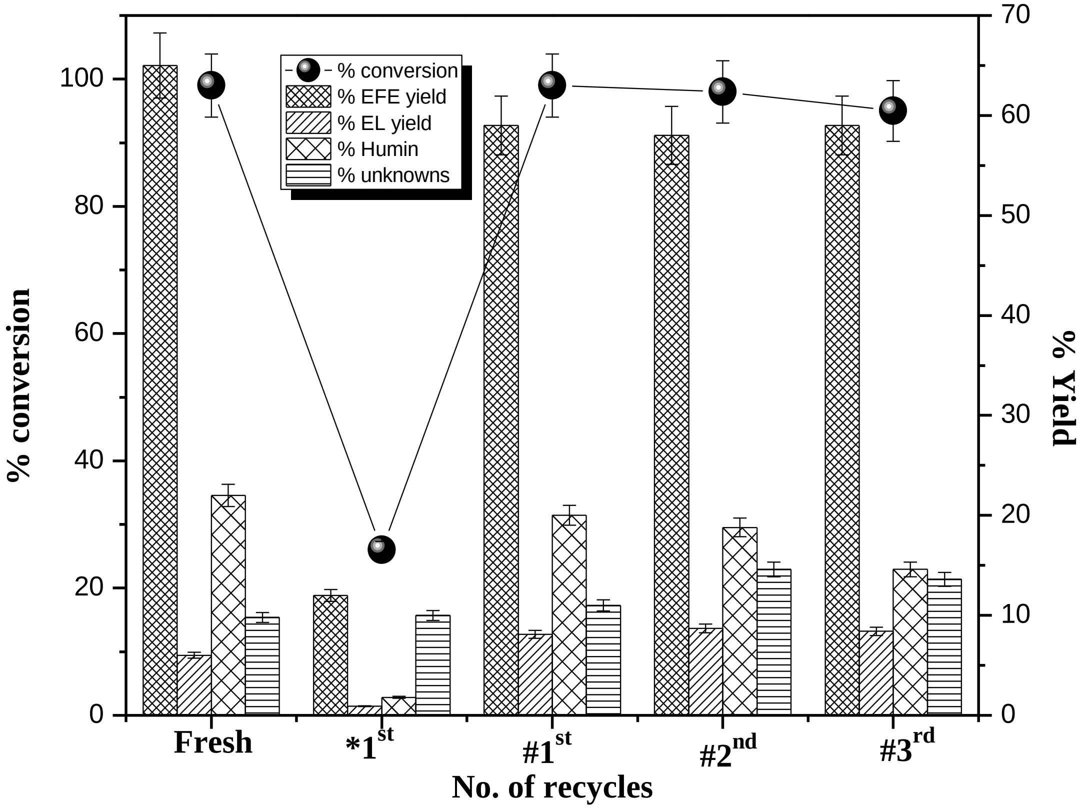

Figure 3.11 Catalyst Reusability **Washed and dried, # washed and calcined at 350 °C for 5 h Reaction conditions: - 1:10 FAlc to Ethanol mol. ratio, 2.5h Time, 15 wt. % Catalyst loading w.r.t. FAlc, 120 °C Temp*

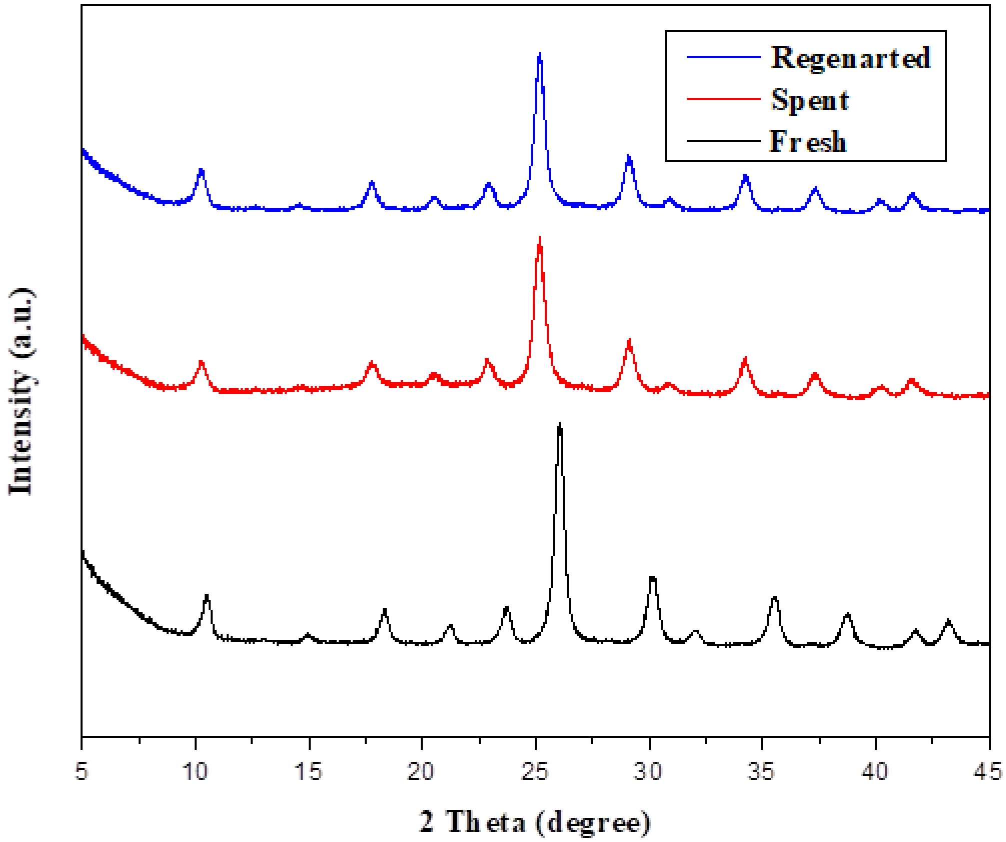

Figure 3.12 Powder XRD of fresh, spent, and regenerated $H_1Cs_2PW_{12}O_{40}$ samples

3.4 Comparison of the present catalytic system with the literature

Table 3.3 Comparison of the present catalytic system with the literature

Sr. No.	Catalyst	Catalyst loading (wt % of FAlc)	Reaction conditions Temp. °C	Time h	% Conversion	% Yield	Ref.
1	$SiO_2{-}Al_2O_3$	60	200	4.5	99	68	[34]
2	HZSM-5 (25)	80	55	18	90.6	47.0	[10]
3	Kaolinite	50	180	2	57	34.2	[35]
4	$H_1Cs_2PW_{12}O_{40}$	15	120	2.5	98	65	This work

Table 3.3 highlights the catalytic activity of the current works in contrast to the reported literature. Cao et al. employed a mixed oxide of silica and alumina (SiO_2-Al_2O_3) as a catalyst to etherify FALc. Using a 60% weight proportion of catalyst loading relative to FALc, they were able to achieve 99 % FALc conversion and 68 % EFE production in 4.5 hours at temperatures up to 200°C.[34] In another investigation, Cao et al. employed Si/Al-25 as a catalyst with typical zeolite ZSM-5.[10] At a low reaction temperature of 50°C and 80% catalyst loading, they obtained 90% conversion and 47% EFE yield. Natsir et al. used natural clay Kaolinite as a catalyst for the etherification of FALc using different alcohols, using ethanol as the alcohol supply and 50% Kaolinite loading, achieving 57% conversion and 34.2% EFE production after 2 hours of reaction at 180°C [35]. In our current study, we achieved 98% conversion and 65% EFE yield at moderate reaction conditions using a Cs exchanged HPW catalyst ($H_1Cs_2PW_{12}O_{40}$) with a 15% loading against FALc loading.

3.5 Conclusions

A successful attempt was made to heterogenize hetero-polyacid in the polar medium by exchange of Cs (from 0.5 to 2.5 moles) in place of H^+ proton. The prepared catalysts were meticulously characterized by several characterization techniques such as XRD; TPD; BET Surface area; XPS; Pyridine –FTIR, and established fingerprint of these samples. Etherification reaction of furfuryl alcohol with ethanol to Ethyl Furfuryl Ether, a biofuel was carried out. $H_1Cs_2PW_{12}O_{40}$ catalyst having total acidity of 786 µmol/g; B/L ratio of 3.6; Surface area of 43m^2/g was found to be optimum catalyst composition for maximum FAlc conversion of 98%; 65% EFE yield at 120°C; 1:10 (FAlc: Ethanol); 15% catalyst loading w.r.t FAlc; 2.5h reaction time. $H_1Cs_2PW_{12}O_{40}$ catalyst was found to be reusable 4 times (fresh + 3 reuse) by solvent washing

(THF + Acetone) 50:50 ratio and then calcination at 350°C for 5h. This study has shown the effective development of catalysts and optimization of process parameters for the selective synthesis of biofuel from renewable furfuryl alcohol.

3.6 References

1 J. A. J. Ragauskas, C. K. Williams, B. H. Davison, G. Britovsek, D. J. L. Cainey, C. A. Eckert, W. J. Frederick, Jr., J. P. Hallett and T. T. C. L. Liotta, J. R. Mielenz, R. Murphy, R. Templer, *Science (1979)*, 2006, **311**, 884–489.

2 R. V. S. K.Dalai, *Appl Catal A Gen*, 2013, **454**, 127–136.

3 T. Wang, A. Hu, G. Xu, C. Liu, H. Wang and Y. Xia, *Catal Letters*, 2019, **149**, 1845–1855.

4 G. Gómez, Z. El, K. Nieminen, S. Hellsten, J. Llorca and H. Sixta, *Fuel Processing Technology*, 2018, **182**, 56–67.

5 T. Zhao, Y. Zhang, G. Zhao, X. Chen, L. Han and W. Xiao, *Fuel Processing Technology*, 2018, **180**, 14–22.

6 V. E. Tarabanko, M. Yu. Chernyak, K. L. Kaygorodov, N. F. Orlovskaya, A. A. Morozov, A. A. Kondrasenko and Yu. N. Bezborodov, *Journal of Siberian Federal University*, 2016, **2**, 221–229.

7 US 8,372,164 B2, *United States Patent*, 2013.

8 Y. Nakagawa, M. Tamura and K. Tomishige, *Fuel Processing Technology*, 2019, **193**, 404–422.

9 J. Lange, E. Van Der Heide, J. Van Buijtenen and R. Price, *ChemSusChem 2012*, 2012, **5**, 150–166.

10 Q. Cao, J. Guan, G. Peng, T. Hou, J. Zhou and X. Mu, *CATCOM*, 2015, **58**, 76–79.

11 Z. Zhang, K. Dong and Z. Kent, 2011, **116023**, 112–118.

12 L. L. and B. X. 1 Geng Zhao, Ming Liu, Xinkui Xia, *Molecules*, 2019, **24**, 1881.

13 Y. Wang, D. Zhao, K. S. Triantafyllidis and W. Ouyang, *Molecular Catalysis*, 2020, **480**, 110630.

14 X. Gao, L. Peng, H. Li and K. Chen, 2015, **10**, 6548–6564.

15 D. R. Cha, T. E. Davies, S. H. Taylor and A. E. Graham, *ACS Sustainable Chem. Eng.*, 2018, 4996–5002.

16 F. Zaccheria, N. Scotti, N. Ravasio and D. E. E. Dbe, *catalysts*, , DOI:10.3390/catal9020172.

17 X. Kong, S. Wu, L. Liu, S. Li and J. Liu, *Molecular Catalysis*, 2017, **439**, 180–185.

18 M. W. Fang Su, Qingyin Wu, Daiyu Song, Xianghuan Zhang and and Y. Guo, *J Mater Chem A Mater*, 2013, **1**, 13209–13221.

19 M. José, D. Silva, A. Aparecida, S. Olavo, R. Chagas, D. Silva and D. Morais, *Fuel*, 2019, **254**, 115607.

20 Z. Sun, X. Duan, P. Gnanasekarc, N. Yan and J. Shi, , DOI:10.1007/s13399-020-00802-1/Published.

21 M. N. Timofeeva, *Appl Catal A Gen*, 2003, **256**, 19–35.

22 I. V. Kozhevnikov and K. I. Matveev, *Appl Catal*, 1983, **5**, 135–150.

23 K. Narasimharao, D. R. Brown, A. F. Lee, A. D. Newman, P. F. Siril, S. J. Tavener and K. Wilson, *J Catal*, 2007, **248**, 226–234.

24 H. Eom, D. Lee, S. Kim, S. Chung, Y. Gul and K. Lee, *Fuel*, 2014, **126**, 263–270.

25 T. Okuhara and T. Nakato, *Catalysis Surveys from Japan*, 1998, **2**, 31–44.

26 K. Inumaru, T. Ito and M. Misono, *Microporous and Mesoporous Materials 21*, 1998, **21**, 629–635.

27 C. Travers, N. Essayem, M. Delage and S. Quelen, *Catal Today*, 2001, **65**, 355–361.

28 A. E. R. S. Khder, H. M. A. Hassan and M. S. El-Shall, *Appl Catal A Gen*, 2012, **411–412**, 77–86.

29 M. Tao, L. Xue, Z. Sun, S. Wang, X. Wang and J. Shi, *Sci Rep*, , DOI:10.1038/srep13764.

30 X. Yang, Y. Liu, X. Li, J. Ren, L. Zhou, T. Lu and Y. Su, , DOI:10.1021/acssuschemeng.8b00177.

31 L. Pesaresi, D. R. Brown, A. F. Lee, J. M. Montero, H. Williams and K. Wilson, *Appl. Catal. A Gen.*, 2009, **360**, 50–58.

32 P. Neves, S. Lima, M. Pillinger, S. M. Rocha, J. Rocha and A. A. Valente, *Catal Today*, 2013, **218–219**, 76–84.

33 L. L. Geng Zhao, Lei Hu, Yong Sun, Xianhai Zeng, *Bioresources*, 2014, **9**, 2634–2644.

34 Q. Cao, W. Zhang, S. Luo, R. Guo and D. Xu, *Energy and Fuels*, 2021, **35**, 12725–12733.

35 T. A. Natsir, T. Hara, N. Ichikuni and S. Shimazu, *ACS Appl Energy Mater*, 2018, **1**, 2460–2463.

Chapter-4

Alcoholysis of Furfuryl alcohol and Furfuryl aldehyde over UiO-66-NH_2-HPW catalyst

4.1 Introduction

Heteropolyacids (HPAs) are an interesting class of well-defined strong solid Brønsted acids with exceptional catalytic activity in a variety of acid-catalyzed processes such as esterification, transesterification, hydrolysis, alkylation, acylation, and redox reactions [1,2]. However, HPAs are often soluble in a wide range of polar solvents, making recovery, separation, and recycling of the catalysts problematic, limiting their eco-friendly applications. As a result, developing a reusable HPA-based catalyst will be advantageous. Nonetheless, heterogeneous HPA-based catalysts typically have several drawbacks, such as poor surface area, active site leaching, and low activity [1–5]. Many techniques, such as immobilization and solidification, have been proposed to address the aforementioned restrictions and improve the stability and catalytic performance. HPAs can be immobilized using a variety of supports, including mesoporous silica, metal-organic frameworks, transition metal oxides, zeolites, and mesoporous carbon [1,2,5–7]. It is well known that HPAs have strong acidity and even it reacts with weak bases and form bonding with them. HPAs will get heterogeneity by interacting with bases such as alkali metals and organic amines[2,4,5,8–12]. Materials such as organically modified silica with amine functionality, organic polymers containing an amino-functional group, organic amines, ionic liquids, and organic surfactants containing amino groups were often used as a carrier for anchoring HPA employing strong bonding[11–15]. For acid-base dispersion and anchoring of HPAs on Metal-Organic frameworks (MOF) containing amine functionality may be the best option because MOFs have high porosity and high surface area which will provide more active sites for host-guest interaction.

MOFs are a class of crystalline, well-ordered inorganic-organic porous hybrid material with tunable textural and diverse framework functionalities. MOFs can be used as multifunctional catalysts in tandem reactions and their catalytic properties can be enhanced by engineering metal nodes as active sites, the post-synthetic introduction of active sites, and engineering of active sites in pores cavities[16–19]. Zirconium-based MOFs, such as UiO-66 and its amine derivative UiO-66-NH_2, have a high surface area and are more hydrothermally and chemically stable throughout a wide pH range in aqueous solutions. This makes UiO-66 extremely useful as a catalyst and an ideal platform to introduce active sites [19–21]. Biomass conversion involves hydrolysis, dehydration, alcoholysis, esterification, and etherification over Lewis as well as Brønsted acid sites. Brønsted acidity in MOFs is introduced by using acid-functionalized ligands, by encapsulation of HPAs during solvothermal synthesis, and by impregnation of HPAs on MOFs. Encapsulation of HPAs in MOF may lead to pores blockage, extensive drop-down in total surface area, slow diffusion, and less contact of reactants with active sites, while impregnation of HPAs on MOFs may lead to low homogeneity in dispersion, occupation of the large cavities and leaching during the reaction[17,22]. Thus, the objective of this work is to overcome the above-mentioned problems by firm anchoring/binding of HPAs on UiO-66-NH_2, by reacting it with the basic sites (-NH_2).

In this chapter, we have demonstrated the post-synthetic modification of UiO-66-NH_2 by binding with phosphotungstic acid (HPW). The prepared UiO-66-NH_2-HPW catalyst was characterized by XRD, ATR-FTIR, XPS, STEM-EDS, SEM, HR-TEM, N_2 adsorption-desorption analysis, and ammonia-temperature programmed desorption (NH_3-TPD). Preparation of furfuryl ethers (FE) such as Ethyl furfuryl ether (FEF), Methyl furfuryl ether (MFE), Isopropyl furfuryl ether (IPFE), and alkyl levulinates (AL) such as Ethyl levulinate (EL), Methyl levulinate (ML), and Isopropyl levulinate (IPL) significantly considered in recent years, due to their applicability as a fuel and fuel additive along with other applications[23–27]. Hence, we carried out the catalytic evaluation of prepared UiO-66-NH_2-HPW for hydrogenation and alcoholysis of Furfural (FFR) and Furfuryl alcohol (FALc) to FE and AL

4.2 Experimental

4.2.1 *Materials and Methods*

Zirconium tetrachloride procured from Acros, 2-amino terephthalic acid purchased from Alfa Aesar, N-N-dimethylformamide and Keggin-type 12-tungstophosphoric acid (AR) purchased from Thomas Baker, Mumbai (India) and analytical standard's EFE, EL, ML, FAlc and FFR were purchased from Sigma Aldrich, Ethanol from Changshu Hongsheng Fine chemical China.

4.2.2 *Catalyst synthesis*

4.2.2.1 *Synthesis of UiO66-NH_2 MOF*

Based on past studies, UiO-66-NH_2 was created using a hydrothermal method with slight modifications [2]. At room temperature, 5.6 mol of N-N-dimethylformamide was dissolved in 13.5 mmol of $ZrCl_4$, 13.5 mmol of 2-amino terephthalic acid, and 13.5 mmol of water. A 1 L stainless steel Teflon-lined reactor was used to crystallize the material under static circumstances for 18 hours at 120°C in a prepared oven. The reactor was then removed from the oven and allowed to cool naturally until it reached room temperature. To remove the unreacted ligand, the resulting solid was centrifuged and repeatedly washed with DMF and methanol. It was then dried at 80°C for two hours in the oven to produce dry powder.

4.2.2.2 *Immobilization of HPW on UiO-66-NH_2*

The Immobilization of HPW on UiO-66-NH_2 was done by dissolving 2.3 mmol of HPW in 60 mL of acetonitrile, and 1.14 mmol of freshly prepared powder of UiO-66-NH_2 was added to HPW solution and kept under vigorous stirring for 30 min. The resulting material was separated by centrifugation washed multiple times with acetonitrile to remove unreacted HPW, and dried in an oven at 80°C for 2 hours to yield UiO-66-NH_2-HPW.

4.2.3 Catalyst characterization

Wide-angle X-ray diffraction (XRD) patterns were produced using a Rigaku Miniflex X-ray diffractometer with a Cu K radiation source, operating at 40 kV and 30 mA over a 2 range of 5° to 50° at a scanning rate of 3°/min.

On a Bruker Alpha-P ATR FTIR spectrometer, the functional groups of the generated compounds were characterized using Fourier Transform Infrared Spectroscopy (FTIR).

The surface area of the samples was calculated using the BrunauerEmmettTeller (BET) method from nitrogen adsorption-desorption isotherms in liquid nitrogen on Quantachrome Autosorb iQ equipment, and all samples were degassed to 0.1 Pa at 200 °C for 3 hours before measurement.

Images of Field Emission Scanning Electron Microscopy (FE-SEM) were obtained using a NOVA NANOSEM 450 equipment, while images of High-Resolution Transmission Electron Microscopy (HRTEM), STEM, and Elemental mapping were captured using a JEOL JEM-F200 (URP) instrument.

Thermo Fisher Scientific K-Alpha+ model XPS apparatus with an Al K source was used for X-ray Photoelectron Spectroscopy (XPS). The Shirley-type background subtraction method was used to fit the XPS data of all compounds using Fitiyk software.

Micrometric AutoChem 2950 HP equipment was used to measure the temperature-programmed desorption (TPD) profiles of NH_3 from the synthesized catalysts. The sample cell was originally treated with a helium flow of 40ml min-1 at 200°C for 2 hours, then cooled to 100°C and exposed to pulses of ammonia (10% in helium) until saturation, and finally purged with a helium flow at 100°C for 1 hour. The sample cell was then heated to 600°C with a 10°C min-1 ramp. The concentration of desorbed ammonia was continually measured using a TCD detector.

4.2.4 Reaction procedure and analysis

Reactions were carried out in a high-pressure Parr reactor (4871 series controller) with a volume of 100 mL and external temperature and stirring controllers. Based on the FFR or FALc concentration, 7.2 mmol of FFR or FAlc, 360 mmol of alcohol, and 20% catalyst were loaded in a typical reaction. The reactor was then sealed and placed in a heating unit with 300 rpm churning. After the completion of the reaction, the reactor was cooled to room temperature using a cooling water bath. Centrifugation was used to remove the used catalyst. The used catalyst was washed and dried before being utilized in the next run to examination of its stability and reusability.

The quality of the liquid products was determined using gas chromatography-mass spectrometry (GC-MS-QP2020 NX, Shimadzu) using a TR-5 MS column (30 m 250 m 0.25 m). The quantitative analysis of liquid products was performed using a Varian CP-3800 series with an RTX-5 capillary column (60 m 320 m 0.25 m) fitted with a flame ionization detector (FID). For both GCMS and GC analyses, the following temperature program was used: the initial temperature was 50 °C, followed by heating at a rate of 20 °C/min to 220 °C. The quantities of product samples were quantified using external standard curves with commercial samples. Product yields were calculated as the ratio of moles of the product obtained to moles of the substrate in the feed. The yield of IPFE, EFE, and MFE was calculated via calibration data of FALc. It is commercially unavailable and was confirmed by GC−MS. The yield of products and conversion were determined according to the following equations:

$$\%\, Conversion = \frac{Reactant\ initial\ moles - Reactant\ final\ moles}{Reactant\ initial\ moles} * 100$$

$$\%\, Yield = \frac{moles\ of\ product}{Reactant\ initial\ moles} * 100$$

$$Weight\ of\ humin = Residue\ collected(dried) - Weight\ of\ Catalyst$$

$$\%\ Humin = \frac{Weight\ of\ humin}{Initial\ weight\ of\ Reactant} * 100$$

4.3 Results and Discussion

4.3.1 Catalysts characterization

4.3.1.1 *X-Ray diffraction*

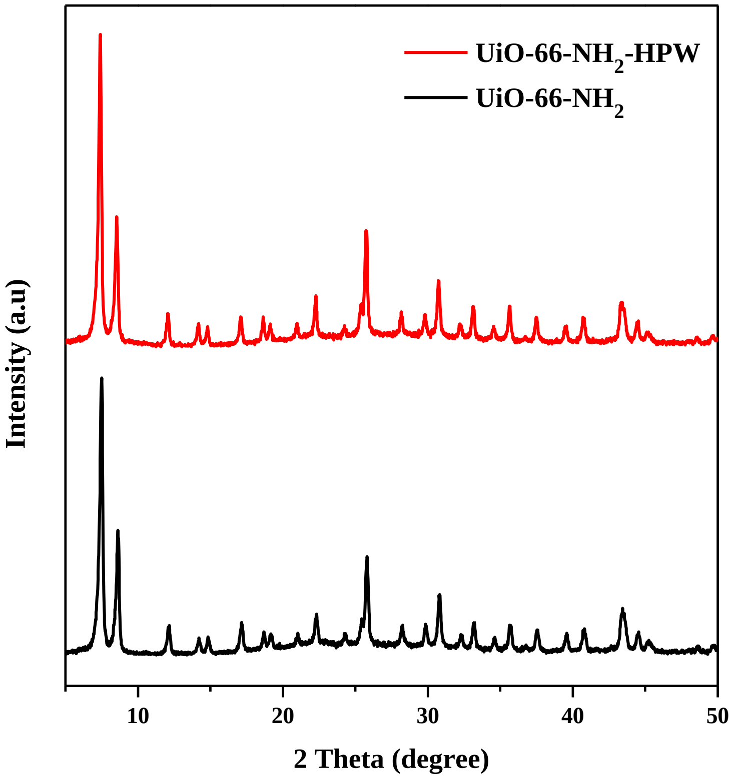

Figure 4.1 Powder XRD of parent UiO-66-NH_2 and UiO-66-NH_2-HPW

Figure 4.1 depicts the powder XRD patterns of the samples before and after modification. The powder XRD patterns of the samples both before and after modification are shown in Figure 4.1. The XRD patterns of the synthesized UiO-66-NH_2 are analogous to those of earlier studies [28–

[30]. Moreover, the morphology and XRD pattern remains the same after post-synthetic modification.

4.3.1.2 SEM, TEM, and elemental mapping

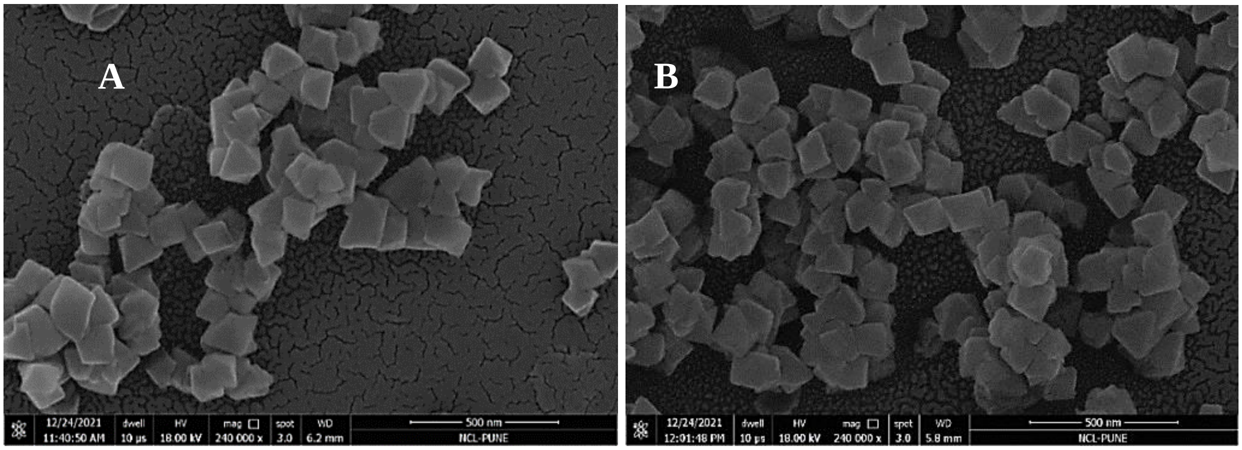

Figure 4.2. SEM image of (A) UiO-66-NH$_2$ and (B) UiO-66-NH$_2$-HPW

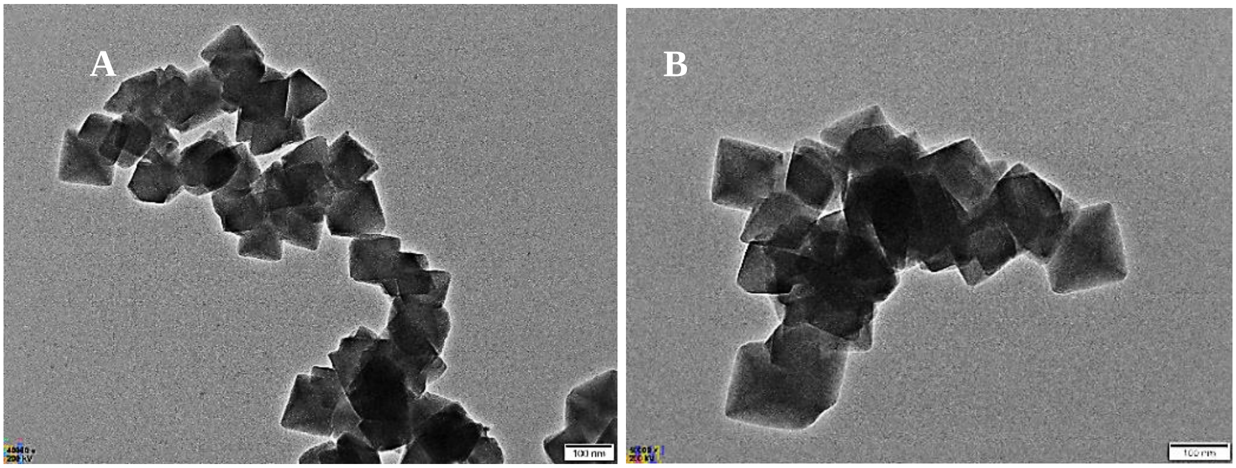

Figure 4.3 HR-TEM image of (A) UiO-66-NH$_2$ and (B) UiO-66-NH$_2$-HPW

The surface morphology of the sample was detected by the SEM and TEM imaging techniques and images are given in Figure 4.2 A and B and Figure 4.3 A and B, images indicate the crystals of UiO-66-NH$_2$ and UiO-66-NH$_2$-HPW were regular octahedrons in shape. Figure 4.4 TEM and EDS mapping images of UiO-66-NH$_2$-HPW indicate that well dispersion and distribution of HPW throughout the UiO-66-NH$_2$ crystal, while Figure 4.5 represents the parent sample (UiO-66-NH$_2$) only shows framework elements- Zr, O, C, and N in EDS mapping.

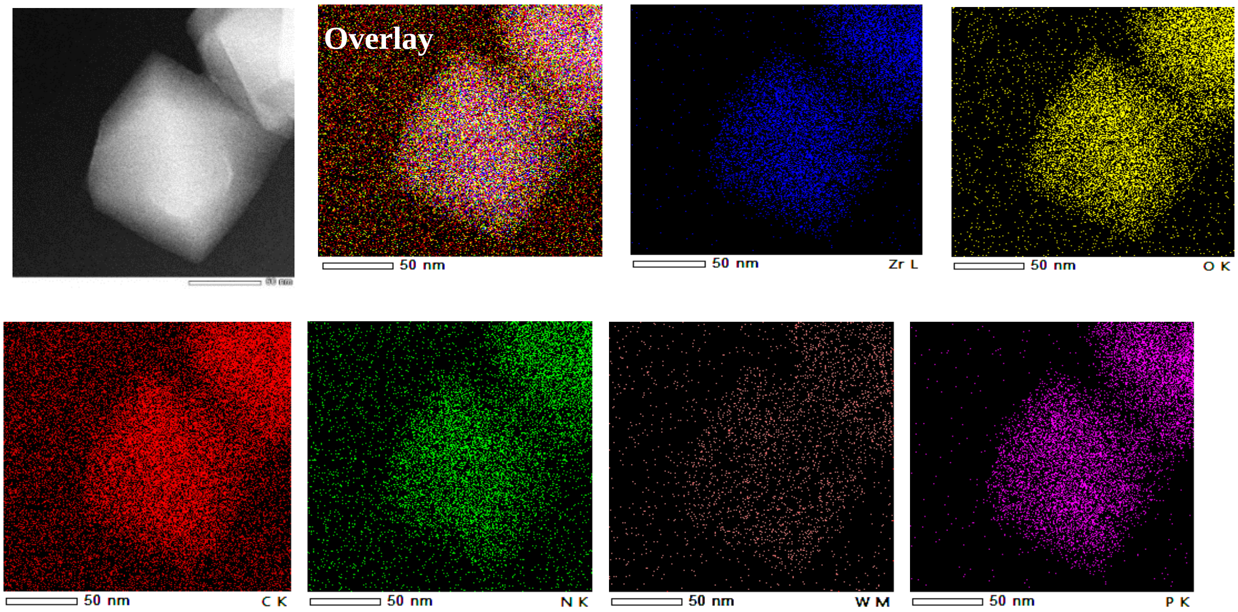

Figure 4.4 STEM image and Elemental mapping of UiO-66-NH$_2$-HPW

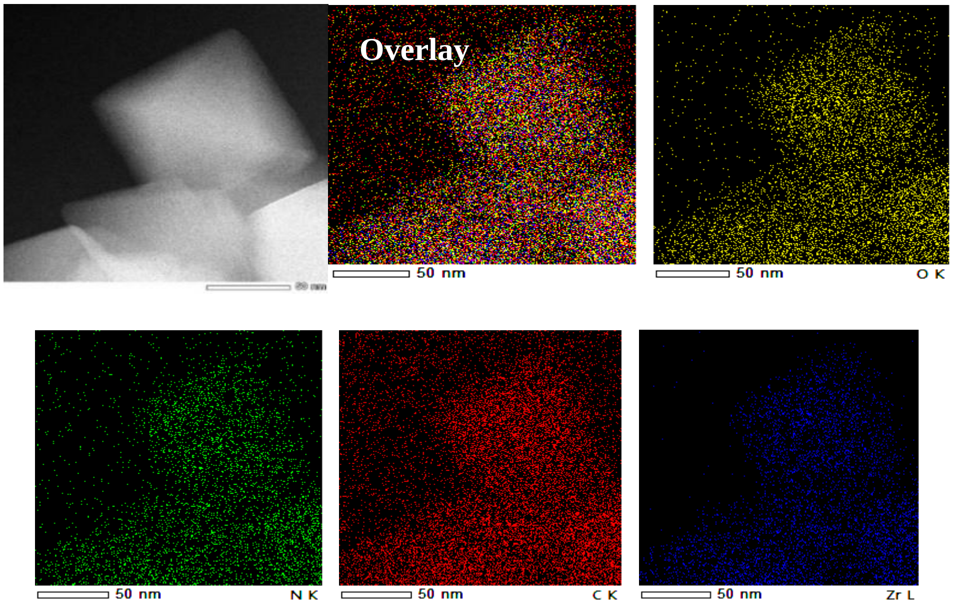

Figure 4.5 STEM image and Elemental mapping of UiO-66-NH$_2$

4.3.1.3 ATR-FTIR

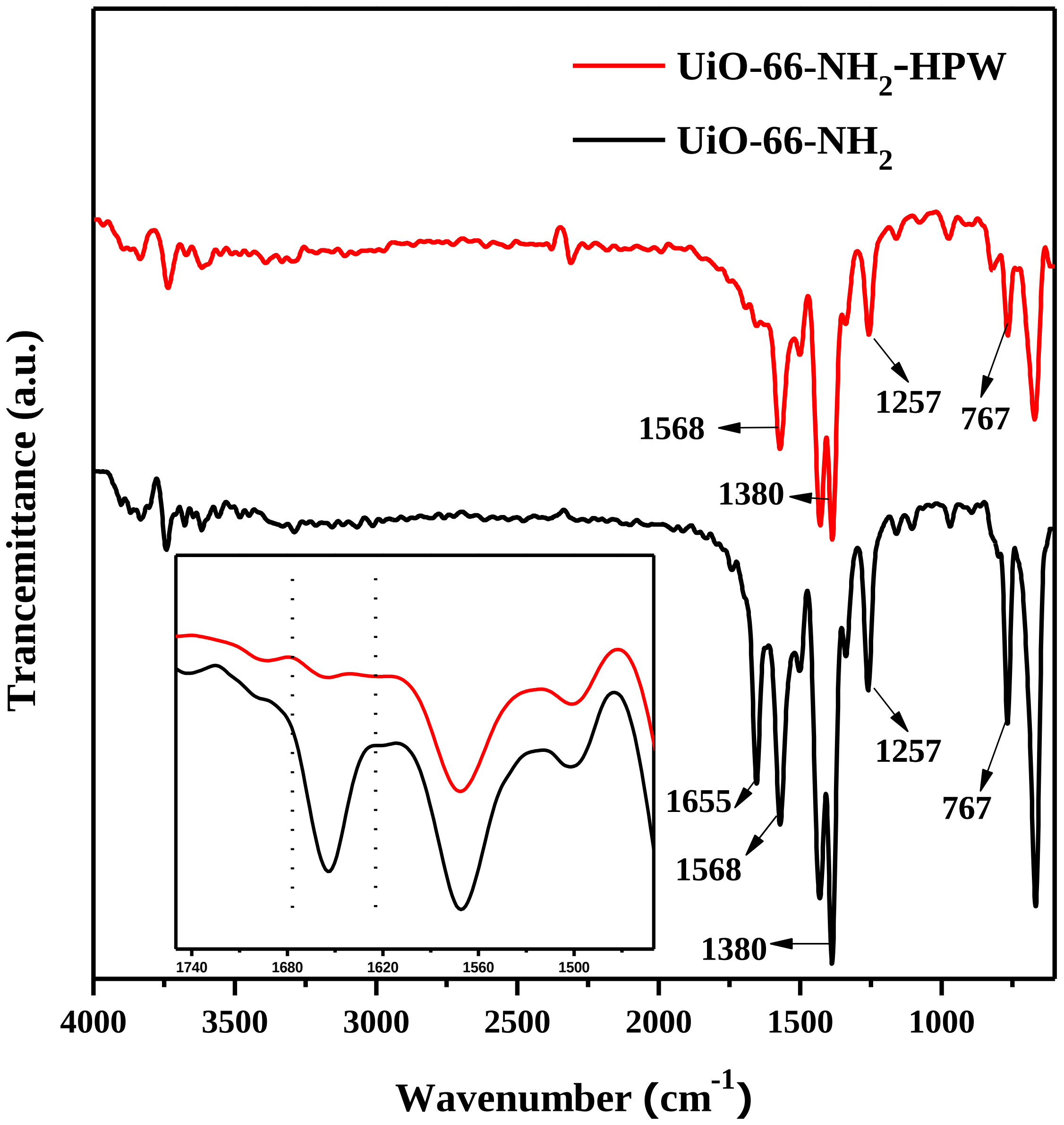

Figure 4.6 ATR-FTIR of parent UiO-66-NH_2 and UiO-66-NH_2-HPW

The ATR-FTIR spectra of the UiO-66-NH_2 and UiO-66-NH_2-HPW samples are displayed in Figure 4.6. The ligand of UiO-66-NH_2 was an amine-functionalized terephthalic acid (2-amino terephthalic acid), and the spectrum of UiO-66-NH_2 showed the strong uncoordinated free -NH_2 band of aromatic primary amine N-H stretching at 1655 cm-1 [31]. The spectral band at 1568 cm^{-1}

was caused by the skeletal vibration of the benzene ring. Additionally, the vibrational spectrum of the C–N stretching is assigned to a component at 1257 cm-1, while a component at 1400 cm-1 corresponds to the OCO symmetric stretching [28–31]. After the modification of UiO-66-NH_2 with HPW to UiO-66-NH_2-HPW, only a reduction in the characteristic N-H stretching band of primary amine at 1655 cm^{-1} (shown in the inset of Figure 4.6) was observed. Hence it specifies that there is a strong chemical interaction between the -NH_2 group and HPW.

4.3.1.4 X-ray photoelectron spectroscopy

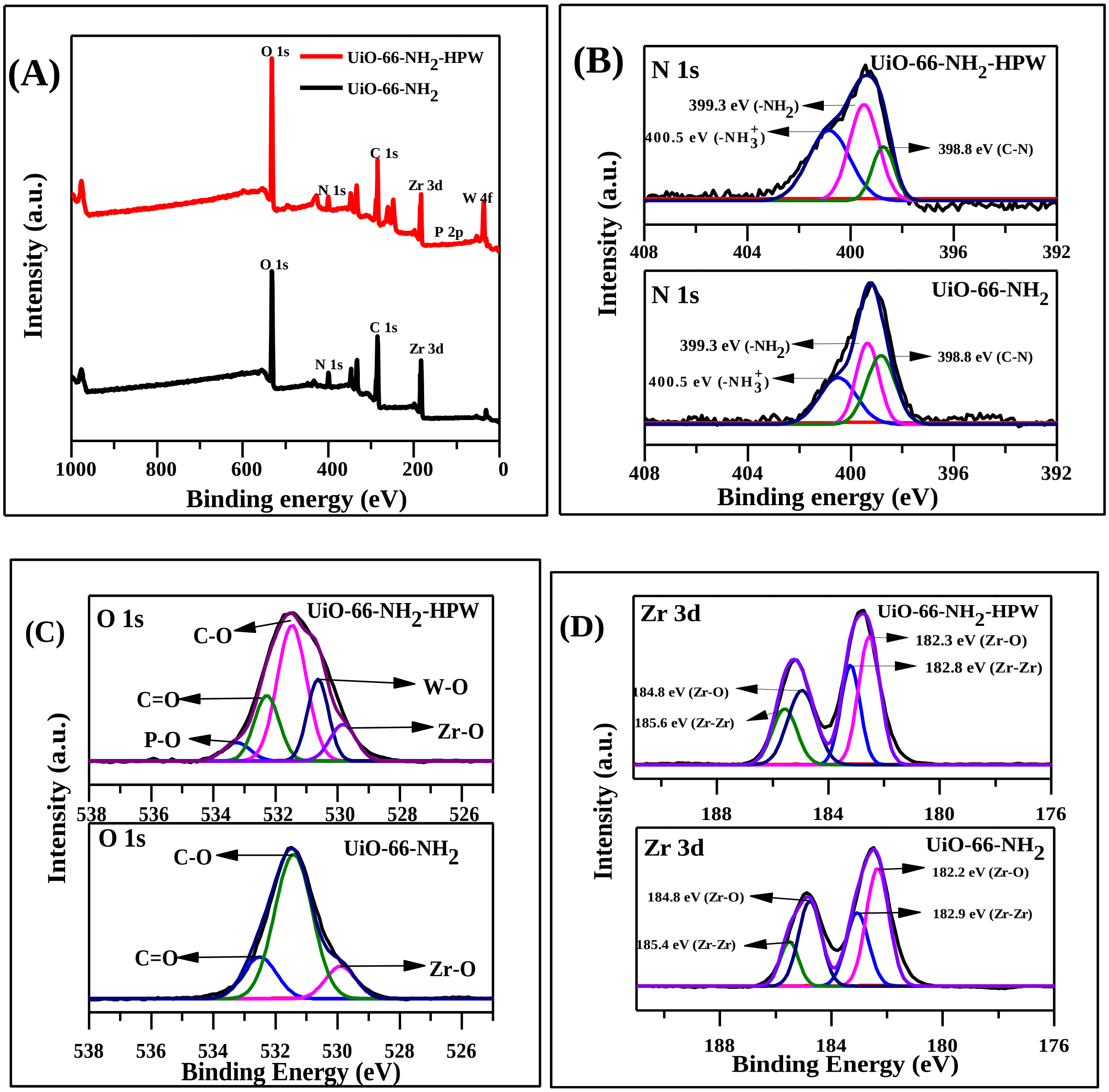

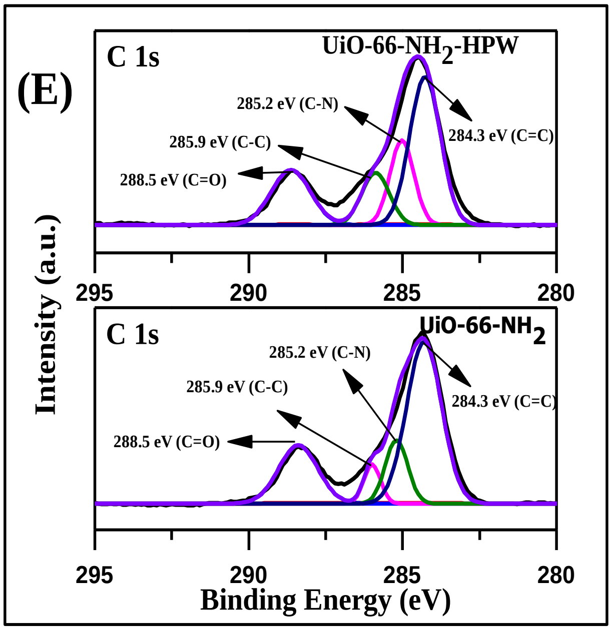

Figure 4.7 (A) XPS survey scan of UiO-66-NH$_2$ and UiO-66-NH$_2$-HPW, and high-resolution XPS data of UiO-66-NH$_2$ and UiO-66-NH$_2$-HPW (B) N 1, (C) O 1s, (D) Zr 3d, (E) C 1s

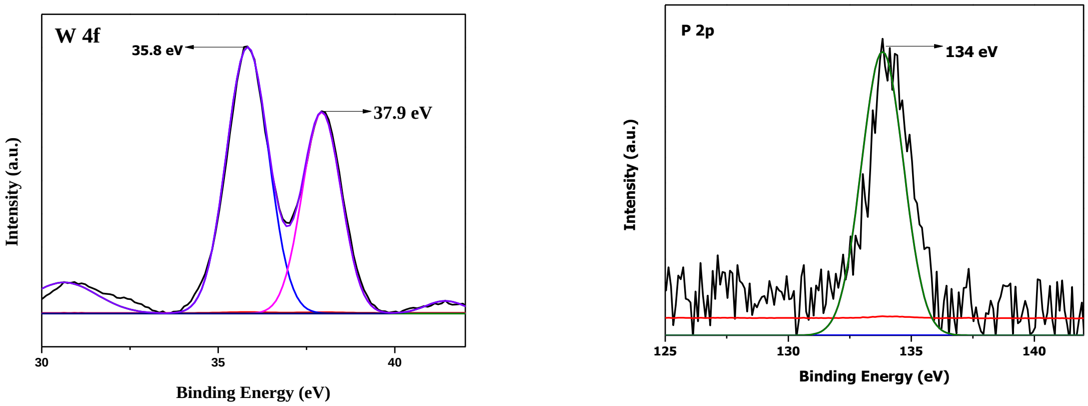

Figure 4.8 High-resolution XPS data of W 4f and P 2p scan of UiO-66-NH$_2$-HPW

Table 4.1 SEM-EDAX analysis of the chemical composition of UiO-66-NH_2 and UiO-66-NH_2-HPW

Catalyst	Chemical composition (Mass%)					
	C	N	O	Zr	W	P
UiO-66-NH_2	62.95	5.39	15.67	15.98	ND	ND
UiO-66-NH_2-HPW	64.80	4.41	14.0	14.60	2.20	ND

ND stands for Not Detected

To check the chemical state of the element, XPS analysis was done and the spectra are shown in Figure 4.7. Figure 4.7 A. is the XPS survey scan of UiO-66-NH_2 and UiO-66-NH_2-HPW which signifies the elements Zr 3d, O 1s, C 1s, N 1s, and Zr 3d, O 1s, C 1s, N 1s, W 4f, P 1s respectively. Table 4.1. displays the elemental composition of UiO-66-NH_2 and UiO-66-NH_2-HPW by XPS and EDS analysis. Three unique peaks can be seen in the N 1s XPS spectra of the samples UiO-66-NH_2 and UiO-66-NH_2-HPW (Figure 4.7 B); the peak at 398.8 eV is attributed to C-N, the peak at 399.3 eV is attributed to -NH_2, and the peak at 400.5 eV is caused by the interaction between the amino group and proton [11,12,30,32]. After post-synthetic modification of UiO-66-NH_2 with HPW to UiO-66-NH_2-HPW, the area under the peak at 400.5 eV attributed to -NH_3^+ grows exponentially. As a result, the strong ionic bond could have formed between -NH_3^+ and phosphotungstic ion (HPW-) [11,12]. Figure 4.7 C represents the O 1s XPS spectra of samples UiO-66-NH_2 and UiO-66-NH_2-HPW. Post synthetically modified sample clearly shows a total of five peaks, three peaks for Zr-O, C-O, and C=O at the binding energy level of 590.9 eV, 531.4 eV, 531.8 eV, and two peaks for W-O-W, P-O-W at the energy level of 330.6 eV and 333.2 eV respectively, while UiO-66-NH_2 shows only three peaks links to Zr-O, C-O, C=O at the binding energy level of 590.9 eV, 531.4 eV, 531.8 eV. [3,33] As shown in Figure 4.7 D, the Zr 3d spectrum can be separated into four peaks [30]. The peaks at 182.3 eV and 184.8 eV are ascribed to Zr-O bonds, and the peaks at 182.8 eV and 185.6 eV are accredited to Zr-Zr bonds. As shown in Figure 5.7. E, the C 1s spectrum can be divided into four peaks; C=C, C-N, C-C, and C=O link to 284.3 eV, 285.2 eV, 285.9 eV, and 288.5 eV, binding energies [30,31]. Figure 4.8 shows high-resolution XP spectra of W 4f and P 2p of the sample UiO-66-NH_2-HPW, the W 4f XP spectra show the two distinctive peaks at the energy level of 35.8 eV and 37.9 eV while P 2p XP spectra show a single peak at 134 eV [3]. According to the literature and our XPS and ATR-FTIR analysis, there is a specific interaction between the basic -NH_2 group and Brønsted acidic HPW, as illustrated in Scheme 4.1.

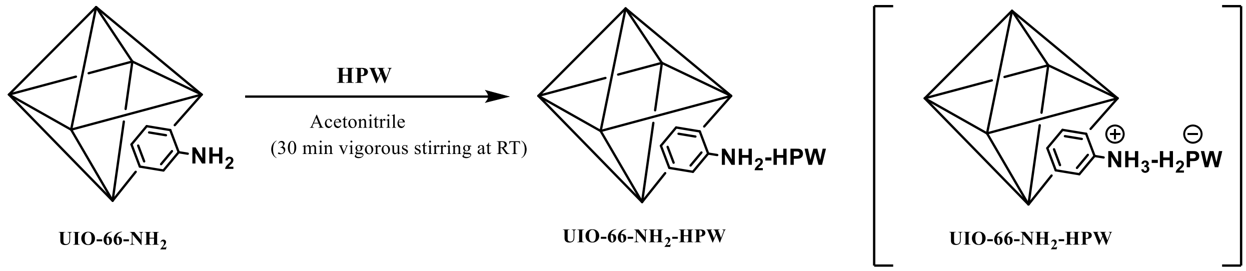

Scheme 4.1 Schematic illustration of post-synthetic formulation of UiO-66-NH_2-HPW from UiO-66-NH_2

4.3.1.5 N_2-Physisorption

Table 4.2 Surface properties and Ammonia TPD acidity of UiO-66-NH_2 and UiO-66-NH_2-HPW

Sample	$S_{(BET)}$ m^2g^{-1}	V_{total} (cm^3g^{-1})	D nm	Total Acidity mmol g^{-1}
UiO-66-NH_2	907	0.543	3.793	0.301
UiO-66-NH_2-HPW	669	0.399	3.385	0.436

The N_2 adsorption-desorption isotherm of UiO-66-NH_2 and UiO-66-NH_2-HPW is provided in Figure 4.9, and listed in Table 4.2 the specific surface area of UiO-66-NH_2 and post synthetically modified UiO-66-NH_2-HPW were 907 m^2g^{-1} and 669 m^2g^{-1} respectively. The total pore volume and pore diameter of UiO-66-NH_2 was 0.543 cm^3g^{-1} and 3.793 nm which is reduced to 0.399 cm^3g^{-1} and 3.385 nm subsequent post-synthetic modification of UiO-66-NH_2 to UiO-66-NH_2-HPW. The decrease in specific surface area, pore diameter total, and pore volume indicated anchoring of HPW to the framework -NH_2 group

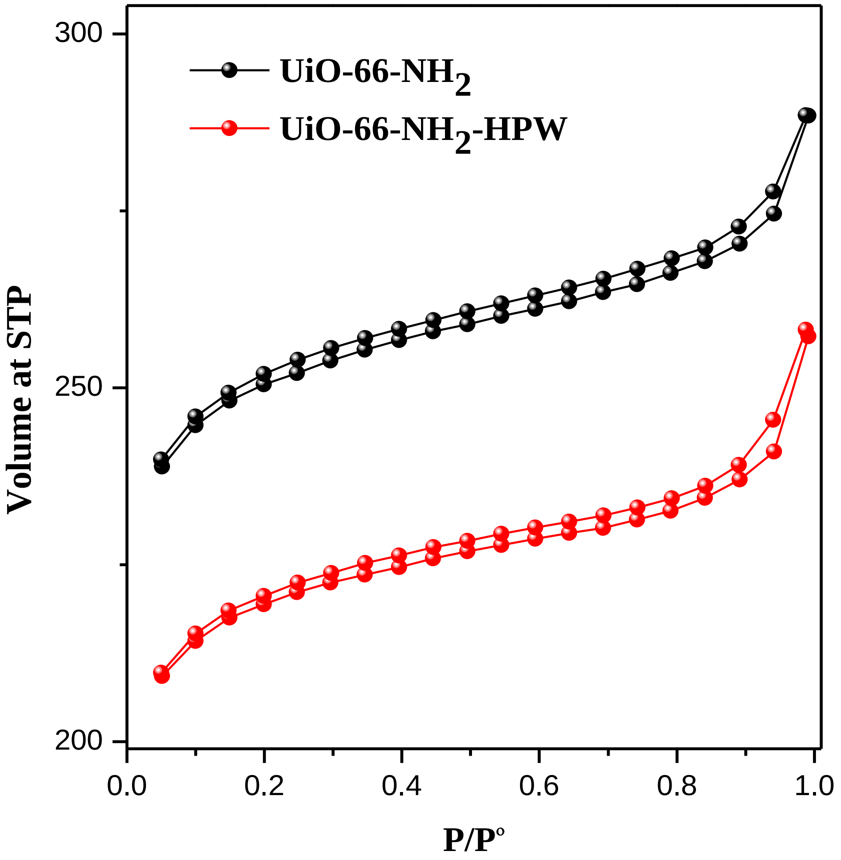

Figure 4.9 Nitrogen adsorption-desorption isotherms of UiO-66-NH_2 and UiO-66-NH_2-HPW

4.3.1.6 *NH_3-TPD*

NH_3-TPD plots of UiO-66-NH_2 and UiO-66-NH_2-HPW are shown in Figure 4.10 (in supporting information) and acid values are given in Table 4.2. Two desorption peaks were identified in the 185-430°C and 446-600°C temperature ranges, which are attributable to weak acid sites and strong acid sites, respectively. It can be seen that the intensity of the strong acid site is higher in post-synthetically modified UiO-66-NH_2-HPW than in parent UiO-66-NH_2, and the total acidity of UiO-66-NH_2-HPW is more (0.436 mmol g^{-1}) than parent UiO-66-NH_2 (0.301 mmol g)

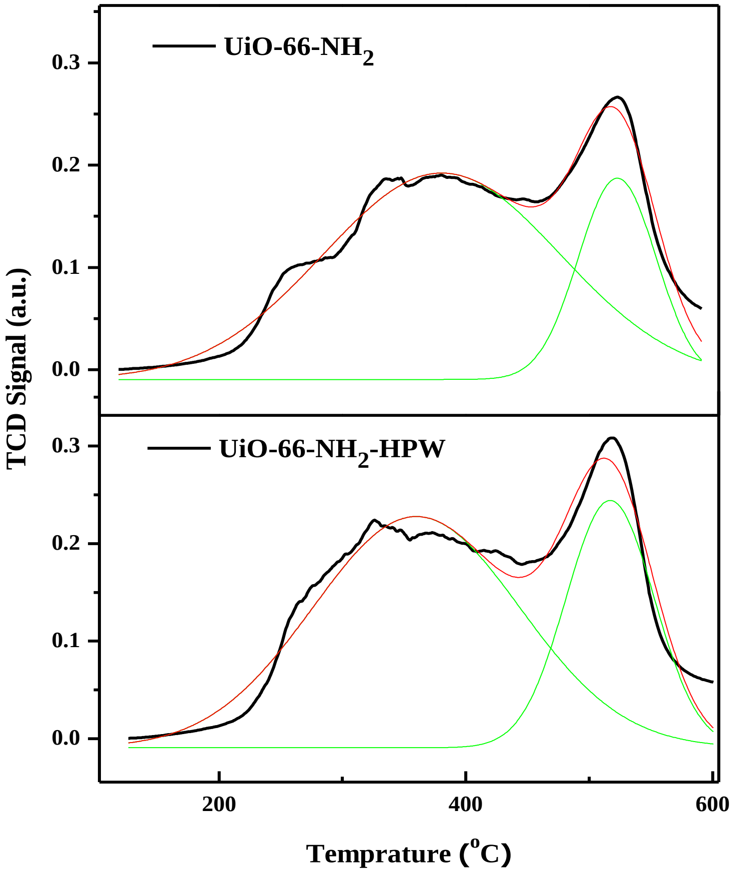

Figure 4.10 Temperature-programmed Ammonia desorption of UiO-66-NH_2 and UiO-66-NH_2-HPW

4.3.2 Catalyst screening

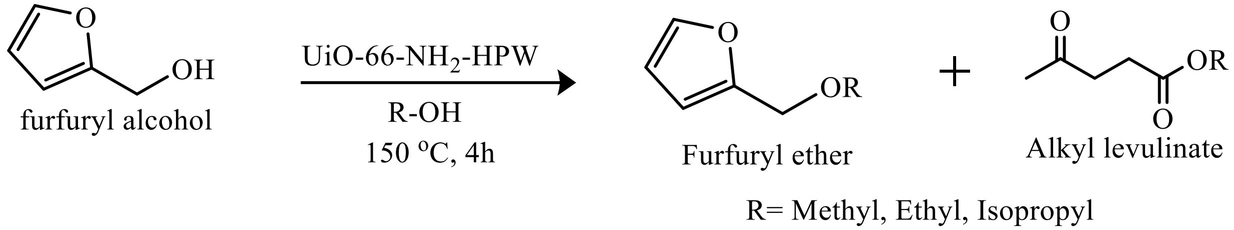

Scheme 4.2 Catalytic conversion of FALc to FE and AL

Table 4.3 Activity comparison of parent and modified Catalyst

Catalyst name	% Conversion	%Yield of EFE	%Yield of EL	% Humins
UiO-66-NH_2	20	8.7	5.4	0
UiO-66-NH_2-HPW	83	34	23	2.5

Reaction conditions: FAlc to Ethanol 1:50 mol ratio, 20 wt. % catalyst wrt FALc, Reaction Time 2 h, stirring speed 300 rpm

Scheme 4.2. reveals, catalytic etherification and alcoholysis of FALc to EFE and EL. EFE and EL formation were confirmed by GC-MS along with these products small fraction of byproducts such as 2,2-methylene difuran, 2-Pentanone-5-5-diethoxy levulinaldehyde, 2,5-(2-Furylmethyl), Ethyl 5-(5-methyl-2-furyl)-2,4-pentadienoate is also identified by GC-MS. Table 4.3 shows the initial catalytic screening of etherification and alcoholysis of FALc to EFE and EL over 20 wt. % catalyst loading wrt FALc weight, at 150℃, for 2 h. UiO-66-NH_2 has shown only 20% catalytic conversion of FALc with 8.7% EFE and 5.4% EL yield, while UiO-66-NH_2-HPW showed high catalytic activity to 83% FALc conversion with 34% and 23 % yield of EFE and EL, respectively. Such drastic catalytic activity enhancement is due to the anchoring of highly acidic HPW and more acidity of UiO-66-NH_2-HPW (0.436 mmol g^{-1}) than the parent UiO-66-NH_2 (0.301

mmol g^{-1}). To investigate whether the catalytic system is heterogeneously or homogeneously catalyzed, a leaching test was performed in which the UiO-66-NH_2-HPW sample was heated at 150°C for 2 h in ethanol after 2 h, then cooled to room temperature and the catalyst was removed by centrifugation and then FALc added and the reaction was continued for 2 h at 150°C. After 2 h of reaction, it has shown 10% conversion without yielding the desired product confirming that the reaction is purely heterogeneous.

4.3.3 Optimization of reaction parameters

In addition to the physical properties of UiO-66-NH_2-HPW, the etherification and alcoholysis conversion of FALc to EFE and EL equally depends on various reaction parameters.

4.3.3.1 Effect of catalyst amount

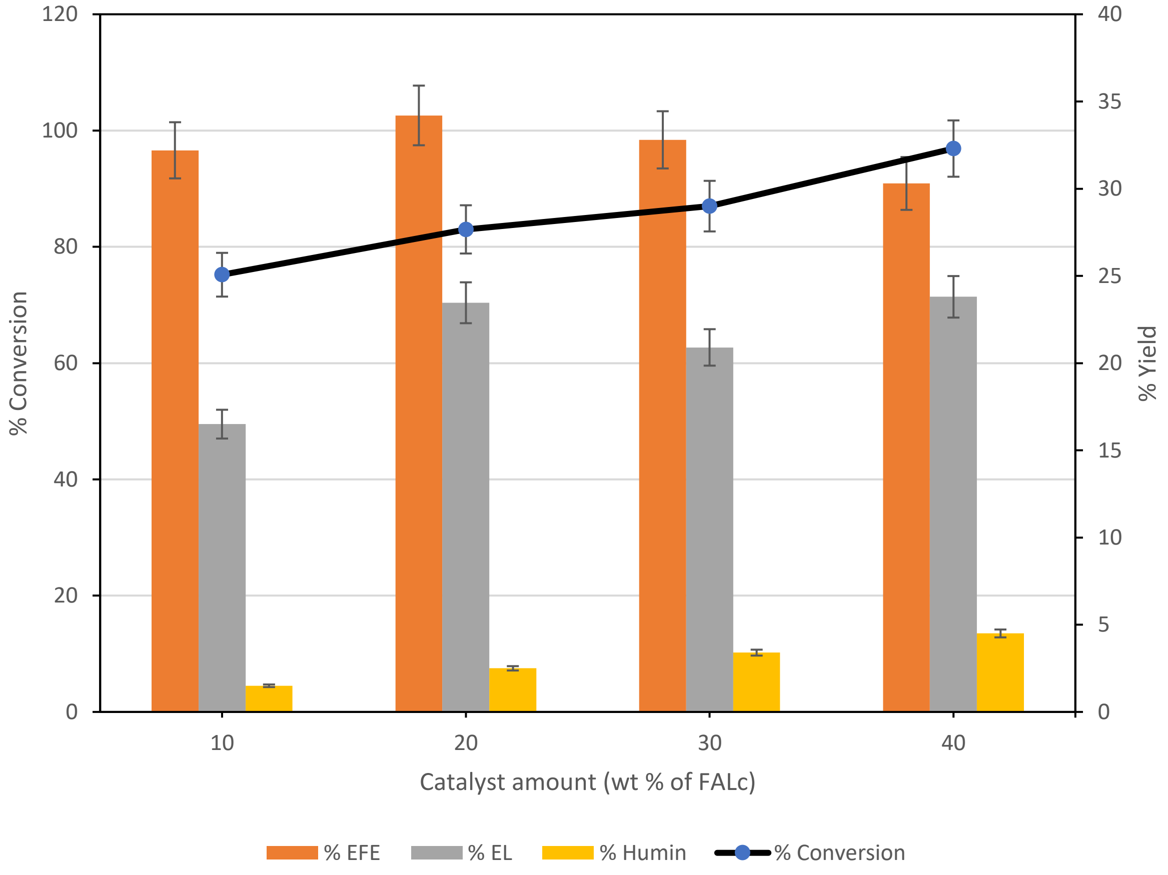

Figure 4.11 Effect of UiO-66-NH_2-HPW amount

Reaction conditions: FAlc to Ethanol 1:50 mol ratio, Reaction temperature 150℃, Reaction Time 2 h, stirring speed 300 rpm

Figure 4.11 displays, the effect of catalyst loading wrt to FALc on the etherification and alcoholysis of FALc to EFE and EL. An increasing catalytic amount from 10 wt.% to 40 wt.% of initial FALc reflects the considerable increase in the conversion of FALc. However, unwanted products such as humins were also observed to be increased. Thus, 20 wt. % catalyst amount was considered optimum loading with low humins (2.5%), 83% FALc conversion, 34% EFE yield, and 24% EL yield.

4.3.3.2 *Effect of Temperature*

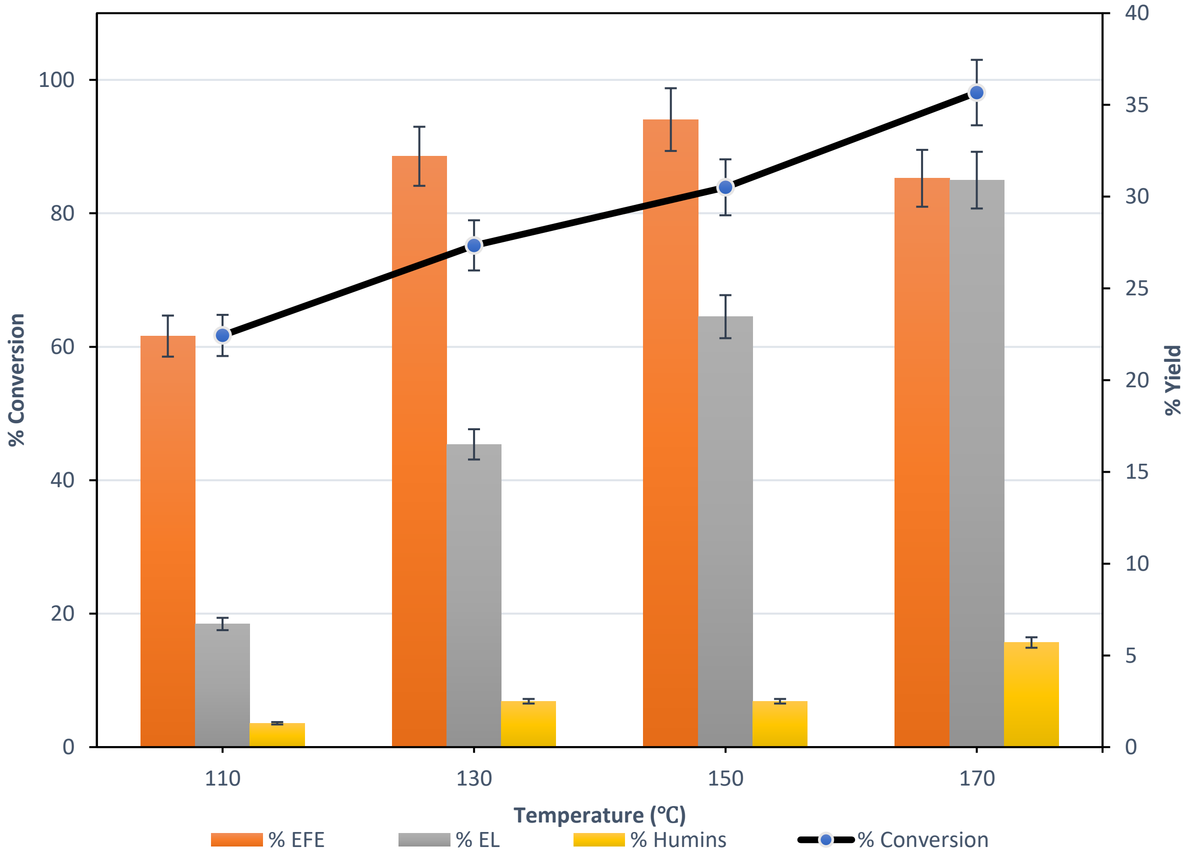

Figure 4.12 Effect of Temperature on the catalytic activity of UiO-66-NH$_2$-HPW

Reaction conditions: FAlc to Ethanol 1:50 mol ratio, 20 wt. % catalyst wrt FALc, Reaction Time 2 h, stirring speed 300 rpm.

Figure 4.12 displays the effect of temperature on etherification and alcoholysis of FALc to EFE and EL over UiO-66-NH_2-HPW. It can be seen that reaction temperature showed an exponential impact on the conversion of FALc and yield of EFE and EL. With an increase in temperature from 110°C to 170°C, there is a positive impact on FAlc conversion from 61% to 98% with a yield of EFE from 22% to 34% and EL from 7% to 30%. At lower temperatures of 110°C and 130°C, there is a significant formation of EFE within the reaction time of 2 h. Lower formation of EL suggests that at lower temperature further transformation of EFE to EL is limited. However, above 130°C, a constant increment in EL yield was observed. It is worth observing that when the temperature increases to 170°C favor the formation of EL but simultaneously there is an increase in unwanted humins (5.7%) also. Thus, 150°C temperature is optimum with 20 wt.% catalyst loading.

4.3.3.3 *Effect of reaction time*

Figure 4.13 denotes the effect of reaction time on etherification and alcoholysis of FALc to EFE and EL over UiO-66-NH_2-HPW. It can be seen that at FAlc conversion increased from 83% (2 h) to 97% (4 h). After 4 h, FAlc conversion is almost constant at 98%. At the initial stage of reaction, there is a substantial formation of EFE than EL. After 4 h, equilibrium formation of EFE (31%) and EL (33%) with humins formation of 3%.

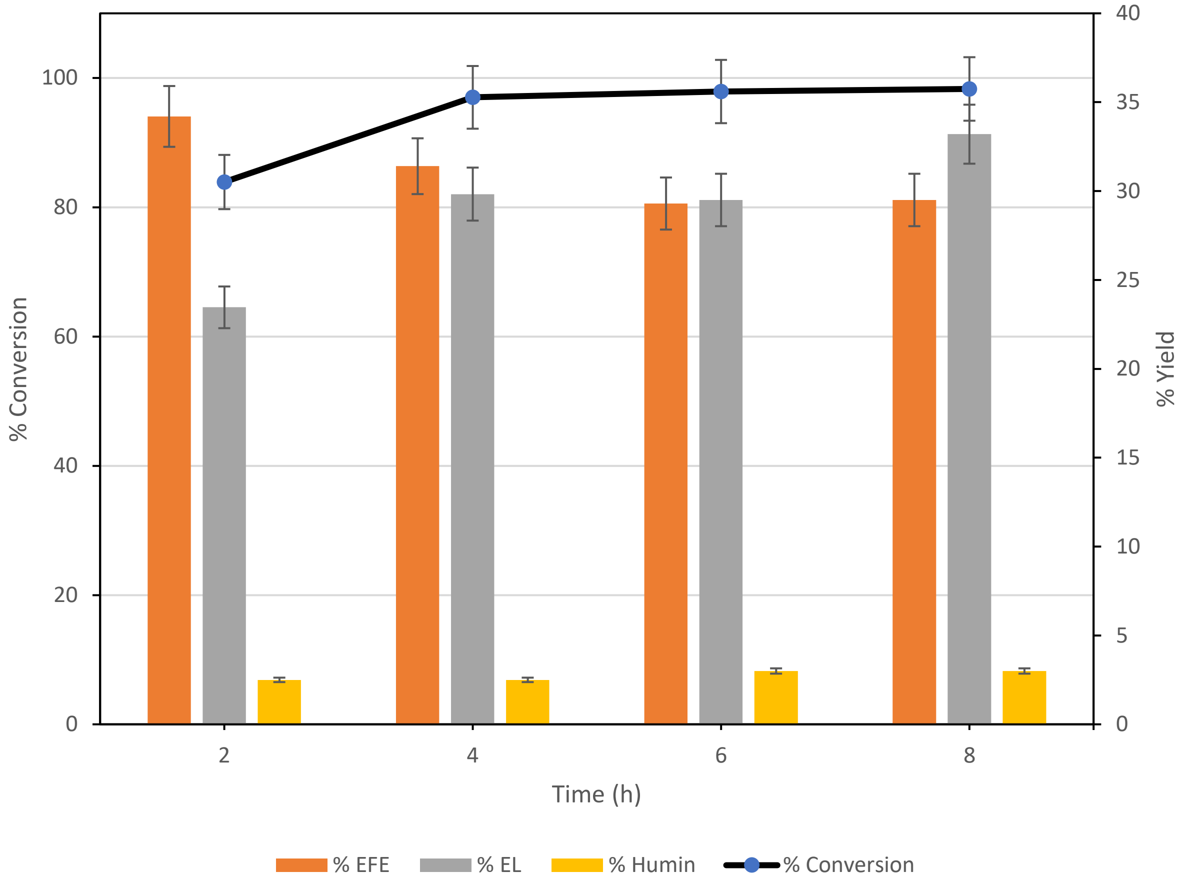

Figure 4.13 Effect of Time on the catalytic activity of UiO-66-NH$_2$-HPW

Reaction conditions: FAlc to Ethanol 1:50 mol ratio, 20 wt. % catalyst wrt FALc, Reaction temperature 150℃, stirring speed 300 rpm

4.3.3.4 Effect of type of alcohol

Alcohols such as methanol, ethanol, and isopropyl alcohol (IPA) were tested under optimal reaction conditions for FALc conversion to FE and AL, and the results are displayed in Figure 4.14. As expected, ethanol and IPA are good solvents for this type of reaction and have shown higher etherification and alcoholysis activity than methanol. With ethanol, there is 97 % FALc conversion with 31% and 29% EFE and EL yield, respectively. Whereas, IPA has shown 80% FAlc conversion with 38 and 17% IPFE and IPL yield respectively with low (2%) humins formation. In the case of methanol only 19% ML formation with high humins of 14% at 76% of FALc conversion, indicates methanol is not a good solvent for this reaction.

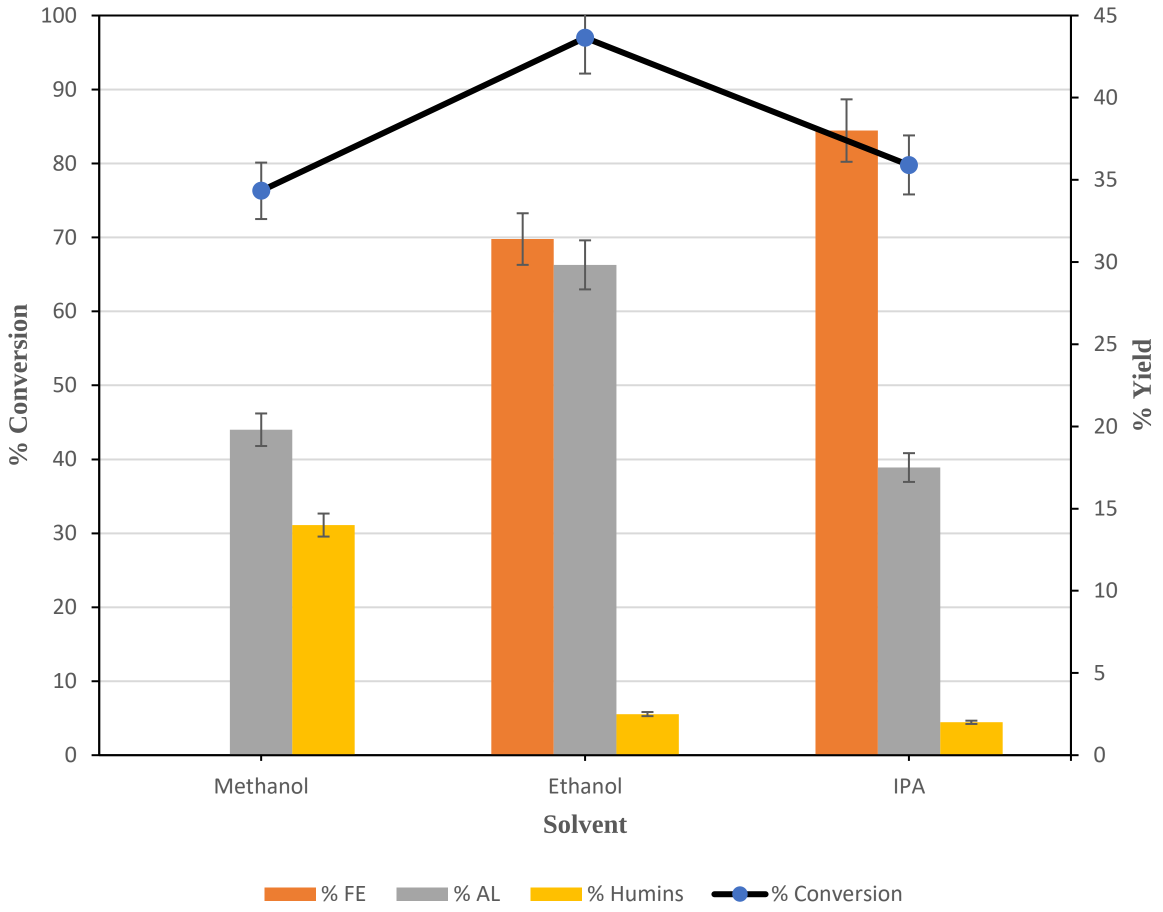

Figure 4.14 Effect of type of alcohol type on etherification and alcoholysis of FALc over UiO-66-NH$_2$-HPW

Reaction conditions: FAlc to alcohol 1:50 mol ratio, 20 wt. % catalyst wrt FALc, Reaction temperature 150℃, Reaction time 4 h, stirring speed 300 rpm.

4.3.3.5 *Catalysts reusability*

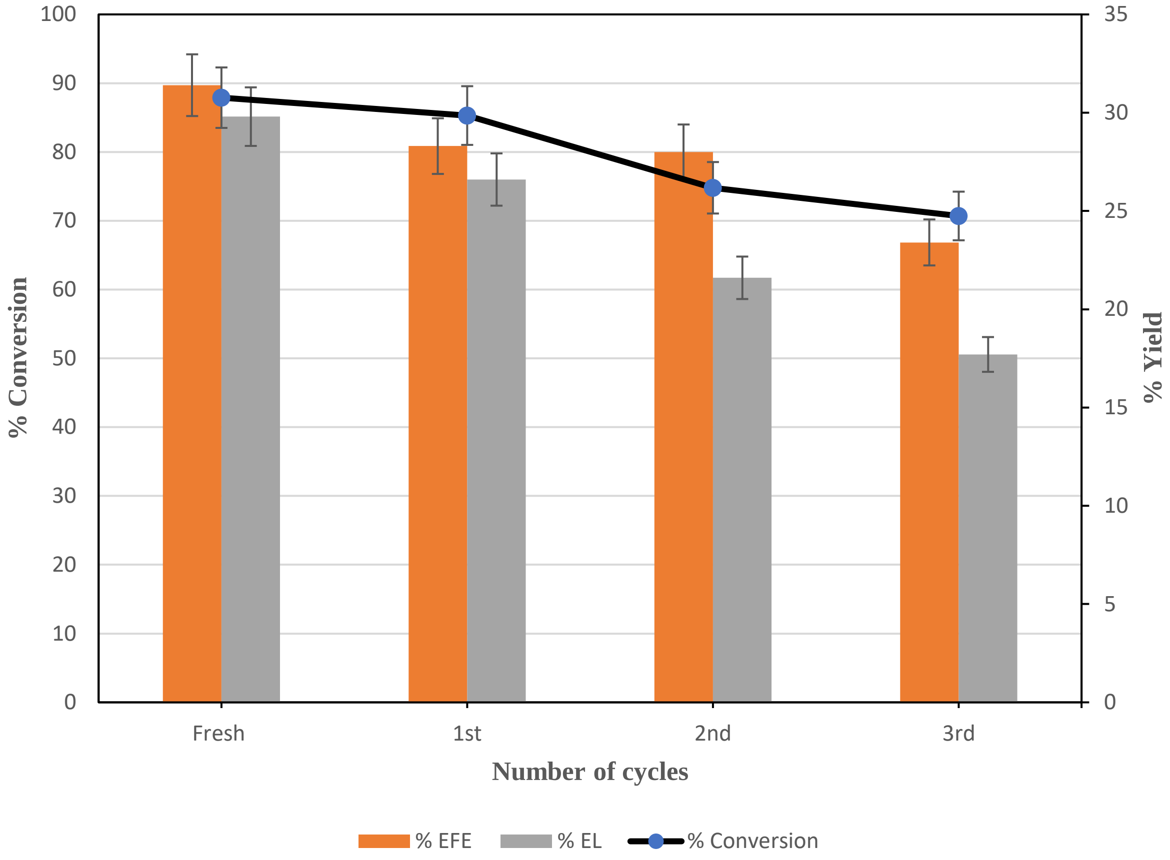

Figure 4.16 Catalyst recycling for FALc conversion over UiO-66-NH$_2$-HPW in Ethanol

Reaction conditions: FAlc to alcohol 1:50 mol ratio, 20 wt. % catalyst wrt FALc, Reaction temperature 150℃, Reaction time 4 h, stirring speed 300 rpm

The reusability of heterogeneous catalysis is its primary advantage. The reusability test was carried out by reacting FALc with Ethanol for 4 hours at 150 °C (Figure 4.16). Following the completion of the reaction, the catalyst was centrifuged out of the reaction mixture, washed with methanol, dried at 80 °C for 2 hours, and reused for the next cycle. As revealed in Figure 10, the use of UiO-66-NH$_2$-HPW is still capable of converting FALc to EFE and EL even after 2nd recycling. Though there is a decrease in FALc conversion (85% to 71%) and yield of EFE (28% to 23%), and EL (26% to 17%). The decrease in catalytic activity is caused by the deposition of insoluble humins on active sites, as confirmed by the ATR-FTIR measurement of the employed catalyst (Figure 4.17).

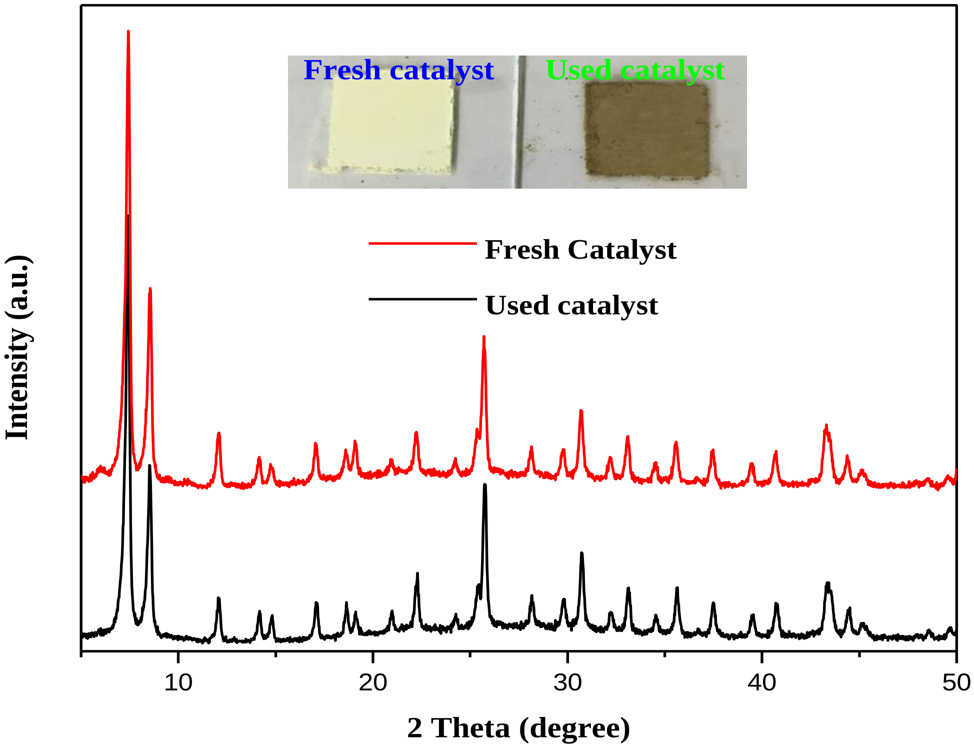

Figure 4.17 Powder XRD of Fresh and used catalyst (UiO-66-NH$_2$-HPW) with an image of fresh and used catalyst in the inset

The comparative ATR-FTIR spectra of the fresh and used catalysts given in Figure 4.18 clearly show that there are emerging new IR bands at 1708 cm^{-1}, 1625 cm^{-1}, 1436 cm^{-1}, 1079 cm$^{-1,}$ and 1018 cm^{-1} along with little suppression in IR transmittance as compared to the fresh sample. The new IR band at 1708 cm-1 corresponds to stretching vibrations of C=O conjugated with C=C, while the band at 1625 cm-1 corresponds to stretching vibrations of C=C conjugated with C=O, and these are the typical bands for humins [34,35]. The band at 1436 can be assigned to CH$_2$ deformation vibration in aliphatic chains while the band at 1018 cm^{-1} in humins resembles C=C stretching, in the olefinic group and the Strong band at 1076 cm^{-1} corresponds to C–O stretching[34,35]. ATR-FTIR study confirmed a deposition of humins on the catalyst's active surface, which is the foremost reason for catalyst deactivation. While powder XRD of the fresh and used samples (Figure 4.17) shows no distinct crystallographic changes in UiO-66-NH_2-HPW after the reaction. However, the used catalyst becomes brown (Image in the inset of Figure 4.17) due to the deposition of humins.

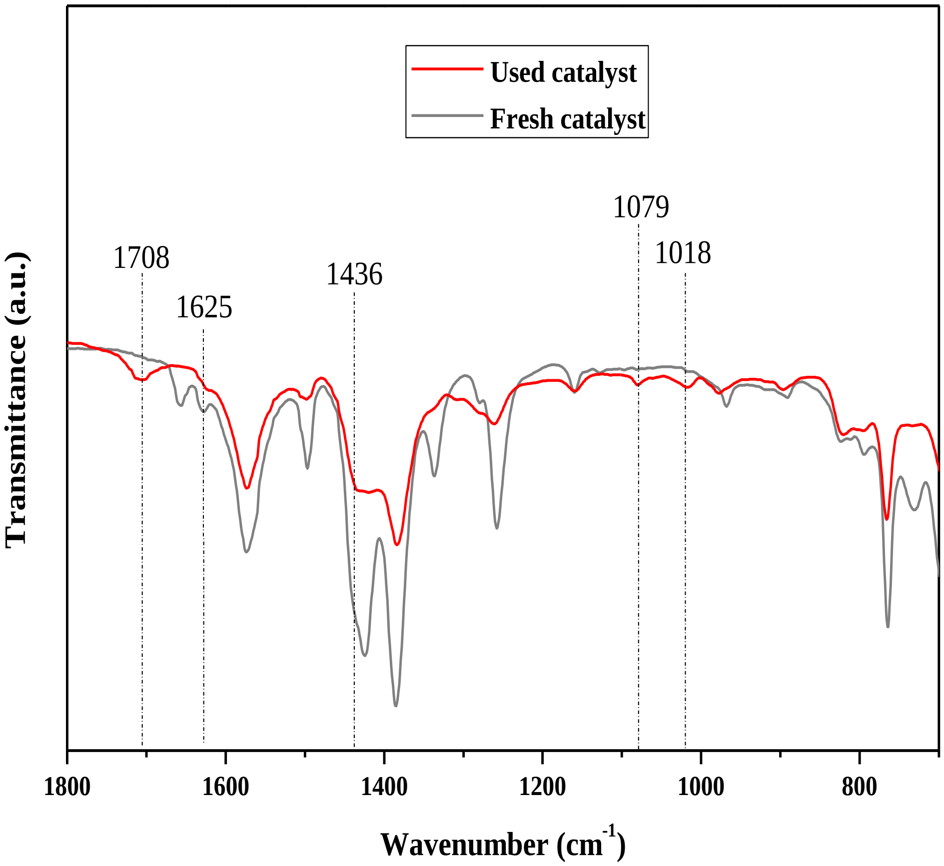

Figure 4.18 ATR-FTIR of Fresh and used catalyst (UiO-66-NH2-HPW)

4.3.4 Catalytic conversion of FFR

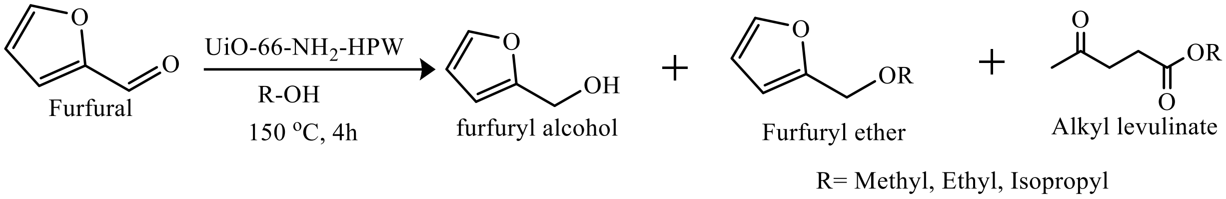

Scheme 4.3 Catalytic conversion of FFR to FALc, FE, AL

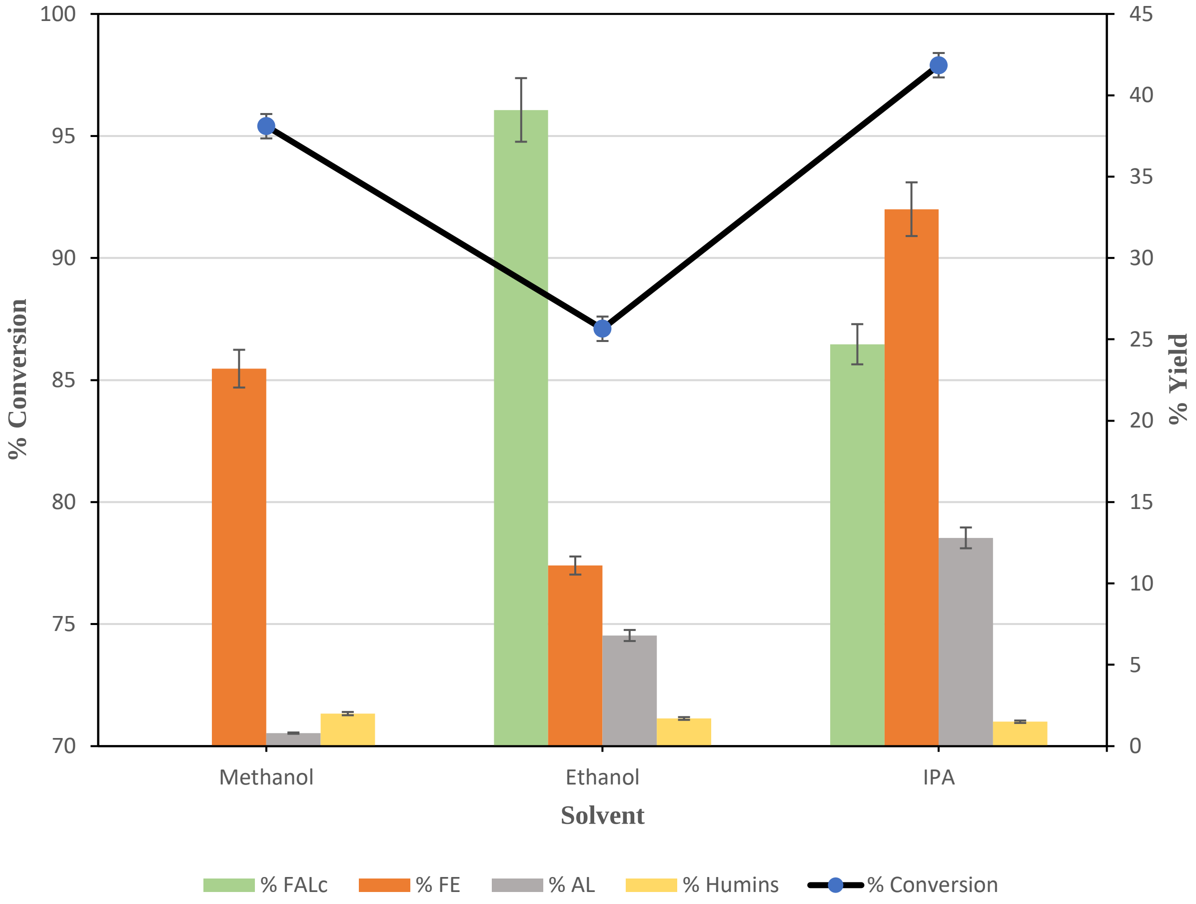

Figure 4.19 Catalytic hydrogenation of FFR over UiO-66-NH$_2$-HPW in the presence of different alcohols as a solvent and hydrogen donor

Reaction conditions: FFR to alcohol 1:50 mol ratio, 20 wt. % catalyst wrt FFR, Reaction temperature 150℃, Reaction time 4 h, stirring speed 300 rpm

UiO-66-NH_2-HPW catalyst was further evaluated for direct conversion of FFR to FALc, EFE, and EL in one step. FFR has been considered one of the most promising platform molecules directly derived from biomass. The hydrogenation of FFR is one of the most versatile reactions for upgrading furanic components to FALc, FE, and AL (Scheme 4.3) in a single step via catalytic transfer hydrogenation, etherification, and alcoholysis. UiO-66-NH_2-HPW was then tested in this one-step reaction with other alcohols such as methanol, ethanol, and IPA. These solvents were also used as hydrogen donors for the hydrogenation of FFR to FAlc along with its consumption for etherification to FE and further to AL. Formed products were identified by GC-MS and data are given in Figure 4.19. Despite 95% FFR conversion in methanol media, it shows only 23% MFE formation while in the case of ethanol, 87% FFR conversion with 39% FAlc, 11% EFE and 7% EL formation was observed. IPA as a well-known hydrogen donor for the catalytic transfer hydrogenation type of reaction has shown 25% FALc, 33% IPFE, and 13% IPL with 98% conversion of FFR. This confirmed that, amongst those studied, IPA is the best hydrogen donor and solvent system for this reaction.

4.4 Comparison of the present catalytic system with the literature

The catalytic activity of present works has been compared with reported literature and summarized in Table 4. Gao et al. directly used inorganic Brønsted acidic H_3PO_4 with Lewis acidic $CrCl_3$ for conversion of FALc with ethanolic media gave 38% EL at 96% conversion[36]. Annatelli et al., used highly acidic commercial sulfated resin Purolite CT151, with 50 wt.% catalyst loading at reflux conditions to get 63% EL yield [37]. Natsir et al. evaluated commercial kaolinite at a high temperature of 180°C with external N_2 pressure (0.8 MPa) and 50 wt.% catalyst loading to achieve 57 % FALc conversion and 62 % EFE selectivity[38]. Zuo et al. used conventional zeolite Silico-Alumino-Phosphate-34 (SAPO-34) with 35 wt. % loading and with 0.5 MPa external argon pressure to convert 43 % FALc with 16 % EFE and 4% EL yield[39]. Li et al. developed an H-ZSM-5 catalyst with Nano b-axis channels (CNB-H-ZSM-5) with Si/Al=75, 30 wt. % catalyst amount in reaction, with 2 MPa N_2 pressure, and a longer reaction time (6 h), achieved 100% FALc conversion at a low EFE yield of 6.1% and EL yield of 60.5% [40]. Siva et al. used TPA (tungstophosphoric acid) impregnated on mesoporous silica SBA-16, sample 25TS (25 % TPA impregnated on SBA-16) with high acidity (2.17 mmol/g) and higher loading in reaction (3.05 substrate to catalyst ratio) converted 100% FALc with 20% EL selectivity[41]. In the present work, the catalyst (UiO-66-NH$_2$-HPW) with moderate acidity (0.436 mmol g^{-1}), low catalyst loading concerning the substrate (20 wt. %), and without any external pressure converted 97 % FALc and achieved 31 % EFE and 29% EL yield, the present catalyst was also able to convert FFR by catalytic transfer hydrogenation to FALc, FE, and AL, in one step. In short, the present catalyst UiO-66-NH$_2$-HPW has high SA, moderate acidity, and well-dispersed HPW active sites on the porous framework of UiO-66-NH$_2$ is collectively responsible for high catalytic activity at a low catalyst amount in reaction.

Table 4. Comparison of the present catalytic system with the literature

9	**Catalyst (wt. % wrt FALc)**	**Catalyst properties**		**Reaction conditions**			**% Conversion**	**% Yield**		**Ref. No.**
		SA (m^2/g)	Acidity (mmol/g)	Temp. (°C)	Time (h)	E.P. MPa		EFE	EL	
1	$CrCl_3 + H_3PO_4$ (3.5 mol%)	NA	np	110	2h	-	96	-	38	[36]
2	Purolite CT151 (50 wt.%)	12-25	np	80^a	5	NA	100	-	63	[37]
3	Kaolinite (50 wt.%)	np	0.431	180	2	0.8 N_2	57	62^b	-	[38]
4	SAPO-34 (35 wt.%)	444	0.399	160	2	0.5 Ar	43	16	4	[39]
5	CNB-H-ZSM-5 Si/Al=75(30 wt.%)	455	0.25	120	6	2 N_2	100	6.1	60.5	[40]
6	25TS (TPA/SBA-16) (300 wt.%)	216	2.17	80	3	-	100	-	20^b	[41]
7	UiO-66-NH$_2$-HPW (20 wt.%)	669	0.436	150	4	-	97	31	29	This work

SA=BET Surface area, E.P.=External pressure, NA=Not applicable, np=not provided, a Reaction under reflux condition, b Selectivity (%)

4.5 Conclusions

In this study, UiO-66-NH_2 MOF was successfully modified at a molecular level by a post-synthetic modification approach and immobilized a superacid HPW by acid-basic interaction of -NH_2 group of UiO-66-NH_2 and HPW to obtain UiO-66-NH_2-HPW as a catalyst. The prepared catalyst has a BET surface area of 669 m^2g^{-1} with a total pore volume and pore diameter of 399 cm^3g^{-1} and 3.385 nm, respectively. SEM, HR-TEM, and powder XRD were performed to analyze the morphology and phase of UiO-66-NH_2-HPW and confirm the intactness of octahedral morphology and similar phase of UiO-66-NH_2 after post-synthetic modification. ATR-FTIR spectroscopy and XPS results confirmed the protonation and interaction between HPW and the -NH_2 group of UiO-66-NH_2 and EDS mapping confirms the good distribution of HPW in the UiO-66-NH_2 crystal. NH_3-TPD results showed that there is a high increment in strong acid sites with an increase in total acidity in a post-synthetical modified sample UiO-66-NH_2-HPW (0.436 mmol g^{-1}) than the parent UiO-66-NH_2 (0.301 mmol g^{-1}). Well-characterized catalysts were evaluated for catalytic etherification and alcoholysis of FALc and found to be better than the parent one. UiO-66-NH_2-HPW catalyst has shown 97 mol% FALc conversions, 31 mol% EFE yield, and 29 mol% EL yield. This catalyst could also be reused after reaction by simple washing and drying for multiple reuses. Further, this acidic catalyst was also evaluated for direct conversion of FFR to FALc, FE, and AL, in one step.

4.6 References

1 Y. Zhou, G. Chen, Z. Long and J. Wang, *RSC Adv*, 2014, 4, 42092–42113.

2 M. A. Hanif, S. Nisar and U. Rashid, *Catal Rev Sci Eng*, 2017, **59**, 165–188.

3 P. A. Jalil, M. Faiz, N. Tabet, N. M. Hamdan and Z. Hussain, *J Catal*, 2003, **217**, 292–297.

4 M. José, D. Silva, A. Aparecida, S. Olavo, R. Chagas, D. Silva and D. Morais, *Fuel*, 2019, **254**, 115607.

5 X. Kong, S. Wu, L. Liu, S. Li and J. Liu, *Mol. Catal.*, 2017, **439**, 180–185.

6 C. Travers, N. Essayem, M. Delage and S. Quelen, *Catal Today*, 2001, **65**, 355–361.

7 H. P. Winoto, Z. A. Fikri, J.-M. Ha, Y.-K. Park, H. Lee, D. J. Suh and J. Jae, *Appl Catal B*, 2019, **241**, 588–597.

8 L. Pesaresi, D. R. Brown, A. F. Lee, J. M. Montero, H. Williams and K. Wilson, *Appl. Catal. A Gen.*, 2009, **360**, 50–58.

9 K. Narasimharao, D. R. Brown, A. F. Lee, A. D. Newman, P. F. Siril, S. J. Tavener and K. Wilson, *J Catal*, 2007, **248**, 226–234.

10 H. Eom, D. Lee, S. Kim, S. Chung, Y. Gul and K. Lee, *Fuel*, 2014, **126**, 263–270.

11 Q. Zeng, S. Guo, Y. Sun, Z. Li and W. Feng, *Nanomaterials*, 2020, **10**, 1–18.

12 M. Hasik, A. Pron, J. Poźniczek, A. Bielański, Z. Piwowarska, K. Kruczala and R. Dziembaj, *J. Chem. Soc., Faraday Trans.*, 1994, **90**, 2099–2106.

13 K. Inumaru, T. Ishihara, Y. Kamiya, T. Okuhara and S. Yamanaka, *Angew. Chem. Int. Ed.*, 2007, **46**, 7625–7628.

14 N. Mizuno, S. Uchida, K. Kamata, R. Ishimoto, S. Nojima, K. Yonehara and Y. Sumida, *Angew. Chem. Int. Ed*, , DOI:10.1002/anie.201005275.

15 L. Leclercq, A. Mouret, A. Proust, V. Schmitt, P. Bauduin, J.-M. Aubry and V. Nardello-Rataj, *Chem. Eur. J.*, 2012, **18**, 14352–14358.

16 A. Dhakshinamoorthy, A. M. Asiri and H. García, *Trends Chem*, 2020, **2**, 454–466.

17 F. G. Cirujano and A. Dhakshinamoorthy, *Adv Sustain Syst*, 2021, **5**, 2100101.

18 R. Fang, A. Dhakshinamoorthy, Y. Li and H. Garcia, *Chem Soc Rev*, 2020, 49, 3638–3687.

19 A. Dhakshinamoorthy, A. Santiago-Portillo, A. M. Asiri and H. Garcia, *ChemCatChem*, 2019, **11**, 899–923.

20 M. J. Katz, Z. J. Brown, Y. J. Colón, P. W. Siu, K. A. Scheidt, R. Q. Snurr, J. T. Hupp and O. K. Farha, *Chem. Commun.*, 2013, **49**, 9449–9451.

21 R. J. Marshall and R. S. Forgan, *Eur J Inorg Chem*, 2016, 2016, 4310–4331.

22 M. Samaniyan, M. Mirzaei, R. Khajavian, H. Eshtiagh-Hosseini and C. Streb, *ACS Catal*, 2019, 9, 10174–10191.

23 V. E. Tarabanko, M. Y. Chernyak, I. L. Simakova, K. L. Kaigorodov, Y. N. Bezborodov and N. F. Orlovskaya, *Russ. J. Appl. Chem.*, 2015, **88**, 1778–1782.

24 J. P. Lange, R. Price, P. M. Ayoub, J. Louis, L. Petrus, L. Clarke and H. Gosselink, *Angew. Chem. Int. Ed.* , 2010, **49**, 4479–4483.

25 A. Démolis, N. Essayem and F. Rataboul, *ACS Sustain Chem Eng*, 2014, **2**, 1338–1352.

26 F. Zaccheria, N. Scotti, N. Ravasio and D. E. E. Dbe, *catalysts*, , DOI:10.3390/catal9020172.

27 US 8,372,164 B2, *United States Patent*, 2013.

28 F. Vermoortele, A. Vimont, C. Serre and D. De Vos, *Chem. Commun.*, 2011, **47**, 1521–1523.

29 M. Kandiah, S. Usseglio, S. Svelle, U. Olsbye, K. P. Lillerud and M. Tilset, *J Mater Chem*, 2010, **20**, 9848–9851.

30 X. Fang, S. Wu, Y. Wu, W. Yang, Y. Li, J. He, P. Hong, M. Nie, C. Xie, Z. Wu, K. Zhang, L. Kong and J. Liu, *Appl Surf Sci*, , DOI:10.1016/j.apsusc.2020.146226.

31 X. Yang, X. Jiang, Y. Huang, Z. Guo and L. Shao, *ACS Appl Mater Interfaces*, 2017, **9**, 5590–5599.

32 Q. Chen, Q. He, M. Lv, Y. Xu, H. Yang, X. Liu and F. Wei, *Appl Surf Sci*, 2015, **327**, 77–85.

33 M. Peñas-Garzón, M. J. Sampaio, Y. L. Wang, J. Bedia, J. J. Rodriguez, C. Belver, C. G. Silva and J. L. Faria, *Sep Purif Technol*, , DOI:10.1016/j.seppur.2022.120467.

34 X. Gao, L. Peng, H. Li and K. Chen, *Bioresources*, 2015, **10**, 6548–6564.

35 J. M. Pin, N. Guigo, A. Mija, L. Vincent, N. Sbirrazzuoli, J. C. Van Der Waal and E. De Jong, *ACS Sustain Chem Eng*, 2014, **2**, 2182–2190.

36 X. Gao, X. Yu, R. Tao and L. Peng, *Bioresources*, 2017, **12**, 7642–7655.

37 M. Annatelli, G. Trapasso, L. Lena and F. Aricò, *Sustain. Chem.*, 2021, **2**, 493–505.

38 T. A. Natsir, T. Hara, N. Ichikuni and S. Shimazu, *ACS Appl Energy Mater*, 2018, **1**, 2460–2463.

39 Y. Ji, Y. Zuo, H. Liu, F. Wang and X. Guo, *ChemSusChem*, 2022, **15**, e202200747.

40 Y. Li, S. Wang, S. Fan, B. Ali, X. Lan and T. Wang, *ACS Sustain Chem Eng*, 2022, **10**, 3808–3816.

41 E. Siva Sankar, K. Saidulu Reddy, Y. Jyothi, B. David Raju and K. S. Rama Rao, *Catal Letters*, 2017, **147**, 2807–2816.

Chapter-5

Summary and Conclusions

Catalysis is critical in offering appropriate solutions to societal challenges. The topics attracting global attention include energy security and environmental pollution. This stimulated the drive to develop long-term energy production plans. The catalytic conversion of biomass to renewable transport fuels and chemicals ensures long-term energy security by reducing the scarcity of fossil fuels. The intricacy of the carbohydrate feedstock, as well as the creation of ecologically friendly procedures, provide significant hurdles in the design of biomass conversion catalysts. To produce crucial chemicals with critical applications, lignocellulose transformation employs some processes such as hydrolysis, dehydration, isomerization, aldol condensation, hydrogenation, and reforming. A solid acid catalyst is frequently preferable to a homogeneous acid catalyst for reducing waste generation and enabling straightforward catalyst separation.

The present thesis has tried to cover the effective conversion of renewable carbohydrate biomass-derived Sugars and Furanics to highly important platform chemicals Alkyl levulinate and Fururyl ethers. Using commercially available, highly soluble, highly acidic, non-corrosive, phosphotungstic acid by a modification to such extent that it gains heterogeneity along with improvement in other properties such as generation of Lewis acid sites, and gain in surface area. The current study is therefore crucial for sustainability and green chemistry.

As a result, in this study, we used ion exchange and immobilization methods to convert easily available HPW into a recoverable and reusable catalyst. Metal salts (Cs, Zr, Mg, and Ce) were used to exchange metal with the mobile proton of HPW, and HPW was immobilized on UiO66-NH_2 MOF by reactive immobilization. X-ray diffraction (XRD), electron microscopy, infrared spectroscopy (IR), and N2 sorption for BET surface area were used to characterize the catalysts. The kind of acid sites was evaluated using Fourier transform infrared spectroscopy with pyridine as a probe molecule (Pyridine-FTIR), and the acidity was investigated using temperature-programmed ammonia desorption (NH3-TPD). The synthesis of AL and furfuryl ether from sugars and furanics (glucose and furfuryl alcohol) produced from biomass was carried out using well-characterized catalysts. The thesis is divided into five chapters based on these findings, one of which contains an overview of the work done for this dissertation.

C**hapter 1** provides an overview of biomass and heteropolyacids. It gives an overview of green chemistry and the potential of biomass-derived carbohydrates for chemical synthesis. The dehydration of sugars and the etherification of furfuryl alcohol to alkyl levulinate and furfuryl ethers, which are key platform chemicals and fuels, are given priority. It emphasizes the importance of these industrially significant organic transformations. It also emphasizes the possibility of developing catalysts employing less corrosive HPA (than mineral acids) and its applicability for carbohydrate-derived feedstock to produce fuels and chemicals.

Chapter 2 described the modification of HPW by zirconium nitrate (ion exchange) exchange with the mobile proton of HPW. Powder XRD and FTIR of Zirconium HPW samples revealed the intactness of the HPW's characteristic kegging structure, while Pyridine IR unveiled the generation of some Lewis acid sites with increased Zr content. On the other hand, NH_3-TPD unfolds a slight increase in total acidity with not much gain in BET surface area. The preliminary evaluation of produced samples ($H_2Zr_1PW_{12}O_{40}$ and $H_1Zr_2PW_{12}O_{40}$) for acid-driven glucose alcoholysis revealed less EL yield (26% and 14%) with 50% to 60% catalyst recovery. As pyridine IR revealed, some Lewis acid sites were generated, but they were insufficient, so we added co-catalysts (Sn-beta, TiO_2, and SnO_2) and it revealed an increase in EL yield. Among all tested catalysts, the physical mixture of $H_2Zr_1PW_{12}O_{40}$ + Sn-Beta (80:20) produced the highest EL (47.6%). This admits that the right combination of B+L and a B/L >2.5 ratio is critical for converting glucose to EL in a single step. It encouraged the screening of various physical mixtures (different weight ratios) of Zr exchaged HPW ($H_2Zr_1PW_{12}O_{40}$ and $H_1Zr_2PW_{12}O_{40}$) with Lewis acid co-catalyst Sn-beta for glucose ethanolysis to EL. After screening and parameter optimization, unveiled that a 3.7 B/L ratio is required for maximum EL (54%) generation with the lower contribution of ELA and humins.

Chapter 3 represents a modification of HPW by Cesium nitrate exchange (ion exchange method) with the mobile proton of HPW and its applications for catalytic etherification of renewable FAl to fuel additive EFE. The powder XRD of Cs exchanged samples revealed the intactness of typical characteristics of the Keggin diffraction pattern but with an increase in Cs content, there was a drop in % crystallinity. The XPS analysis admits that there is a shifting of binding energy levels of W 4f and O 1s levels towards low energy sites due to the presence of electropositive Cs. The acidity analysis by NH_3-TPD gave out that there is a drop in total acidity with an increase in Cs content but Pyridine FTIR disclosed there was the generation of Lewis acid sites with an increase in Cs content. This prepared series of samples are screened for etherification reaction and initial screening showed that the sample ($H_1Cs_2PW_{12}O_{40}$) with moderate acidity (786 µmol g^{-1}) with 3.6 B/L ratio is found to be ideal for this reaction. After optimization of all reaction parameters with the $H_1Cs_2PW_{12}O_{40}$ sample, it has shown a maximum FAlc conversion of 98%; and 65% EFE yield. $H_1Cs_2PW_{12}O_{40}$ catalyst was found to be reusable 4 times (fresh + 3 reuse) after washing and calcination. This study has shown the effective development of catalysts and optimization of process parameters for the selective synthesis of biofuel from renewable furfuryl alcohol.

Chapter 4 demonstrates the immobilization of HPW on UiO-66-NH_2 MOF by acid-basic interaction of the -NH_2 group of UiO-66-NH_2 and HPW to obtain UiO-66-NH_2-HPW as a catalyst. The prepared catalyst has a high BET surface area (669 m^2g^{-1}). SEM, HR-TEM, and powder XRD were performed to analyze the morphology and phase of UiO-66-NH_2-HPW and confirm the intactness of octahedral morphology and matching phase of UiO-66-NH_2 after post-synthetic modification. ATR-FTIR spectroscopy and XPS analysis confirmed the protonation and contact between HPW and the -NH_2 group of UiO-66-NH_2 and EDS mapping confirms the good distribution of HPW in the UiO-66-NH_2 crystal. The acid analysis using NH_3-TPD showed that there is a high increment in strong acid sites with an increase in total acidity after HPW immobilization. Well-characterized catalysts were evaluated for catalytic etherification and alcoholysis of FALc and found to be improved than the parent one. UiO-66-NH_2-HPW catalyst has shown 97 mol% FALc conversions, 31 mol% EFE yield, and 29 mol% EL yield. This catalyst could also be reused after reaction by simple washing and drying for multiple reuses. Further, this acidic catalyst was also evaluated for direct conversion of FFR to FALc, FE, and AL, in one step.

The major purpose of this thesis is to use modified Heteropolyacid as a suitable heterogeneous (recoverable and reusable) catalyst for the conversion of biomass-derived sugars and chemicals to value-added chemicals and fuels. The study found that highly soluble and high Brønsted acidic HPW can be modified to become heterogenous/hydrophobic, as well as gain some beneficial properties such as an increase in surface area and the generation of some active Lewis acid sites, which are suitable for the selective conversion of biomass-derived feedstock to value-added products. As a result, our work advances the science of catalysis for the conversion of biomass into renewable fuels and chemicals.

Suggestions for future research: The current studies aim to use renewable carbohydrate biomass to produce essential platform and bulk chemicals, which can then contribute to the sustainable manufacturing of chemicals. From an industrial and economic standpoint, the process must be efficient, and it should operate in continuous mode. As a result, the obtained catalyst can be further developed and evaluated in continuous operation mode to synthesize AL and FE from biomass-derived furanics and sugars. Switching from batch to continuous mode may help to overcome the side reaction and, to some extent, the generation of humin. Also, catalysts investigated in this thesis have the potential to catalyze other processes, such as the creation of other essential compounds such as lactic acid or alkyl lactates, HMF ethers, and alkyl levulinates diols and triols from carbohydrates.

This research can also be expanded to create MOFs with more basic sites by employing various ligands to improve HPA immobilization and dispersion. This will result in catalysts with characteristics like high acidity and high SA, which may work better as catalysts for tandem reactions involving the transformation of carbohydrates.

ABSTRACT

Name of the Student: Mulik Nagesh Laxman **Registration No.: 10CC19J26003**
Faculty of Study: Chemical Sciences **Year of Submission: 2023**
AcSIR academic centre/CSIR Lab: CSIR -NCL **Name of the Supervisor(s): Dr. V. V. Bokade**

Title of the thesis: Heteropolyacids and its modified version for the transformation of renewable feedstock's to value-added products

The purpose of this thesis was to discuss the efficient conversion of renewable carbohydrate biomass-derived Sugars and Furanics to very important platform chemicals, Alkyl levulinate and Fururyl ethers. Using commercially available highly soluble, very acidic, and non-corrosive phosphotungstic acid. As a result, we used ion exchange and immobilization approach to convert readily available HPW into a recoverable and reusable catalyst.

The zirconium (ion) exchanged sample improves the heterogeneity in the polar medium by 50%, and the combination of a physical mixture of $H_2Zr_1PW_{12}O_{40}$ + Sn-Beta with an 80:20 weight ratio was found to be optimum for the maximum EL yield formation of 54% from glucose at 180℃ in ethanol medium. This study discovered that an ideal combination of B and L catalysts is required, and its ratio has been identified to be critical for the direct transformation of glucose to EL in one step. While Cesium (ion) exchanged HPW samples were used for Furfuryl alcohol etherification, $H_1Cs_2PW_{12}O_{40}$ samples with a total acidity of 786 µmol/g, B/L ratio of 3.6, and surface area of 43 m^2/g were found to be ideal for maximum FAlc conversion (98%) with 65% EFE yield at 120℃, with only 15% catalyst loading w.r.t. FAlc. After solvent washing and calcination, this catalyst was discovered to be reusable four times.

HPW was immobilized at room temperature by protonation of the $-NH_2$ group of UiO-66-NH_2 MOF to UiO-66-NH_2-HPW. ATR-FTIR spectroscopy and XPS results validated the protonation and chemical interaction between HPW and UiO-66-NH_2. STEM-EDS mapping revealed a uniform distribution of HPW on UiO-66-NH_2. The reduction in specific surface area, total pore volume, and increase in total acidity for UiO-66-NH_2-HPW was validated by BET and NH_3-TPD. Furthermore, powder XRD, SEM, and HR-TEM revealed that the phase and shape of UiO-66-NH_2 did not change following HPW immobilization. The developed catalyst was effective in the etherification and alcoholysis of furfuryl alcohol (FALc) to furfuryl ether (FE) and alkyl levulinate (AL). In an ethanolic medium, UiO-66-NH_2-HPW demonstrated 97 mol% FALc conversions, 31 mol% Ethyl furfuryl ether (EFE) yield, and 29 mol% Ethyl levulinate (EL) yield. UiO-66-NH_2-HPW has also been proven efficient in the multistep conversion of Furfural (FFR) to FALc, FE, and AL.

The primary goal of this thesis was to develop a heterogeneous (recoverable and reusable) catalyst for the conversion of biomass-derived sugars and chemicals to value-added chemicals and fuels. The study discovered that highly soluble and high Bronsted acidic HPW can be modified to become heterogeneous/hydrophobic. Modification helped to gain some beneficial properties, such as an increase in surface area alongside the generation of some active Lewis acid sites, which are helpful for the selective conversion of biomass-derived feedstock to value-added products. As a result, our research adds to the catalysis field for converting biomass into renewable fuels and chemicals.

List of publication(s) in SCI Journal(s) (published & accepted) emanating from the thesis work, with complete bibliographic details.

1. **Nagesh L. Mulik**, Prashant S. Niphadkar, Vijay V. Bokade. Synthesis of ethyl furfuryl ether (potential biofuel) by etherification of furfuryl alcohol with ethanol over heterogenized reusable $H_1Cs_2PW_{12}O_{40}$ catalyst. *Research on Chemical Intermediates* 46 (2020) 2309–2325. https://doi.org/10.1007/s11164-020-04093-z

2. **Nagesh L. Mulik**, Vijay V. Bokade. Immobilization of HPW on UiO-66-NH_2 MOF as efficient catalyst for synthesis of Furfuryl Ether and Alkyl Levulinate as biofuel. *Molecular Catalysis* 531 (2022) 112689. https://doi.org/10.1016/j.mcat.2022.112689

List of publication(s) in SCI Journal(s) (published & accepted) other than thesis

1) **Nagesh L. Mulik**, Prashant S. Niphadkar, Vijay V. Bokade. Synergetic Combination of $H_2Zr_1PW_{12}O_{40}$ and Sn Beta as Potential Solid Acid Catalyst for Direct One-Step Transformation of Glucose to Ethyl Levulinate, a Biofuel Additive. *Environ Prog Sustainable Energy*, 38 (2019) 13173. https://doi.org/10.1002/ep.13173

2) Shahabazuddin, M., Banuvalli, B.K., **Mulik, N**. *et al.* Comparative studies of the influence of particle size on various pretreatments of rice husk by assessment of chemical and structural components and wastewater characteristics of liquid fraction. *Biomass Conv. Bioref.* **13**, 5243–5252 (2023). https://doi.org/10.1007/s13399-021-01565-z

Work Presented in Conferences

Science day at NCL 2020 (Poster presentation).

Synthesis of ethyl furfuryl ether (potential biofuel) by etherification of furfuryl alcohol with ethanol over heterogenized reusable $H_1Cs_2PW_{12}O_{40}$ catalyst

Nagesh L. Mulik · Prashant S. Niphadkar · Vijay V. Bokade

Abstract

Ethyl furfuryl ether (EFE) considered as potential biofuel can replace petroleum diesel up to 100%. EFE also has efficient blending properties with biodiesel to improve its cold flow properties. Herein we demonstrate efficient synthesis of EFE by etherification of renewable furfuryl alcohol (FAlc) with ethanol over heterogenized heteropoly acids. Cs exchanged heterogenized heteropoly acids ($H_{3-x}Cs_xPW_{12}O_{40,}$ x= 0.5, 1, 2, 2.5) was prepared using ion exchange method. The $H_{3-x}Cs_xPW_{12}O_{40}$ catalysts were well characterized by the XRD; BET; XPS; NH_3-TPAD and pyridine IR. The etherification of renewable FAlc with ethanol over $H_{3-x}Cs_xPW_{12}O_{40}$; $H_1Cs_2PW_{12}O_{40}$ catalyst having moderate acidity of 786µmol/g; B/L of 3.6 has shown 65% EFE yield and low humin formation with after 98% FAlc conversion and catalyst was observed to be reusable for 4 cycles (fresh + 3 recycles).

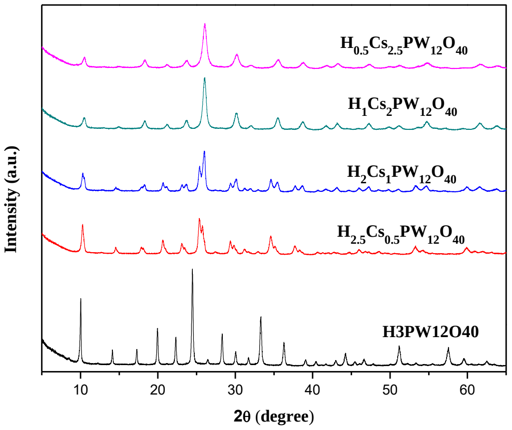

Figure 1: Powder XRD of $H_3PW_{12}O_{40}$ and $Cs_xH_{3-x}PW_{12}O_{40}$ samples

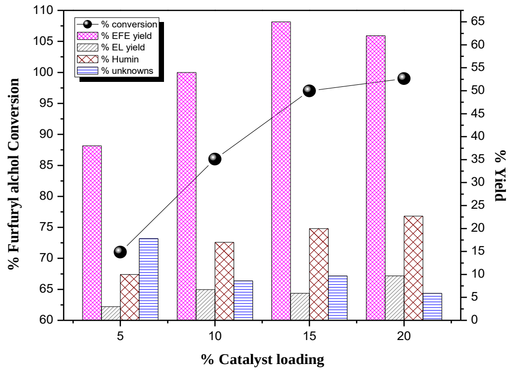

Figure 2: Effect of catalyst loading with respect to FAlc on EFE yield

Reaction conditions: 1:10 FAlc to Ethanol mol ratio, 2.5h Time, 120°C Temp

Reference

1. Mulik, N.L et al., *Res Chem Intermed* (2020). https://doi.org/10.1007/s11164-020-04093-z
2. J. Lange et al., ChemSusChem 2012, 5 (2012) 150–166.

Research on Chemical Intermediates
https://doi.org/10.1007/s11164-020-04093-z

Synthesis of ethyl furfuryl ether (potential biofuel) by etherification of furfuryl alcohol with ethanol over heterogenized reusable $H_1Cs_2PW_{12}O_{40}$ catalyst

Nagesh L. Mulik[1,2] · **Prashant S. Niphadkar**[1] · **Vijay V. Bokade**[1,2]

Received: 9 November 2019 / Accepted: 21 January 2020

Abstract

Ethyl furfuryl ether (EFE) considered as potential biofuel can replace petroleum diesel up to 100%. EFE also has efficient blending properties with biodiesel to improve its cold flow properties. Herein we demonstrate efficient synthesis of EFE by etherification of renewable furfuryl alcohol (FAlc) with ethanol over heterogenized heteropoly acids. Cs-exchanged heterogenized heteropoly acid ($H_{3-x}Cs_xPW_{12}O_{40}$, $x=0.5$, 1, 2, 2.5) was prepared using ion exchange method. The $H_{3-x}Cs_xPW_{12}O_{40}$ catalysts were well characterized by the XRD, BET, XPS, NH_3-TPAD and pyridine IR. The etherification of renewable FAlc with ethanol over $H_{3-x}Cs_xPW_{12}O_{40}$; $H_1Cs_2PW_{12}O_{40}$ catalyst having moderate acidity of 786 µmol/g; and B/L of 3.6 have shown 65% EFE yield and low humin formation with after 98% FAlc conversion and catalyst was observed to be reusable for four cycles (fresh + 3 recycles).

Keywords Heterogenized heteropoly acid · $H_{3-x}Cs_xPW_{12}O_{40}$ · Etherification · B/L ration · Ethyl furfuryl ether · Furfuryl alcohol

Introduction

With decreasing crude-oil reserves and the worldwide increase in demand for fossil fuel, it necessitates opting for alternate renewable options like biomass, solar, water splitting, etc. Among these options, biomass could be most preferred due to its high sustainability. The biomass especially agricultural waste is an abundant

---

Electronic supplementary material The online version of this article (https://doi.org/10.1007/s11164-020-04093-z) contains supplementary material, which is available to authorized users.

✉ Vijay V. Bokade
vv.bokade@ncl.res.in

[1] Catalysis and Inorganic Chemistry Division, CSIR-National Chemical Laboratory, Dr. Homi Bhabha Road, Pashan, Pune 411008, India

[2] Academy of Scientific and Innovative Research (AcSIR), Ghaziabad 201002, India

carbon-based renewable source for the production of biofuels and value-added chemicals. From Indian perspective, biomass based on agricultural waste such as rice husk, wheat straw, rice straw and sugarcane bagasse contributes almost 75% of total biomass availability. Utilization of renewable biomass is also an important contribution toward the establishment of favorable conditions for the climate and a sustainable economy [1]. Biofuels Directive of the European Union (EU) Commission emphasizes on 20% biofuels blending in fossil fuel by 2020 [2]. Thus, research on biobased especially furan catalytic converting technologies is vital in the present and future world scenario. Furfuryl alcohol (FAlc), one of the most important furan derivatives, is industrially produced via hydrogenation of furfural which is the potential platform chemical for its conversion to more useful chemicals [3–6]. Furonic ethers are the interesting class of the compounds to be used as fuel additives or diesel blends due to their efficient fuel properties [7–9]. Moreover, according to the analysis report by Lange et al. [10], among the mainly studied products from furan upgrading, ethyl furfural ether (EFE) shows a very limited footprint in terms of CO_2 emission with high octane number (ON 110). Further, from furfuryl ether, other fuel molecules such as alkyl tetrahydrofuryl ether and ethyl levulinate(EL) can be synthesized [11–14]. Thus, furanic ethers represent an interesting class of potential biofuel to consider for its wide applications.

Furanics (furfural, FAlc and HMF) have poor stability in the presence of acids and represent strong limitations when working under harsh conditions due to their tendency of self-polymerization to humins [15]. There is a very limited study on catalytic etherification of furfuryl alcohol. Few reports reveal that catalysts such as ZSM-5, Zr-SBA-15 and Amberlyst-15 have been used [10, 16, 17]. It looks that acid catalyst especially the combination of Lewis and Brønsted acid catalyst may work for this reaction. The etherification reaction of furfuryl alcohol with ethanol seems to perform on Lewis or Lewis + Brønsted acidic catalyst [16, 17] to form two main biofuel products: ethyl furfuryl ether (EFE) and ethyl levulinate (EL). Among two, ethylfurfuryl ether is more advantageous in terms of its utilization as a blend in petroleum diesel or 100% replacement. If higher Brønsted acidity is present in catalyst, then there is a chance of polymerization of furfuryl alcohol and then to humin. Thus, the proper combination of Lewis and Brønsted property is required to have desired biofuel products. There are limited reports on the selective formation of ethyl furfuryl ether than ethyl levulinate. The present study is an attempt to selectively synthesize ethyl furfuryl ether than ethyl levulinate. Thus, this study was mainly focused on the formation of EFE as the main product over Lewis + Brønsted acidic properties of $Cs_xH_{3-x}PW_{12}O_{40}$ catalyst.

Heteropolyacids (HPAs) are an interesting class of well-defined strong solid Brønsted acids, exhibiting excellent catalytic behavior in a wide variety of acid-catalyzed reactions such as synthesis of biofuels [17–20]. HPA as such has strong Brønsted acidity which may lead to more humin formation as furanic compounds are highly unstable. Moreover, HPAs are soluble in a polar medium like water and alcohol. In order to reduce Brønsted acidity and to make HPA insoluble in the polar medium is possible by exchanging H^+ proton of HPAs with other monovalent ions such as NH^{4+}, Cs^+, K^+ and Rb^+. [21–25]. Among various monovalent ions, Cs^+ seems to be more preferred due to its mirror replacement with H^+ which lowers

Brønsted acid site, leads formation of new Lewis acid sites, increases surface area, develops mesoporosity and also helps to make HPA completely insoluble in a polar medium [21–25].

Thus, in the present work, attempts were made to synthesize Cs-modified HPA catalyst; its characterization by various techniques such as X-ray diffraction (XRD), X-ray photoelectron spectroscopy (XPS), nitrogen adsorption, ammonia–temperature programmed desorption (TPD) and FTIR (Fourier transform infrared spectroscopy). The prepared and well-characterized catalyst was evaluated in furanic reaction especially etherification of furfuryl alcohol to ethyl furfuryl ether, a potential biofuel.

Experimental

Material

Keggin-type 12-tungstophosphoric acid (AR) and cesium nitrate (LR) was purchased from Thomas Baker, Mumbai (India), and analytical standard's EFE, EL and FAlc were purchased from Sigma-Aldrich, Ethanol from Changshu Hongsheng Fine chemical China.

Catalyst preparation

Synthesis of $Cs_xH_{3-x}PW_{12}O_{40}$

The procedure for the synthesis of $Cs_xH_{3-x}PW_{12}O_{40}$ ($x = 0.5,1,2,2.5$) is similar to be reported [22]. Metal-exchanged 12-tungstophosphoric acid was prepared by adding the required molar quantity of an aqueous solution of $CsNO_3$ to the aqueous solution of tungstophosphoric acid under vigorous stirring for 30 min at room temperature. The total added volume of metal nitrate solution was determined from the elemental stoichiometry of the targeted catalyst. The resultant milky suspension was aged at room temperature for overnight (12 h). The white powder was isolated by slow evaporation of water in an oil bath at 100 °C. The samples were further dried in an oven at 120 °C for 12 h and calcined at 350 °C for 3 h. For the comparison purpose, Ce and Mg exchange samples of $H_1Ce_2PW_{12}O_{40}$ and $H_1Mg_2PW_{12}O_{40}$ were prepared using similar method.

Characterization

X-ray diffraction (XRD) patterns of the catalysts powder were recorded on PANalytical system (model Xpert-PRO-1712) with monochromated Cu Kα radiation ($\lambda = 0.154$) in the 2θ range of 5°–90°. Bulk chemical compositions were determined using an X-ray photoelectron spectroscopy (XPS). XPS measurements were performed on a Thermo Scientific K-Alpha + instrument equipped with a charge neutralizer and a monochromated Al K_α X-ray source.

A conventional volumetric nitrogen adsorption apparatus (Micromeritics ASAP 2010 system) was used for evaluating the textural properties of samples. The specific surface area of the sample was calculated using the Brunauer–Emmett–Teller (BET) method.

The overall acidity and acid strength associated with sites were measured by temperature programmed ammonia desorption (TPAD) using a MicromeriticsAutoChem (2910, USA) equipped with a thermal conductivity detector. Prior to the measurements, the sample was dehydrated at 300 °C in He (30 cm^3 min^{-1}) for 1 h. The temperature was then decreased to 100 °C, and then NH_3 was allowed to adsorb by exposing the sample to a gas stream containing 10% NH_3 in He for 1 h. It was then flushed with He for another 1 h. The NH_3 desorption was carried out in He flow (30 cm^3 min^{-1}) by increasing the temperature up to 800 °C with a heating rate of 10 °C min^{-1}. The concentration of desorbed ammonia was quantified by a thermal conductivity detector (TCD).

FTIR and pyridine IR spectrum was recorded on Thermo-Nicolet 670 spectrometer in the range of 400–4000 cm^{-1}. To predict secondary structure variation, circular dichroism spectrum was monitored. To record spectra, JASCO J810 spectrometer equipped with peltier water circulation thermostated six positions automatic cell changer and variable slit system was used. To check heterogeneity of the catalyst, the reaction mixture after the reaction ICP-OES is done using the Perkin-Elmer Optima 3000DV inductive-coupled plasma-optical emission spectroscopy (ICP-OES).

Reaction procedure and product analysis

The experiments were carried out in SS316 closed reactor of 30 mL capacity with pressure gauge. In a typical reaction, 0.42 g furfuryl alcohol (FAlc), 5 wt% catalyst w.r.t. FAlc (0.021 g) and 11.51 g ethanol were added into the reactor. Then, the reactor was electrically heated in the temperature range of 90–130 °C on the heating plate (Remi) with continuous stirring of 800 rpm for 2.5 h. At the end of the reaction, the reactor was cooled down to room temperature by quenching to stop the reaction. Catalyst along with insoluble humin was separated by centrifugation. The product liquid sample was further diluted and analyzed by GC gas chromatography (Chemito-1000) equipped with TR-5 capillary column (60.0 m×0.32 mm× 0.25 µm) and a flame ionization detector with He as carrier gas flow rate of 1.0 mL min^{-1}, the injection port temperature was 230 °C, the oven temperature was programmed from 50 to 260 °C at a heating rate of 20 °C min^{-1}, and the detector temperature was 260 °C. The product formation was confirmed by the standard in GC and GC–MS (Figure S1).

The FA conversion and yield were calculated by using the following equations.

$$\%\ \text{Conversion} = \frac{\text{Initial FA mols} - \text{Final FAlc mols}}{\text{Initial FAlc mols}} \times 100$$

$$\%\ \text{Yield} = \frac{\text{Mols of product formed}}{\text{Initial FAlc mols}} \times 100$$

Table 1 Surface properties of $H_3PW_{12}O_{40}$ and $Cs_xH_{3-x}PW_{12}O_{40}$ samples

Entry	Catalyst name	% crystallinity (relative)	The crystallite size (nm)	BET surface area m^2/g	Mesopore surface area (m^2/g)
1	$H_3PW_{12}O_{40}$	100	40	4	–
2	$H_{2.5}Cs_{0.5}PW_{12}O_{40}$	93	13	4.2	0.06
3	$H_2Cs_1PW_{12}O_{40}$	83	21	9.1	3.1
4	$H_1Cs_2PW_{12}O_{40}$	69	17	36.4	10
5	$H_{0.5}Cs_{2.5}PW_{12}O_{40}$	66	14	43.2	16

Table 2 Investigation of acidic properties by NH_3 temperature programmed desorption and B/L ratio (pyridine-FTIR) of $H_3PW_{12}O_{40}$ and $Cs_xH_{3-x}PW_{12}O_{40}$ samples

Entry	Catalyst name	Weak acidity (μmol/g)	Strong acidity (μmol/g)	S/W ratio	Total acidity (μmol/g)	B/L ratio
1	$H_3PW_{12}O_{40}$	994.1	1541.8	1.5	2536	na
2	$H_{2.5}Cs_{0.5}PW_{12}O_{40}$	595.3	1356.6	2.2	1952	5.8
3	$H_2Cs_1PW_{12}O_{40}$	478.7	881.2	1.8	1360	4.3
4	H_1Cs_2 $PW_{12}O_{40}$	277.4	585	2.1	786	3.6
5	$H_{0.5}Cs_{2.5}PW_{12}O_{40}$	152.5	211.4	1.3	364	1.7

$$\text{Mass of humin} = \text{Residue collected(dried)} - \text{weight of Catalyst}$$

$$\%\ \text{Humin} = \frac{\text{Mass of humin obtained}}{\text{Initial mass of FAlc}} \times 100$$

Result and discussion

Catalyst characterization

All prepared catalysts were characterized by various characterization techniques such as XRD, nitrogen adsorption and TPD, and results are presented as Tables 1 and 2.

Powder XRD

The structural changes as a function of Cs, Ce and Mg exchange with H^+ in $H_3PW_{12}O_{40}$ were carried out by XRD (Fig. 1 and S2). All Cs-exchanged samples have shown typical cubic crystalline XRD pattern of Keggin units. After initial Cs doping in $H_{2.5}Cs_{0.5}PW_{12}O_{40}$, new set of peaks at two thetas of 25.6° evolve as shoulders on the main 25° of $H_3PW_{12}O_{40}$ reflections. Diffraction peaks corresponding

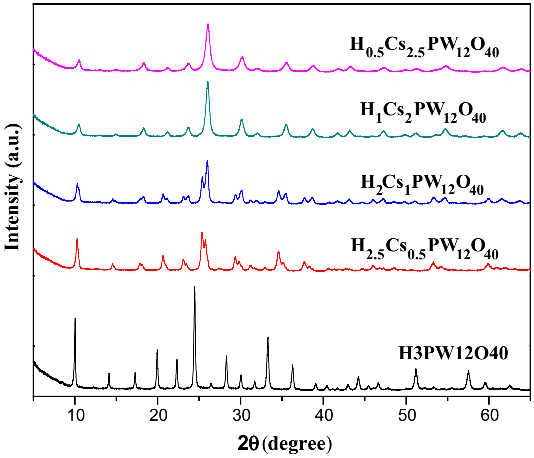

Fig. 1 Powder XRD of $H_3PW_{12}O_{40}$ and $Cs_xH_{3-x}PW_{12}O_{40}$ samples

to the free acid disappear as the Cs content increases beyond $x = 2$. The shift in $H_3PW_{12}O_{40}$ peaks toward higher angles (shift by 1.4°) in the $Cs_xH_{3-x}PW_{12}O_{40}$ samples is consistent with the body-centered cubic structure of $Cs_3PW_{12}O_{40}$ salts [21]. The effect of Cs exchange was studied by calculating its crystallite size (D nm) with Scherrer's equations (Table 1). The crystallinity was observed to be decreased from 100% (plane HPA) to 66% due to insertion of Cs^+ up to 2.5 in HPA Keggin framework. The corresponding crystallite size was also found dropped down to 14 nm from 40 nm. This is likely because of bond stretching due to insertion of Cs in the Keggin framework, which weakens the structure and so the crystallinity and crystallite size. In case of magnesium ($H_1Mg_2PW_{12}O_{40}$), insertion in $H_3PW_{12}O_{40}$ leads to a partial loss of Keggin structure along with the formation of WO species, its reflections can be seen in XRD (S2), whereas cerium ($H_1Ce_2PW_{12}O_{40}$) insertion in $H_3PW_{12}O_{40}$ leads to complete collapse of Keggin structure.

The BET surface area (Table 1) pointed that as Cs insertion in $H_3PW_{12}O_{40}$ increases from 0 to 2.5, the corresponding surface area found to be increased from 4 to 43.2 m^2/g and mesopore surface area has elevated to 16 m^2/g. According to the literature, Cs insertion in HPA generates micro-crystallites which lead to void formation [23, 24]. As insertion of Cs increases, the void formation and bond stretching increase which creates more surface area and mesoporosity.

XPS

The high-resolution W 4f XP and O 1s XP spectra (Fig. 2) reveals the W and O environments are perturbed upon Cs exchange. Figure 1a shows XP spectra of $W4f_{7/2}$ of pure $H_3PW_{12}O_{40}$ occurs at 35.7 eV with a peak width of 2.8 eV. Following Cs inclusion of 0.5 to 2.5, this peak with the centroid shifts to lower binding energy from 35.7 to 35.6 eV and it confirmed that new binding of W is generated with the insertion of Cs. This shift is more at Cs2.5 than at Cs0.5, confirming stretching of W bonding. Similar trend was also observed for O 1s (Fig. 2b) with the binding energy of the O 1s envelope decreasing from 530.8 to

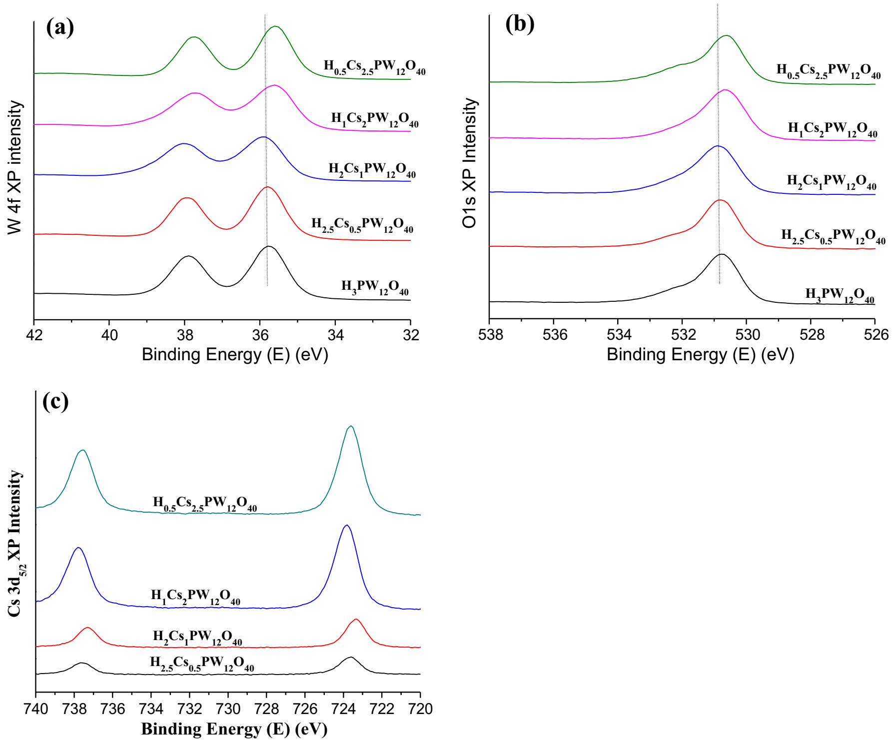

Fig. 2 XP spectra of $H_3PW_{12}O_{40}$ and $Cs_xH_{3-x}PW_{12}O_{40}$ samples as a function of Cs content (**a**) W4f XP spectra of $H_3PW_{12}O_{40}$ and $Cs_xH_{3-x}PW_{12}O_{40}$ samples (**b**) O 1s XP spectra of $H_3PW_{12}O_{40}$ and $Cs_xH_{3-x}PW_{12}O_{40}$ samples (**c**) Cs $3d_{5/2}$ XP spectra of $Cs_xH_{3-x}PW_{12}O_{40}$ sample

530.5 eV with increasing Cs doping from 0 to 2.5 in $H_3PW_{12}O_{40}$. It can be postulated that the greater electropositive character of cesium increased the electron density of both O and W, by lowering their binding energies. Figure 2c shows the XP spectra of Cs $3d_{5/2}$ on prior to Cs exchange leads to increase in intensity along with the area under the peak. As with 0.5 Cs doping, the first binding energy peak at 724.1 eV with peak width of 1.18 eV and second binding energy peak at 738.1 with peak width of 1.16 eV are found to be increased with the increase in Cs doping: 1.26 (Cs1), 1.28 (Cs2), 1.29 eV (Cs2.5) for first binding energy and 1.18 (Cs1), 1.41(Cs2), 1.42 eV (Cs2.5) for second binding energy. It indicates that the increase in Cs doping leads to saturation of Cs on the surface.

Table 2 represents the acidic properties of all studied catalysts investigated by NH_3-TPD and pyridine-FTIR. TPD profiles of Mg- , Ce- and Cs-exchanged tungstophosphoric acid catalysts are provided in the supplementary information (Figure S3.) All samples showed distinctive desorption in two temperature ranges: 150–250 °C and 600–700 °C. The intensity of the high-temperature desorption peak was decreased as cesium content increased. The high-temperature desorption peak is related to the strong acid sites generated from partial exchange of Cs.

As a function of Cs insertion, both strong and weak acid sites were found to be dropped. In case of Cs insertion of 0.5, 1, 2 and 2.5 mol in exchange with H^+ proton, the strong acidity was observed to be reduced to 12, 42, 62 and 82%, respectively, whereas weak acidity was decreased by 40, 51, 72 and 84%, respectively. These results are obvious, due to less availability of H^+ protons for acidity.

Pyridine-FTIR

Type of acidity is also an important factor to consider for any organic transformation, and there are many intermediate steps which required both Brønsted and Lewis acid sites. The prepared catalysts were further characterized for the type of acidity (Fig. 3), which was generated or changed after insertion of Cs in HPA. The peaks at 1438 cm^{-1} and 1537 cm^{-1} represent the pyridine interaction with Lewis and Brønsted acidic sites. The peak at 1487 cm^{-1} is combination effect of Brønsted + Lewis acidity. As Cs insertion in HPA increases, Lewis acidity was found to be increased, which downgrades B/L ratio (Table 2).

Etherification of furfuryl alcohol with ethanol to ethyl furfuryl ether

Catalytic transformation of furanic compounds to value-added product is an important reaction to investigate aiming for new potential catalyst with an improved yield of the desired product. In this work, the prepared and well-characterized Cs-inserted $Cs_xH_{3-x}PW_{12}O_{40}$ catalyst having Brønsted and Lewis acidity was evaluated for one-step etherification of furfuryl alcohol to ethyl furfuryl ether as a biofuel additive (Scheme 1).

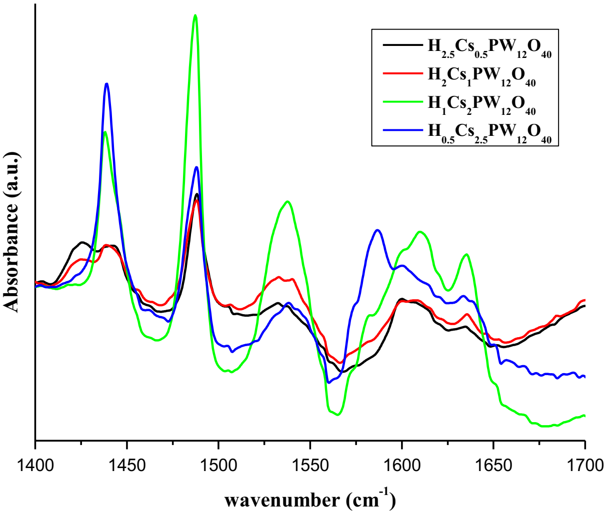

Fig. 3 Pyridine IR spectra of $H_3PW_{12}O_{40}$ and $Cs_xH_{3-x}PW_{12}O_{40}$ samples

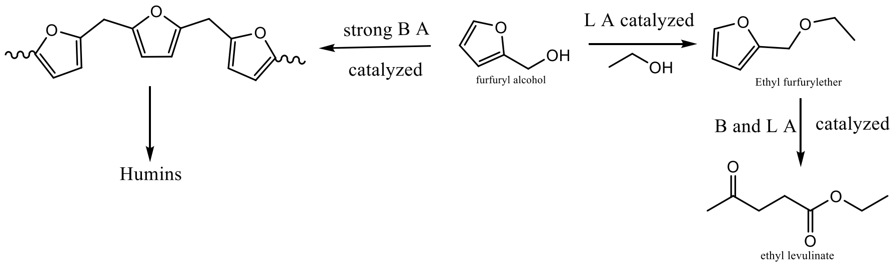

Scheme 1 Etherification of furfuryl alcohol to ethyl furfuryl ether

Catalyst screening

Being highly Brønsted acidity of $H_3PW_{12}O_{40}$ tends to have almost 98% conversion of FAlc. The activity trends follows: $H_3PW_{12}O_{40} = H_1Ce_2PW_{12}O_{40} > H_1Mg_2PW_{12}O_{40}$ (90%) > $H_1Cs_2PW_{12}O_{40}$ (58%) which is in replica of acidity values (Fig. 4). EFE formation was observed to be maximum (43%) with $H_1Mg_2PW_{12}O_{40}$ as compared to $H_1Ce_2PW_{12}O_{40}$ (35%); $H_1Cs_2PW_{12}O_{40}$ (32%) and TPA (28%). EL formation is in the range of 10–15% which is forming at the expense of EFE consumption. Lowest formation of EL (3%) is recorded for $H_1Cs_2PW_{12}O_{40}$. The humin formation of 25–30% was found with highly acidic catalysts viz, $H_3PW_{12}O_{40}$ and $H_1Ce_2PW_{12}O_{40}$, whereas in the case of $H_1Mg_2PW_{12}O_{40}$ and $H_1Cs_2PW_{12}O_{40}$ it is < 10%. The unknown product due to side reactions of furfuryl alcohol was found to be maximum of 25–30% with the catalysts having considerably high B and L acidity, whereas in case of $H_1Cs_2PW_{12}O_{40}$ which is less acidic than other studied shown unknown formation of 15%. Even though $H_3PW_{12}O_{40}$, $H_1Ce_2PW_{12}O_{40}$ and $H_1Mg_2PW_{12}O_{40}$ are a highly active catalyst for this reaction, these catalysts are almost completely soluble in ethanol (polar medium) whereas $H_1Cs_2PW_{12}O_{40}$ is completely insoluble in nature. According to the report, the introduction of Cs in

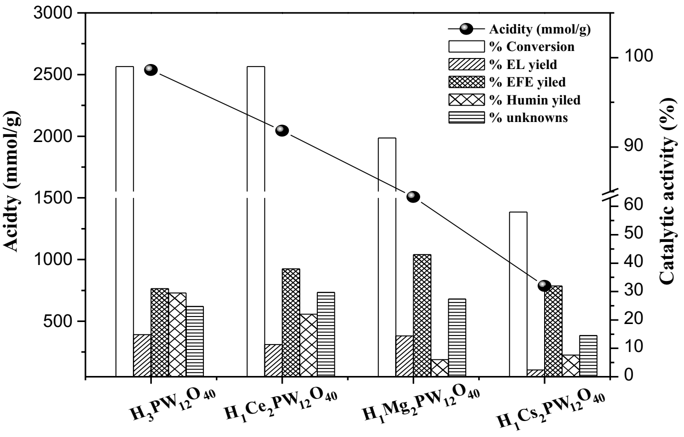

Fig. 4 Catalyst screening as a function of total acidity. Reaction conditions: 1:10 FAlc/ethanol mol. ratio, 110 °C temp, 2.5 h time, 5 wt% w.r.t. FAlc catalyst

HPA knocks out $H_5O_2^+$ moiety and strongly interact with W=O and W–O–W by bridging, terminal attachment leads to widening of structure and sample become insoluble in the polar medium [26].

Considering the fact that catalyst should be more reusable; the process should have a clean and green approach $H_1Cs_2PW_{12}O_{40}$ is the best option to go ahead and optimize the process parameters to improve the activity and EEF yield. Thus, the optimization of process parameters was done on $H_1Cs_2PW_{12}O_{40}$ catalyst.

Influence of Cs insertion in $H_3PW_{12}O_{40}$ on the acidity and catalytic activity

As from the above discussion, it can be concluded that Cs-exchanged sample ($H_1Cs_2PW_{12}O_{40}$) is found to be more useful for this type of reaction. So the various amounts of Cs-inserted samples (from 0.5 to 2.5 mol) in TPA were prepared thoroughly and screened under the same set of reaction conditions, ICP-OCS of reaction mixture after the reaction was done to check heterogeneity of the catalyst, and all Cs-exchanged samples have shown no sign of W from HPA unit and no sign Cs leaching in the reaction mixture. The graphical data of all the Cs-exchanged samples under identical set of reaction conditions are given in Fig. 5. As after 0.5 mol Cs exchange designated as $H_{2.5}Cs_{0.5}PW_{12}O_{40}$, there is 24% loss in total acidity (1952 µmol/g) along with the generation of Lewis acid sites in Fig. 3 with 5.8 B/L ratio, which showed 35% EFE, 14.4% EL yield 26% humins and 24% unknowns at the complete conversion of FAlc. In case of $H_2Cs1PW_{12}O_{40}$, there is 47% loss in total acidity than the parent and generation of more Lewis acids with 4.3 B/L ratio that showed 39% EFE, 13.4% EL, 19.9% humins and 25% unknowns with complete conversion of FAlc. Though there is 24% and 47% drop in total acidity of $H_{2.5}Cs_{0.5}PW_{12}O_{40}$ and $H_2Cs1PW_{12}O_{40}$, sample has high B/L ratio (5.8 and 4.3, respectively) indicating the number of Brønsted acid sites till present there and

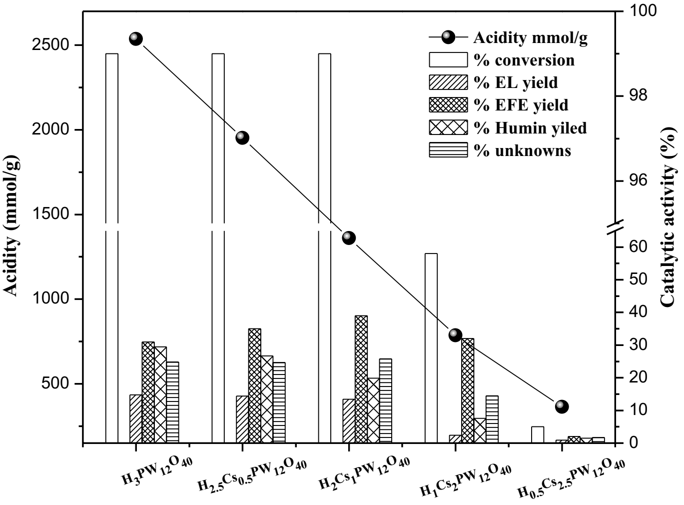

Fig. 5 Effect of Cs insertion on the acidity and catalytic activity. Reaction conditions: 1:10 FAlc/ethanol mol. ratio, 110°C temp, 2.5 h time, 5 wt% w.r.t. FAlc catalyst

responsible for complete conversion of FAlc as like parent ($H_3PW_{12}O_{40}$). Further increase in Cs exchange from 1 to 2 mol leads to 69% drop in total acidity especially in Brønsted acidity leading to B/L ratio of 3.6, which showed 58% FAlc conversion 32% EFE, 2.4% EL, 14.5% unknowns and 7.6% humins. High drop in humin generation, EL formation and high EFE selectivity are due to the low Brønsted acidity (3.6 B/L) with low total acidity (786 µmol/g) which might be slowing down the polycondensation among FAlc and ethanolysis of formed EFE. From Fig. 5 and Table 2, it indicates that with the increase in Cs exchange from 0.5 to 2 there is a constant drop in total acidity and generation of more Lewis acid sites was noticed. This allows less EL and humins as well as unknown compound formation without compromising EFE yield. From the above Cs insertion of 2, i.e., $H_{0.5}Cs_{2.5}PW_{12}O_{40}$, there is a drastic drop in total acidity ~85% (364 µmol/g) than the parent with the formation of more Lewis acid sites, which leads only 5% FAlc conversion and 2% EFE, 0.9% EL, 1.5% humins and 1.8% unknowns formations. Among Cs-inserted samples, $H_1Cs_2PW_{12}O_{40}$ with 3.6 B/L ratio showed a high selectivity of 55% with 30% EFE yield and 60% FAlc conversion. This may be due to the cumulative effect of moderate acidity, B/L ratio and high surface area (43 m^2/g). Thus, further optimization of parameters was done using $H_1Cs_2PW_{12}O_{40}$ catalyst.

Effect of molar ratio

One of the important process parameters is the substrate concentration, which affects the utilization efficiency of FAlc and final concentrations of products. Experiments were conducted by varying ethanol concentration from 1:2.5 to 1:20 FAlc to ethanol mole ratio, and the results are depicted in Fig. 6. As can be seen from Fig. 6, there is the impact of ethanol concentration on conversion, with an increase in ethanol concentration there is drop in FAlc conversion and maximum conversion was observed at 1:2.5 which is 61%. The formation of EFE is marginally reduced from 34% (1:2.5) to 33% (1:5) and was identical up to 1:15. Above 1:15 ratio, the EFE yield has decreased to 25% (1:20). EL formation has shown an unstable range of $<5\%$, whereas the humin contribution was 12% (1:2.5) to 6% (1:20). Higher formation of humin at 1:2.5 may be due to the more concentration of FAlc. The unknown formations were in the range of 15–17%. Thus, 1:10 (FAlc: ethanol) molar ratio looks to be optimum for this reaction to get optimum FAlc conversion and EFE yield with the lower formation of humin.

Effect of temperature

Most of the etherification and esterification reactions are temperature-dependent. The effect of temperature on FAlc conversion and products yield was studied, and the test was carried out in temperature range from 90 to 130 °C in a closed system to keep the reaction in the liquid phase. It was observed that, as temperature increases from 90 to 120 °C, the FAlc conversion was found to be increased from 50 to 72%; thereafter, FAlc conversion was identical (Fig. 7). As the temperature increases, the rate of reaction increases which enhance the etherification reaction of FAlc to EFE. The further ethanolysis of EFE to EL and condensation to humins is almost

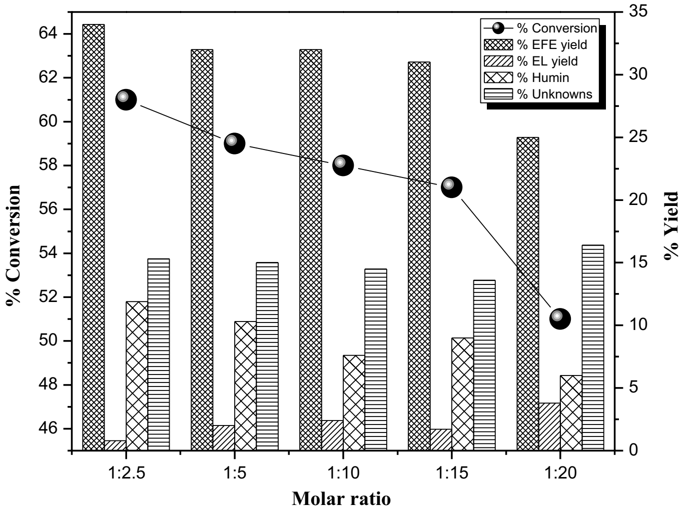

Fig. 6 Effect of the molar ratio of FAlc to ethanol. Reaction conditions: 110 °C temp, 2.5 h time, 5 wt% catalyst loading w. r.t. FAlc

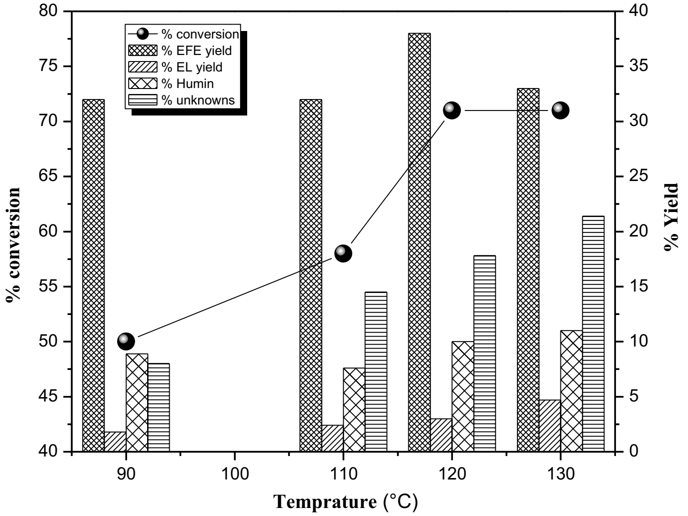

Fig. 7 Effect of temperature. Reaction conditions: 1:10 FAlc/ethanol mol. ratio, 2.5 h time, 5 wt% catalyst loading w.r.t. FAlc

the same at 3% and 7%, respectively. The unknown products were increased from 8 to 15% and this is obvious at the higher temperature. Above 110 °C, at 120 °C maximum, EFE yield of 37% was observed. Above 120 °C, other reactions rate is higher over etherification rate which leads to an increase in EL, humin and unknown formation at the cost of EFE. Thus, 120 °C is found to be the identical temperature for maximum formation of EFE.

Effect of catalyst loading

Enhancement in the active site by increasing catalyst loading is also one of the important parameters to consider for process optimization. Higher the availability of active site improves overall activity or conversion. The FAlc conversion was increased from 70 to 95% by increasing catalyst loading from 5 to 15%. This increase in active sites also changes the overall product distribution due to favoring of one reaction over others (Fig. 8). In the present study, etherification of FAlc to EFE is favoured in a major way with increment in EFE formation up to 65% (15 wt% catalyst loading) from 38% (5 wt% catalyst loading). Similar increasing trend by 10% was also observed for humin formation with the increase in catalyst loading to 15%, whereas unknown product formation was reduced up to 10% with EL formation of 5%. Above 15% catalyst loading, almost identical FAlc conversion was found with marginal decreased in EFE yield by 2%.

Effect of reaction time

Another important parameter to study catalytic activity is time. Considering 15% catalyst loading, 1:10 molar ratio of FAlc to ethanol and 120 °C as a reaction temperature as the best parameters were considered to estimate the minimum time required to complete FAlc conversion. The reaction was stopped and quenched after 0.5, 1.5 and 2.5 h analyzed thoroughly. Initially at 0.5 h, conversion of FAlc and yield of EFE is 88% and 58%, respectively, which is increased up to 93% and 61%

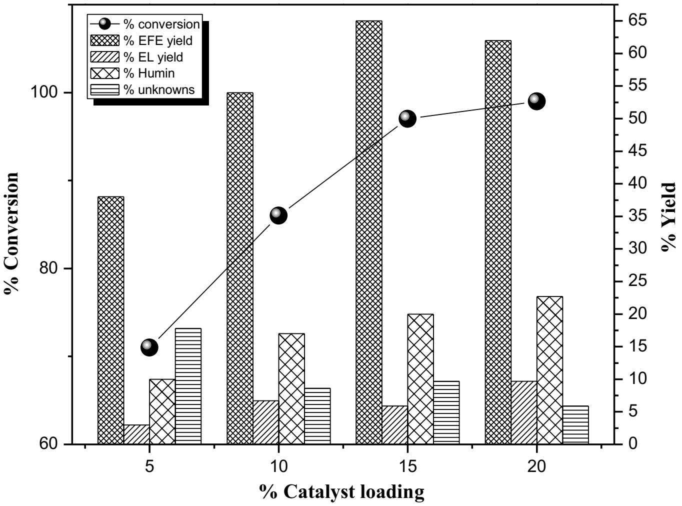

Fig. 8 Effect of catalyst loading with respect to FAlc. Reaction conditions: 1:10 FAlc to ethanol mol ratio, 2.5 h time, 120 °C temp

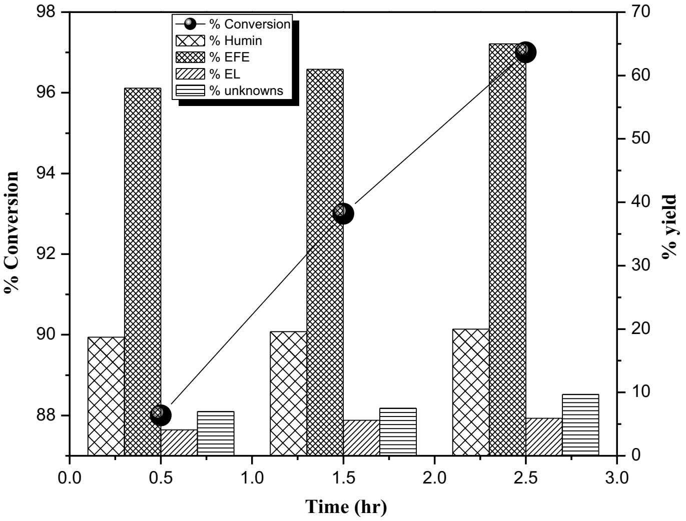

Fig. 9 Effect of reaction time. Reaction conditions: 1:10 FAlc to ethanol mol. ratio, 15 wt% catalyst loading w.r.t. FAlc, 120 °C temp

within 1.5 h; further reaction was carried out up to 2.5 h and got almost complete conversion (97%) yielding 65% EFE along with 6% EL, 20% humins and remaining are unknowns (Fig. 9). Within 0.5 h, there is 60% EFE yield and there is only 7% EL formation along with 20% humins is due to the fastest etherification and polycondensation; however, further ethanolysis of EFE to EL becomes much slower and complex and require more time to produce [15].

Catalyst regeneration

In FAlc conversion, catalyst regeneration and its reusability is an important issue because of the formation of insoluble humins which is blocking the active sites. It is quite difficult to dissolve the humins [27, 28], by taking the consideration of the standard analytical protocol developed for dissolution of humin-type poly-condensed compound in wood and pulp approved by the standard analytical Technical Association of the Pulp and Paper Industry (TAPPI) "T204 cm 97." Using said protocol used catalyst having humin was washed with a solvent mixture of THF + acetone (50:50 ratio) for 1 h to regenerate the catalyst. After washing and drying at 120c for 4 h, catalyst has shown only 20% FAlc conversion and 12% EFE. In another case, the used catalyst having humin was washed with THF + acetone (50:50 ratio) for 1 h and then was calcined at 350C for 5 h which has shown regain in catalyst activity as that of fresh (Fig. 10) and was maintained for next two cycles. Figure 11 depicts XRD plots for fresh, spent and treated (washing + calcination) catalysts, and it confirmed that after washing with THF + acetone and calcinations at 350 °C for 5-h catalyst has regained its crystallinity as compared to spent.

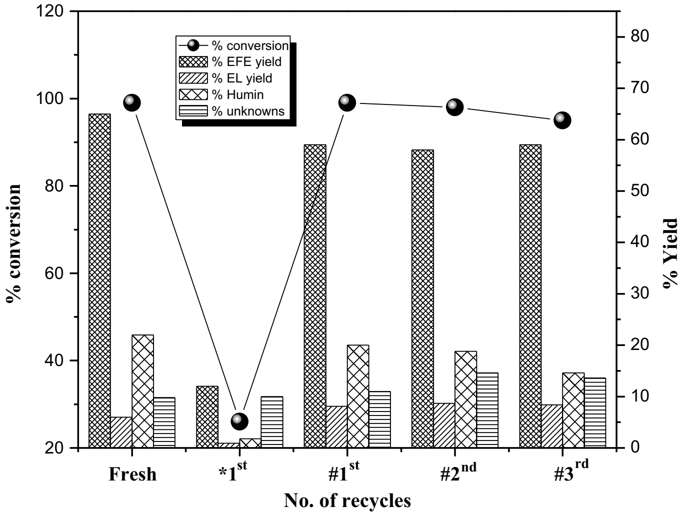

Fig. 10 Catalyst reusability *washed and dried, # washed and calcined at 350 °C for 5 h. Reaction conditions: 1:10 FAlc to ethanol mol. ratio, 2.5 h time, 15 wt% catalyst loading w.r.t. FAlc, 120 °C temp

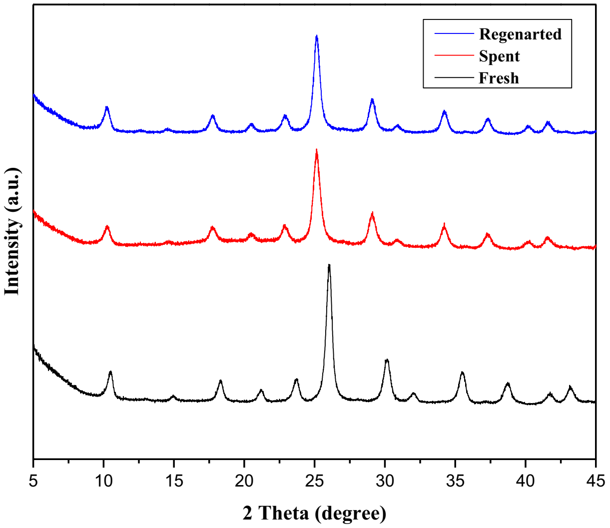

Fig. 11 Powder XRD of fresh, spent and regenerated $H_1Cs_2PW_{12}O_{40}$ samples

Conclusion

The successful attempt was made to heterogenized heteropolyacid in the polar medium by exchange of Cs (from 0.5 to 2.5 mol) in place of H^+ proton. The prepared catalysts were thoroughly characterized by various characterization techniques such as XRD, TPD, BET surface area, XPS, pyridine–FTIR and established fingerprint of these samples. Etherification reaction of furfuryl alcohol with ethanol to ethyl furfuryl ether, a biofuel was carried out. $H_1Cs_2PW_{12}O_{40}$ catalyst having total acidity of 786 μmol/g, B/L ratio of 3.6, and surface area of 43 m^2/g was found to be optimum catalyst composition for maximum FAlc conversion of 98%, 65% EFE yield at 120°C, 1:10 (FAlc: Ethanol) and 15% catalyst loading w.r.t. FAlc; 2.5 h reaction time. $H_1Cs_2PW_{12}O_{40}$ catalyst is found to be reusable for four times (fresh + 3 reuse) by solvent washing (THF + acetone) 50:50 ratio and then calcination at 350 °C for 5 h. This study has shown effective development of catalyst and optimization of process parameters for the selective synthesis of biofuel from renewable furfuryl alcohol.

Acknowledgements Authors acknowledge funding from Department of Biotechnology, New Delhi under Sanction Number: BT/PR12277/PBD/26/434/2014.

References

1. A.J. Ragauskas, C.K. Williams, B.H. Davison, G. Britovsek, J. Cairney, C.A. Eckert, W.J. Frederick Jr., J.P. Hallett, D.J. Leak, C.L. Liotta, J.R. Mielenz, R. Murphy, R. Templer, T. Tschaplinski, Science **311**, 484 (2006)
2. Dir. 2009/28/Ec Eur. Parliam. Counc. 23 April 2009, Off. J. TheEuropean Union, (2009) L140/16-L140/62
3. R.V. Sharma, U. Das, R. Sammynaiken, A.K. Dalai, Appl. Catal. A Gen. **454**, 127 (2013)
4. T. Wang, A. Hu, G. Xu, C. Liu, H. Wang, Y. Xia, Catal. Letters **149**, 1845 (2019)
5. G. Gómez, Z. El, K. Nieminen, S. Hellsten, J. Llorca, H. Sixta, Fuel Process. Technol. **182**, 56 (2018)
6. T. Zhao, Y. Zhang, G. Zhao, X. Chen, L. Han, W. Xiao, Fuel Process. Technol. **180**, 14 (2018)
7. V.E. Tarabanko, M.Y. Chernyak, I.L. Simakova, K.L. Kaigorodov, Yu.N. Bezborodov, N.F. Orlovskaya, Russ. J. Appl. Chem. **88,** 1178 (2015)
8. R.J. Haan, J.P. Lange, US Patent 8372164 B2 (2013)
9. Y. Nakagawa, M. Tamura, K. Tomishige, Fuel Process. Technol. **193**, 404 (2019)
10. J. Lange, E. Van Der Heide, J. Van Buijtenen, R. Price, ChemSusChem **5**, 150 (2012)
11. Q. Cao, J. Guan, G. Peng, T. Hou, J. Zhou, X. Mu, Catal. Commun. **58**, 76 (2015)
12. Z. Zhang, K. Dong, Z. Zhao, ChemSusChem **4**, 112 (2011)
13. G. Zhao, M. Liu, X. Xia, L. Li, B. Xu, Molecules **24**, 1881 (2019)
14. Y. Wang, D. Zhao, K.S. Triantafyllidis, W. Ouyang, Mol. Catal. **480**, 110630 (2020)
15. X. Gao, L. Peng, H. Li, K. Chen, BioResource, **10**, 6548 (2015)
16. D.R. Chaffey, T.E. Davies, S.H. Taylor, A.E. Graham, ACS Sustainable Chem. Eng. **6**, 4996 (2018)
17. F. Zaccheria, N. Scotti, N. Ravasio, Catalysts **9**, 172 (2019)
18. X. Kong, S. Wu, L. Liu, S. Li, J. Liu, Mol. Catal. **439**, 180 (2017)
19. M. Wang, F. Su, Q. Wu, D. Song, X. Zhang, Y. Guo, J. Mater. Chem. A **1**, 13209 (2013)
20. M. José, D. Silva, A. Aparecida, S. Olavo, R. Chagas, D. Silva, D. Morais, Fuel **254**, 115607 (2019)
21. K. Narasimharao, D.R. Brown, A.F. Lee, A.D. Newman, P.F. Siril, S.J. Tavener, K. Wilson, J. Catal. **248**, 226 (2007)
22. H. Eom, D. Lee, S. Kim, S. Chung, Y. Gul, K. Lee, Fuel **126**, 263 (2014)
23. T. Okuhara, T. Nakato, Catal. Surv. From Japan **2**, 31 (1998)
24. K. Inumaru, T. Ito, M. Misono, Microporous Mesoporous Mater. **21**, 629 (1998)
25. C. Travers, N. Essayem, M. Delage, S. Quelen, Catal. Today **65**, 355 (2001)
26. L. Pesaresi, D.R. Brown, A.F. Lee, J.M. Montero, H. Williams, K. Wilson, Appl. Catal. A Gen. **360**, 50 (2009)

27. P. Neves, S. Lima, M. Pillinger, S.M. Rocha, J. Rocha, A.A. Valente, Catal. Today **218–219**, 76 (2013)
28. L.L. Geng Zhao, L. Hu, Y. Sun, X. Zeng, BioResources **9**, 2634 (2014)

Molecular Catalysis 531 (2022) 112689

Contents lists available at ScienceDirect

Molecular Catalysis

journal homepage: www.journals.elsevier.com/molecular-catalysis

Immobilization of HPW on UiO-66-NH_2 MOF as efficient catalyst for synthesis of furfuryl ether and alkyl levulinate as biofuel

Nagesh Mulik [a,b], Vijay Bokade [a,b,*]

[a] Catalysis and Inorganic Chemistry Division, CSIR-National Chemical Laboratory, Dr. Homi Bhabha Road, Pashan, Pune 411008, India
[b] Academy of Scientific and Innovative Research (AcSIR), Ghaziabad 201002, India

ARTICLE INFO

Keywords:
Immobilization
Phosphotungstic acid
UiO-66-NH_2-HPW
Etherification
Alcoholysis

ABSTRACT

Phosphotungstic Acid (HPW) is an inorganic super acid, that is highly soluble in polar solvents limiting its applicability as acid catalysis. To overcome these limitations immobilization of HPW was carried out at room temperature by protonation of -NH_2 group of UiO-66-NH_2 MOF to UiO-66-NH_2—HPW. ATR-FTIR spectroscopy and XPS results confirmed the protonation and chemical interaction between HPW and UiO-66-NH_2. STEM-EDS mapping showed homogeneous distribution of HPW on UiO-66-NH_2. BET and NH_3-TPD confirmed the reduction in specific surface area, total pore volume, and increase in total acidity for UiO-66-NH_2—HPW. Further, powder XRD, SEM, and HR-TEM prevailed that there is no change in phase and morphology after post-synthetic modification of UiO-66-NH_2. The prepared catalyst is found to be effective for etherification and alcoholysis of furfuryl alcohol (FALc) to Furfuryl ether (FE) and Alkyl levulinate (AL). UiO-66-NH_2—HPW has shown 97 mol % FALc conversions in ethanolic media and 31 mol% Ethyl furfuryl ether (EFE) yield and 29 mol% Ethyl levulinate (EL) yield. UiO-66-NH_2—HPW is also found to be efficient for the multistep conversion of Furfural (FFR) to FALc, FE, and AL.

1. Introduction

Heteropolyacids (HPAs) are an interesting class of well-defined strong solid Brønsted acids, exhibiting excellent catalytic behavior in a wide variety of acid-catalyzed reactions such as esterification, transesterification, hydrolysis, alkylation, acylation as well as a redox reaction [1,2]. However, HPAs are usually soluble in many polar solvents, causing difficulties in the recovery, separation, and recycling of the catalysts, which affects their eco-friendly applications. Thus, it will be beneficial to develop a reusable HPA-based catalyst. Nonetheless, heterogeneous HPA-based catalysts usually have some disadvantages, such as low surface area, leaching of the active sites, and low activity [1–5]. To overcome the above limitations, many approaches such as immobilization and solidification have been proposed to improve the stability and catalytic performance. HPAs can be immobilized using various supports such as mesoporous silica, metal-organic frameworks, mesoporous transition metal oxides, zeolites, and mesoporous carbon, [1,2,5–7]. It is well known that HPAs have strong acidity and even it reacts with weak bases and form bonding with them. HPAs will get heterogeneity by interacting with bases such as alkali metals and organic amines [2,4,5,8–12]. Materials such as organically modified silica with amine functionality, organic polymers containing an amino-functional group, organic amines, ionic liquids, and organic surfactants containing amino groups were often used as a carrier for anchoring of HPA employing strong bonding [11–15]. For acid-base dispersion and anchoring of HPAs on Metal-Organic frameworks (MOF) containing amine functionality may be the best option because MOFs have high porosity and high surface area which will provide more active sites for host-guest interaction.

MOFs are a class of crystalline, well-ordered inorganic-organic porous hybrid material with tunable textural and diverse framework functionalities. MOFs can be used as a multifunctional catalyst in tandem reactions and their catalytic properties can be enhanced by engineering metal nodes as active sites, the post-synthetic introduction of active sites, and engineering of active sites in pores cavities [16–19]. Zirconium-based MOFs such as UiO-66 and its amine derivative UiO-66-NH_2 are highly porous with high surface area, hydrothermally and chemically more stable in a wide range of pH in aqueous solutions. This makes UiO-66 extremely useful as a catalyst and an ideal platform to introduce active sites [19–21]. Biomass conversion involves hydrolysis, dehydration, alcoholysis, esterification, and etherification over Lewis as well as Brønsted acid sites. Brønsted acidity in MOFs is

---

* Corresponding author at: Catalysis Division, CSIR-National Chemical Laboratory, Pune 411008, India.
E-mail address: vv.bokade@ncl.res.in (V. Bokade).

https://doi.org/10.1016/j.mcat.2022.112689
Received 14 July 2022; Received in revised form 13 September 2022; Accepted 14 September 2022

introduced by using acid functionalized ligands, by encapsulation of HPAs during solvothermal synthesis, and by impregnation of HPAs on MOFs. Encapsulation of HPAs in MOF may lead to pores blockage, extensive drop-down in total surface area, slow diffusion, and less contact of reactants with active sites, while impregnation of HPAs on MOFs may lead to low homogeneity in dispersion, occupation of the large cavities and leaching during the reaction [17,22]. Thus, the objective of this work is to overcome the above-mentioned problems by firm anchoring/binding of HPAs on UiO-66-NH_2, by reacting it with the basic sites (-NH_2). In this work, we have demonstrated post-synthetic modification of UiO-66-NH_2 by binding with phosphotungstic acid (HPW). The prepared UiO-66-NH_2—HPW catalyst was characterized by XRD, ATR-FTIR, XPS, STEM-EDS, SEM, HR-TEM, N_2 adsorption-desorption analysis, and ammonia-temperature programmed desorption (NH_3-TPD). Preparation of furfuryl ethers (FE) such as Ethyl furfuryl ether (FEF), Methyl furfuryl ether (MFE), Isopropyl furfuryl ether (IPFE), and alkyl levulinates (AL) such as Ethyl levulinate (EL), Methyl levulinate (ML), and Isopropyl levulinate (IPL) attracts much attention in recent years, due to their applicability as a fuel and fuel additive along with other applications [23–27]. Hence, we carried out the catalytic evaluation of prepared UiO-66-NH_2—HPW for hydrogenation and alcoholysis of Furfural (FFR) and Furfuryl alcohol (FALc) to FE and AL.

2. Experimental

2.1. Catalyst synthesis

2.1.1. Synthesis of UiO-66-NH_2

UiO-66-NH_2 was synthesized by hydrothermal method, with a little modification based on the previous study [28], 13.5 mmol $ZrCl_4$ (Acros), 13.5 mmol 2-aminoterephthalic acid (Alfa Aesar), and 13.5 mmol H_2O were dissolved in 5.6 mol N—N-dimethylformamide (Thomas baker) at room temperature. Crystallization was carried out in a 1 L stainless steel Teflon-lined reactor under static conditions in a preheated oven at 120 °C for 18 h. Then the reactor was removed from the oven and naturally cool down to RT, the resulting solid was centrifuged and repeatedly washed with DMF and with methanol to remove the unreacted ligand and then kept at 80 °C for 2 h in the oven to get dry powder.

2.1.2. Post-Synthetic modification of UiO-66-NH_2 to UiO-66-NH_2-HPW

The post-synthetic modification was done by dissolving 2.3 mmol of HPW in 60 mL of acetonitrile, and 1.14 mmol of freshly prepared powder of UiO-66-NH_2 were added to HPW solution and kept under vigorous stirring for 30 min. The final solid was separated by centrifugation and washed several times with acetonitrile to remove unreacted HPW and dried in the oven at 80 °C for 2 h to get UiO-66-NH_2—HPW.

3. Catalyst characterization

Wide-angle X-ray diffraction (XRD) patterns were obtained on a Regaku Miniflex X-ray diffractometer with a Cu Kα radiation source operated at 40 kV and 30 mA over a 2θ range from 5° to 50° at a scanning rate of 3°/min.

Functional groups of the prepared materials were characterized by Fourier Transform Infrared Spectroscopy (FTIR), which was performed on a Bruker Alpha-P ATR FTIR spectrometer.

The surface area of the samples was determined from nitrogen adsorption–desorption isotherms in liquid nitrogen on Quantachrome Autosorb iQ equipment, using the Brunauer–Emmett–Teller (BET) method, and all samples were degassed to 0.1 Pa at 200 °C for 3 h before measurement.

Field Emission Scanning Electron Microscopy (FE-SEM) images have been captured on a NOVA NANOSEM 450 instrument while High-Resolution Transmission Electron Microscopy (HRTEM) images, STEM images, and Elemental mapping were done on JEOL JEM-F200 (URP) instrument.

X-ray Photoelectron Spectroscopy (XPS) was carried out using the K-Alpha+ model Thermo Fisher Scientific an XPS instrument with an Al Kα source. XPS data of all the compounds were fitted with the Shirley-type background subtraction method using Fitiyk software.

Temperature-Programmed Desorption (TPD) profiles of NH_3 from the synthesized catalysts were measured using a Micrometric AutoChem 2950 HP instrument. The sample cell loaded with 0.050 g of sample was initially treated under a helium flow of 40 mL min^{-1} at 200 °C for 2 h, then cooled to 100 °C, and subsequently exposed to pulses of ammonia (10% in helium) until saturation and then purged with a helium flow at 100 °C for 1 h. Afterward, the sample cell was heated up to 600 °C with a ramp of 10 °C min^{-1}. The concentration of the desorbed ammonia was monitored continuously with a TCD detector.

4. Catalytic activity test

All reactions were performed in a 100 mL high-pressure Parr reactor (4871 series controller) equipped with external temperature and stirring controllers. In a typical reaction 7.2 mmol of FFR or FAlc, 360 mmol of alcohol, and 20 wt% catalyst were loaded based on FFR or FALc concentration. Then the reactor was sealed and placed in a heating unit with stirring at 300 rpm., After completion of the reaction, the reactor was cooled in a cooling water bath to room temperature. The spent catalyst was separated by centrifugation. After washing and drying, the spent catalyst was used for the next run to evaluate its stability and reusability.

The liquid products were qualitatively determined using gas chromatography–mass spectrometry (GC–MS-QP2020 NX, Shimadzu) fitted with a TR-5 MS column (30 m × 250 μm × 0.25 μm). The quantitative analysis of liquid products was conducted on a Varian CP-3800 series with an RTX-5 capillary column (60 m × 320 μm × 0.25 μm) equipped with a flame ionization detector (FID). Both GC–MS and GC analysis employed the following temperature program: the initial temperature was 50 °C, followed by heating at a rate of 20 °C/min to 220 °C. The amounts of product samples were quantitatively analyzed based on the external standard curves with commercial samples. The yields of products were calculated as the ratio of the moles of products obtained to the moles of the substrate in the feed. The yield of IPFE, EFE, and MFE was calculated using calibration data of FALc it is commercially unavailable and was confirmed by GC–MS. The yield of products and conversion were determined according to the following equations:

$$\%\ Conversion = \frac{Reactant\ initial\ moles - Reactant\ final\ moles}{Reactant\ initial\ moles} * 100$$

$$\%\ Yield = \frac{moles\ of\ product}{Reactant\ initial\ moles} * 100$$

$$Weight\ of\ humin = Residue\ collected(dried) - Weight\ of\ Catalyst$$

$$\%\ Humin = \frac{Weight\ of\ humin}{Initial\ weight\ of\ Reactant} * 100$$

5. Result and discussion

5.1. Characterization of prepared catalysts

The surface morphology of the sample was detected by HR-TEM and is presented in Fig. 1A, B, and the SEM images are given in the supporting (Fig. S1. A, B). The forms of UiO-66-NH_2 and UiO-66-NH_2—HPW were regular octahedrons in shape. Powder XRD patterns of the samples before and after modification are shown in Fig. 3. It is demonstrated the well-comparable synthesis of UiO-66- NH_2 as that of the previous studies [28–30]. Moreover, the morphology and XRD pattern remains the same after post-synthetic modification. Fig. 2. STEM and EDS mapping images indicate that well dispersion and distribution of HPW throughout the

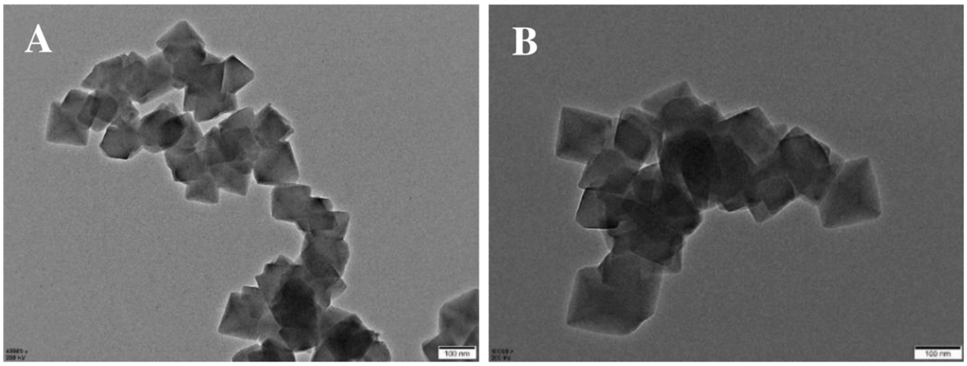

Fig. 1. HR-TEM image of (A) UiO-66-NH_2 and (B) UiO-66-NH_2—HPW.

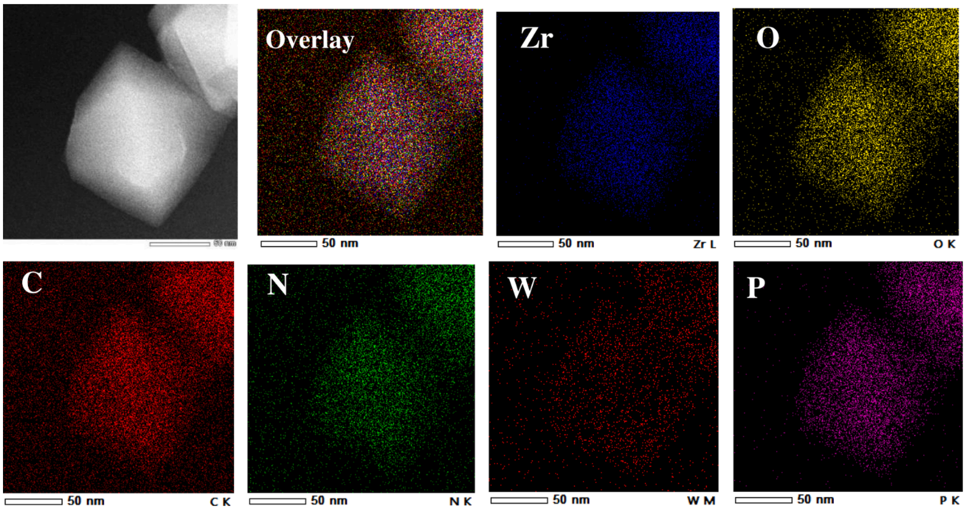

Fig. 2. STEM image and Elemental mapping of UiO-66-NH_2—HPW.

UiO-66-NH_2 crystal, while the parent sample (UiO-66-NH_2) only shows framework elements- Zr, O, C, and N in EDS mapping (Fig. S2. In supplementary).

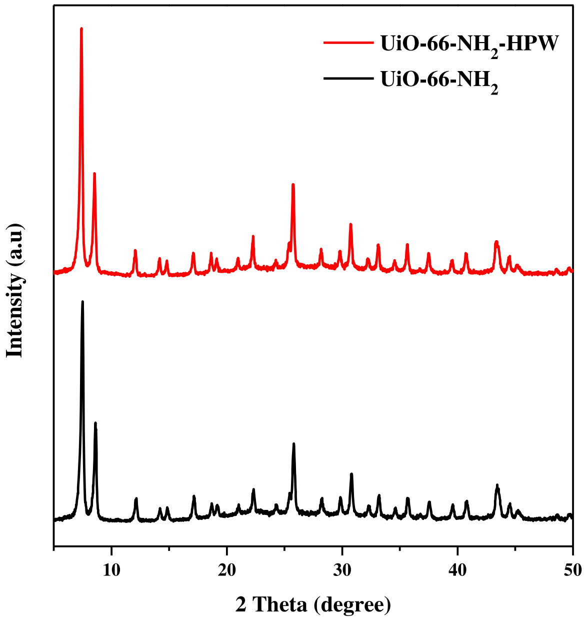

Fig. 3. Powder XRD of parent UiO-66-NH_2 and UiO-66-NH_2—HPW.

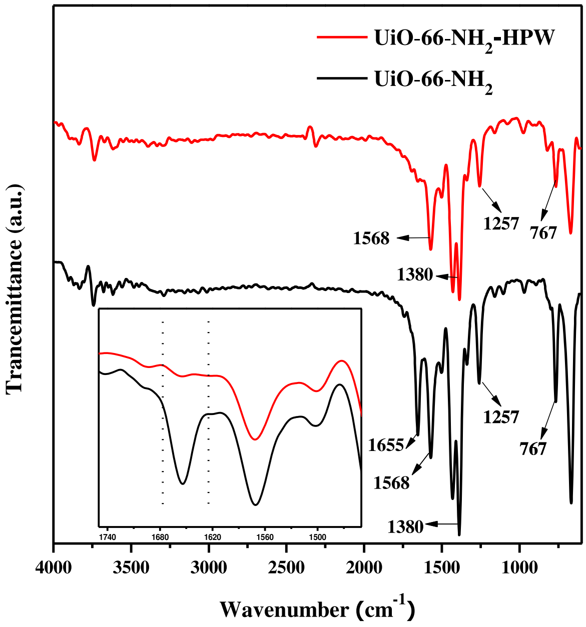

Fig. 4. ATR-FTIR of parent UiO-66-NH_2 and UiO-66-NH_2—HPW.

Fig. 4. Shows the ATR-FTIR spectra of UiO-66-NH_2 and UiO-66-NH_2—HPW samples. The ligand of UiO-66-NH_2 was an amine-functionalized terephthalic acid (2-amino terephthalic acid), with the uncoordinated free –NH_2 strong band of aromatic primary amine N—H stretching appeared at 1655 cm^{-1} in the spectra of UiO-66-NH_2 [31]. The spectral band at 1568 cm^{-1} was caused by the skeletal vibration of the benzene ring. Moreover, a component located at 1400 cm^{-1} corresponds to the OCO symmetric stretching, and 1257 cm^{-1} is assigned to the C – N stretching vibrational spectrum [28–31]. After the modification of UiO-66-NH_2 with HPW to UiO-66-NH_2—HPW, only a reduction in the characteristic N—H stretching band of primary amine at 1655 cm^{-1} (shown in the inset of Fig. 4.) is observed. Hence it indicates that there is a strong chemical interaction between the -NH_2 group and HPW.

To confirm the chemical state of each element, XPS analysis was done and the spectra are illustrated in Fig. 5. Fig. 5A. is the XPS survey scan of UiO-66-NH_2 and UiO-66-NH_2—HPW which represents the elements Zr 3d, O 1 s, C 1 s, N 1 s, and Zr 3d, O 1 s, C 1 s, N 1 s, W 4f, P 1 s respectively. Table S1. shows the elemental composition of UiO-66-NH_2 and UiO-66-NH_2—HPW by XPS and EDS analysis. The N 1 s XPS spectra (Fig. 5B) of both the samples UiO-66-NH_2 and UiO-66-NH_2—HPW indicate that three distinct peaks; peak at 398.8 eV are assigned to C—N, peak at 399.3 eV is assigned to -NH_2 and the other peak at 400.5 eV is

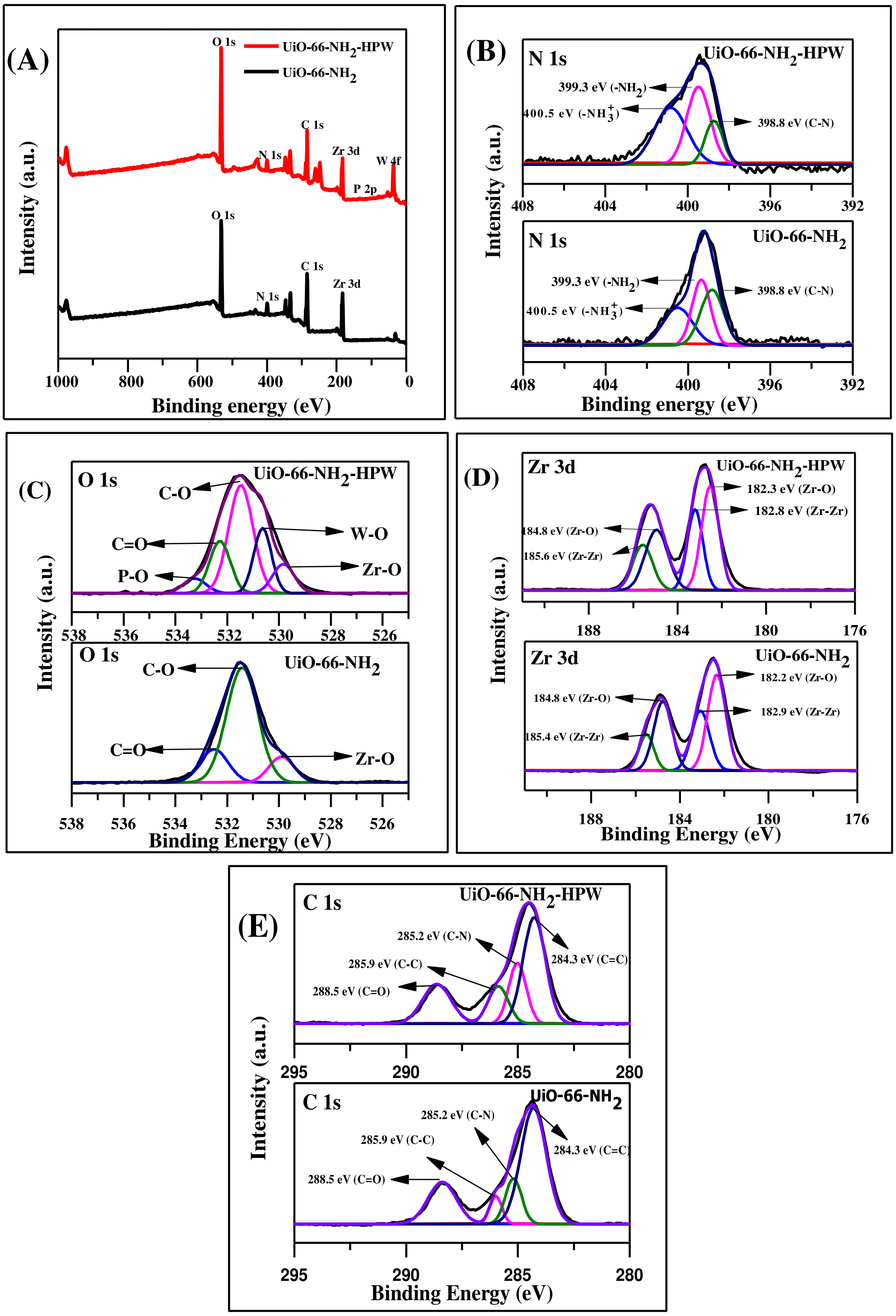

Fig. 5. (A) XPS survey scan of UiO-66-NH_2 and UiO-66-NH_2—HPW, and high-resolution XPS data of UiO-66-NH_2 and UiO-66-NH_2—HPW (B) N 1, (C) O 1 s, (D) Zr 3d, (E) C 1 s.

due to the interaction between the amino group and proton [11,12,30,32]. Hence it can be seen that area under the peak at 400.5 eV which is assigned to -NH_3^+ is exponentially increased after post-synthetic modification of UiO-66-NH_2 with HPW to UiO-66-NH_2—HPW. Thus, there may be strong ionic bonding between -NH_3^+ and phosphotungstic ion (HPW^-) [11,12]. Fig. 5C. represents the O 1 s XPS spectra of samples UiO-66-NH_2 and UiO-66-NH_2—HPW. Post synthetically modified sample clearly shows a total of five peaks, three peaks for Zr-O, C—O, and C = O at the binding energy level of 590.9 eV, 531.4 eV, 531.8 eV, and two peaks for W-O-W, P-O-W at the energy level of 330.6 eV and 333.2 eV respectively, while UiO-66-NH_2 shows only three peaks corresponds to Zr-O, C—O, C = O at the binding level of 590.9 eV, 531.4 eV, 531.8 eV. [3,33] As shown in Fig. 5D, the Zr 3d spectrum can be divided into four peaks [30]. The peaks at 182.3 eV and 184.8 eV are attributed to Zr-O bonds, and the peaks at 182.8 eV and 185.6 eV are attributed to Zr-Zr bonds. As shown in Fig. 5E, the C 1 s spectrum can be divided into four peaks; C = C, C—N, C—C, and C = O correspond to 284.3 eV, 285.2 eV, 285.9 eV, and 288.5 eV, respectively [30,31]. Fig. S3. shows high-resolution XP spectra of W 4f and P 2p of the sample UiO-66-NH_2—HPW, the W 4f XP spectra show the two distinctive peaks at the energy level of 35.8 eV and 37.9 eV while P 2p XP spectra show a single peak at 134 eV [3]. According to the literature and our XPS and ATR-FTIR analysis, there is a specific interaction between the basic -NH_2 group and Brønsted acidic HPW, as illustrated in Scheme 1.

The nitrogen adsorption-desorption isotherm of UiO-66-NH_2 and UiO-66-NH_2—HPW is provided in supporting information as Fig. S4., and as listed in Table 1. the specific surface area of UiO-66-NH_2 and post synthetically modified UiO-66-NH_2—HPW were 907 m^2g^{-1} and 669 m^2g^{-1} respectively. The total pore volume and pore diameter of UiO-66-NH_2 was 0.543 cm^3g^{-1} and 3.793 nm which is reduced to 0.399 cm^3g^{-1} and 3.385 nm after post-synthetic modification of UiO-66-NH_2 to UiO-66-NH_2—HPW. The decrease in specific surface area, total pore volume, and pore diameter indicated anchoring of HPW to the framework -NH_2 group.

NH_3-TPD curves of UiO-66-NH_2 and UiO-66-NH_2—HPW are shown in Fig. S5 (in supporting information) and acid values are given in Table 1. Two desorption peaks were observed in the ranges of 185–430 °C and 446–600 °C, which are attributed to weak acid sites and strong acid sites, respectively. It can be seen that the intensity of the strong acid site is more in post synthetically modified UiO-66-NH_2—HPW than in parent UiO-66-NH_2, and the total acidity of UiO-66-NH_2—HPW is more (0.436 mmol g^{-1}) than parent UiO-66-NH_2 (0.301 mmol g^{-1}).

5.2. Catalyst screening

Scheme 2 reveals, catalytic etherification and alcoholysis of FALc to EFE and EL. EFE and EL formation were confirmed by GC–MS along with these products small fraction of byproducts such as 2,2-methylene difuran, 2-Pentanone-5–5-diethoxy levulinaldehyde, 2,5-(2-Furylmethyl), Ethyl 5-(5-methyl-2-furyl)−2,4-pentadienoate is also identified by GC–MS (Fig. S6.). Table 2, shows the initial catalytic screening of etherification and alcoholysis of FALc to EFE and EL over 20 wt.% catalyst loading wrt FALc weight, at 150 °C, for 2 h. UiO-66-NH_2 has shown only 20% catalytic conversion of FALc with 8.7% EFE and 5.4% EL yield, while UiO-66-NH_2—HPW showed high catalytic activity to 83% FALc conversion with 34% and 23% yield of EFE and EL, respectively. Such drastic catalytic activity enhancement is due to the anchoring of highly acidic HPW and more acidity of UiO-66-NH_2—HPW (0.436 mmol g^{-1}) than the parent UiO-66-NH_2 (0.301 mmol g^{-1}). To investigate whether the catalytic system is heterogeneously or homogeneously catalyzed, a leaching test was performed in which the UiO-66-NH_2—HPW sample was heated at 150 °C for 2 h in ethanol after 2 h, the system was cooled to room temperature and the catalyst was removed by centrifugation and then FALc added and the reaction was continued for 2 h at 150 °C. After 2 h of reaction, it has shown 10% conversion without yielding the desired product it confirming that reaction is purely heterogeneous.

Table 1
Surface properties and Ammonia TPD acidity of UiO-66-NH_2 and UiO-66-NH_2—HPW.

Sample	S (BET) m^2g^{-1}	V_{total} (cm^3g^{-1})	D nm	Total Acidity mmol g^{-1}
UiO-66-NH_2	907	0.543	3.793	0.301
UiO-66-NH_2—HPW	669	0.399	3.385	0.436

5.3. Optimization of reaction parameters

In addition to the physical properties of UiO-66-NH_2—HPW, the etherification and alcoholysis conversion of FALc to EFE and EL equally depends on various reaction parameters.

5.3.1. Effect of UiO-66-NH_2-HPW amount

Fig. 6. shows, the effect of catalyst loading wrt to FALc on the etherification and alcoholysis of FALc to EFE and EL. An increasing catalytic amount from 10 wt.% to 40 wt.% of initial FALc reflects the considerable increase in the conversion of FALc. However, unwanted products such as humin were also observed to be increased. Thus, 20 wt.% catalyst amount was considered optimum loading with low humin (2.5%), 83% FALc conversion, 34% EFE yield, and 24% EL yield.

5.3.2. Effect of temperature

Fig. 7. displays the effect of temperature on etherification and alcoholysis of FALc to EFE and EL over UiO-66-NH_2—HPW. It can be seen that reaction temperature showed an exponential influence on the conversion of FALc and yield of EFE and EL. With an increase in temperature from 110 °C to 170 °C, there is a positive impact on FAlc conversion from 61% to 98% with a yield of EFE from 22% to 34% and EL from 7% to 30%. At lower temperatures of 110 °C and 130 °C, there is a significant formation of EFE within the reaction time of 2 h. Lower formation of EL suggests that at lower temperature further transformation of EFE to EL is limited. However, above 130 °C, a constant increment in EL yield was observed. It is worth noticing that when the

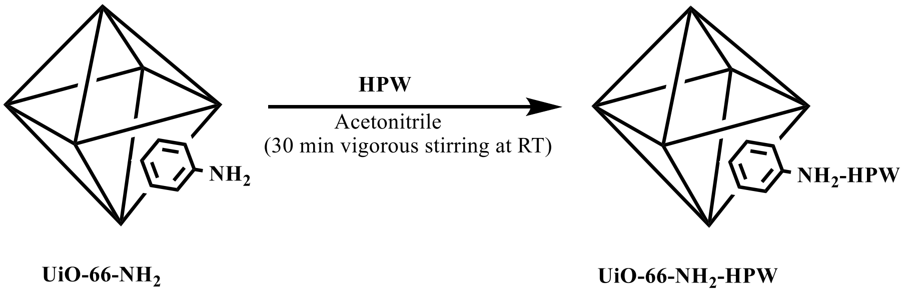

Scheme 1. Schematic illustration of post-synthetic formulation of UiO-66-NH_2—HPW from UiO-66-NH_2.

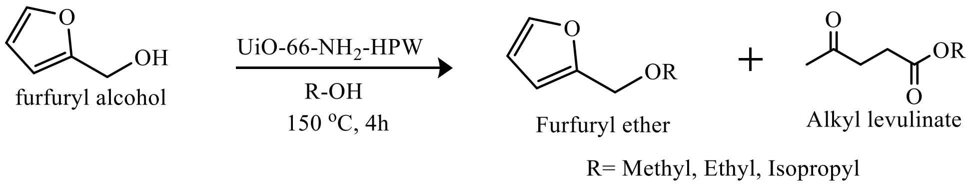

Scheme 2. Catalytic conversion of FALc to FE and AL.

temperature increases to 170 °C favor the formation of EL but simultaneously there is an increase in unwanted humins (5.7%) also. Thus, 150 °C temperature is optimum with 20 wt.% catalyst loading.

Table 2
Activity comparison of parent and modified Catalyst.

Catalyst name	% Conversion	%Yield of EFE	%Yield of EL	% Humins
UiO-66-NH_2	20	8.7	5.4	0
UiO-66-NH_2—HPW	83	34	23	2.5

Reaction conditions: FAlc to Ethanol 1:50 mol ratio, 20 wt.% catalyst wrt FALc, Reaction Time 2 h, stirring speed 300 rpm.

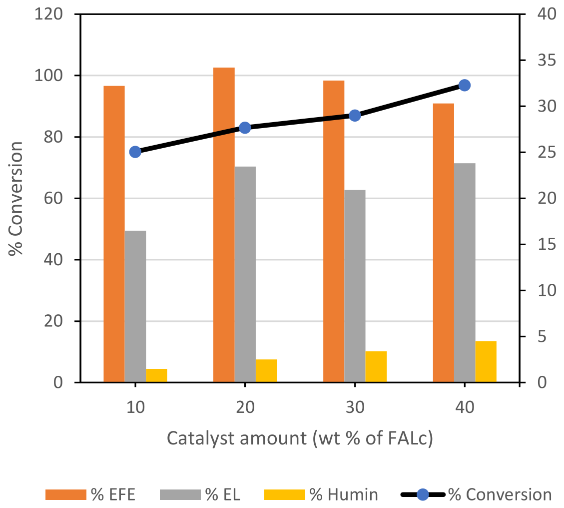

Fig. 6. Effect of UiO-66-NH_2—HPW amount.
Reaction conditions: FAlc to Ethanol 1:50 mol ratio, Reaction temperature 150 °C, Reaction Time 2 h, stirring speed 300 rpm.

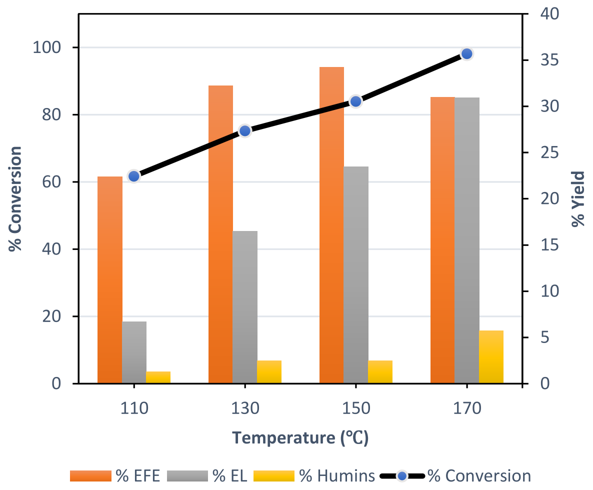

Fig. 7. Effect of Temperature on the catalytic activity of UiO-66-NH_2—HPW.
Reaction conditions: FAlc to Ethanol 1:50 mol ratio, 20 wt.% catalyst wrt FALc, Reaction Time 2 h, stirring speed 300 rpm.

5.3.3. *Effect of reaction time*

Fig. 8. depicts the effect of reaction time on etherification and alcoholysis of FALc to EFE and EL over UiO-66-NH_2—HPW. It can be seen that at FAlc conversion increased from 83% (2 h) to 97% (4 h). After 4 h, FAlc conversion is almost constant at 98%. At the initial stage of reaction, there is a substantial formation of EFE than EL. After 4 h, equilibrium formation of EFE (31%) and EL (33%) with humins formation of 3%.

5.3.4. *Effect of type of alcohol*

Alcohols such as methanol, ethanol, and Isopropyl alcohol (IPA) were evaluated under optimum reaction conditions for FALc conversion to FE and AL, Products were identified by GC–MS (Fig. S4) and results are shown in Fig. 9. As expected, ethanol and IPA are good solvents for this type of reaction and have shown higher etherification and alcoholysis activity than methanol. With ethanol, there is 97% FALc conversion with 31% and 29% EFE and EL yield, respectively. Whereas, IPA has shown 80% FAlc conversion with 38 and 17% IPFE and IPL yield respectively with low (2%) humins formation. In the case of methanol only 19% ML formation with high humins of 14% at 76% of FALc conversion, indicates methanol is not a good solvent for this reaction.

5.4. *Catalysts reusability*

The major benefit of heterogeneous catalysis is its reusability. The reusability test was conducted by reacting FALc with Ethanol at 150 °C for 4 h (Fig. 10). After completion of the reaction, the catalyst was removed from the reaction mixture by centrifugation and washed with methanol, dried at 80 °C for 2 h, and then reused for the next cycle. As revealed in Fig. 10, the use of UiO-66-NH_2—HPW is still capable of

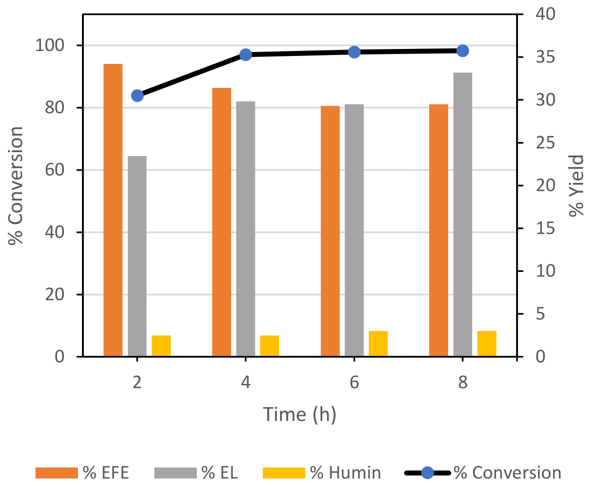

Fig. 8. Effect of Time on the catalytic activity of UiO-66-NH_2—HPW.
Reaction conditions: FAlc to Ethanol 1:50 mol ratio, 20 wt.% catalyst wrt FALc, Reaction temperature 150 °C, stirring speed 300 rpm.

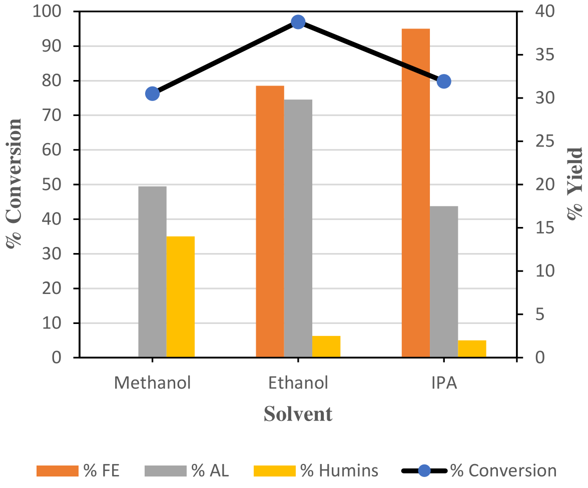

Fig. 9. Effect of type of alcohol type on etherification and alcoholysis of FALc over UiO-66-NH$_2$—HPW.
Reaction conditions: FAlc to alcohol 1:50 mol ratio, 20 wt.% catalyst wrt FALc, Reaction temperature 150 °C, Reaction time 4 h, stirring speed 300 rpm.

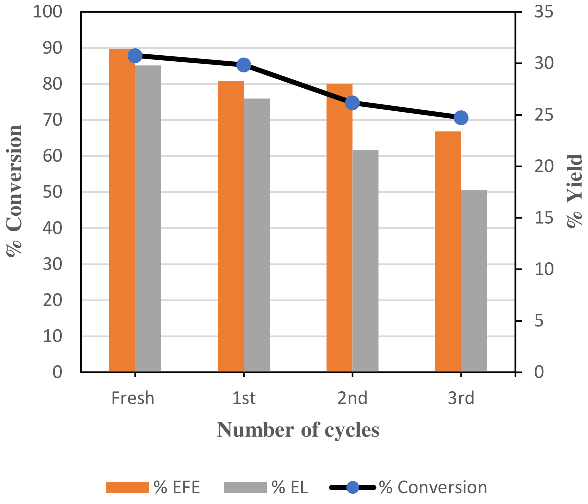

Fig. 10. Catalyst recycling for FALc conversion over UiO-66-NH$_2$—HPW in Ethanol.
Reaction conditions: FAlc to alcohol 1:50 mol ratio, 20 wt.% catalyst wrt FALc, Reaction temperature 150 °C, Reaction time 4 h, stirring speed 300 rpm.

converting FALc to EFE and EL even after 2nd recycling. Though there is a decrease in FALc conversion (85% to 71%) and yield of EFE (28% to 23%), and EL (26% to 17%). The decrease in catalytic activity is due to the deactivation of active sites by the deposition of insoluble humins which is confirmed by the ATR-FTIR analysis of the used catalyst (Fig. S8.). The comparative ATR-FTIR spectra of the fresh and used catalyst given in the supplementary file (Fig. S8.) clearly show that there are emerging new IR bands at 1708 cm^{-1}, 1625 cm^{-1}, 1436 cm^{-1}, 1079 cm^{-1}, and 1018 cm^{-1} along with little suppression in IR transmittance as compared to fresh sample. The new IR band that emerged at 1708 cm^{-1} corresponds to stretching vibrations of C = O which is conjugated with C = C, while the band at 1625 cm^{-1} corresponds to C = C stretching conjugated with C = O and these are the characteristic bands for humins [34,35]. The band at 1436 can be assigned to CH$_2$ deformation vibration in aliphatic chains while the band at 1018 cm^{-1} in humins corresponds to C = C stretching, in the olefinic group and the Strong band at 1076 cm^{-1} corresponds to C–O stretching [34,35]. ATR-FTIR study confirmed a deposition of humins on the catalyst's active surface, which is the main reason for catalyst deactivation. While powder XRD of the fresh and used samples (Fig. S7. provided in supporting file) shows no distinct crystallographic changes in UiO-66-NH$_2$—HPW after the reaction. However, the used catalyst becomes brown (Image in the inset of Fig. S7.) due to the deposition of humins.

5.5. *Catalytic conversion of FFR*

UiO-66-NH$_2$—HPW catalyst was further evaluated for direct conversion of FFR to FALc, EFE, and EL in one step. FFR has been considered one of the most promising platform molecules directly derived from biomass. The hydrogenation of FFR is one of the most versatile reactions to upgrade furanic components to FALc, FE, and AL (Scheme 3) via catalytic transfer hydrogenation, etherification, and alcoholysis, in one step. UiO-66-NH$_2$—HPW was further evaluated for this one-step reaction using different alcohols such as methanol, ethanol, and IPA. These solvents were also used as a hydrogen donor for hydrogenation of FFR to FAlc along with its consumption for etherification to FE and further to AL. Formed products were identified by GC–MS (Fig. S6.) and data is given in supporting files as Fig. S9. Despite 95% FFR conversion in methanol media it shows only 23% MFE formation while in the case of ethanol 87% FFR conversion with 39% FAlc, 11% EFE and 7% EL formation was observed. IPA as a well-known hydrogen donor for the catalytic transfer hydrogenation type of reaction has shown 25% FALc, 33% IPFE, and 13% IPL with 98% conversion of FFR. This confirmed that, amongst those studied, IPA is the best hydrogen donor and solvent system for this reaction.

5.6. *Comparison of present catalytic system with literature*

The catalytic activity of present works has been compared with reported literature and summarized in Table 3. Gao et al. directly used inorganic Brønsted acidic H$_3$PO$_4$ with lewis acidic CrCl$_3$ for conversion of FALc with ethanolic media gave 38% EL at 96% conversion [36]. Annatelli et al., used highly acidic commercial sulfated resin Purolite CT151, with 50 wt.% catalyst loading at reflux conditions to get 63% EL yield [37]. Natsir et al. evaluated commercial kaolinite at a high temperature of 180 °C with external N$_2$ pressure (0.8 MPa) and 50 wt.% catalyst loading to achieve 57% FALc conversion and 62% EFE selectivity [38]. Zuo et al. used conventional zeolite Silico-Alumino-Phosphate-34 (SAPO-34) with 35 wt.% loading and with 0.5 MPa external argon pressure to convert 43% FALc with 16% EFE and 4% EL yield [39]. Li et al. developed an H-ZSM-5 catalyst with Nano b-axis channels (CNB-H-ZSM-5) with Si/Al=75, 30 wt.% catalyst amount in reaction, with 2 MPa N$_2$ pressure, and a longer reaction time (6 h), achieved 100% FALc conversion at a low EFE yield of 6.1% and EL yield of 60.5% [40]. Siva et al. used TPA (tungstophosphoric acid) impregnated on mesoporous silica SBA-16, sample 25TS (25% TPA impregnated on SBA-16) with high acidity (2.17 mmol/g) and higher loading in reaction (3.05 substrate to catalyst ratio) converted 100% FALc with 20% EL selectivity [41]. In the present work, the catalyst (UiO-66-NH$_2$—HPW) with moderate acidity (0.436 mmol g^{-1}), low catalyst loading with respect to the substrate (20 wt.%), and without any external pressure converted 97% FALc and achieved 31% EFE and 29% EL yield, the present catalyst was also able to convert FFR by catalytic transfer hydrogenation to FALc, FE, and AL, in one step. In short, the present catalyst UiO-66-NH$_2$—HPW has high SA, moderate acidity and well dispersed HPW active sites on the porous framework of UiO-66-NH$_2$ is collectively responsible for high catalytic activity at a low catalyst amount in reaction.

6. Conclusion

In this study, UiO-66-NH$_2$ MOF was successfully modified at a molecular level by a post-synthetic modification approach and immobilized a superacid HPW by acid-basic interaction of -NH$_2$ group of UiO-66-NH$_2$ and HPW to obtain UiO-66-NH$_2$—HPW as a catalyst. The prepared

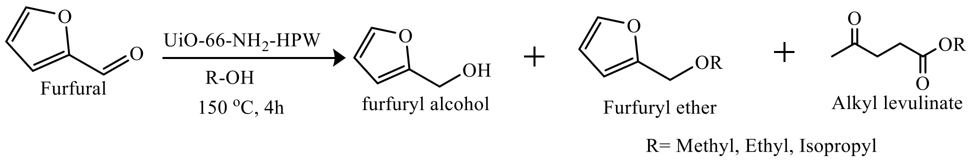

Scheme 3. Catalytic conversion of FFR to FALc, FE, AL.

Table 3
Comparison of present catalytic system with literature.

Sr.No.	Catalyst(wt.% wrt FALc)	Catalyst properties		Reaction conditions			% Conversion	% Yield		Ref.No.
		SA(m^2/g)	Acidity(mmol/g)	Temp. (°C)	Time (h)	E.P. MPa		EFE	EL	
1	CrCl$_3$ + H$_3$PO$_4$ (3.5 mol%)	NA	Np	110	2h	–	96	–	38	[36]
2	Purolite CT151 (50 wt.%)	12–25	Np	80[a]	5	NA	100	–	63	[37]
3	Kaolinite (50 wt.%)	np	0.431	180	2	0.8 N$_2$	57	62[b]	–	[38]
4	SAPO-34 (35 wt.%)	444	0.399	160	2	0.5 Ar	43	16	4	[39]
5	CNB-H-ZSM-5 Si/Al=75(30 wt.%)	455	0.25	120	6	2 N$_2$	100	6.1	60.5	[40]
6	25TS (TPA/SBA-16) (300 wt.%)	216	2.17	80	3	–	100	–	20[b]	[41]
7	UiO-66-NH$_2$—HPW (20 wt.%)	669	0.436	150	4	–	97	31	29	This work

SA=BET Surface area, E.P.=External pressure, NA=Not applicable, np=not provided
[a] Reaction under reflux condition
[b] Selectivity (%),.

catalyst has a BET surface area of 669 m^{2}g^{-1} with a total pore volume and pore diameter of 399 cm^{3}g^{-1} and 3.385 nm, respectively. SEM, HR-TEM, and powder XRD were performed to analyze the morphology and phase of UiO-66-NH$_2$—HPW, and confirm the intactness of octahedral morphology and identical phase of UiO-66-NH$_2$ after post-synthetic modification. ATR-FTIR spectroscopy and XPS results confirmed the protonation and interaction between HPW and the -NH$_2$ group of UiO-66-NH$_2$ and EDS mapping confirms the good distribution of HPW in the UiO-66-NH$_2$ crystal. NH$_3$-TPD results showed that there is a high increment in strong acid sites with an increase in total acidity in a post synthetical modified sample UiO-66-NH$_2$—HPW (0.436 mmol g^{-1}) than the parent UiO-66-NH$_2$ (0.301 mmol g^{-1}). Well-characterized catalysts were evaluated for catalytic etherification and alcoholysis of FALc and found to be better than the parent one. UiO-66-NH$_2$—HPW catalyst has shown 97 mol% FALc conversions, 31 mol% EFE yield, and 29 mol% EL yield. This catalyst could also be reused after reaction by simple washing and drying for multiple reuses. Further, this acidic catalyst was also evaluated for direct conversion of FFR to FALc, FE, and AL, in one step.

Declaration of Competing Interest

The authors declare no conflict of interest.

Data Availability

Data will be made available on request.

Supplementary materials

Supplementary material associated with this article can be found, in the online version, at doi:10.1016/j.mcat.2022.112689.

References

[1] Y. Zhou, G. Chen, Z. Long, J. Wang, Recent advances in polyoxometalate-based heterogeneous catalytic materials for liquid-phase organic transformations, RSC Adv. 4 (2014) 42092–42113, https://doi.org/10.1039/c4ra05175k.

[2] M.A. Hanif, S. Nisar, U. Rashid, Supported solid and heteropoly acid catalysts for production of biodiesel, Catal. Rev. Sci. Eng. 59 (2017) 165–188, https://doi.org/10.1080/01614940.2017.1321452.

[3] P.A. Jalil, M. Faiz, N. Tabet, N.M. Hamdan, Z. Hussain, A study of the stability of tungstophosphoric acid, H3PW 12O40, using synchrotron XPS, XANES, hexane cracking, XRD, and IR spectroscopy, J. Catal. 217 (2003) 292–297, https://doi.org/10.1016/S0021-9517(03)00066-6.

[4] M. José, D. Silva, A. Aparecida, S. Olavo, R. Chagas, D. Silva, D. Morais, Tin (II) phosphotungstate heteropoly salt: an efficient solid catalyst to synthesize bioadditives ethers from glycerol, Fuel 254 (2019), 115607, https://doi.org/10.1016/j.fuel.2019.06.015.

[5] X. Kong, S. Wu, L. Liu, S. Li, J. Liu, Continuous synthesis of ethyl levulinate over Cerium exchanged phosphotungstic acid anchored on commercially silica gel pellets catalyst, Mol. Catal. 439 (2017) 180–185, https://doi.org/10.1016/j.mcat.2017.07.005.

[6] C. Travers, N. Essayem, M. Delage, S. Quelen, Heteropolyanions based catalysts for paraffins isomerization, Catal. Today 65 (2001) 355–361, https://doi.org/10.1016/S0920-5861(00)00590-3.

[7] H.P. Winoto, Z.A. Fikri, J.-.M. Ha, Y.-.K. Park, H. Lee, D.J. Suh, J. Jae, Heteropolyacid supported on Zr-Beta zeolite as an active catalyst for one-pot transformation of furfural to γ-valerolactone, Appl. Catal. B 241 (2019) 588–597, https://doi.org/10.1016/j.apcatb.2018.09.031.

[8] L. Pesaresi, D.R. Brown, A.F. Lee, J.M. Montero, H. Williams, K. Wilson, Cs-doped H4SiW12O40 catalysts for biodiesel applications, Appl. Catal. A Gen. 360 (2009) 50–58, https://doi.org/10.1016/j.apcata.2009.03.003.

[9] K. Narasimharao, D.R. Brown, A.F. Lee, A.D. Newman, P.F. Siril, S.J. Tavener, K. Wilson, Structure – activity relations in Cs-doped heteropolyacid catalysts for biodiesel production, J. Catal. 248 (2007) 226–234, https://doi.org/10.1016/j.jcat.2007.02.016.

[10] H. Eom, D. Lee, S. Kim, S. Chung, Y. Gul, K. Lee, Hydrocracking of extra-heavy oil using Cs-exchanged phosphotungstic acid (Cs x H 3 À x PW 12 O 40, x = 1 –3) catalysts, Fuel 126 (2014) 263–270, https://doi.org/10.1016/j.fuel.2014.02.060.

[11] Q. Zeng, S. Guo, Y. Sun, Z. Li, W. Feng, Protonation-induced enhanced optical-light photochromic properties of an inorganic-organic phosphomolybdic acid/polyaniline hybrid thin film, Nanomaterials 10 (2020) 1–18, https://doi.org/10.3390/nano10091839.

[12] M. Hasik, A. Pron, J. Poźniczek, A. Bielański, Z. Piwowarska, K. Kruczala, R. Dziembaj, Physicochemical and catalytic properties of ployaniline protonated with 12-molybdophosphoric acid, J. Chem. Soc., Faraday Trans. 90 (1994) 2099–2106, https://doi.org/10.1039/FT9949002099.

[13] K. Inumaru, T. Ishihara, Y. Kamiya, T. Okuhara, S. Yamanaka, Water-tolerant, highly active solid acid catalysts composed of the keggin-type polyoxometalate H3PW12O40 immobilized in hydrophobic nanospaces of organomodified mesoporous silica, Angew. Chem. Int. Ed. 46 (2007) 7625–7628, https://doi.org/10.1002/ANIE.200702478.

[14] N. Mizuno, S. Uchida, K. Kamata, R. Ishimoto, S. Nojima, K. Yonehara, Y. Sumida, Heterogeneous Catalysis A Flexible Nonporous Heterogeneous Catalyst for Size-Selective Oxidation through a Bottom-Up Approach**, Angew. Chem. Int. Ed. 49 (2010) 9972–9976, https://doi.org/10.1002/anie.201005275.

[15] L. Leclercq, A. Mouret, A. Proust, V. Schmitt, P. Bauduin, J.-.M. Aubry, V. Nardello-Rataj, Pickering emulsion stabilized by catalytic polyoxometalate nanoparticles: a new effective medium for oxidation reactions, Chem. Eur. J. 18 (2012) 14352–14358, https://doi.org/10.1002/chem.201201799.

[16] A. Dhakshinamoorthy, A.M. Asiri, H. García, Metal–organic frameworks as multifunctional solid catalysts, Trend. Chem. 2 (2020) 454–466, https://doi.org/10.1016/j.trechm.2020.02.004.

[17] F.G. Cirujano, A. Dhakshinamoorthy, Engineering of active sites in metal–organic frameworks for biodiesel production, Adv. Sustain. Syst. 5 (2021), 2100101, https://doi.org/10.1002/adsu.202100101.

[18] R. Fang, A. Dhakshinamoorthy, Y. Li, H. Garcia, Metal organic frameworks for biomass conversion, Chem. Soc. Rev. 49 (2020) 3638–3687, https://doi.org/10.1039/d0cs00070a.

[19] A. Dhakshinamoorthy, A. Santiago-Portillo, A.M. Asiri, H. Garcia, Engineering UiO-66 metal organic framework for heterogeneous catalysis, ChemCatChem 11 (2019) 899–923, https://doi.org/10.1002/cctc.201801452.

[20] M.J. Katz, Z.J. Brown, Y.J. Colón, P.W. Siu, K.A. Scheidt, R.Q. Snurr, J.T. Hupp, O. K. Farha, A facile synthesis of UiO-66, UiO-67 and their derivatives, Chem. Commun. 49 (2013) 9449–9451, https://doi.org/10.1039/c3cc46105j.

[21] R.J. Marshall, R.S. Forgan, Postsynthetic modification of zirconium metal-organic frameworks, Eur. J. Inorg. Chem. 2016 (2016) 4310–4331, https://doi.org/10.1002/ejic.201600394.

[22] M. Samaniyan, M. Mirzaei, R. Khajavian, H. Eshtiagh-Hosseini, C. Streb, Heterogeneous catalysis by polyoxometalates in metal-organic frameworks, ACS Catal. 9 (2019) 10174–10191, https://doi.org/10.1021/acscatal.9b03439.

[23] V.E. Tarabanko, M.Y. Chernyak, I.L. Simakova, K.L. Kaigorodov, Y.N. Bezborodov, N.F. Orlovskaya, Antiknock properties of furfural derivatives, Russ. J. Appl. Chem. 88 (2015) 1778–1782, https://doi.org/10.1134/S10704272150110063.

[24] J.P. Lange, R. Price, P.M. Ayoub, J. Louis, L. Petrus, L. Clarke, H. Gosselink, Valeric biofuels: a platform of cellulosic transportation fuels, Angew. Chem. Int. Ed. 49 (2010) 4479–4483, https://doi.org/10.1002/anie.201000655.

[25] A. Démolis, N. Essayem, F. Rataboul, Synthesis and applications of alkyl levulinates, ACS Sustain. Chem. Eng. 2 (2014) 1338–1352, https://doi.org/10.1021/sc500082n.

[26] F. Zaccheria, N. Scotti, N. Ravasio, D.E.E. Dbe, Solid acids for the reaction of bioderived alcohols into ethers for fuel applications, Catalysts 9 (2019), 9020172, https://doi.org/10.3390/catal9020172.

[27] Rene Johan Haan, J.-.P. Lange, (12) United States Patent, US 8,372,164 B2, 2013. https://doi.org/10.1038/incomms1464.

[28] F. Vermoortele, A. Vimont, C. Serre, D. de Vos, An amino-modified Zr-terephthalate metal–organic framework as an acid–base catalyst for cross-aldol condensation, Chem. Commun. 47 (2011) 1521–1523, https://doi.org/10.1039/c0cc03038d.

[29] M. Kandiah, S. Usseglio, S. Svelle, U. Olsbye, K.P. Lillerud, M. Tilset, Post-synthetic modification of the metal-organic framework compound UiO-66, J. Mater. Chem. 20 (2010) 9848–9851, https://doi.org/10.1039/c0jm02416c.

[30] X. Fang, S. Wu, Y. Wu, W. Yang, Y. Li, J. He, P. Hong, M. Nie, C. Xie, Z. Wu, K. Zhang, L. Kong, J. Liu, High-efficiency adsorption of norfloxacin using octahedral UIO-66-NH2 nanomaterials: dynamics, thermodynamics, and mechanisms, Appl. Surf. Sci. 518 (2020), 146226, https://doi.org/10.1016/j.apsusc.2020.146226.

[31] X. Yang, X. Jiang, Y. Huang, Z. Guo, L. Shao, Building nanoporous metal-organic frameworks “armor” on fibers for high-performance composite materials, ACS Appl. Mater. Interface. 9 (2017) 5590–5599, https://doi.org/10.1021/acsami.6b15098.

[32] Q. Chen, Q. He, M. Lv, Y. Xu, H. Yang, X. Liu, F. Wei, Selective adsorption of cationic dyes by UiO-66-NH2, Appl. Surf. Sci. 327 (2015) 77–85, https://doi.org/10.1016/J.APSUSC.2014.11.103.

[33] M. Peñas-Garzón, M.J. Sampaio, Y.L. Wang, J. Bedia, J.J. Rodriguez, C. Belver, C. G. Silva, J.L. Faria, Solar photocatalytic degradation of parabens using UiO-66-NH2, Sep. Purif. Technol. 286 (2022), 120467, https://doi.org/10.1016/j.seppur.2022.120467.

[34] X. Gao, L. Peng, H. Li, K. Chen, Formation of humin and alkyl levulinate in the acid-catalyzed conversion of biomass-derived furfuryl alcohol, Bioresources 10 (2015) 6548–6564.

[35] J.M. Pin, N. Guigo, A. Mija, L. Vincent, N. Sbirrazzuoli, J.C. van der Waal, E. de Jong, Valorization of biorefinery side-stream products: combination of humins with polyfurfuryl alcohol for composite elaboration, ACS Sustain. Chem. Eng. 2 (2014) 2182–2190, https://doi.org/10.1021/sc5003769.

[36] X. Gao, X. Yu, R. Tao, L. Peng, Enhanced conversion of furfuryl alcohol to alkyl levulinates catalyzed by synergy of CrCl3 and H3PO4, Bioresources 12 (2017) 7642–7655.

[37] M. Annatelli, G. Trapasso, L. Lena, F. Aricò, Alkyl levulinates from furfuryl alcohol using CT151 Purolite as heterogenous catalyst: optimization, purification, and recycling, Sustain. Chem. 2 (2021) 493–505, https://doi.org/10.3390/suschem2030027.

[38] T.A. Natsir, T. Hara, N. Ichikuni, S. Shimazu, Kaolinite catalyst for the production of a biodiesel-based compound from biomass-derived furfuryl alcohol, ACS Appl. Energy Mater. 1 (2018) 2460–2463, https://doi.org/10.1021/acsaem.8b00694.

[39] Y. Ji, Y. Zuo, H. Liu, F. Wang, X. Guo, Synthesis of silico-phospho-aluminum nanosheets by adding amino acid and its catalysis in the conversion of furfuryl alcohol to fuel additives, ChemSusChem 15 (2022), e202200747, https://doi.org/10.1002/cssc.202200747.

[40] Y. Li, S. Wang, S. Fan, B. Ali, X. Lan, T. Wang, Nano-H-ZSM-5 with short b-axis channels as a highly efficient catalyst for the synthesis of ethyl levulinate from furfuryl alcohol, ACS Sustain. Chem. Eng. 10 (2022) 3808–3816, https://doi.org/10.1021/acssuschemeng.1c06695.

[41] E. Siva Sankar, K. Saidulu Reddy, Y. Jyothi, B. David Raju, K.S. Rama Rao, Alcoholysis of furfuryl alcohol into n-butyl levulinate over SBA-16 supported heteropoly acid catalyst, Catal. Lett. 147 (2017) 2807–2816, https://doi.org/10.1007/s10562-017-2155-9.